ALMA MATER STUDIORUM - UNIVERSITÀ DI BOLOGNA

DOTTORATO DI RICERCA IN
CHIMICA
Ciclo XXXIII

Settore concorsuale: 03/C2 – Chimica Industriale

Settore scientifico disciplinare: CHIM/04 – Chimica Industriale

Advanced electrospun nanofibrous mats for hindering delamination, improving damping and for sensing of composite laminates

Presentata da **Emanuele Maccaferri**

Coordinatore dottorato   Supervisore

Prof.ssa Domenica Tonelli   **Prof. Loris Giorgini**

Co-supervisori

Prof.ssa Laura Mazzocchetti
Prof. Andrea Zucchelli
Prof.ssa Tiziana Benelli
Prof.ssa Stefania Albonetti

Esame finale anno 2021

Index

Abstract

Chapter 1

INTRODUCTION

Chapter 2

RUBBERY NANOFIBERS BY CO-ELECTROSPINNING OF ALMOST IMMISCIBLE NBR AND PCL BLENDS

Chapter 3

RUBBERY NANOFIBROUS INTERLEAVES ENHANCE FRACTURE TOUGHNESS AND DAMPING OF CFRP LAMINATES .... 3•1

Chapter 4

DAMPING AND MECHANICAL BEHAVIOUR OF COMPOSITE LAMINATES INTERLEAVED WITH RUBBERY NANOFIBERS .... 4•1

Chapter 5

SELF-ASSEMBLY NBR/NOMEX NANOFIBERS AS LIGHTWEIGHT RUBBERY NONWOVENS FOR HINDERING DELAMINATION IN EPOXY CFRPs

Chapter 6

SELF-SENSING HYBRID COMPOSITE LAMINATE BY PIEZOELECTRIC NANOFIBERS INTERLEAVING

Chapter 7

MORPHOLOGY, THERMAL, MECHANICAL PROPERTIES AND AGEING OF NYLON 6,6/GRAPHENE NANOFIBERS AS NANO² MATERIALS

Chapter 8

HOW NANOFIBERS CARRY THE LOAD: TOWARDS A UNIVERSAL AND RELIABLE APPROACH FOR TENSILE TESTING OF POLYMERIC NANOFIBROUS MEMBRANES

Chapter 9
CONCLUSIONS

Abstract

Carbon Fiber Reinforced Polymers (CFRPs) display high specific mechanical properties, allowing the creation of lightweight components and products by metals replacement. To reach outstanding mechanical performances, the use of stiff thermoset matrices, like epoxy, is preferred. Laminated composites are commonly used for their ease of manipulation during object manufacturing. However, the natural anisotropic structure of laminates makes them vulnerable toward delamination. Moreover, epoxy-based CFRPs are very stiff materials, thus showing low damping capacity, which results in unwanted vibrations and structure-borne noise that may contribute to delamination triggering.

Hence, searching for systems able to limit these drawbacks is of primary importance for safety reasons, as well as for economic ones.

In this experimental thesis, the production and integration of innovative rubbery nanofibrous mats into CFRP laminates are presented. A smart approach, based on single-needle electrospinning of rubber-containing blends, is proposed for producing dimensionally stable rubbery nanofibers without the need for rubber crosslinking. Nano-modified laminates aim at obtaining structural composites with improved delamination resistance and enhanced damping capacity, without significantly lowering other relevant mechanical properties. The possibility of producing nanofibers nano-reinforced with graphene to be applied for reinforcing composite laminates is also investigated. Moreover, the use of piezoelectric nanofibrous mats in hybrid composite laminates for achieving self-sensing capability is presented too as a different approach to prevent the catastrophic consequences of possible structural laminate failure.

Finally, an accurate, systematic, and critical study concerning tensile testing of nonwovens, using electrospun Nylon 66 random nanofibrous mats as a case study, is proposed. Nanofibers diameter and specimen geometry were investigated to thoroughly describe the nanomat tensile behaviour, also considering the polymer thermal properties, and the number of nanofibers crossings as a function of the nanofibers diameter. Stress-strain data were also analysed using a phenomenological data fitting model to interpret the tensile behaviour better.

Chapter 1

INTRODUCTION

This chapter aims at introducing composite materials, their strengths and weaknesses, and solutions for limiting the critical aspects regarding these engineered materials.

High-performance composites, like epoxy-based Carbon Fiber Reinforced Polymers (CFRPs), show an increasing use as replacement for metallic materials. Laminated composites are promising, but show some drawbacks, e.g. delamination and low damping capacity, that may limit their use.

Possible solutions to contrast these limitations will be presented, focusing on the use of electrospun nanofibrous mats to be interleaved into composite laminates during the lamination step before curing. Indeed, nanofibers are smart and versatile nanomaterials currently used in lots of different fields and applications, including (but not limited to) the ones reported in FIGURE 1.1.
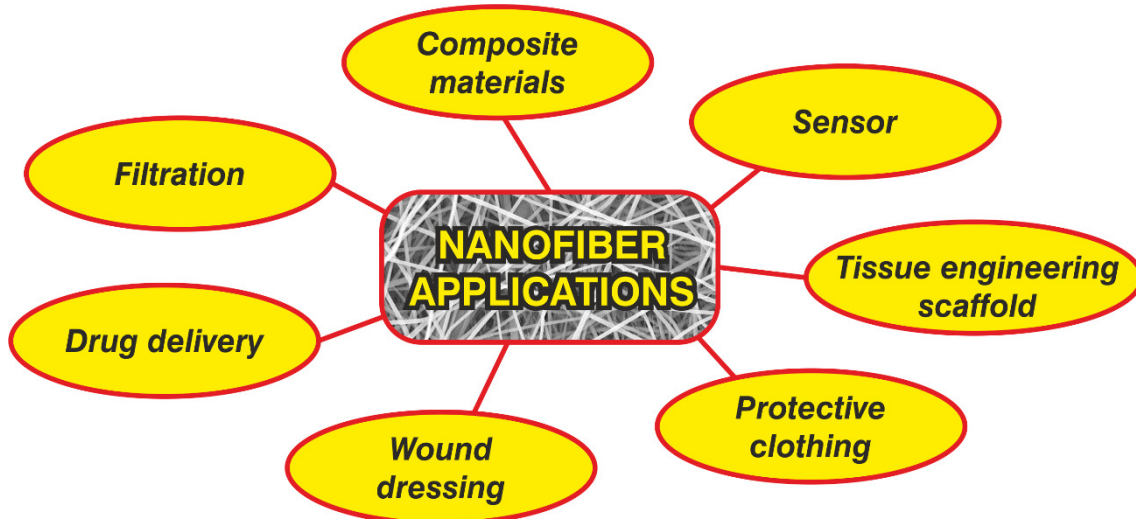
FIGURE 1.1 • Examples of possible applications of nanofibers.
(Author's own illustration.)

Electrospinning process will be presented too in SECTION 1.6 for better understanding the parameters which affect the production of nanofibrous mats.

1.1 • COMPOSITE MATERIALS AND CFRP LAMINATES

Recently, composites are replacing an increasing number of traditional materials, like metals, in several structural applications for benefitting of lightweight without sacrificing mechanical performances.

A composite is a material consisting of at least two components of distinct nature, joined together with a clear interface to obtain a new material that displays different properties with respect to the ones of the single constituents [1]. Indeed, composites aim at obtaining a more suitable material for the application for which they are designed, exploiting one or more properties exhibited by the single constituents.

In general, composites consist of a matrix (continuous phase) and a reinforcement (discontinuous phase). Both phases can be organic or inorganic; however, the reinforcement must have a stiffness, i.e. an elastic modulus, significantly higher than the matrix to bring remarkable benefits to mechanical properties.

Limiting the present discussion to composites with carbon fibers as reinforcement and polymeric matrix, carbon fiber reinforced polymers are among the most widely used. Particularly, thermosetting CFRPs, such as epoxy-based ones (FIGURE 2), are much appreciated for their excellent specific properties. Thanks to their low density, they show high specific elastic modulus and strength, so that they may compete with traditional metallic materials like aluminium and steel.
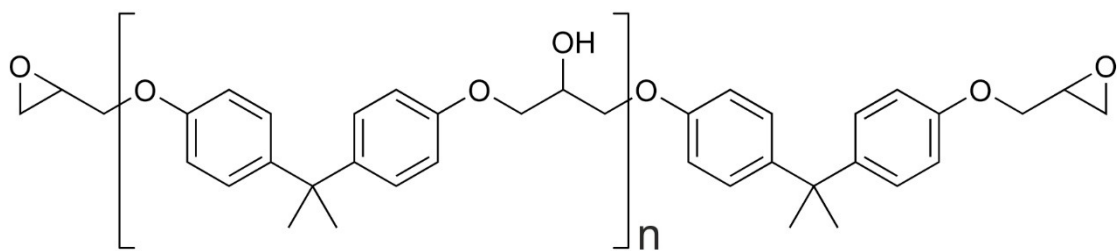
FIGURE 2 • A common epoxy resin based on Bisphenol A diglycidyl ether (DGEBA).
(Author's own illustration.)

CFRPs allow the creation of lightweight objects with excellent mechanical properties, making them highly valued in fields where lightness is a crucial factor. Present applications of CFRPs include aerospace, military airplanes, racing cars and sailboats,

blades for wind turbines and constructions [2]. However, this field has been experiencing steady growth which is lately expanding towards more mass-oriented market segments such as the mainstream automotive and motorcycle.

Laminated composites, i.e. constituted by the juxtaposition of prepregs, are commonly used for their ease of manipulation during object manufacturing (lamination step), being processable by vacuum bag and autoclave technology, as well as by moulding technology.

A schematic representation of thermosetting composite laminates production is depicted in FIGURE 1.3.
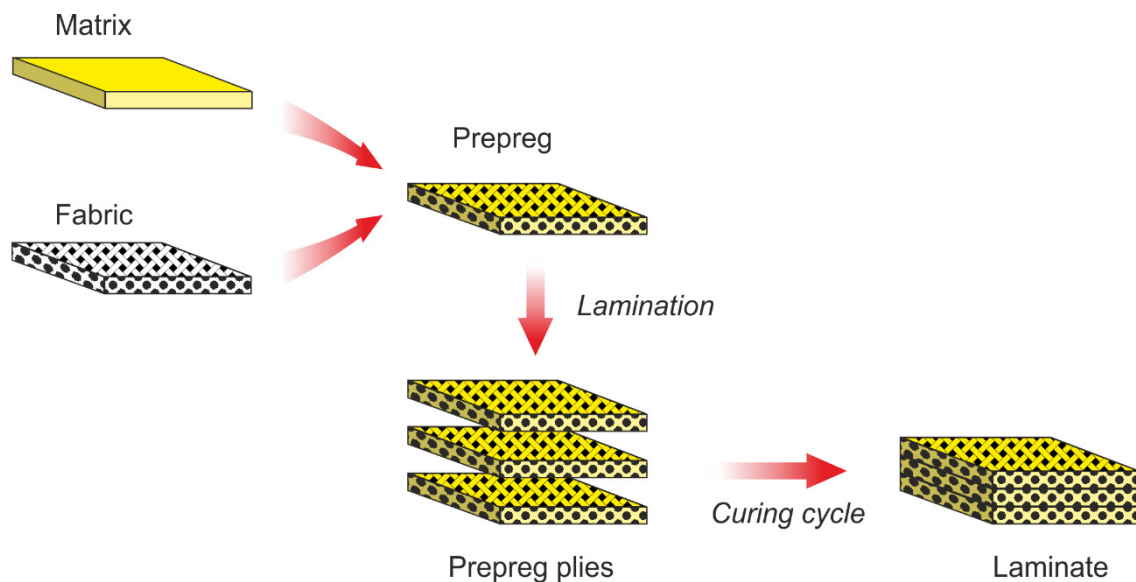
FIGURE 1.3 • Schematic representation of a thermosetting composite laminate production, such as epoxy-based CFRP.
(Author's own illustration.)

While displaying many attractive specific mechanical properties, laminated CFRPs show severe drawbacks, like delamination [3] and low damping capacity [4], that still today may limit their widespread application.

To avoid the catastrophic consequences of delamination, it is possible to act on two sides: i) providing technical solutions able to promptly detect hazardous conditions, and ii) increasing the intrinsic resistance of the laminate. Systems that allow the Structural Health Monitoring (SHM) [5], i.e. the monitoring of component health, like the use of Bragg fibers or piezoelectric fibers [6], face the safety problem acting mainly on

protection enhancement (case i). However, some of these systems may themselves promote crack triggering [7], thus limiting their application. The other way (case ii) aims at producing laminates with improved interlaminar fracture toughness, making more difficult the crack triggering and, consequently, the failure by delamination. This approach addresses the issue upstream, so from a *prevention* point of view.

In the following SECTIONS 1.2, 1.3 and 1.5, these problematic aspects related to CFRP laminates will be addressed, together with possible solutions to limit the related issues.

1.2 • DELAMINATION AND SOLUTIONS FOR LIMITING THE PHENOMENON

The natural anisotropic structure of composite laminates makes them vulnerable toward delamination. This phenomenon relates to the debonding of the constituent laminae, caused by microcracks formation, which leads to the development of cracks and, finally, to complete component failure [8] (FIGURE 1.4).
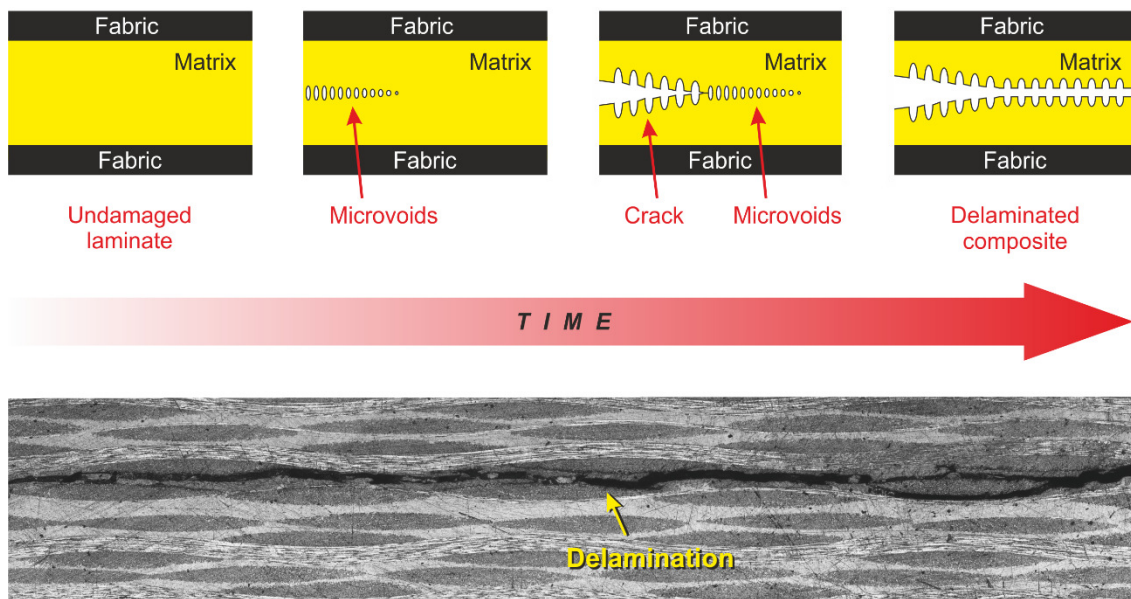
FIGURE 1.4 • Top: schematic representation of microcracks and cracks formation in fabric composite laminates; bottom: optical micrograph showing delamination in a CFRP composite.
(Author's own illustration.)

Although delamination is not the unique failure mode of a laminate, among the others (e.g. intra-ply cracking and fiber breaking) is the most common one [3].

While in the *x-y* plane the laminate strength is relatively high, with mechanical properties possibly orthotropic or even, by using properly oriented fabric (warp and weft) prepregs, *quasi*-isotropic, along the *z*-axis the situation is entirely different. Indeed, between adjacent plies there is only the matrix, which undoubtedly exhibits poorer mechanical properties than the fabric, be it carbon, aramidic or glass one.

Given sufficient bonding strength between matrix and reinforcement, the continuous phase is the most sensitive toward delamination. Epoxy resins used for high-performance CFRPs, as well as thermosets in general, show a mechanical behaviour characterized by a fragile fracture, as a consequence of their high stiffness, at least when compared to other

thermoplastics. Therefore, cracks mainly propagate in the lowest stiffness medium, which is the interlaminar matrix-rich region [8,9]. It is worth noting that high overall stiffness determines a low damping capacity, i.e. the ability to dampen vibrations, leading not only to unwanted vibrations, but may also trigger delamination [4]. For these reasons, commercial epoxy matrices are toughened to mitigate their fragile behaviour and, consequently, to hinder delamination [10,11]. To this end, the addition of thermoplastics, like poly(ε-caprolactone) (PCL), to the resin, is common. Also toughening achieved by adding rubbery (elastomeric) materials is since long one of the possible ways to limit the fragile resin behaviour [10]. Indeed, rubbers show a higher damping capacity than non-elastomeric thermoplastics and thermosets counterparts.

There are several ways to add tougheners to the matrix; the main difference regards the extension of the modification: it may interest the resin bulk or only limited areas (volumes). In the first case, the toughener is necessarily blended with the resin before its use; then it is employed for prepreg production. In the latter one, instead, the modification can take place directly during the lamination step.

The bulk resin modification is often attained by adding rubbery particles, core-shell particles with a glassy shell to contain the rubbery core, or via mixing with liquid rubber (i.e. not crosslinked), often in the range of 5–20%wt [10,12–15]. The large amount of rubbery materials necessary to toughen the matrix may lower the superior mechanical properties which characterize epoxy-based composites, like the high glass transition temperature (T_g), tensile strength and elastic modulus [12]. The use of local modifiers is thus preferable with respect to bulk resin modification.

Polymeric nanofibers were proposed as local laminate modifiers about 20 years ago by Reneker and Dzenis, as reported in their patent [16]. Interleaving nanofibrous mats between CFRP plies, during prepreg lamination, is a smart and convenient way to locally modify the laminate solely in the matrix-rich region placed inter-laminae, to limit delamination [17–20], FIGURE 1.5. Indeed, these nanostructured materials can be well integrated into the composite matrix and allow to raise the interlaminar fracture toughness, i.e. the energy per square meter required for a crack to propagate.
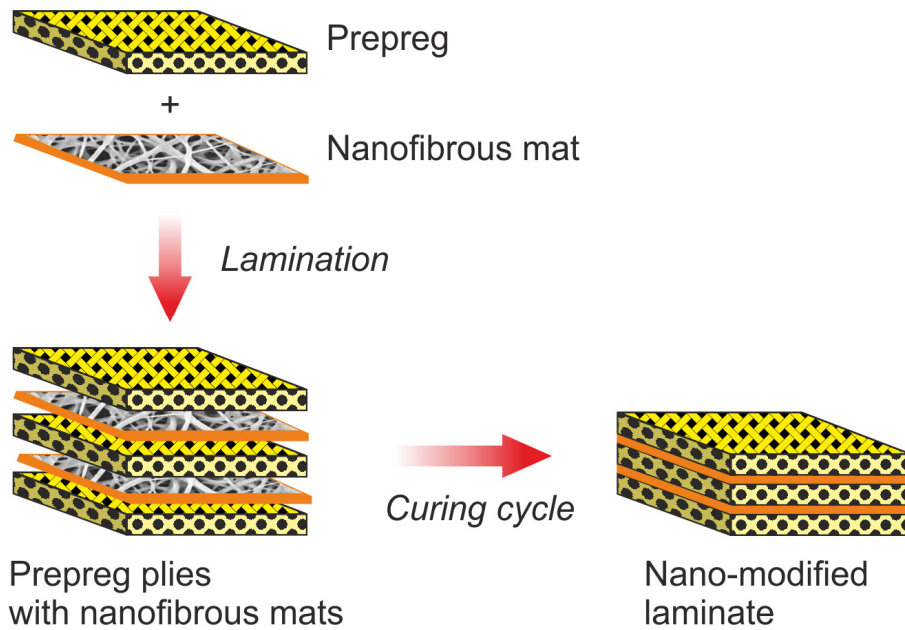
FIGURE 1.5 • Composite laminate modified with interleaved nanofibrous mats.

(Author's own illustration.)

Depending on the thermal properties of the polymers used for producing nanofibrous mats, two mechanisms of action against delamination can be outlined. These are the so-called nanofiber bridging and matrix toughening (FIGURE 1.6).
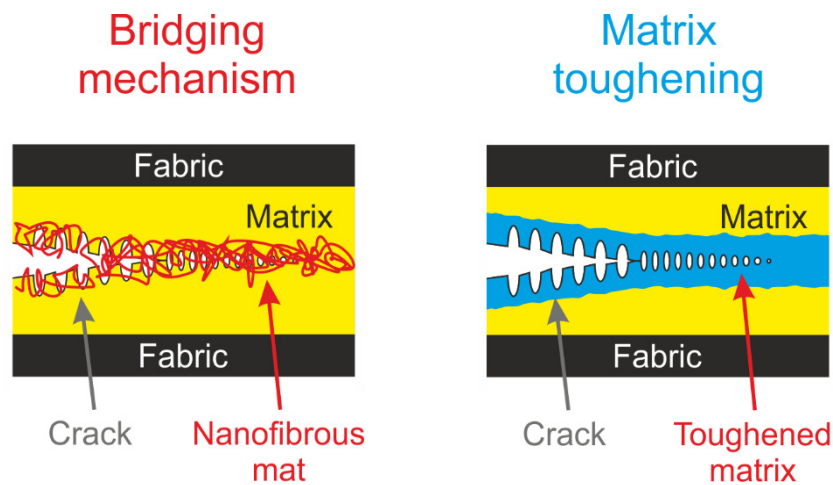
FIGURE 1.6 • Mechanisms of nanofibrous mat action against delamination.

(Author's own illustration.)

Limiting the present discussion to polymeric nanofibers, the discriminating factor is the temperature at which the nanofibers "fluidize" respect to the temperature reached during laminate curing. Semi-crystalline thermoplastic polymers with a melting temperature, T_m,

(or with a glass transition temperature, T_g, for amorphous ones) above the curing temperature still maintain the nanofibrous structure, and the nanofiber bridging is the selected mechanism [3]. In the opposite case, matrix toughening occurs with fibers that upon fluidification blend with the continuous resin phase. In the first case, the crack to propagate needs to overcome the 3D network constituted by the nanofibrous mat, thus requiring additional energy to break it. In the other case, the crack faces a less fragile matrix because of toughening induced by the thermoplastic polymer mixing with the resin. Again, the energy for propagating the crack grows. In both cases, the result can be quite similar: the interlaminar fracture toughness is improved. It is worth underlining that polymers employed should be "compatible" with the epoxy matrix: a good polymer/resin interaction at the interface is necessary for non-melting nanofibers, while miscibility for low-T_m polymers (or low-T_g for not-crystallizable ones) is required.

Microcracks and cracks develop due to external mechanical solicitations, like out-of-plane loadings (impacts) and/or relatively low loadings continuously applied (fatigue). Specific tests have been developed to evaluate the composite delamination resistance, by intentionally provoking delamination and measure the energy release rate (G) related to crack propagation.

Three different ways of applying a force to enable crack propagation can be outlined: opening mode (Mode I), sliding mode (Mode II) and tearing mode (Mode III), FIGURE 1.7.
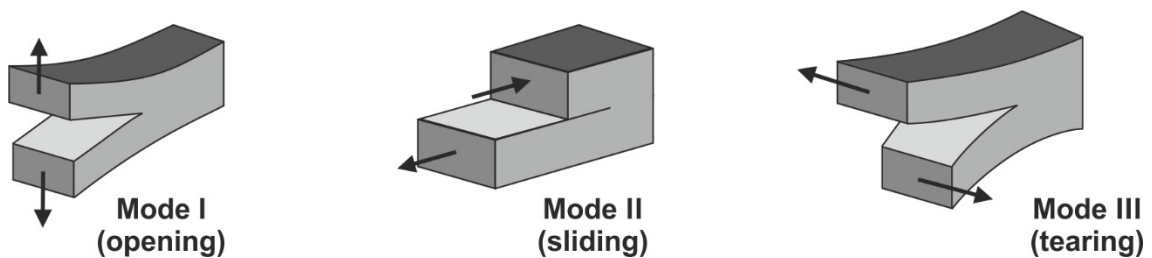
FIGURE 1.7 • Different modes of mechanical solicitation applied to a laminate.
(Author's own illustration.)

In the first one, a tensile stress is applied normal to the crack plane; in the second one, a shear stress is applied parallel to the crack plane and perpendicular to the crack front. The third mode also involves a shear stress applied parallel to the crack plane, but, differently to Mode II, it is parallel to the crack front.

In the present elaborate, only Mode I and Mode II will be discussed. Specific tests are carried out to investigate each of these two fracture modes:

• DCB – *Double Cantilever Beam* test for Mode I, according to ASTM D5528;

• ENF – *End-Notched Flexure* test for Mode II, according to DIN EN 6034.

While the testing mode is different for DCB and ENF tests (specimen tested in tensile mode and three-point bending mode, respectively), data treatment is similar. Raw load-displacement data, recorded by a Universal Testing Machine (UTM), are correlated to the crack length, continuously filmed by a video camera during testing, to obtain the energy release rate (G). As prescribed by the abovementioned standards, specimens have a pre-existent crack made by a polymeric film (commonly Teflon) conveniently inserted into the laminate mid-plane, i.e. in the central interface, for a certain length (a_0).

The energy release rate for Mode I loading (G_I, in J/m^2) is evaluated using the following formula [21]:

$$G_I = \frac{3P\delta}{2ba}1000 \qquad \text{EQUATION 1.1}$$

where P is the load (in N), δ the crosshead displacement (in mm), a the crack length (in mm), b the specimen width (in mm).

In a similar way, the energy release rate for Mode II loading (G_{II}, in J/m^2) can be evaluated using the following formula [22]:

$$G_{II} = \frac{9P\delta a^2}{2b(\frac{1}{4}L^3 + 3a^3)}1000 \qquad \text{EQUATION 1.2}$$

where L is the span length between supports (in mm).

All the presented systems used for enhancing delamination resistance aims at increasing the energy release rate (G).

The best results are clearly obtained if a significant improvement of G is achieved for G_I and G_{II}, both at initiation ($G_{I,C}$ and $G_{II,C}$) and propagation ($G_{I,R}$ and $G_{II,R}$).

As will be explained in the following SECTION 1.3, and experimentally demonstrated in CHAPTERS 3 and 4, the use of thermoplastic and elastomeric nanofibers may also contribute to improve the damping capacity of stiff materials like CFRPs laminates.

1.3 • DAMPING AND SOLUTIONS FOR ITS IMPROVEMENT

As explained in SECTION 1.1, epoxy-based CFRPs are very stiff materials, thus showing low damping capacity [4], which results in unwanted vibrations and structure-borne noise. Reduction of vibrations is desirable not only for achieving a better *comfort*, but also for lowering maintenance costs and for increasing component life [23], especially for objects operating under continuous dynamic loadings, and in agreement with the requirement of mass production [24]. For these reasons, searching for new low vibration transmission lightweight materials, or the improvement of existing ones, is of primary importance.

A viable solution to reduce structural vibrations is through damping [23], a phenomenon that involves the conversion of vibrational energy into other forms of energy, especially into heat [25]. Viscoelastic materials, such as polymers, may be exploited to add or increase damping capacity. A measure of this property is commonly carried out via the evaluation of the tanδ [26], which is also known as damping factor, loss factor or loss tangent. It represents the ratio between the loss modulus (E") and the storage modulus (E'): the first one is related to the viscous properties of the material, while the latter to the elastic behaviour. δ represents the phase shift angle between the input stress and the output strain, when the material is subjected to a sinusoidal solicitation. Polymers are viscoelastic materials, thus stress and strain curves are always out-of-phase. This behaviour is exploited for measuring the tanδ, also called damping factor, via instruments like Dynamic Mechanical Analysis (DMA).

In FIGURE 1.8 is displayed the response of a viscoelastic material upon sinusoidal solicitation.
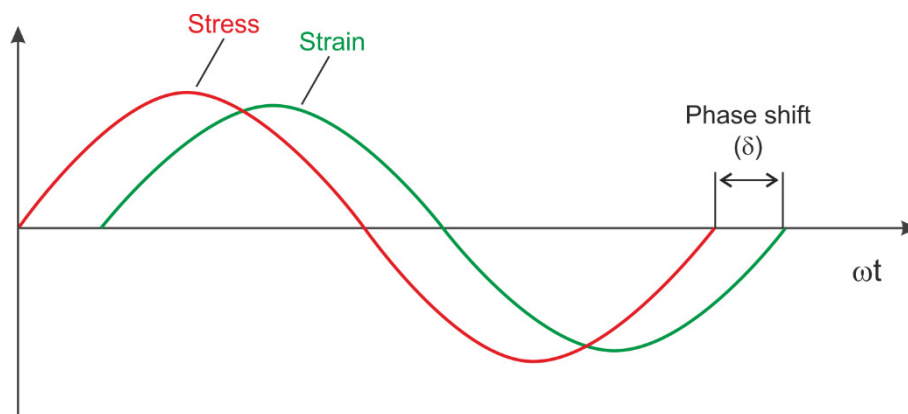
FIGURE 1.8 • Strain response of a viscoelastic material subjected to a sinusoidal input strain.
(Author's own illustration.)

To achieve improved damping properties two different pathways can be addressed: i) by applying a viscoelastic component to the structure suffering from insufficient damping or, in the case of CFRPs, ii) it is also possible to play on the modification of the matrix and/or fiber/matrix interface.

The first approach, suitable for a broad range of applications, includes passive, active and semi-active methods [27]. Passive methods, existing since the 1960s, are the most used for their cheapness and relative simplicity of implementation [28]. In the market there are several commercially available products, such as Free-Layer Damping (FLD), Constrained-Layer Damping (CLD) and Tuned Viscoelastic Damper (TVD) treatments [29]. FLD treatment is the most straightforward strategy to improve damping capacity without affecting the stiffness of the original structure. It consists in the application of a layer of high damping material (with adhesives, under pressure or sprayed) to the rigid structure to improve. The drawbacks are a significant increase of thickness and weight, since the damping capacity is proportional to the thickness of the viscoelastic layer [30], in addition to a modification of the surface appearance. The latter surely makes unpracticable FLD treatment to components also demanding aesthetic requirements. CLD treatments involve the use of sandwich-structured composites constituted by an inner layer of viscoelastic material and two outer layers that provide the required stiffness. This method is more effective than FLD approach [30], but, again, suffers from a significant increase in thickness, since vibration reduction is still proportional to the core thickness [28]. TVD treatment implies the use of viscoelastic material between two rigid objects, acting as a damper. It can filtrate single or a narrow range of frequencies, and it should be used far from the glass transition temperature (T_g) of the damping material to retain its mechanical properties [30].

The second main approach to provide damping capability is through polymer/matrix modification or by interleaving high damping materials in case of laminated composites. In CFRPs, the fibers are the stiff component, while the matrix is the tough one with some damping capability: it is thus evident that using a more damping matrix the overall composite damping will be improved. However, polymers and composites that show high damping capacity are not suitable for structural applications because of the insufficient elastic modulus in common environmental conditions. The challenge is, therefore, to increase the damping while keeping the original, or at least an acceptable,

material stiffness. Reinforcements and fillers are commonly used in the polymer industry for achieving better mechanical performances or for obtaining particular properties. For instance, epoxidized natural rubber blended with the resin may improve damping capacity, but at the expense of a drop in stiffness caused by the high fraction of rubber necessary (up to 20%wt). The use of "stiff" inorganic materials was also investigated, such as the integration of SiO_2 particles, which allows excluding drawbacks like a drop of the composite T_g. However, the enhancement of the damping factor was limited to only 4% [12].

Interlayer modification of CFRP laminates with viscoelastic materials can also represent a convenient way to improve damping capability [31]. However, a common drawback is a loss in the overall elastic modulus and strength [17], especially above the glass transition temperature of the viscoelastic material. Interlayering polymeric films [32] or micrometric nonwoven fabrics [33] are promising approaches. The use of inorganic materials or metals usually do not decrease the composite stiffness, but at the expense of increased weight. A study [13] reports that copper interlayers in glass fiber epoxy resin composites raise the loss factor of 30% at room temperature; however, copper represents up to 20% of the total weight.

Nanoscale reinforcements represent a recent additional possibility for modifying polymer and composite properties. Thanks to their nano-dimensions, they may be integrated into polymer matrix without negatively affecting weight and size, since their presence accounts for a few percentages. Although this type of reinforcements is usually applied to improve mechanical properties, when they are smartly tailored, they can be a suitable way to enhance damping capacity. Nanoscale fillers have a high aspect ratio, so a high surface area can interact with matrix and adjacent fillers, providing a positive effect on damping [34]. Several works show the use of carbon nanofibers and carbon nanotubes for damping improvement. The rise in damping stems from the interfacial friction between the nano-fillers and the polymer [35]. In particular, carbon nanotubes give excellent results, with a damping improvement of up to 4 times [34,36], and also excellent enhancements of epoxy resin and composites up to 700% [4,37]. However, these nano-fillers have high costs and may present several difficulties in the incorporation process.

Nanofibrous polymer membranes are a relatively new class of versatile materials. Nanofibers are already used in filtration, tissue engineering scaffold, drug delivery carrier, protective clothing, electronic materials and for reinforcing composites [38]. Nanofibrous mats are successfully employed for hindering delamination and for improving impact damage resistance in laminated CFRPs [17,38,39]. Composites reinforced with nanofibers show a limited increase in thickness. Moreover, the overall weight is not significantly affected, thanks to the general low density of polymers.

In this scenario, rubbery nanofibers may significantly contribute to improve the composite damping with limited effects on its size and weight. Their use will be presented in CHAPTERS 3 and 4.

1.4 • RUBBERY NANOFIBERS AS COMPOSITE MODIFIERS: STATE OF THE ART

For the reasons presented in SECTIONS 1.2 and 1.3, the possibility of producing rubbery nanofibers to be used as toughener for local modification of composite laminates appears relevant.

While the use of interleaved thermoplastic nanofibrous mats is well established in the literature since years [3,16], the integration of rubbery nanofibers is not. Until now (end of 2020) only a few works propose the production of rubbery fibers. Some example of such rubber electrospun materials is discussed below, and a selection of them also presented in FIGURE 1.9.
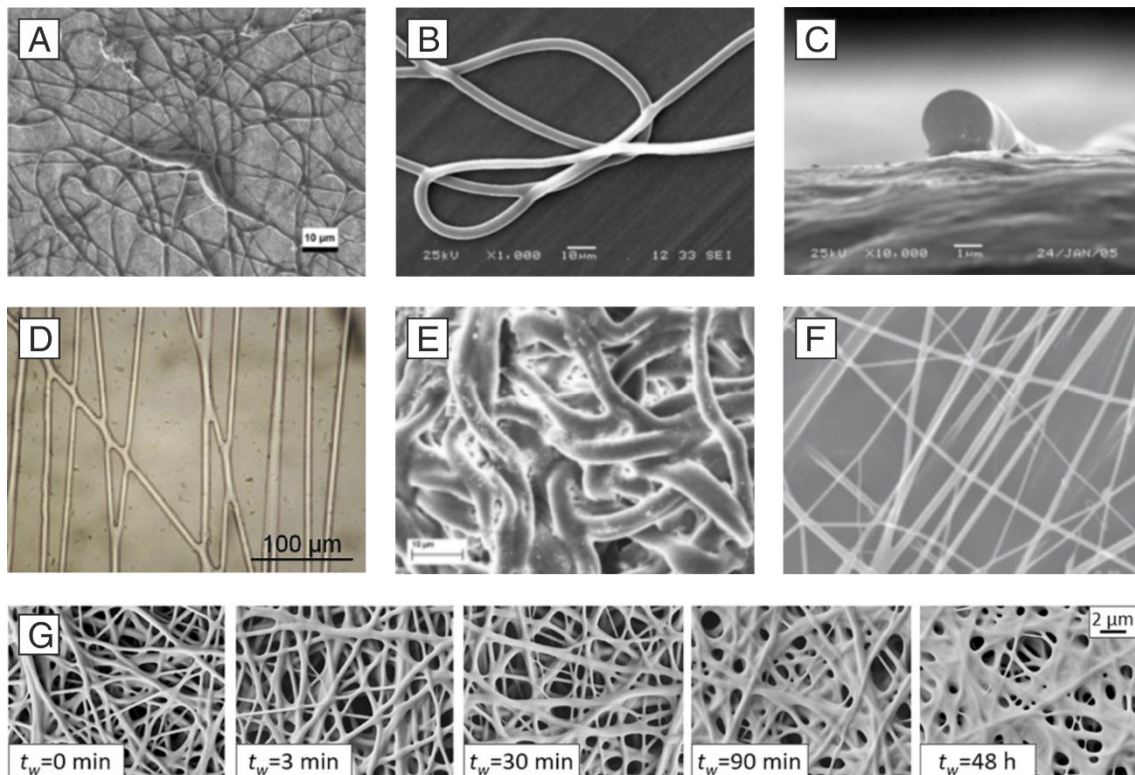
FIGURE 1.9 • Examples of electrospun rubbery materials: A) uncrosslinked Nitrile Butadiene Rubber (NBR) [40]; B) and C) polybutadiene (butadiene rubber, BR) fiber photo-crosslinked after electrospinning process [41]; D) and E) in-situ photo-crosslinked BR fibers [42,43]; F) core-shell nanofibers with a BR core and a polyvinylpirrolydone (PVP) shell [44]; G) styrene-butadiene copolymer nanofibers photo-crosslinked at different times after electrospinning process [45].
(Reproduced with permissions of the relative editors.)

Nanofibrous mats are commonly produced via electrospinning process (a presentation of the technique is given in SECTION 1.6), which represents the easiest way to obtain

fibers with nanometric diameter. However, due to the mandatory requirement of processing polymers dissolved in a suitable solvent system (i.e. homogeneous solutions), the possibility of electrospinning already crosslinked rubbers is prevented. Processing rubber precursors which are not still crosslinked (liquid rubber) is a challenging task because of the viscous behaviour at room temperature [46], that prevents the retention of a given shape for an indefinite amount of time [41,42,45]. Consequently, attempts at obtaining rubbery nanofibers are scarcely reported in the literature. In some cases, papers report just the proof of concepts of the possibility to electrospin rubber polymeric solutions [40,44,47], or they attain microfibers rather than nanofibers, with diameters in the micrometre range [43,48]. In most cases, however, the use of a curing agent in the formulation to crosslink the polymer is mandatory for avoiding nanofibers coalescence. The rubber cold flow phenomenon may be so relevant that the curing step has to be applied during electrospinning [41,42] or, at the latest, straightforwardly after the process [43,48,49], within a tightly limited time-span, down to a few minutes [45], that strongly limits the execution of the electrospinning process for a prolonged time and, in turn, the final membrane thickness attained [45].

Other attempts involve more complicated procedures. Nie *et al.* coated nanofibers in gelatin before curing to avoid coalescence [50]. Although the process brings nanofibrous membranes with good mechanical properties, it appears tricky and multistep. Kim and Kim describe the possibility of producing fully Epoxidised Natural Rubber (ENR) fibers, but they obtain microfibers and, possibly owing to the poor handling of the material, they have to electrospin it directly onto a crude resin bed [51].

Finally, a method has been reported for rubbery nanofiber production, where the ENR is blended in a variable range with polyvinylchloride (PVC) [52]. While nanofibers are reported to form, their characterization is poor, and no mechanical behaviour is discussed. Nitrile rubber has been blended with epoxy resin and electrospun to produce highly stretchable electrodes, but the crosslinking step is still required to maintain the nanofibrous morphology [49]. In this context, searching for simple procedures to obtain rubbery nanofibers is highly valuable.

The blending approach, i.e. the rubber mixing with a thermoplastic not-elastomeric polymer, to produce stable nanofibers could be a premiant idea. Nonetheless, blending

is a simple and effective way to favourably combine attractive properties of different polymers in a single material, thus overcoming limitations and drawbacks associated with the single component. Miscible polymer blends can be easily recognised, since they form a single phase characterized by a single T_g, and a behaviour that lies in between the two pure polymeric extremes. Since the final properties of the blend also depend on the actual mixture composition, a fine tailoring of the material properties can be made merely modifying the formulation [53]. If a suitable rubber/thermoplastic polymer pair is found, the blending approach is a simple and versatile method for the production of electrospun nanofibers without tricky processing steps [53–55].

1.5 • STRUCTURAL HEALTH MONITORING (SHM)

Fiber-reinforced plastics (FRPs) composite laminates, due to their laminar structure, are prone to delamination and are susceptible to out-of-plane impact loads, as anticipated in SECTION 1.2. Often, the flaw initiates and propagates inside the laminate without any visible damage on the outer surfaces, until it reaches a critical dimension that causes the sudden and catastrophic failure of the component. The safety is therefore guaranteed by over-dimensioning them and by time-consuming periodic non-destructive testing (NDT) inspections, that negatively impact on the overall weight and life-cycle cost of the structure [56,57].

To overcome these limitations, Structural Health Monitoring (SHM) systems are being developed to continuously watch over the health status of the structure during operation and immediately detect the damage. The monitoring sensors can be either externally mounted or integrated into the laminate. External sensors usually do not affect the laminate mechanical performance; however, they are bulky and exposed to external environmental conditions, electronic interferences and impacts [56]. For this reason, efforts have been made to embed commercial sensors into the composite between the laminate plies. The most widely used are Fiber Bragg Grating (FBG) [58] and piezoelectric ceramic-based sensors, like lead zirconate titanate (PZT) wafers [59] or microfibers [60]. FBG sensors allow the strain measurement on different spots with a single optical fiber [61,62]. However, inserting a *sub*-millimetric optical fiber between composite plies produce a resin pocket defect which can cause matrix cracking and subsequent delamination [63]. Piezoelectric sensors are widely employed to measure frequency vibrations, due to their reduced weight, size and cost [61]. Thanks to their high piezoelectric constant, PZT wafers show an excellent sensitivity with respect to other conventional sensors like strain gauges, fiber optics and more flexible piezoelectric polymers [64,65]. However, their inherent ceramic nature makes them extremely brittle. In fact, PZT fracture causes an interface crack nucleation, which brings to unstable delamination [66]. This aspect affects the composite fatigue strength and limits the bearing strength capacity of the laminate [67]. By changing the morphology of the PZT from wafer disks to microfibers (micro-sized lead zirconate titanate fibers) the intrusiveness of the sensor on the hosting laminate can be reduced. For instance, the laminate shear strength is reduced by 7% by embedding PZT

microfibers in unidirectional Glass Fiber Reinforced Polymer (GFRP) prepreg plies compared to 15% by embedding PZT disks [60]. An alternative to brittle piezoceramic sensors is polyvinylidene fluoride (PVDF) polymeric films. Their advantages include high flexibility, low mass, cheapness and high internal damping [68,69]. However, the interface strength between the sensor and the hosting matrix can be an issue [70,71].

Another possibility is to make the matrix system self-sensing through additives, e.g. by adding carbon nanotubes (CNTs) [72]. Compared to the previously described extrinsic sensors, that constitute a foreign body hosted in the laminate, the matrix itself when reinforced with CNTs intrinsically becomes a sensor. This concept overcomes the issues related to mechanical performance reduction [72–74]. The use of a small amount of CNTs makes the polymer matrix electrically conductive and piezo-resistive, ensuring a strict relationship between the mechanical deformations and the measured electrical resistance [75]. However, the sensing performance is susceptible to the unavoidable inhomogeneous dispersion of the filler (entanglements) within the resin, which impacts on the electrical response of the obtained nanocomposites [72,75].

The exploitation of piezoelectric polymers, like PVDF and its copolymer with trifluoroethylene (PVDF-TrFE), in the form of nanofiber may be a smart solution. Indeed, as presented in SECTION 1.2, nanofibrous mats can be successfully integrated into composite laminates, also leading to improved structures against delamination without affecting the overall stiffness [76–78]. The use of piezoelectric nanofibers to produce a self-sensing aluminium/GFRP hybrid laminate will be discussed in CHAPTER 6.

1.6 • ELECTROSPINNING: A VERSATILE TECHNIQUE FOR NANOFIBERS PRODUCTION

Electrospinning, or *electrostatic spinning*, is the most versatile technique for producing nanofibers and their assemblies, i.e. nanofibrous mats. As suggested by the name, this process takes place thanks to the application of an external intense electrostatic field [79].

While in traditional spinning the polymer is forced through a die by applying pressure, in electrospinning a strong electrostatic field is used to "extract" fibers characterized by nanometric diameters. Both polymeric solutions and fused polymers can be electrospun; however, solution electrospinning is the most common (in the present discussion, only this one will be illustrated).

The material to electrospin is contained in a syringe, equipped with a metallic needle joined to a high potential power supply. A potential difference is placed between the needle and a collecting screen, called *collector*: the electrostatic field generated allows the solution drop at the needle tip to charge and deform. At a specific intensity of applied field, the repulsion between charges of the same sign (positive or negative) overcomes the surface tension forces, provoking the expulsion of a polymeric jet toward the collector, at the electrical ground. Finally, dry nanofibers are produced and collected on the collector [79].

The process just described requires an electrostatic field of remarkable intensity, which derives from a high potential difference: for this reason, apparatuses for electrospinning are relatively recent. The first patented apparatus dates back to 1900 (FIGURE 1.10).

An electrospinning process apparatus can be more or less complex; however, the fundamental elements to carry out the process are:
- a reservoir for the polymeric solution;
- a high voltage power supply;
- a metallic needle, from which the solution comes out;
- a fiber collector.
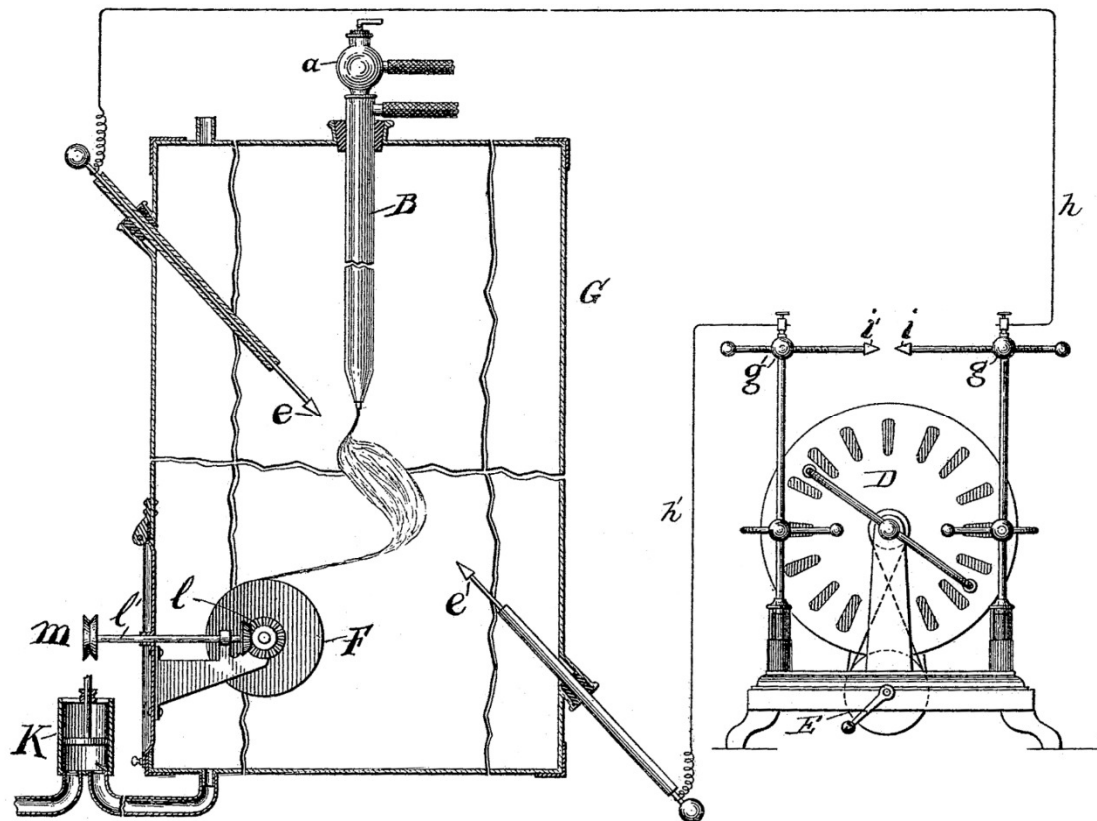
FIGURE 1.10 • Electrospinning apparatus patented by Cooley in 1900.

(Reproduced from patent US No. 745,276 [80].)

A basic configuration, such as the one shown in FIGURE 1.11, consists of:

- an infusion syringe pump;

- a syringe for containing the polymer solution;

- a metal needle, connected to the positive (or negative) pole of the high voltage power supply;

- a high power supply generator;

- a metal collector, connected to the electrical ground.

The most critical drawback of the electrospinning process is the very low productivity, i.e. the low amount of nanofibers produced per time unit. This is due to the low volumetric flow rate that the process requires, often limited to or below 1 mL/h. To overcome or, at least, improve the situation multi-needle or needleless machines can be used [81].
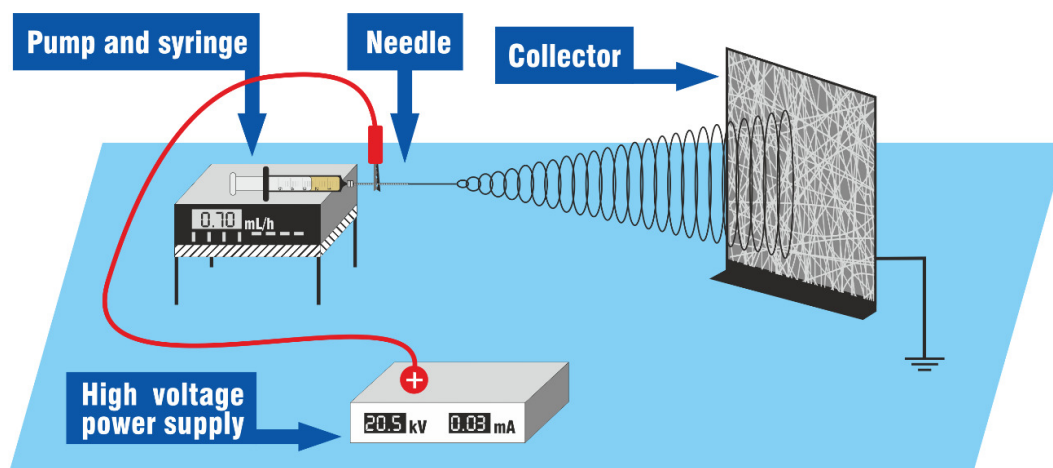
FIGURE 1.11 – Basic configuration of an electrospinning apparatus.

(Author's own illustration)

Although the installation of an electrospinning apparatus is simple and cheap, the process is influenced by many variables, which must be optimized to obtain nanofibers with good quality. These parameters can be divided into three categories:

- solution parameters: polymer molecular weight, solution concentration, solution viscosity, surface tension, type and dielectric constant of solvent, overall solution conductivity;

- process parameters: applied voltage (on which depends the electrostatic field), flow rate, needle-to-collector distance, type of collector, needle diameter;

- environmental parameters: temperature and relative humidity (RH).

These variables, to a more or less strict extent and in a convergent or divergent sense, discriminate among the real possibility of developing an electrospinning process, having electrospray or just causing the separation of bulk material from the needle. All the mentioned parameters can have a strong influence also on the fiber diameter, fiber morphology (smooth, porous, single or associated in bundles), and on their disposition (random or aligned along a preferential direction). Below these parameters will be discussed in detail.

Polymer molecular weight and solution concentration act in a similar manner: indeed, they determine the solution viscosity. To positively conduct an electrospinning process, it is necessary to operate within an optimal viscosity range. If viscosity is too low, the polymeric jet may break, leading to the formation of nano- or micro-particles (electrospray). In the opposite case, the process may be interrupted by material clogging

at the needle tip [82], or it may be necessary the application of a potential higher than the air dielectric breakdown [83]. In FIGURE 1.12 the effect of solution viscosity on the electrospun material is shown.
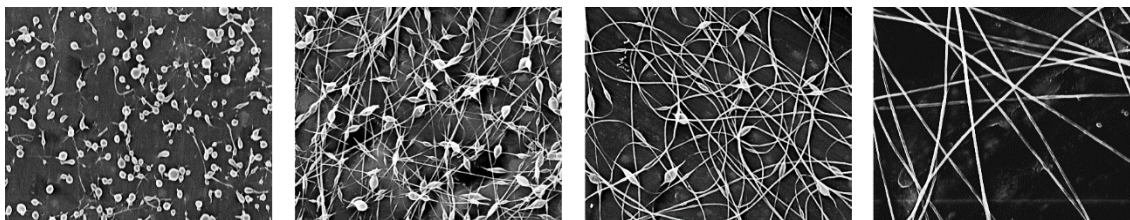
FIGURE 1.12 • Effect of solution viscosity on beads formation and nanofiber diameter. From left to right: 13, 74, 289 and 1,250 centipoise.
(Reproduced from Ref. [84] with permissions of Elsevier.)

An insufficient solution viscosity causes electrospray, while a low solution viscosity leads to the formation of beads. The general tendency is to have beads with a less spherical shape for increasing viscosity, until they disappear above a particular threshold value [85] (see FIGURE 1.12).

Viscosity also influences the diameter of the fibers: for "low" viscosities, smaller diameters are obtained because the polymeric jet is stretched more effectively [86], while for "high" viscosities, the diameter generally increases [85,87].

The solvent (or solvent system) choice is primarily dependent on the polymer solubility. Among the possible candidates, the best solvent is clearly the one that allows obtaining high-quality nanofibers at the best productivity. The electrospinning process requires an electrically charged polymer jet to interact with the electrostatic field. If the solution is not able to charge, i.e. its conductivity is close to zero, the process cannot take place. It is also possible to add a co-solvent for improving and facilitating the electrospinning process, provided that this does not cause the polymer precipitation [88].

The choice of a solvent or a solvent system is of paramount importance when dealing with electrospinning of polymer blends since the solubility of the polymers is required.

For what concerns process parameters, electric potential and needle-to-collector distance determine the intensity of the electrostatic field, deriving from these two. Their optimisation, as well as flow rate adjustment, is necessary to have a stable electrospinning process and to produce good nanofibers.

A high electric potential, as well as an intense electrostatic field, allowing a high stretching of the polymeric jet, generally favours the formation of thinner fibers [83,86]. For the same reason, low flow rates usually leads to small diameters [87]. Clearly, the flow rate should not be too low for avoiding inferior productivity.

The needle-to-collector distance is not "standard", but needs to be experimentally determined to obtain a stable electrospinning process. The distance can also determine the nanofiber and nanofibrous mat morphology, as depicted in FIGURE 1.13 [83].
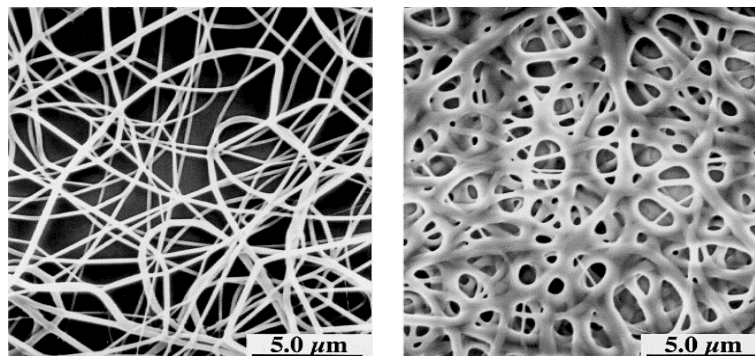
FIGURE 1.13 • Electrospun fibers deriving from different needle-to-collector distances:
"high" (left) and "low" (right).
(Reproduced from Ref. [83] with permissions of Elsevier.)

In particular cases, also environmental conditions may considerably affect the electrospun nanofibers. As an example, Nomex nanofibers display an overall random arrangement when RH ≈ 20%, while are prevalently aligned if RH is above 45% [89].
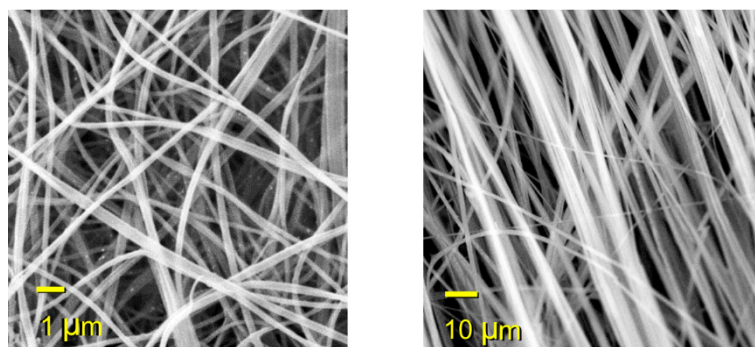
FIGURE 14 • Electrospun Nomex nanofibrous mat in different environmental conditions:
low (left) and high (right) RH [90].

1.7 • AIM OF THE WORK AND THESIS OVERVIEW

Polymer Matrix Composites (PMCs) are progressively replacing traditional materials. Where high mechanical properties and low weight are required, Fiber Reinforced Polymers (FRPs) are the best choice. In particular, Carbon Fiber Reinforced Polymers (CFRPs) display high specific mechanical properties, allowing the creation of lightweight components and products by the replacement of metals. To reach outstanding mechanical performance, stiff thermosets as matrices, like epoxy resins, are preferred. The use of prepregs is common, thanks to their ease of manipulation during object manufacturing. However, when dealing with laminates, delamination may seriously affect the structural integrity during component service life, as discussed in SECTION 1.2. This may imply a lack of sufficient reliability, which precludes the widespread use of laminated FRPs as metals substitutes. Moreover, the high stiffness characterizing this composite type leads also to low damping capacity, as presented in SECTION 1.3. Low material damping causes structure-borne noise and undesirable vibrations that may contribute to delamination triggering [4], besides a low comfort in some applications, like automotive.

For the above presented reasons, searching for systems able to limit the catastrophic consequences of composite laminates failure is of primary importance for safety reasons, as well as for economic ones.

Rubber toughening has been done since long to limit delamination; however, the impact on composite thermomechanical properties may be relevant. By contrast, nanofibers represent a smart approach to locally modify the resin only where required [16], without affecting the overall bulk material and without the need to chemically modify the whole resin formulation. Indeed, interlaminar stresses in a structural component develop in specific and localised areas, due to geometric discontinuities, such as free edges, holes, ply-drops and adhesive bonding [91].

In this frame, the use of rubbery nanofibers might increase both toughness and damping, without excessively affecting the overall mechanical performance of the material or significantly increase its weight and size. Yet, to the best of the Author knowledge, no literature exists about the use of rubbery fibers for composite laminate modification. While rubbery materials are well renowned for their damping [92], they cannot be easily

formed in nanofibers, due to the low glass transition temperature (T_g) of the spinnable uncrosslinked precursors which promote filming of the fibers. Due to this limitation, until now (end of 2020) only a few works propose the production of rubbery fibers, as presented in SECTION 1.4.

During my PhD, I developed different "elastomeric polymeric systems" able to be electrospun, thus allowing the creation of rubbery nanofibers, without the need of a crosslinking step. Such rubbery nanofibrous mats were then integrated into epoxy-based CFRP laminates with the aim to hinder delamination by increasing the interlaminar fracture toughness, and, possibly, also to enhance the damping capacity of such stiff materials.

Nitrile Butadiene Rubber (NBR) was chosen as the elastomer component, also for its high compatibility with epoxy resins, while thermoplastic polymers with different thermal properties were chosen as the non-elastomeric counterpart to enable the retention of the nanofiber structure. In FIGURE 15 is depicted a scheme of the polymers used (also in a blend) for producing nanofibrous mats in the present PhD thesis.

Nitrile Butadiene Rubber
(NBR)

Poly(ε-caprolactone)
(PCL)

Poly(m-phenylene isophthalamide)
(Nomex)

Poly[imino(1,6-dioxohexamethylene) iminohexamethylene]
(Nylon 66)

Poly(vinylidenefluoride-trifluoroethylene)
(PVDF-TrFE)
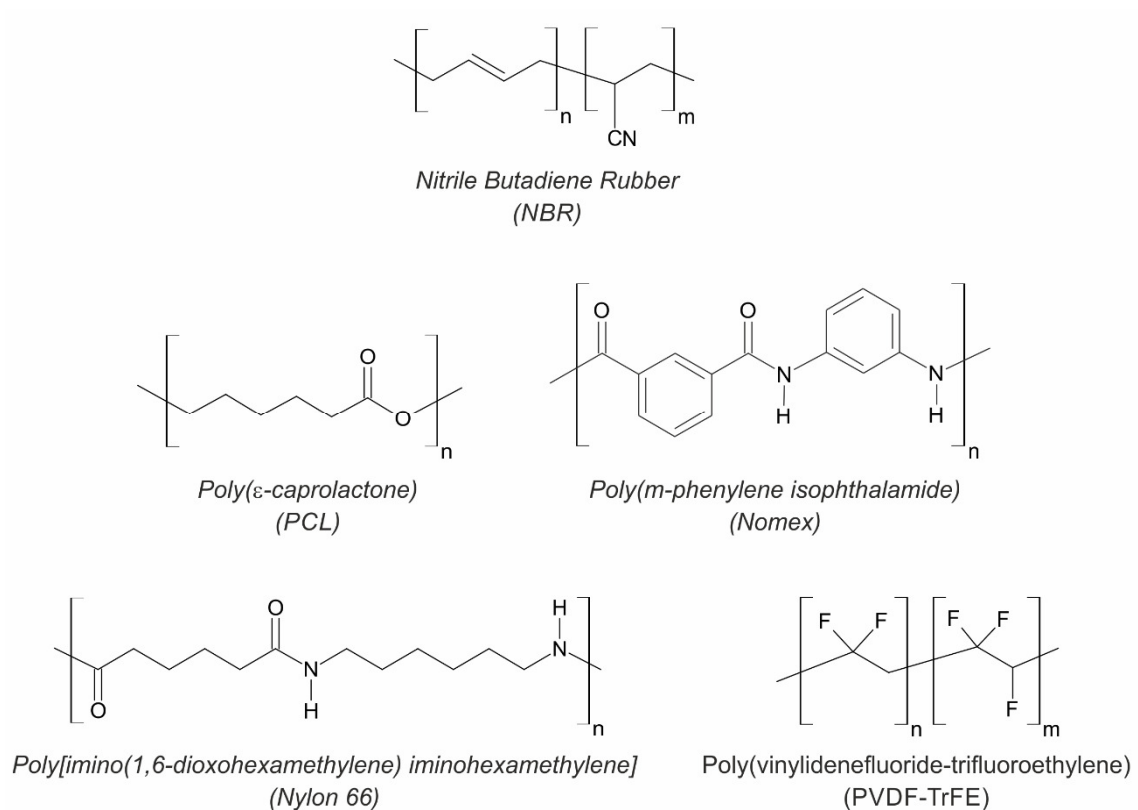
FIGURE 15 • Electrospun polymers (also in a blend) for producing nanofibrous mats.
(Author's own illustration.)

To perform the desired function, all the thermoplastics used are semi-crystalline polymers with a melting temperature (or a T_g) higher than the room temperature. The "liquid" rubber blending with thermoplastics aims at exploiting their crystalline fraction to create dimensionally stable nanofibers with elastomeric properties, still maintaining the rubber uncrosslinked.

The produced nanofibrous mats were fully characterized (morphologically, thermally, and mechanically) before their integration in CFRP laminates. The nano-modified composites, as well as an unmodified one (reference), were mechanically and thermomechanically characterized. Proper tests were carried out to evaluate the rubbery nanofibrous mat effect on the composite delamination behaviour. More specifically, the CFRP interlaminar fracture toughness was assessed via Mode I and II loading tests (*Double Cantilever Beam*, DCB, and *End-Notched Flexure*, ENF, tests, respectively). The damping of laminates was investigated via Dynamic Mechanical Analysis (DMA) and single cantilever beam vibration tests. DMA was also used to evaluate the overall thermomechanical behaviour.

I also contribute to the development of piezoelectric nanofibrous mats, made of poly(vinylidenefluoride-trifluoroethylene) (PVDF-TrFE), and to their integration into composite laminates for Structural Health Monitoring (SHM) purpose. Since microcracks formation and propagation usually occurs without external signs of damage, the development of systems able to continuously monitor the component health can surely provide a valuable help against catastrophic laminate failure by delamination.

In the present experimental thesis, the results achieved are organized as follows:

• CHAPTER 2 deals with the production and characterization of rubbery NBR/PCL nanofibrous mats;

• CHAPTER 3 investigates the effect of NBR/PCL nanofibers on interlaminar fracture toughness, damping and overall thermomechanical properties of CFRP laminates;

• CHAPTER 4 presents a deeper evaluation of damping capacity of CFRPs with interleaved NBR/PCL mats;

• CHAPTER 5 reports the production, characterization and use of NBR/Nomex self-assembled nanofibers for hindering delamination in CFRPs;

• CHAPTER 6 illustrates the production and testing of self-sensing aluminium-GFRP hybrid laminates by piezoelectric nanofibers interleaving;

• CHAPTER 7 describes the production and characterization of Nylon 66 nanofibers nano-reinforced with graphene;

• CHAPTER 8 shows an insight about tensile mechanical properties of nonwoven nanofibrous mats, presenting, among the others, a new simple and effective method of load normalization to obtain reliable stress-strain curves.

The reader will find dedicated state-of-the-art of the topics presented in CHAPTERS 7 and 8 directly inside the relative chapters.

References

[1]   R.M. Jones, Mechanics of composite materials, 1999.

[2]   F.C. Campbell, Introduction to Composite Materials, in: Struct. Compos. Mater., 2010: pp. 1–29.

[3]   R. Palazzetti, A. Zucchelli, Electrospun nanofibers as reinforcement for composite laminates materials – A review, Compos. Struct. 182 (2017) 711–727. https://doi.org/10.1016/j.compstruct.2017.09.021.

[4]   S.U. Khan, C.Y. Li, N. a. Siddiqui, J.-K. Kim, Vibration damping characteristics of carbon fiber-reinforced composites containing multi-walled carbon nanotubes, Compos. Sci. Technol. 71 (2011) 1486–1494. https://doi.org/10.1016/j.compscitech.2011.03.022.

[5]   K.C. Jung, S.H. Chang, Performance evaluation of smart grid fabrics comprising carbon dry fabrics and PVDF ribbon sensors for structural health monitoring, Compos. Part B Eng. 163 (2019) 690–701. https://doi.org/10.1016/j.compositesb.2019.01.050.

[6]   C. Tuloup, W. Harizi, Z. Aboura, Y. Meyer, K. Khellil, R. Lachat, On the use of in-situ piezoelectric sensors for the manufacturing and structural health monitoring of polymer-matrix composites: A literature review, Compos. Struct. 215 (2019) 127–149. https://doi.org/10.1016/j.compstruct.2019.02.046.

[7]   E. Ghafari, N. Lu, Self-polarized electrospun polyvinylidene fluoride (PVDF) nanofiber for sensing applications, Compos. Part B Eng. 160 (2019) 1–9. https://doi.org/10.1016/j.compositesb.2018.10.011.

[8]   D. Geng, Y. Liu, Z. Shao, Z. Lu, J. Cai, X. Li, X. Jiang, D. Zhang, Delamination formation, evaluation and suppression during drilling of composite laminates: A review, Compos. Struct. 216 (2019) 168–186. https://doi.org/10.1016/j.compstruct.2019.02.099.

[9]   N. Takeda, S. Ogihara, S. Suzuki, A. Kobayashi, Evaluation of microscopic deformation in CFRP laminates with delamination by micro-grid methods, J. Compos. Mater. 32 (1998) 83–100. https://doi.org/10.1177/002199839803200105.

[10]   E.B. Caldona, A.C.C. De Leon, B.B. Pajarito, R.C. Advincula, A Review on Rubber-Enhanced Polymeric Materials, Polym. Rev. 57 (2017) 311–338. https://doi.org/10.1080/15583724.2016.1247102.

[11]   S.M. George, P. Vijayan, S. Thomas, Nanostructures and the toughening of thermosets, in: Thermosets, Elsevier, 2012: pp. 118–161. https://doi.org/10.1533/9780857097637.1.118.

[12]   R. Bagheri, B.T. Marouf, R.A. Pearson, Rubber-toughened epoxies: A critical review, Polym. Rev. 49 (2009) 201–225. https://doi.org/10.1080/15583720903048227.

[13]   C.K. Riew, A.R. Siebert, R.W. Smith, M. Fernando, A.J. Kinloch, Toughened Epoxy Resins: Preformed Particles as Tougheners for Adhesives and Matrices, in: Toughened Plast. II, American Chemical Society, 1996: pp. 33–44.

[14]   R.J.J. Williams, B.A. Rozenberg, J. Pascault, Reaction-induced phase separation in modified thermosetting polymers, 1997. https://doi.org/10.1007/3-540-61218-1_7.

[15]   C.W. Wise, W.D. Cook, A.A. Goodwin, CTBN rubber phase precipitation in model epoxy resins, Polymer (Guildf). 41 (2000) 4625–4633. https://doi.org/10.1016/S0032-3861(99)00686-2.

[16]   D.. Reneker, Y.. Dzenis, Delamination resistant composites prepared by small diameter fiber reinfrocement at ply interfaces, US 6,265,333, (2001).

[17]   S. van der Heijden, L. Daelemans, B. De Schoenmaker, I. De Baere, H. Rahier, W. Van Paepegem, K. De Clerck, Interlaminar toughening of resin transfer moulded glass fibre epoxy laminates by polycaprolactone electrospun nanofibres, Compos. Sci. Technol. 104 (2014) 66–73. https://doi.org/10.1016/j.compscitech.2014.09.005.

[18]   P. Akangah, S. Lingaiah, K. Shivakumar, Effect of Nylon-66 nano-fiber interleaving on impact damage resistance of epoxy/carbon fiber composite laminates, Compos. Struct. 92 (2010) 1432–1439. https://doi.org/10.1016/j.compstruct.2009.11.009.

[19] J. Zhang, T. Yang, T. Lin, C.H. Wang, Phase morphology of nanofibre interlayers: Critical factor for toughening carbon/epoxy composites, Compos. Sci. Technol. 72 (2012) 256–262. https://doi.org/10.1016/j.compscitech.2011.11.010.

[20] D. Quan, F. Bologna, G. Scarselli, A. Ivankovic, N. Murphy, Mode-II fracture behaviour of aerospace-grade carbon fibre/epoxy composites interleaved with thermoplastic veils, Compos. Sci. Technol. 191 (2020).

[21] D5528-01 2001. Standard Test Method for Mode I Interlaminar Fracture Toughness of Unidirectional Fiber-Reinforced Polymer Matrix Composites, Am. Soc. Test. Mater. (2014) 1–13. https://doi.org/10.1520/D5528-13.2.

[22] BS EN 6033:2015, BS EN 6034 : 2015 BSI Standards Publication Aerospace series — Carbon fibre reinforced plastics — Test method — Determination of interlaminar fracture toughness energy — Mode I —, BSI Stand. Publ. (2015) 14.

[23] P. Holgate, Optimisation of a viscoelastic damping material using dynamic mechanical analysis, 1 (2015) 1–11.

[24] J.-S. Jang, J. Varischetti, J. Suhr, Strain dependent energy dissipation in multi-scale carbon fiber composites containing carbon nanofibers, Carbon N. Y. 50 (2012) 4277–4283. https://doi.org/10.1016/j.carbon.2012.05.012.

[25] H. Abramovich, D. Govich, A. Grunwald, Damping measurements of laminated composite materials and aluminum using the hysteresis loop method, Prog. Aerosp. Sci. 78 (2015) 8–18. https://doi.org/10.1016/j.paerosci.2015.05.006.

[26] ISO 6721-1:2011, n.d.

[27] P.C.O. Martins, T.A.M. Guimaraes, D. de A. Pereira, F.D. Marques, D.A. Rade, Numerical and experimental investigation of aeroviscoelastic systems, Elsevier, 2017. https://doi.org/10.1016/j.ymssp.2016.08.043.

[28] L. Irazu, M.J. Elejabarrieta, The influence of viscoelastic film thickness on the dynamic characteristics of thin sandwich structures, Compos. Struct. 134 (2015) 421–428. https://doi.org/10.1016/j.compstruct.2015.07.086.

[29] R. Kandasamy, F. Cui, N. Townsend, C.C. Foo, J. Guo, A. Shenoi, Y. Xiong, A review of vibration control methods for marine offshore structures, Ocean Eng. 127 (2016) 279–297. https://doi.org/10.1016/j.oceaneng.2016.10.001.

[30] M.D. Rao, Recent applications of viscoelastic damping for noise control in automobiles and commercial airplanes, J. Sound Vib. 262 (2003) 457–474. https://doi.org/10.1016/S0022-460X(03)00106-8.

[31] H. Kishi, M. Kuwata, S. Matsuda, T. Asami, A. Murakami, Damping properties of thermoplastic-elastomer interleaved carbon fiber-reinforced epoxy composites, Compos. Sci. Technol. 64 (2004) 2517–2523. https://doi.org/10.1016/j.compscitech.2004.05.006.

[32] T. Tanimoto, A new vibration damping CFRP material with interlayers of dispersed piezoelectric ceramic particles, Compos. Sci. Technol. 67 (2007) 213–221. https://doi.org/10.1016/j.compscitech.2006.08.022.

[33] N. Ni, Y. Wen, D. He, X. Yi, Z. Zhao, Y. Xu, Synchronous improvement of loss factors and storage modulus of structural damping composite with functionalized polyamide nonwoven fabrics, Mater. Des. 94 (2016) 377–383. https://doi.org/10.1016/j.matdes.2015.12.159.

[34] N.A. Koratkar, J. Suhr, A. Joshi, R.S. Kane, L.S. Schadler, P.M. Ajayan, S. Bartolucci, Characterizing energy dissipation in single-walled carbon nanotube polycarbonate composites, Appl. Phys. Lett. 87 (2005). https://doi.org/10.1063/1.2007867.

[35] X. Zhou, E. Shin, K.W. Wang, C.E. Bakis, Interfacial damping characteristics of carbon nanotube-based composites, Compos. Sci. Technol. 64 (2004) 2425–2437. https://doi.org/10.1016/j.compscitech.2004.06.001.

[36]   M. Kireitseu, D. Hui, G. Tomlinson, Advanced shock-resistant and vibration damping of nanoparticle-reinforced composite material, Compos. Part B Eng. 39 (2008) 128–138. https://doi.org/10.1016/j.compositesb.2007.03.004.

[37]   H. Rajoria, N. Jalili, Passive vibration damping enhancement using carbon nanotube-epoxy reinforced composites, Compos. Sci. Technol. 65 (2005) 2079–2093. https://doi.org/10.1016/j.compscitech.2005.05.015.

[38]   J. Zhang, T. Yang, T. Lin, C.H. Wang, Phase morphology of nanofibre interlayers: Critical factor for toughening carbon/epoxy composites, Compos. Sci. Technol. 72 (2012) 256–262. https://doi.org/10.1016/j.compscitech.2011.11.010.

[39]   P. Akangah, S. Lingaiah, K. Shivakumar, Effect of Nylon-66 nano-fiber interleaving on impact damage resistance of epoxy/carbon fiber composite laminates, Compos. Struct. 92 (2010) 1432–1439. https://doi.org/10.1016/j.compstruct.2009.11.009.

[40]   X. Zhang, G.G. Chase, Electrospun elastic acrylonitrile butadiene copolymer fibers, Polymer (Guildf). 97 (2016) 440–448. https://doi.org/10.1016/j.polymer.2016.05.063.

[41]   S.S. Choi, J.P. Hong, Y.S. Seo, S.M. Chung, C. Nah, Fabrication and characterization of electrospun polybutadiene fibers crosslinked by UV irradiation, J. Appl. Polym. Sci. 101 (2006) 2333–2337. https://doi.org/10.1002/app.23764.

[42]   M. Tian, Q. Hu, H. Wu, L. Zhang, H. Fong, L. Zhang, Formation and morphological stability of polybutadiene rubber fibers prepared through combination of electrospinning and in-situ photo-crosslinking, Mater. Lett. 65 (2011) 3076–3079. https://doi.org/10.1016/j.matlet.2011.06.089.

[43]   M.W. Thielke, E.P. Bruckner, D.L. Wong, P. Theato, Thiol-ene modification of electrospun polybutadiene fibers crosslinked by UV irradiation, Polymer (Guildf). 55 (2014) 5596–5599. https://doi.org/10.1016/j.polymer.2014.09.002.

[44]   H. Wu, Q. Hu, L. Zhang, H. Fong, M. Tian, Electrospun composite nanofibers of polybutadiene rubber containing uniformly distributed Ag nanoparticles, Mater. Lett. 84 (2012) 5–8. https://doi.org/10.1016/j.matlet.2012.06.039.

[45]   A. Vitale, G. Massaglia, A. Chiodoni, R. Bongiovanni, C.F. Pirri, M. Quaglio, Tuning Porosity and Functionality of Electrospun Rubber Nanofiber Mats by Photo-Crosslinking, ACS Appl. Mater. Interfaces. (2019). https://doi.org/10.1021/acsami.9b04599.

[46]   X. Wang, H. Nie, D. Liu, A. He, Retardation of cold flow in immiscible rubber blends by tailoring their microstructures, Polym. Int. 66 (2017) 1473–1479. https://doi.org/10.1002/pi.5395.

[47]   X. Zhang, X. Yang, G.G. Chase, Filtration performance of electrospun acrylonitrile-butadiene elastic fiber mats in solid aerosol filtration, Sep. Purif. Technol. 186 (2017) 96–105. https://doi.org/10.1016/j.seppur.2017.06.002.

[48]   T.E. Kerr-Phillips, V. Woehling, R. Agniel, G.T.M. Nguyen, F. Vidal, P. Kilmartin, C. Plesse, J. Travas-Sejdic, Electrospun rubber fibre mats with electrochemically controllable pore sizes, J. Mater. Chem. B. 3 (2015) 4249–4258. https://doi.org/10.1039/c5tb00239g.

[49]   H.Y. Liu, H.C. Hsieh, J.Y. Chen, C.C. Shih, W.Y. Lee, Y.C. Chiang, W.C. Chen, Fabrication and Application of Highly Stretchable Conductive Fiber-Based Electrode of Epoxy/NBR Electrospun Fibers Spray-Coated with AgNW/PU Composites, Macromol. Chem. Phys. 220 (2019) 1–8. https://doi.org/10.1002/macp.201800387.

[50]   H. rong Nie, C. Wang, A. hua He, Fabrication and chemical crosslinking of electrospun trans-polyisoprene nanofiber nonwoven, Chinese J. Polym. Sci. (English Ed. 34 (2016) 697–708.

[51]   J.R. Kim, J.J. Kim, Epoxy Resins Toughened with Surface Modified Epoxidized Natural Rubber Fibers by One-Step Electrospinning, Materials (Basel). 10 (2017).

[52]   K. Phatcharasit, W. Taweepreda, K. Boonkerd, J.K. Kim, Electrospun Epoxidized Natural Rubber with Poly(vinyl chloride) (ENR-PVC) Nanofibrous for PEMFC Applications, Adv. Mater. Res. 844 (2013) 507–510.

[53]   D.J. Walsh, Polymer Blends, in: Compr. Polym. Sci. Suppl., Pergamon, 1989: pp. 135–154.

[54] A. Aluigi, A. Varesano, C. Vineis, A. Del Rio, Electrospinning of immiscible systems: The wool keratin/polyamide-6 case study, Mater. Des. 127 (2017) 144–153. https://doi.org/10.1016/j.matdes.2017.04.045.

[55] P. Tipduangta, P. Belton, L.L. Fábián, L.Y. Wang, H. Tang, M. Eddleston, S. Qi, Electrospun Polymer Blend Nanofibers for Tunable Drug Delivery: The Role of Transformative Phase Separation on Controlling the Release Rate, Mol. Pharm. 13 (2016) 25–39. https://doi.org/10.1021/acs.molpharmaceut.5b00359.

[56] P. Hofmann, A. Walch, A. Dinkelmann, S.K. Selvarayan, G.T. Gresser, Woven piezoelectric sensors as part of the textile reinforcement of fiber reinforced plastics, Compos. Part A Appl. Sci. Manuf. (2019). https://doi.org/10.1016/j.compositesa.2018.10.019.

[57] J. Cai, L. Qiu, S. Yuan, L. Shi, P. Liu, D. Liang, Structural Health Monitoring for Composite Materials, in: Compos. Their Appl., 2012. https://doi.org/10.5772/48215.

[58] N. Takeda, Y. Okabe, J. Kuwahara, S. Kojima, T. Ogisu, Development of smart composite structures with small-diameter fiber Bragg grating sensors for damage detection: Quantitative evaluation of delamination length in CFRP laminates using Lamb wave sensing, Compos. Sci. Technol. (2005). https://doi.org/10.1016/j.compscitech.2005.07.014.

[59] S. Masmoudi, A. El Mahi, S. Turki, Use of piezoelectric as acoustic emission sensor for in situ monitoring of composite structures, Compos. Part B Eng. (2015). https://doi.org/10.1016/j.compositesb.2015.06.003.

[60] H.P. Konka, M.A. Wahab, K. Lian, The effects of embedded piezoelectric fiber composite sensors on the structural integrity of glass-fiber-epoxy composite laminate, Smart Mater. Struct. (2012). https://doi.org/10.1088/0964-1726/21/1/015016.

[61] A. Loayssa, New Developments in Sensing Technology for Structural Health Monitoring, 2011. https://doi.org/10.1007/978-3-642-21099-0.

[62] H.N. Li, D.S. Li, G.B. Song, Recent applications of fiber optic sensors to health monitoring in civil engineering, Eng. Struct. (2004). https://doi.org/10.1016/j.engstruct.2004.05.018.

[63] K. Shivakumar, A. Bhargava, Failure mechanics of a composite laminate embedded with a fiber optic sensor, J. Compos. Mater. (2005). https://doi.org/10.1177/0021998305048156.

[64] B. Lin, V. Giurgiutiu, Modeling and testing of PZT and PVDF piezoelectric wafer active sensors, Smart Mater. Struct. (2006). https://doi.org/10.1088/0964-1726/15/4/022.

[65] L. Lampani, F. Sarasini, J. Tirillò, P. Gaudenzi, Analysis of damage in composite laminates with embedded piezoelectric patches subjected to bending action, Compos. Struct. (2018). https://doi.org/10.1016/j.compstruct.2018.04.073.

[66] J. Cheng, C. Qian, M. Zhao, S.W.R. Lee, P. Tong, T.Y. Zhang, Effects of electric fields on the bending behavior of PZT-5H piezoelectric laminates, Smart Mater. Struct. (2000). https://doi.org/10.1088/0964-1726/9/6/312.

[67] S. Butler, M. Gurvich, A. Ghoshal, G. Welsh, P. Attridge, H. Winston, M. Urban, N. Bordick, Effect of embedded sensors on interlaminar damage in composite structures, J. Intell. Mater. Syst. Struct. (2011). https://doi.org/10.1177/1045389X11414225.

[68] I.M. De Rosa, F. Sarasini, Use of PVDF as acoustic emission sensor for in situ monitoring of mechanical behaviour of glass/epoxy laminates, Polym. Test. (2010). https://doi.org/10.1016/j.polymertesting.2010.04.006.

[69] J.H. Bae, S.H. Chang, Characterization of an electroactive polymer (PVDF-TrFE) film-type sensor for health monitoring of composite structures, Compos. Struct. (2015). https://doi.org/10.1016/j.compstruct.2015.06.075.

[70] B. Tang, J. Mommaerts, R.K. Duncan, J.C. Duke, D.A. Dillard, Nondestructive evaluation of model adhesive joints by PVDF piezoelectric film sensors, Exp. Mech. (1993). https://doi.org/10.1007/BF02322485.

[71]   N.A. Chrysochoidis, E. Gutiérrez, Evaluation of the sensitivity and fatigue performance of embedded piezopolymer sensor systems in sandwich composite laminates, Smart Mater. Struct. (2015). https://doi.org/10.1088/0964-1726/24/2/025032.

[72]   H. Zhang, E. Bilotti, T. Peijs, The use of carbon nanotubes for damage sensing and structural health monitoring in laminated composites: a review, Nanocomposites. (2015). https://doi.org/10.1080/20550324.2015.1113639.

[73]   I. Kang, Y.Y. Heung, J.H. Kim, J.W. Lee, R. Gollapudi, S. Subramaniam, S. Narasimhadevara, D. Hurd, G.R. Kirikera, V. Shanov, M.J. Schulz, D. Shi, J. Boerio, S. Mall, M. Ruggles-Wren, Introduction to carbon nanotube and nanofiber smart materials, Compos. Part B Eng. (2006). https://doi.org/10.1016/j.compositesb.2006.02.011.

[74]   I. Kang, M.J. Schulz, J.H. Kim, V. Shanov, D. Shi, A carbon nanotube strain sensor for structural health monitoring, Smart Mater. Struct. (2006). https://doi.org/10.1088/0964-1726/15/3/009.

[75]   G. Spinelli, P. Lamberti, V. Tucci, L. Vertuccio, L. Guadagno, Experimental and theoretical study on piezoresistive properties of a structural resin reinforced with carbon nanotubes for strain sensing and damage monitoring, Compos. Part B Eng. (2018). https://doi.org/10.1016/j.compositesb.2018.03.025.

[76]   T. Brugo, R. Palazzetti, The effect of thickness of Nylon 6,6 nanofibrous mat on Modes I–II fracture mechanics of UD and woven composite laminates, Compos. Struct. 154 (2016) 172–178. https://doi.org/10.1016/j.compstruct.2016.07.034.

[77]   H. Zarei, T. Brugo, J. Belcari, H. Bisadi, G. Minak, A. Zucchelli, Low velocity impact damage assessment of GLARE fiber-metal laminates interleaved by Nylon 6,6 nanofiber mats, Compos. Struct. (2017). https://doi.org/10.1016/j.compstruct.2017.01.079.

[78]   L. Daelemans, W. Van Paepegem, K. De Clerck, Effect of interleaved polymer nanofibers on the properties of glass and carbon fiber composites, in: Fiber-Reinforced Nanocomposites Fundam. Appl., 2020. https://doi.org/10.1016/b978-0-12-819904-6.00011-6.

[79]   S. Ramakrishna, K. Fujihara, W.-E. Teo, T.-C. Lim, Z. Ma, An Introduction to Electrospinning and Nanofibers, WORLD SCIENTIFIC, 2005. https://doi.org/10.1142/5894.

[80]   J.F. Cooley, Electrical Method of Dispersing Fluids, US US745276, 1903.

[81]   H. Niu, T. Lin, Fiber generators in needleless electrospinning, J. Nanomater. 2012 (2012). https://doi.org/10.1155/2012/725950.

[82]   J. Doshi, D.H. Reneker, Electrospinning process and applications of electrospun fibers, (1993).

[83]   C.J. Buchko, L.C. Chen, Y. Shen, D.C. Martina, Processing and microstructural characterization of porous biocompatible protein polymer thin films, Polymer (Guildf). 40 (1999) 7397–7407. %5C%5Cmetripol%5CSilk library%5Cb%5CBuchko_1999.pdf.

[84]   H. Fong, I. Chun, D.H. Reneker, Beaded nanofibers formed during electrospinning, Polymer (Guildf). 40 (1999) 4585–4592. https://doi.org/10.1016/S0032-3861(99)00068-3.

[85]   R. Nezarati, Effects of Humidity and Solution Viscosity on Electrospun Fiber Morphology, Tissue Eng. Part C. 19 (2013) 810–819. https://doi.org/10.1089/ten.TEC.2012.0671.

[86]   L. Larrondo, R.S.J. Manley, Electrostatic fiber spinning from polymer melts. I. Experimental observation on fiber formation and properties, J. Polym. Sci. 19 (1981) 909–920. https://doi.org/10.1002/pol.1981.180190602.

[87]   C.J. Thompson, G.G. Chase, a. L. Yarin, D.H. Reneker, Effects of parameters on nanofiber diameter determined from electrospinning model, Polymer (Guildf). 48 (2007) 6913–6922. https://doi.org/10.1016/j.polymer.2007.09.017.

[88]   S.L. Shenoy, W.D. Bates, H.L. Frisch, G.E. Wnek, Role of chain entanglements on fiber formation during electrospinning of polymer solutions: good solvent, non-specific polymer-polymer interaction limit, Polymer (Guildf). 46 (2005) 3372–3384. https://doi.org/10.1016/j.polymer.2005.03.011.

[89]   L. Mazzocchetti, T. Benelli, E. Maccaferri, S. Merighi, J. Belcari, A. Zucchelli, L. Giorgini, Poly-
        m -aramid electrospun nanofibrous mats as high-performance flame retardants for carbon fiber
        reinforced composites, Compos. Part B Eng. 145 (2018) 252–260.
        https://doi.org/10.1016/j.compositesb.2018.03.036.

[90]   E. Maccaferri, Studio di membrane nanofibrose ottenute da elettrofilatura di Poliarammidi,
        Master's thesis, Università di Bologna, A.Y. 2014-2015, (2016).

[91]   T.K. O'Brien, Delamination of Composite Materials, Compos. Mater. Ser. 4 (1991) 181–198.
        https://doi.org/10.1016/B978-0-444-70507-5.50009-3.

[92]   Z.D. Xu, Y.X. Liao, T. Ge, C. Xu, Experimental and theoretical study of viscoelastic dampers
        with different matrix rubbers, J. Eng. Mech. 142 (2016) 1–12.
        https://doi.org/10.1061/(ASCE)EM.1943-7889.0001101.

Chapter 2

RUBBERY NANOFIBERS BY CO-ELECTROSPINNING OF ALMOST IMMISCIBLE NBR AND PCL BLENDS

In this chapter a simple method for producing rubbery nanofibers made of Nitrile Butadiene Rubber / poly(ε-caprolactone) (NBR/PCL) pair without additional crosslinking required is presented. In particular, the ability of the electrospinning process is demonstrated for providing a miscible blend of NBR liquid rubber and PCL, which cannot be obtained with traditional techniques such as solvent casting and spin coating (FIGURE 2.1). The obtained nanofibers are morphologically, thermally, spectroscopically and mechanically characterised.
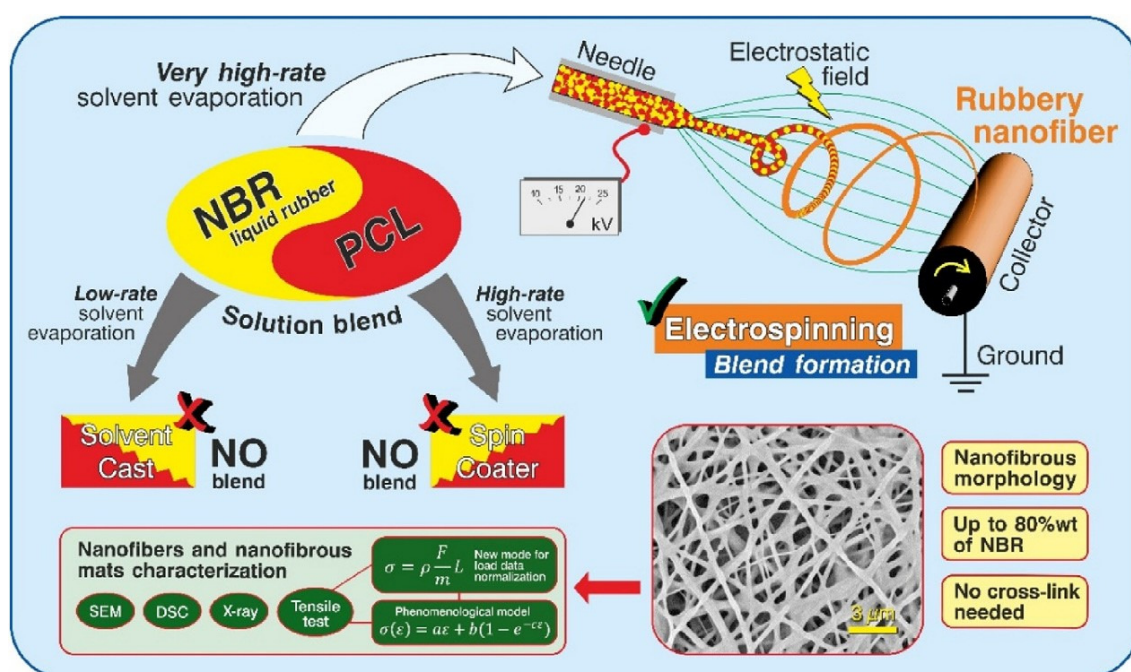
FIGURE 2.1 • Sketch of the paper rationale: electrospinning technique is applied as the only method to obtain homogeneous blend of a crystallizable polymer (PCL) and a liquid rubber (NBR).

2.1 • RESULTS AND DISCUSSION

2.1.1 • Electrospinning of plain NBR

The electrospinning technique, starting from polymeric solutions with conductivity and viscosity suitable for the process, is able to produce virtually continuous nanofibers with diameter well below the micron [1], resulting not only in high surface-to-volume ratio but also in a large aspect ratio. With the aim of electrospinning NBR, the non-crosslinked polymer has hence to be used. In the present case, a carboxylated NBR polymer containing 4%mol methacrylic acid (MAA) was investigated, the latter comonomer used for furthering miscibility with epoxy resins.

Preliminary solubility tests show the formation of rubber homogeneous solutions in acetone, amidic (DMF, DMAc) and chlorinated ($CHCl_3$, CH_2Cl_2) solvents. A first screening of the different solution possibility led to the choice of DMAc, owing to its well-known compatibility with the electrospinning process requirements [2], and a 10%wt solution of NBR in DMAc (S-NBR) was successfully electrospun (FIGURE 2.2 A,B), with a fairly stable process.
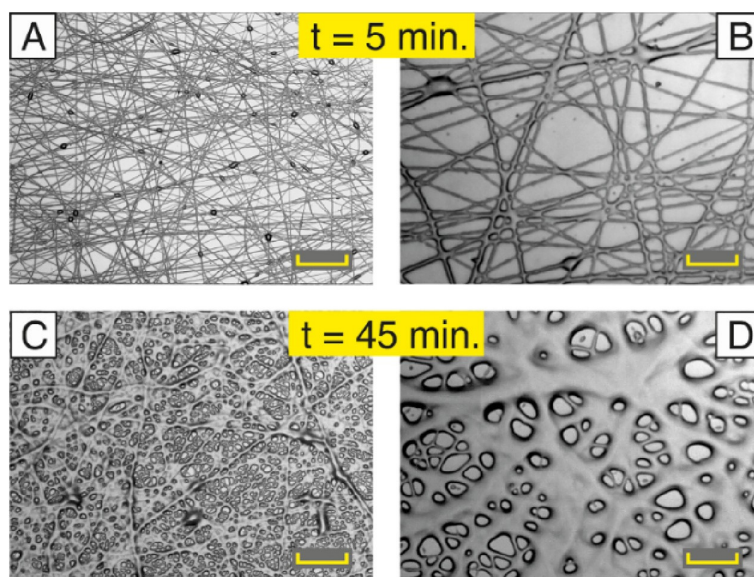
FIGURE 2.2 • Electrospun nanofibers from 10%wt NBR solution in DMAc (S-NBR). Nanofibers after 5 min (A, B) and after 45 min (C, D) of deposition. Scale bar: (A, C) 50 μm; (B, D) 10 μm.

The obtained nanofibers, however, suffer significantly from dimensional instability, as already reported in the literature for similar systems [3–6], since individual fibers tend

to coalesce one with the other, practically resulting in a film within a few minutes (FIGURE 2.2 C,D). This process is displayed in FIGURE 2.2 where optical microscope images of a pure NBR electrospun mat are shown as a function of time.

TABLE 2.1 • DSC data of nanofibrous mats, solvent cast and spin coater films, and the T_g prevision according to the Fox equation.

Sample	NBR	PCL	Experimental Tg I [a]	Experimental Tg II [a]	Expected Tg [b]	Melting temperature (peak)	Fusion enthalpy	Normalized fusion enthalpy [c]	PCL fraction crystallinity [d]
	%wt	%wt	°C	°C	°C	°C	J/g	J/g	%
PCL pellet	—	100	-58.4	—	—	64.0	76.5	76.5	54.8
NBR panel	100	—	-42.2	-13.7	—	—	—	—	—
N-PCL	0	100	-60.3	—	-60.3	60.9	68.7	68.7	49.2
N-20/80	20	80	-50.9	—	-52.4	65.8	63.7	79.6	57.1
N-40/60	40	60	-42.1	—	-44.0	61.0	52.4	87.4	62.7
N-60/40	60	40	-30.4	—	-34.8	60.9	35.5	88.6	63.5
N-80/20	80	20	-24.4	—	-25.0	56.4	19.8	99.1	71.0
N-NBR	100	0	-42.5	-14.2	-14.2	—	—	—	—
F-PCL	0	100	-59.8	—	-59.8	64.9	89.1	89.1	63.9
F-20/80	20	80	-46.6	n.d.	-52.1	64.7	67.8	84.8	60.8
F-40/60	40	60	-39.9	-14.2	-43.8	63.0	51.0	85.1	61.0
F-60/40	60	40	-40.8	-14.7	-34.8	63.6	40.0	100.0	71.7
F-80/20	80	20	-42.9	-17.7	-25.2	62.4	21.3	106.5	76.3
F-NBR	100	0	-42.8	-14.2	-14.7	—	—	—	—
SC-PCL	0	100	-57.0	—	-57.0	60.6	74.6	74.6	53.5
SC-20/80	20	80	-42.3	n.d.	-49.6	60.8	63.8	79.8	57.2
SC-40/60	40	60	-41.1	-12.4	-41.8	59.1	39.1	65.2	46.7
SC-60/40	60	40	-41.1	-14.8	-33.3	57.8	31.9	79.8	57.2
SC-80/20	80	20	-41.3	-18.8	-24.2	52.9	20.2	101.0	72.4
SC-NBR	100	0	-42.5	-14.2	-14.2	—	—	—	—

n.d. = not detectable

[a] from DSC analysis

[b] according to the Fox equation (EQUATION 1)

[c] referred to the PCL weight fraction

[d] considering the fusion enthalpy of 100% crystalline PCL equal to 139.5 J/g [28]

Since this behaviour is due to the low glass transition temperature (T_g, TABLE 2.1) characterizing the elastomer precursor and the lack of crystal phases that help keeping the shape and mechanical properties, the same effect is prone to occur also for prolonged electrospinning deposition time, thus preventing the production of thick nanofibrous membranes as well as hampering the hypothesis of a later crosslinking of the NBR electrospun nanofibers at the end of their deposition.

2.1.2 • *Evaluation of NBR miscibility with PCL*

With the aim of overcoming the poor handling properties of liquid rubbers and obtaining Room Temperature (RT) dimensionally and mechanically stable nanofibrous mats of rubbery materials which would not necessarily require a crosslinking stage during/after deposition, the possibility of blending the polymer with a compatible and miscible candidate has been investigated. The blending candidate should be able to provide nanofibers with good mechanical properties at RT and should be compatible with polymeric matrices (such as epoxies), leading to a positive interaction upon matrix processing. For example, poly(ε-caprolactone) (PCL) proved to be a good epoxy toughener [7], with a crystal phase that, owing to the low melting temperature (T_m about 60 °C), disappears upon epoxy curing (which is usually carried out at least above 80 °C), leading to polymer dissolution within the epoxy matrix; moreover it has been already extensively studied the electrospinnability [7–12]. Assessment of PCL equilibrium miscibility with carboxylated NBR has been thus investigated via evaluation of the thermodynamic solubility parameter (δ) calculated for the polymer pair (see APPENDIX, SECTION 2.4.1). A good miscibility occurs when the difference between the δ parameter for the polymer pair ($\overline{\Delta\delta}$, calculated according to EQUATION 2.6 in the APPENDIX) value is small, i.e. $\overline{\Delta\delta}$ < 5 MPa$^{1/2}$, and partial miscibility could potentially be attained up to 10 MPa$^{1/2}$ [13,14]. Based on the solubility parameter evaluation (see APPENDIX, SECTION 2.4.1), $\overline{\Delta\delta}$ for the NBR/PCL pair was found to be 7.9 MPa$^{1/2}$, a value that does not account for an easy miscibility of the two components, tending instead toward an immiscible system. This behaviour should be critical and would not be expected to lead to the homogeneous and controlled material that is sought after for easy handling. However, while the thermodynamics drives the intrinsic tendency of a polymeric pair to blend, sometimes kinetic factors affect the overall outcomes too. Within this frame, it has already been reported that the particular conditions of the electrospinning process, where a homogeneous solution jet is subjected to almost instantaneous evaporation of the solvent component, might be able to "freeze" partially miscible polymers in a single-phase material that would not separate afterwards [13].

In order to attain a homogeneous miscible blend via solubilization, the obvious prerequisite is to start from a homogenous solution of the two polymeric

components. Hence a suitable solvent system has been sought after, that was able to comply with electrospinning processing requirements and could also represent a good starting point for the alternative wet processes (spin coating and solvent casting). While the DMAc previously used for NBR electrospinning was tested, when used to dissolve PCL it did not succeeded in polymer solubilization, with only some swelling obtained. Hence, after few attempts, a 10%wt PCL solution in $CHCl_3$/DMF 1:1wt mixture (S-PCL) was successfully prepared and homogenously blended with S-NBR (in DMAc, previously discussed). Several polymer ratios were used (see TABLE 2.3) in order to evaluate whether a threshold polymer content would cause precipitation or separation of one of the many components of the complex mixtures: however, in no case such event was detected, and all the produced blend solutions are clear and do not display any evidence of phase separation phenomena while in the liquid phase. Hence starting from the different solution obtained (see TABLE 2.3) they were processed via solvent casting, spin coating and electrospinning, and the results compared in terms of blending efficacy of the two thermodynamically poorly miscible polymers. It is worth to point out that the viscosity of the starting solutions is different and, as reported in FIGURE 2.3, the blends behaviour lies more or less linearly in between the pure polymers.
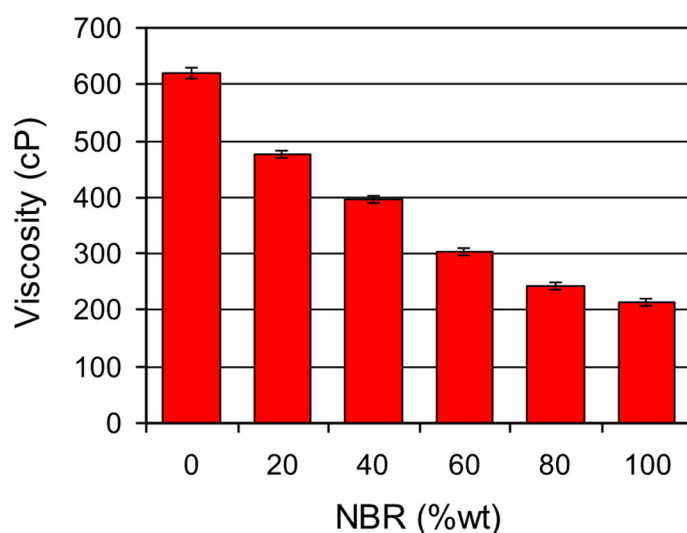
FIGURE 2.3 • Viscosity of PCL and NBR solutions, and of their blends.

2.1.3 • Processing of NBR/PCL solutions

While the film morphology is not the most adequate for the composite modification purpose, nonetheless the investigation of the films that can be obtained from the homogeneous solutions produced (TABLE 2.1) might help getting some insights into the polymers blending ability. When the clear solutions are cast on a flat surface (Petri dish) and the solvent is allowed to evaporate at RT, discs with an average thickness of about 0.5–0.6 mm are obtained. Samples are labelled as F-X/Y, where X represents the NBR weight percentage and Y the PCL counterpart. For the sake of comparison, discs of the pure polymers, NBR and PCL, were also produced (and labelled as F-NBR and F-PCL), in order to check the effect of the processing conditions on the performance of these materials: in this case, pure NBR film appears sticky and inconsistent, thus not allowing its handling. All the obtained blended films appear opaque in the aspect, and white spots marring the surface appear and increase with increasing the PCL content with respect to the plain NBR that is an almost transparent compact film. All the blend cast films consistency and aspect (FIGURE 2.4) suggest that some crystallization occurred in almost all the samples, though its development is not homogeneously distributed in the bulk; moreover, F-60/40 and F-80/20 are sticky and difficult to handle as already reported for F-NBR.
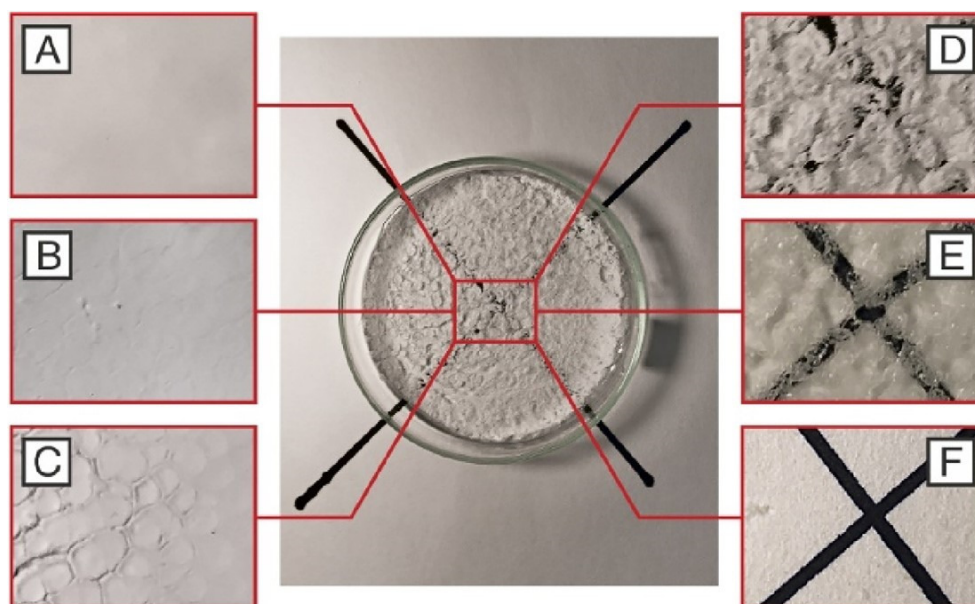
FIGURE 2.4 • Pictures of solvent cast films: A) F-PCL, B) F-20/80, C) F-40/60, D) F-60/40, E) F-80/20, F) F-NBR.

Since the two polymers are expected to hardly blend, and the kinetic aspect of the processing might thus play an important role in the ability to keep together NBR and PCL, an attempt at forming miscible blends via spin coating of the prepared homogenous solutions was also carried out, in order to assess the effect of the rapid solvent evaporation of this processing technique in comparison with the slow solvent evaporation at RT. Thin membranes were obtained, whose aspect appears definitely more homogeneous than cast films and they were labelled SC-X/Y, where once again X represents the NBR weight percentage and Y the PCL counterpart.

The very same solutions already used for solvent casting films, were also electrospun.
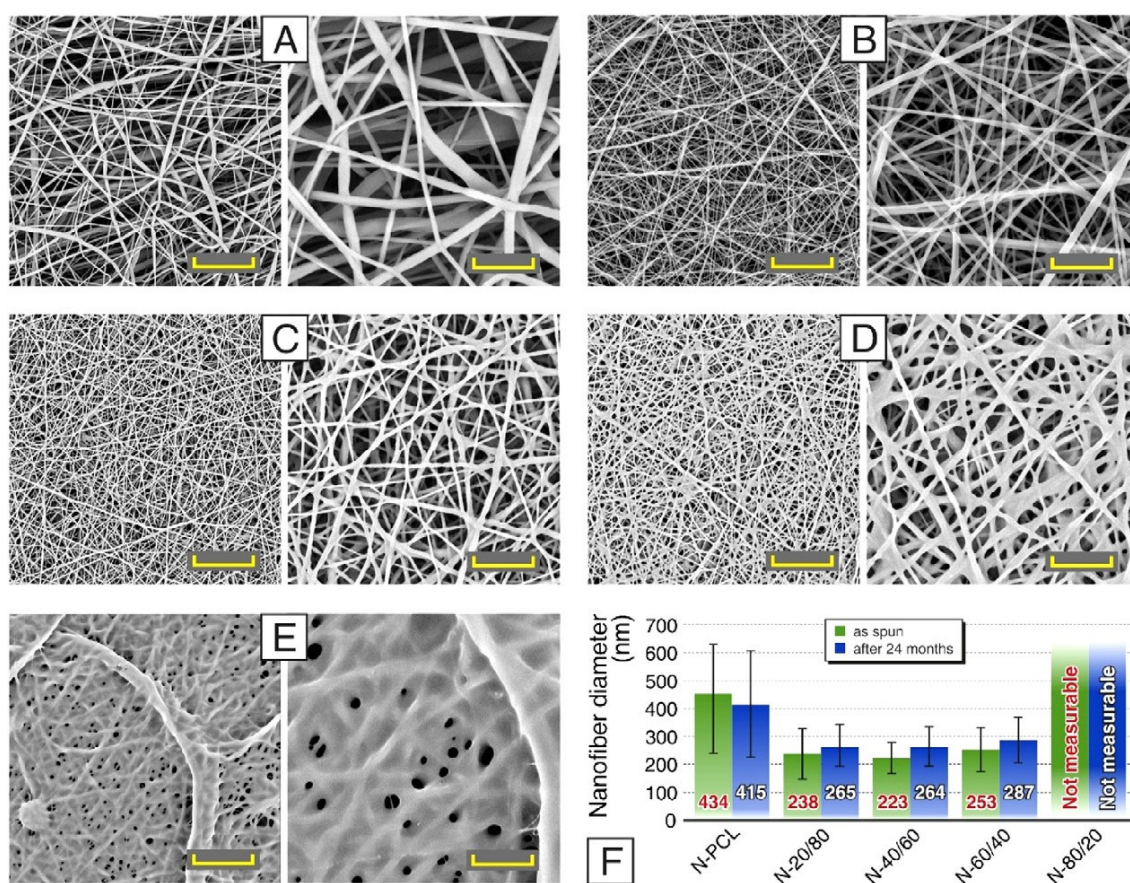
FIGURE 2.5 • SEM images of nanofibrous mats: A) N-PCL, B) N-20/80, C) N-40/60, D) N-60/40, E) N-80/20. Scale bar: left (5,000×) 12 μm, right (15,000×) 4 μm. F) comparison of the average fiber diameters "as spun" and after 24 months.

All the different formulations were able to successfully lead to nanofibers once process parameters optimization has been blandly tailored on the specific solution characteristics (TABLE 2.4), thus providing in each case a stable process, with neither

drops expulsion nor needles obstruction. Nanofibrous mats, labelled as N-X/Y, do not show evidence of macroscopic defects, such as holes or sputtered material. While a wide range of different solution compositions has been investigated with the aim of finding the tentative threshold PCL content required to attain nanofibrous morphology, surprisingly the fibrous morphology is detected for all the produced samples, though at high NBR fractions some filming also occurs. Such a behaviour is clearly displayed in FIGURE 2.5, where SEM micrographs of the different electrospun mixtures are shown at different magnifications, together with plain PCL nanofibers (N-PCL) for the sake of comparison (N-NBR is displayed in FIGURE 2.2): it is worth pointing out that all the images were recorded at least 5 days after deposition, in order to emphasize the stability of the fibrous morphology. Additionally, micrographs taken after 24 months storage at RT still display the same unaltered morphology of the membranes (FIGURE 2.6).
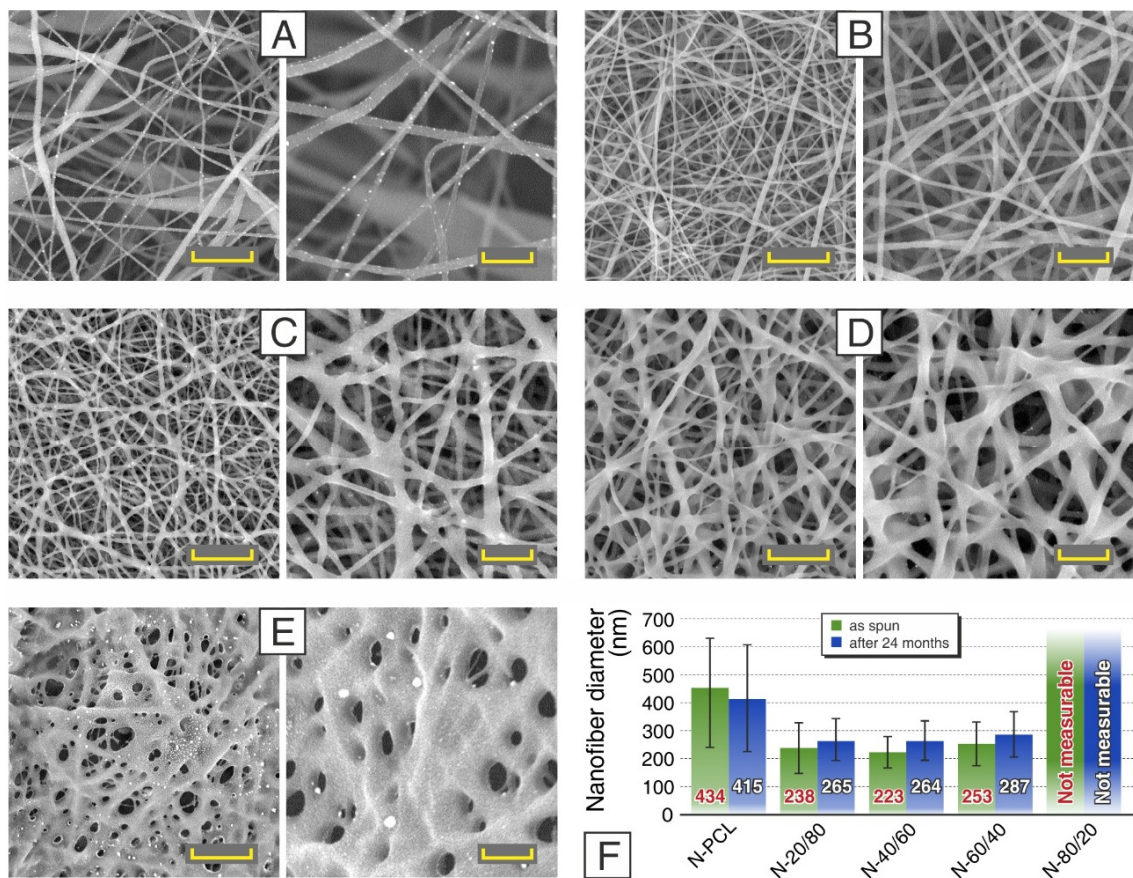
FIGURE 2.6 • SEM images of nanofibrous mats after 24 months from their production: A) N-PCL, B) N-20/80, C) N-40/60, D) N-60/40, E) N-80/20. Scale bar: left (10,000x) 6 μm, right (25,000x) 2 μm. F) comparison of the average fiber diameters "as spun" and after 24 months.

While the fibrous morphology is always obtained, increasing NBR content it can be clearly observed that fibers tend to join at the cross sections, and finally, when NBR represents 80% of the polymeric mass, there is a tendency to fill the cavities with some filming material (FIGURE 2.5E). Nonetheless, it clearly appears that fibrous morphology is present and stable with time even in the most extreme formulations. The average diameter of nanofibers, evaluated via SEM micrograph analysis for all the samples with the exception of the N-80/20 due to the filming effect, stays well below the micrometre threshold in all cases (FIGURE 2.5F). In particular, a sudden drop in the fibers diameter is observed going from pure N-PCL to the blends: this behavior can be attributed to both the different polymer/solvent system mixture used for every electrospun sample that, as depicted in FIGURE 2.3, affects the final solutions viscosity, and to the application of a higher electrostatic field (1.3–1.4 vs 1.0 kV/cm) required for processing polymer mixtures with respect to plain PCL.

2.1.4 • *Thermal characterization of NBR/PCL films and nanofibrous membranes*

All the obtained samples were subjected to thermal analysis for investigating the behaviour of the polymeric components upon processing, and as a function of the processing conditions. A preliminary TGA run (graph not shown) rules out the presence of residual solvent within both films and nanofibers, which could somehow affects thermal behaviour of the polymers in the further investigations. All prepared film samples were analysed by differential scanning calorimetry (DSC) and TABLE 2.1 collects their thermal characterization data together with results obtained for the plain polymeric components NBR and PCL, both in film (F-PCL and F-NBR) and pellet form, for the sake of comparison.

In the present case, as shown in TABLE 2.1, PCL thermogram displays two events, with a low temperature stepwise transition ascribed to the polymer glass transition centered at −58 °C, and an endothermic peak typical of crystal phase melting around 64 °C, whose entity increases upon solvent casting. It is indeed renown that solubilized crystalline polymers are strongly influenced by the solvent in their ability to crystallize [15] thus possibly promoting crystal formation in the cast PCL. Carboxylated NBR, instead, shows only a complex stepwise transition, that can be separated in two different events centered at −14 and −42 °C, respectively. Such a behaviour has been already

observed in poly(butadiene-*co*-acrylonitrile) copolymers [16] where, depending on the polymerization condition, poly(Bu-*alt*-ACN) rich segments form first, and finally poly(butadiene) homopolymer rich blocks add upon ACN depletion [17]. The addition of MAA comonomer does not alter this twofold situation, but tends to increase both T_gs with respect to literature data referred to plain NBR, possibly owing due to the intrinsic stiffness and H-bonding ability [18] of the methacrylic *co*-unit (T_g Poly(MAA) ≈ 230 °C [19]).

When analysing NBR/PCL mixtures, it is expected that, in the case they are able to form a miscible polymer blend, they would display a single T_g, whose value should lie between the glass transition temperature of the individual reference polymers, given that the reference polymers have T_gs values at least 20 °C apart and represent at least 10%wt of the total mass [20]. Moreover, the blend glass transition temperature often exhibits a composition dependence that can be well described by a mathematical equation, of which the most renown is the empirical Fox equation (EQUATION 2.1):

$$\frac{1}{T_g} = \frac{w_1}{T_{g1}} + \frac{w_2}{T_{g2}}$$

EQUATION 2.1

where w_1 and w_2 are the weight fractions and T_{g1} and T_{g2} are the glass transition temperatures of Polymer 1 and 2 respectively, while T_g is the blend glass transition temperature (temperatures expressed in kelvin).

The obtained solvent cast films are all characterized by the presence of both a stepwise transition and an endothermic peak (TABLE 2.1). All but F-20/80 samples display the same complex stepwise transition discussed for NBR, with double T_g, whose values are very similar to those of the plain NBR. F-20/80 shows instead a single step transition centered at an intermediate value between PCL and the lowest T_g in NBR, as plotted in FIGURE 2.7A.

While it could be argued that there is the lack of PCL T_g in all the samples, nonetheless the trend displayed in FIGURE 2.7A is clearly not typical of a blend, since no clear composition correlation is set. For the sake of comparison, the trend of the previously discussed Fox equation (EQUATION 2.1), is also sketched in FIGURE 2.7A. In the present case the lack of PCL T_g could be tentatively ascribed to the presence of a significant crystal phase melting at a temperature that is compatible with that of the polyester (TABLE 2.1).
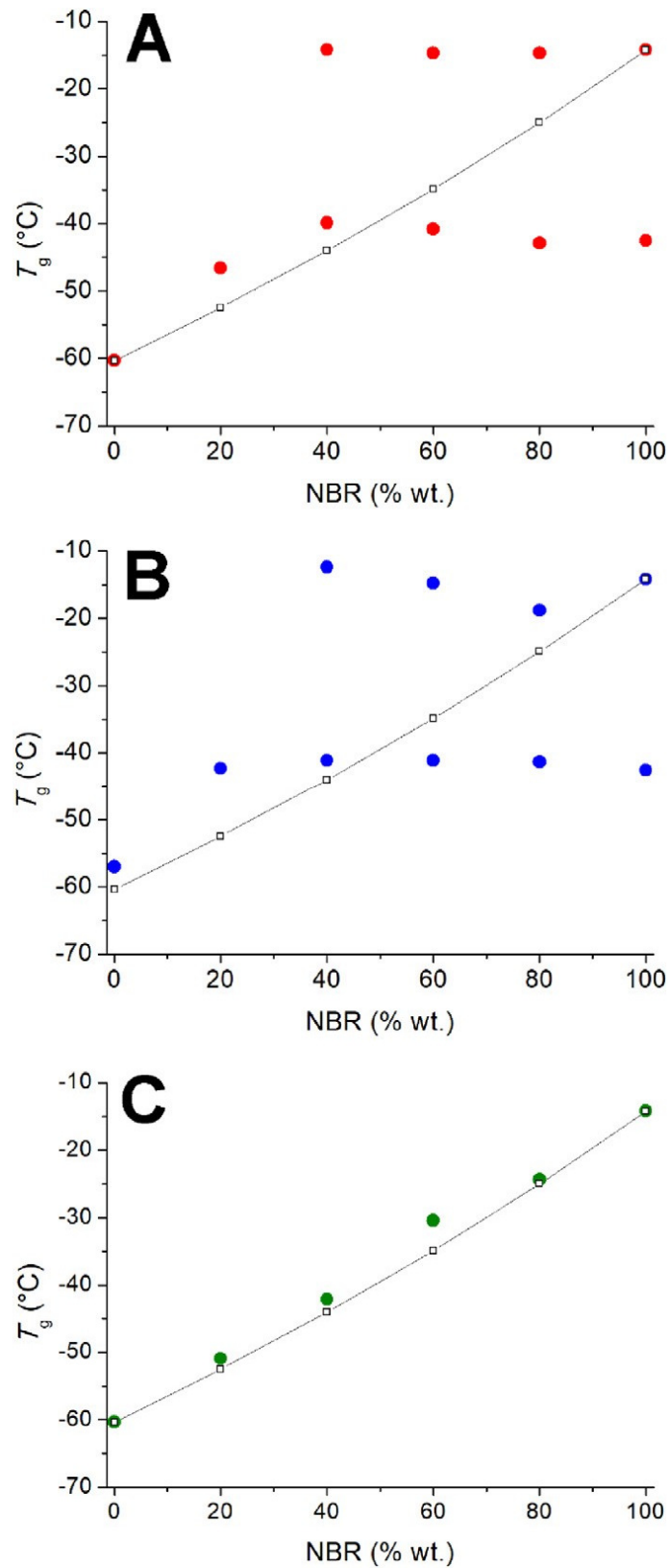
FIGURE 2.7 • Glass transition temperatures (T_g) as a function of NBR fraction (%wt) of A) solvent cast films, B) spin coating films and C) nanofibrous mats. Solid dots: T_g from DSC analyses; white squares: T_g calculated by Fox equation (EQUATION 2.1).

WAXS analysis, carried out on all the solvent cast films and displayed in FIGURE 2.8A, confirms indeed that the crystal phase can be attributed to the PCL, whose typical reflection can be observed in all the diffractograms [21–23], with an increasing broad amorphous halo that becomes more and more visible with increasing NBR fraction in the mixture. Such a condition would render the glass transition of the crystalline polymer (PCL) almost undetectable when the polymer fraction is around 20%wt, which actually corresponds to a mere 11%mol polyester.

Though the visual aspect of the spin coated specimens suggests a higher extent of homogeneity, the T_gs recorded for such samples perfectly match the trend previously discussed for the unblended films, as reported in TABLE 2.1 and displayed in FIGURE 2.7B, showing that not even spin coating was able to provide miscibility. Analogously to the previous films (either cast or spin coated) investigation, electrospun membranes were analysed by DSC, and measurements were carried out on all the obtained nanofibrous samples, as well as on the reference nanofibrous PCL: the obtained data are summarized in TABLE 2.1. NBR/PCL nanofibrous mats all show one single glass transition temperature (T_g) below RT in the whole span of analysed compositions, ranging between the T_g of PCL and the higher value of the NBR glass transition temperature; above RT an endothermic event is detected. When plotted against the mixture composition, the position of the single T_g perfectly agrees with the values calculated on the basis of Fox Equation (EQUATION 2.1), whose trend (obtained using the higher value of T_g NBR) is also sketched in FIGURE 2.7C for the sake of comparison. Such a behaviour, which is substantially different from the one observed for filmed and spin coated mixtures, seems to suggest the formation of a miscible blend [20]. It was indeed found, based on the Hansen solubility coefficient evaluation, that the two polymers are not completely immiscible and, as such, the ability to homogenously blend together and to form a single phase was not completely ruled out. Hence, in the case of the electrospinning process the extremely rapid solvent mixture evaporation occurring during the jet stretching within the electrostatic field might be responsible for freezing the homogenous polymeric solution in a single phase, that does not tend to separate afterwards, owing to some extent of thermo-dynamic interaction highlighted by the $\overline{\Delta\delta}$ value calculated above.

However, such a tendency is not sufficient to actively promote the blending of the polymers at the molecular level and keep them together when the solvent system slowly evaporates upon casting. When, indeed, the film is cast, the complex mixture of different solvents (DMAc, CHCl$_3$, DMF) will sequentially evaporate, creating an environment with different affinity for the two macromolecules that could contribute to their segregation owing to an overall poor tendency to blend together.

The ability of the electrospinning to promote non-equilibrium miscibility of two partially miscible polymer has already been reported and demonstrated on a 50/50%wt mixtures [13]: however, to the best of the author's knowledge, the evaluation of a wide range of blend compositions obtained via electrospinning, such as the one presently discussed, has not yet been explored. Additionally, the analysed nanofibrous blends also display a prominent endotherm along the whole range of composition which can be associated to the presence of crystalline PCL domains.
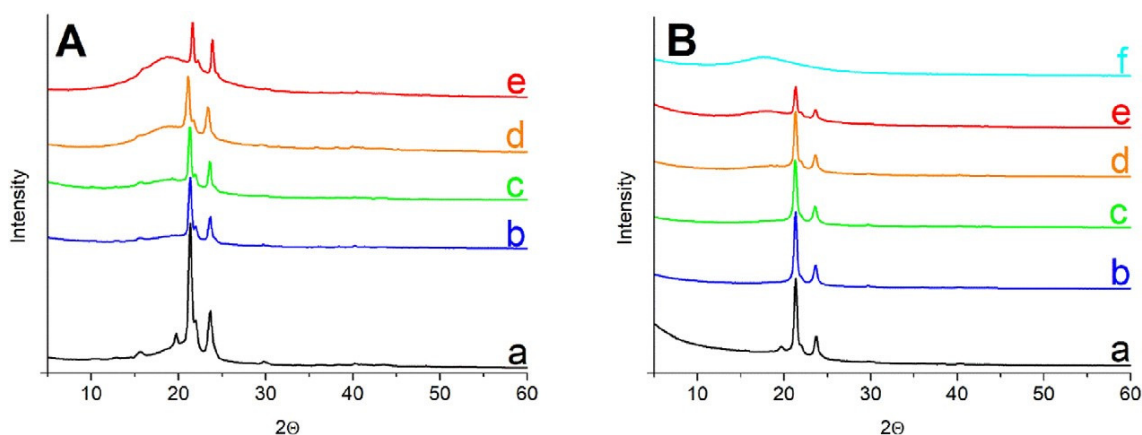
FIGURE 2.8 • WAXS diffractograms of (A) solvent cast films and (B) nanofibrous mats: a) PCL, b) 20/80, c) 40/60, d) 60/40, e) 80/20, f) NBR.

Such an attribution is confirmed by the WAXS diffractograms reported in FIGURE 2.8B, where the typical peaks appear at $2\Theta = 21.40°$ and $23.70°$, corresponding to the (110) and (200) reflections from the orthorhombic unit cell of PCL [21–23].

It is worth pointing out that in the electrospun nanofibrous mats the (102) and (111) reflections substantially decrease, or even disappear, not only in the blends, but also in the plain PCL sample. In such systems, indeed, while the amorphous fraction of polymers is mixed at molecular level, a phase separated crystal region might form, rich

in the crystallizable polymer. In these conditions the decrease in the chemical potential of the crystallizable polymer occurring upon addition of a diluent (a second polymer in the present case) will result in an equilibrium melting point decrease. An additional way to assess the miscibility of the system is, thus, the evaluation of melting point depression for crystalline/compatible polymer blends. The present system, however, does not display the smooth linear trend expected according to the equation drawn by Nishi and Wang [24] (see SECTION 2.4.2 in APPENDIX for the evaluation of the melting point depression according to Nishi-Wang approach). The Nishi-Wang equation, however, has been drawn for equilibrium conditions, and melting points applied to verify the equation should be equilibrium values too. In the present case, though, this is not possible: the electrospinning processing conditions are far from equilibrium, and whatever treatment applied to the nanofibers to evaluate the equilibrium conditions values, such as isothermal crystallization and Hoffman-Weeks extrapolation [25], would remove the nanofibrous morphology thus altering the whole system. Hence the lack of correlation in the present data might strongly be affected by peculiar morphologies due to the processing conditions. In this context, the plot of melting enthalpies calculated for the different blend compositions, as well as for the plain electrospun and pristine PCL, versus the actual weight composition of the blend provides some interesting insight in the crystallization ability within nanofibers. The electrospinning is known to hamper the ability of a polymer to arrange in a crystal phase and the smaller the fiber diameter the higher the draw ratio, which tends too to hamper the formation of big and perfect crystals [11]. Accordingly, the electrospun PCL nanofibers display (FIGURE 2.9) a lower crystal phase content with respect to the reference pristine polymer (ΔH_m decrease by about 10%, see TABLE 2.1).

The addition of a second component should further hamper, or at least leave unaffected, the crystallization ability of the polyester fraction in the blend. Surprisingly, the plot reported in FIGURE 2.9 displays a perfectly linear trend of crystal fraction within the blends, whose extrapolation points to a crystal content in line (actually slightly higher) with the pellet PCL, leading also to a positive intercept at null PCL content (5.7 J/g). This behaviour is even more impressive when considering that, for example, 80%wt corresponds to 66%mol of PCL, and it seems to suggest that not only PCL is unaffected by the electrospinning in its ability to crystallize when homogeneously mixed with

NBR, but the presence of the liquid rubber component has a nucleating effect that overcomes the hampering issues connected to the electrospinning processing: such an effect seems to increase with increasing the non-crystallizable polymer content.
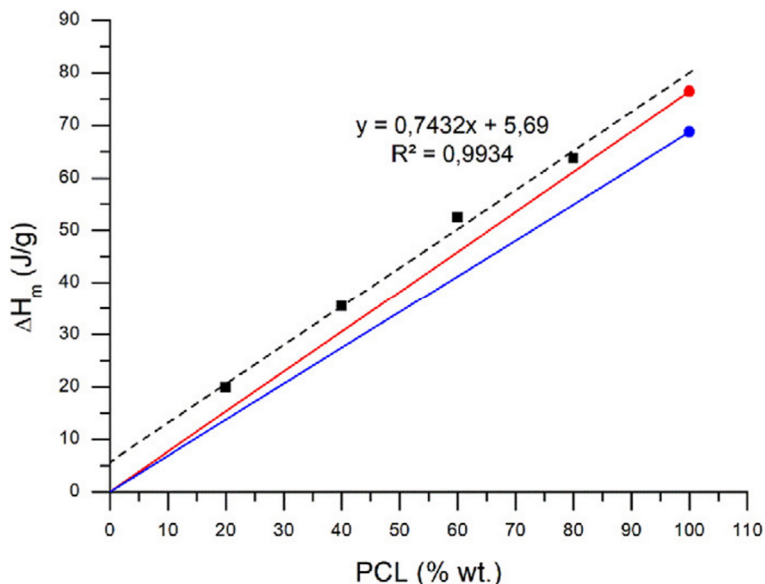
FIGURE 2.9 • PCL melting enthalpy (ΔH_m) of NBR/PCL nanofibrous mats (black squares), PCL pellet (red dot) and PCL nanofibers (N-PCL, blue dot). The red and blue lines represent the ΔH_m extrapolation of the enthalpy trend to 0% of PCL. The black dashed line is, instead, the linear regression line evaluated for NBR/PCL nanofibrous mats ΔH_m values, whose equation is also reported on the graph.

The presence of such a strong crystallizing ability, which is actually boosted by the presence of the co-component, is possibly the reason that makes nanofibrous membranes so manageable even at very high NBR content: while both polymers and their blends have indeed low T_g, the crystal phase promoted at impressively high fraction by the second component allows the system to keep the fibrous morphology without requiring any additional treatment (e.g. rubber crosslinking).

The structure hypothesized above for the nanofibers is actually reminiscent of a thermoplastic elastomer (TPE) [26,27] which comprises at least two interconnected polymer phases, one that is hard at RT but becomes fluid at high temperature (PCL crystal regions), while the other phase is soft and elastic in the same condition (PCL/NBR blended regions). Hence the electrospinning seems able to promote the straightforward formation of thermoplastic elastomeric nanofibers, which are stable at

RT, thus bypassing many of the drawbacks that up to now hampered the production of non-crosslinked rubbery nanofibers.

2.1.5 • *Mechanical characterization of NBR/PCL nanofibrous membranes*

All nanofibrous mats, except the N-80/20, were mechanically tested to evaluate their tensile behaviour. The N-80/20 sample was not tested due to the aspect of the fibers, that appeared partially filmed (FIGURE 2.5E) and cannot be measured. For each type of selected material at least 5 specimens were tested.

Force-displacement results were analysed in terms of stress-strain curves, according to a reliable procedure (see CHAPTER 8 for further details) where stress (σ) is calculated by means of EQUATION 2.2 that describes σ as a function of simple and easy to measure quantities:

$$\sigma = \rho \frac{F}{m} L \qquad \text{EQUATION 2.2}$$

where "ρ", expressed in mg/mm^3, is the material density (not the apparent membrane density), "m" is the specimen mass (in mg), "L" is the specimen initial length (in mm), F is the force (in N) and σ is the stress expressed in MPa. In the present case, ρ has been evaluated as the weighted average value of the two pure polymeric components density, according to nanofiber specific composition (TABLE 2.2).

TABLE 2.2 • Density evaluation of polymer blends.

Sample	NBR fraction	PCL fraction	Density
	g/g	g/g	g/cm^3
NBR	0	1	1.145
NBR/PCL 20/80	0.20	0.80	1.112
NBR/PCL 40/60	0.40	0.60	1.079
NBR/PCL 60/40	0.60	0.40	1.046
PCL	1	0	0.980

In FIGURE 2.10A the relative stress-strain curves are reported. The load normalization based on specimen mass instead of its dimension is useful for discarding any membrane thickness discrepancy due to the instrumentation used for its measurement, and to

obtain more reliable tensile test results, thus unaffected by the membrane porosity (a full investigation on tensile testing of nanofibrous mats is presented in CHAPTER 8).
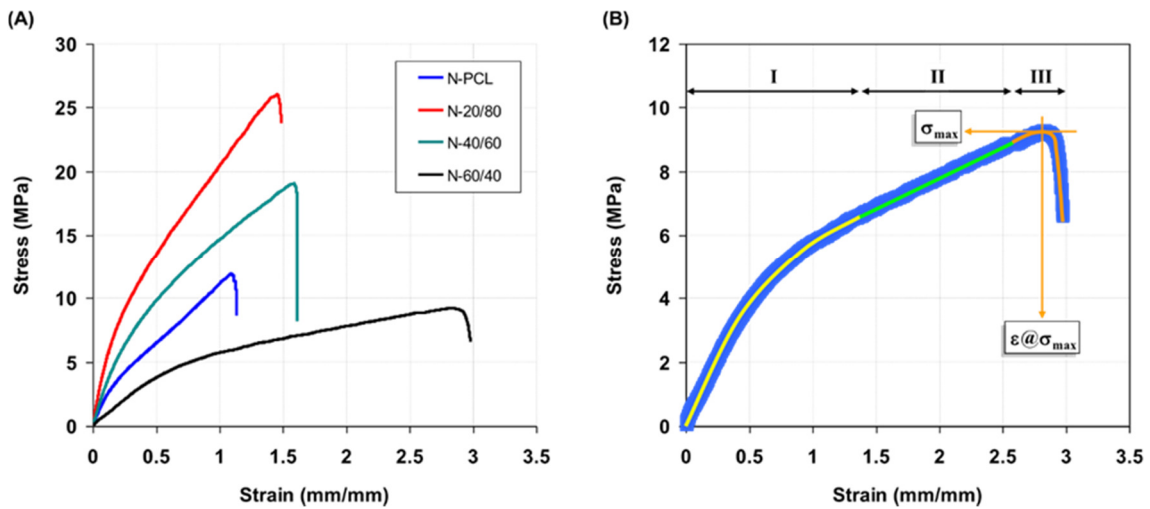
Figure 2.10 • A) Examples of stress-strain curves calculated according to Eq. (2). B) Identification of the three regions which characterize the mechanical behaviour of the material and the two parameters, maximum stress (σ_{max}) and its corresponding strain ($\varepsilon@\sigma_{max}$), which characterize the final nonlinear trend of the curve (Stage III). Curves displayed in the figure were selected to best fit the average values calculated for each batch of specimens.

It is worth mentioning that in all diagrams of FIGURE 2.10A it is possible to distinguish three main stages in the material behaviour, as sketched in FIGURE 2.10B: an initial nonlinear trend (Stage I), a subsequent linear trend (Stage II) at higher strain values, and finally a second nonlinear behaviour (Stage III), at which the stress and strain reach their maximum values before failure. Such a trend has been reported in several works discussing mechanical behaviour of nanofibrous samples [28–30], as well as for the Nylon 66 nanofibers discussed in CHAPTER 7.

The preliminary analysis of stress-strain curves was done considering Stage III and in particular the maximum values of stress (σ_{max}) and the related values of strain ($\varepsilon@\sigma_{max}$) for the four investigated materials were determined. Data displayed in FIGURE 2.11 clearly show that, with respect to the pure PCL nanofibrous mat, there is an almost general tendency to increase both σ_{max} and $\varepsilon@\sigma_{max}$. In particular, N-20/80 shows a significant increment of the mechanical performances of the nanofibrous mat, with the highest increase in terms of stress (+107%), whereas the increment in terms of strain at the maximum stress is limited (+27%). Then, the greater is the NBR fraction in the

blend, the higher is ε@σ$_{max}$, up to +154% in the case of 60%wt of NBR, while a decreasing trend for σ$_{max}$ is observed with respect to the performance of N-20/80, down to a value that in N-40/60 is still significantly higher than pure PCL (+48%) while drops below the pristine polymer for N-60/40.
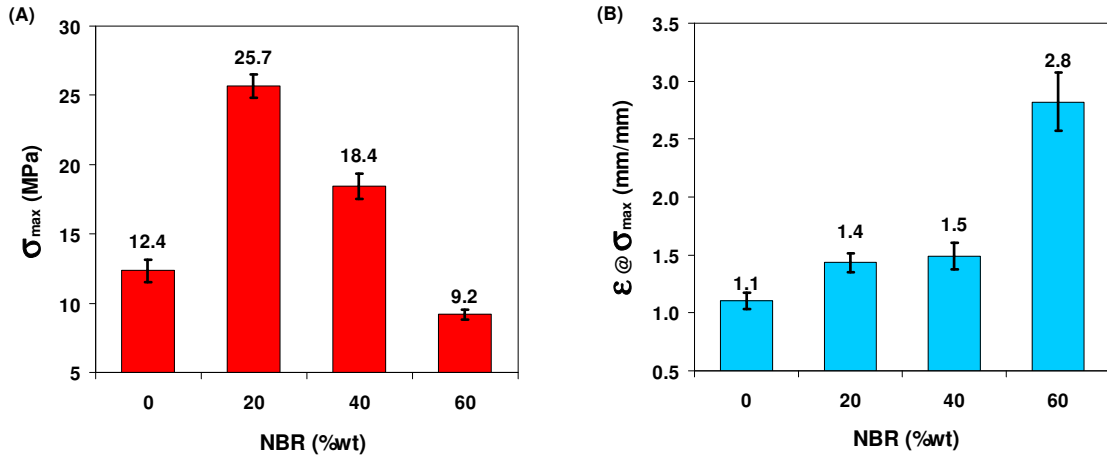
Figure 2.11 • A) Maximum values of stress (σ$_{max}$) and B) the corresponding strain (ε@σ$_{max}$) for samples having different %wt content of NBR.

With the aim of providing a comprehensive picture of the overall nanofibrous mechanical behaviour, Stages I and II of the curves have to be analysed and interpreted and, in order to account for the nonlinear and linear segments of the curves, a mathematical model is thus put forward. The model described by EQUATION 2.3 is based on the combination of two contributions (see CHAPTERS 7,8 for further details), a linear term and a nonlinear exponential one:

$$\sigma(\varepsilon) = a\varepsilon + b - be^{-c\varepsilon} = a\varepsilon + b(1 - e^{-c\varepsilon}) \qquad \text{EQUATION 2.3}$$

where "a", "b" and "c" are adimensional parameters experimentally determined to obtain the best data fitting using the least squares method (values shown in FIGURE 2.12).
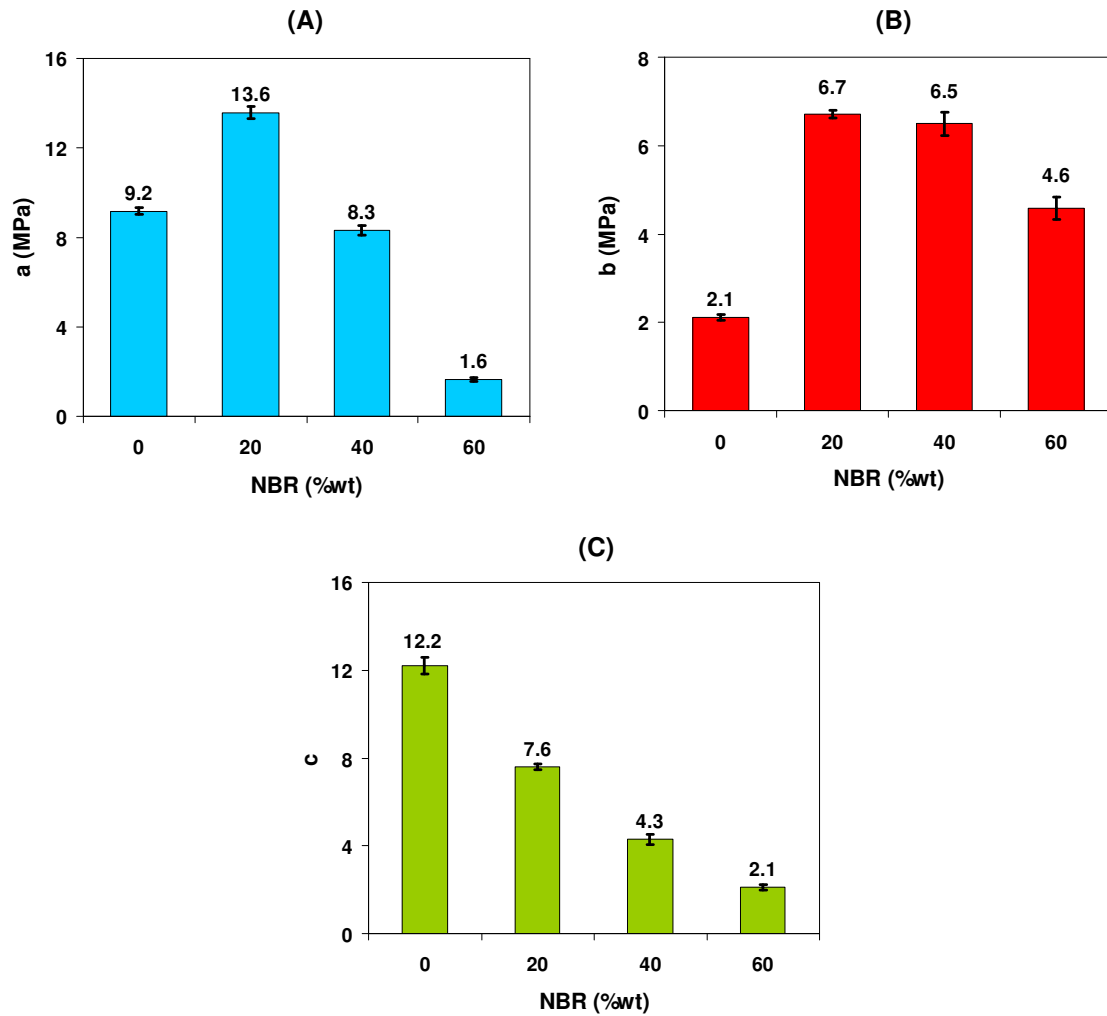
FIGURE 2.12 • Comparison of a, b and c parameters from the model of Eq. 3 for different nanofibrous blends (N-20/80, N-40/60 and N-60/40) and the corresponding PCL (0% NBR).

It was thus possible to obtain an analytical expression for the material stiffness as in EQUATION 2.4:

$$\frac{d\sigma}{d\varepsilon} = E(\varepsilon) = a + bce^{-c\varepsilon} \qquad \text{EQUATION 2.4}$$

EQUATION 2.4 allows to derive two parameters which can be used to study and characterize the material behaviour:

1)   the initial material stiffness (or initial Young's modulus, E_0)

$$E_0 = \lim_{\varepsilon \to 0} E(\varepsilon) = a + bc \qquad \text{EQUATION 2.5}$$

2)	the linear stiffness (or the Young's modulus of the linear trend of stress-strain curve, E_{lin})

$$E_{lin} = \lim_{\varepsilon \to \infty} E(\varepsilon) = a$$

Application of such model to the presently investigated materials highlights an impressive fitting ability of the experimental data (FIGURE 2.13).
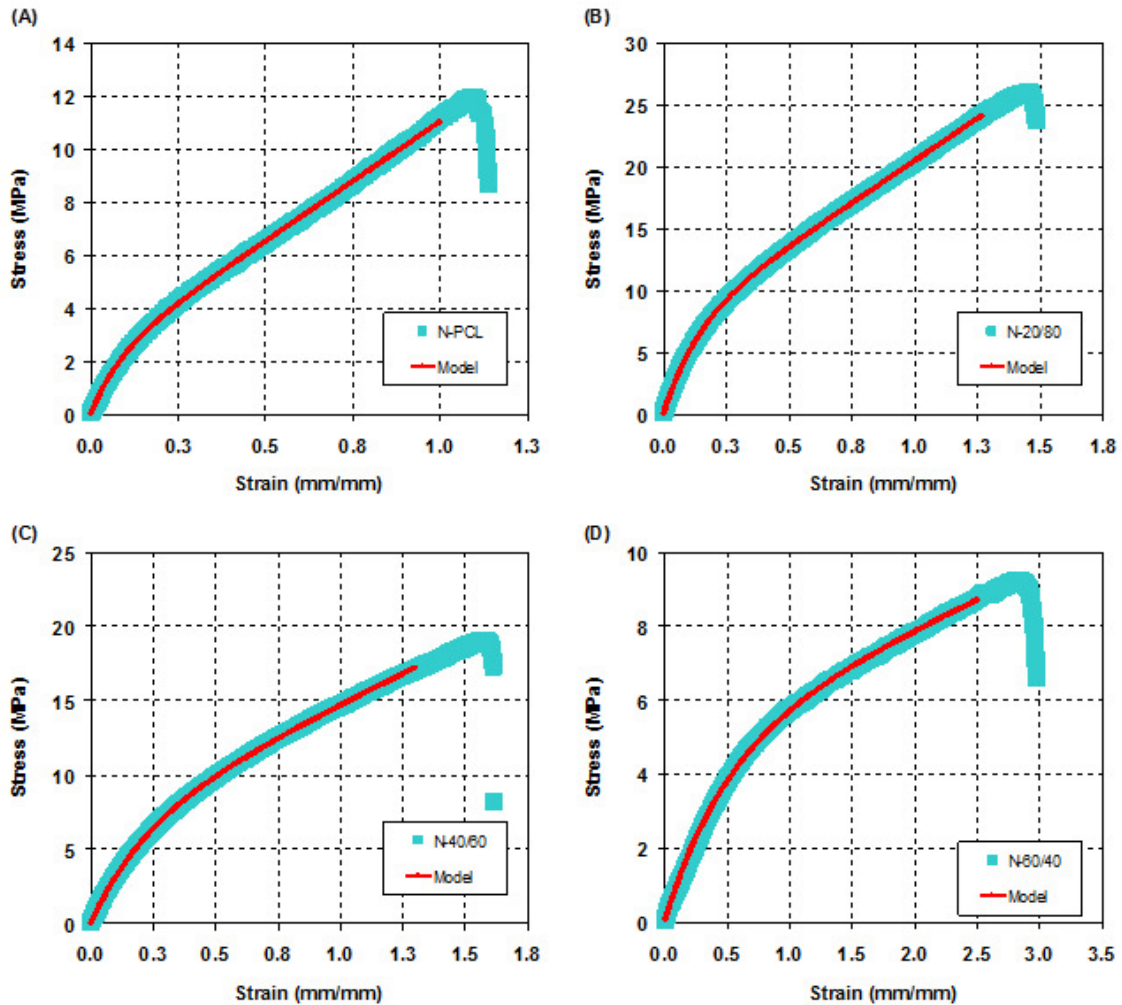
FIGURE 2.13 • Example of the fitting ability of the model proposed in EQUATION 2.8 with experimental data. A single stress-strain curve was selected for each batch: (A) N-PCL, (B) N-20/80, (C) N-40/60, and (D) N-60/40.

It was thus possible to calculate the two main parameters, E_0 and E_{lin} (FIGURE 2.14), for the set of previously discussed specimens.
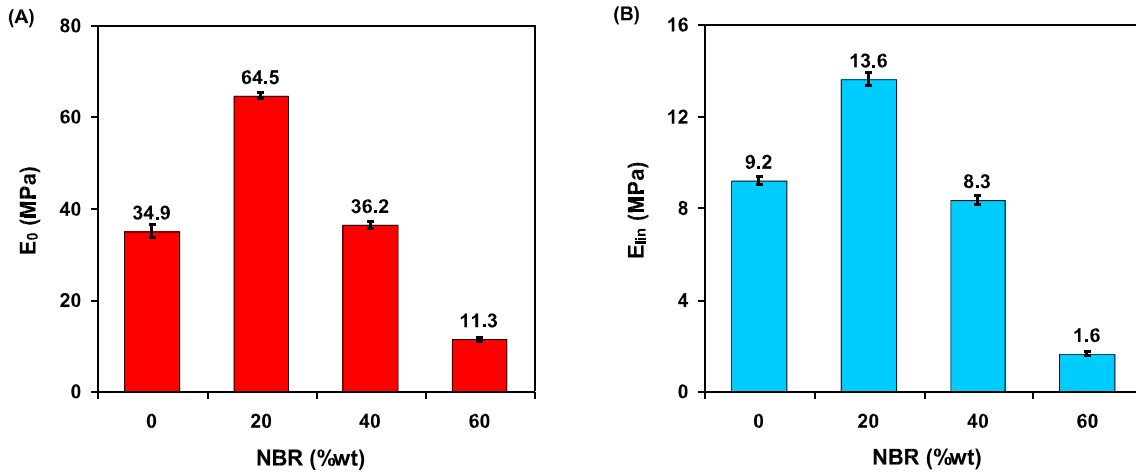
FIGURE 2.14 • Mechanical properties evaluated according to the model proposed in EQUATION 2.3: A) initial material stiffness (E_0) and B) material stiffness in the linear trend (E_{lin}).

When applying the proposed fitting model (EQUATION 2.3), the obtained results for the blend nanofibers clearly display that, starting from plain PCL, NBR addition to the nanofiber composition helps improving both the elastic modulus E_0 and the properties at failure (σ_{max} and $\varepsilon@\sigma_{max}$). F-20/80 has unexpectedly high modulus and toughness (σ_{max} and $\varepsilon@\sigma_{max}$ both increase with respect to plain N-PCL), while F-40/60 has a modulus that almost matches the one of N-PCL, but with far higher properties at break. This effect could be attributed to both the excess of crystal phase and possibly also to some fiber weld joints induced by the presence of the liquid rubber in the system that is increasing in content. Such a behaviour, however, agrees with the previously discussion on the PCL degree of crystallinity (TABLE 2.1), that was found to be surprisingly high considering the presence of a significant amount of the second non-crystalizing component (NBR), and the processing via electrospinning that is renown to depress crystallization. Moreover, the overall behaviour agrees with the assumption that a TPE-like structure is formed upon electrospinning of the mixture and such a morphology not only keeps together the fibers without the need for a chemical crosslinking, but it also provides excellent mechanical properties to the membrane without the need of additional treatment (e.g. rubber crosslinking). Indeed, the elastic modulus (E_0) drops below the plain N-PCL value only at NBR content around 60%wt (F-60/40): while it could have been expected a strong plasticizing effect from NBR in all the range of compositions, this, in fact, only happens at very high liquid rubber fractions and with limited drawback on mechanical performance. F-60/40 still has

impressing toughness and high properties at break, owing to the thermoplastic elastomeric morphology attained during the processing. The reasons underlying such a complex behaviour can be found both in the trend of the crystal phase content and in the nanofibrous mat architecture in terms of joints between fibers. While the latter parameters should increase in efficiency upon growing the fraction of NBR, the crystal phase, which is expected to decrease in the same conditions, has been found surprisingly high, thus justifying an unexpected positive performance of N-20/80 and to some minor extent of N-40/60 in terms of E_0. An additional parameter that has to be taken into account is the average diameter that, in the case of blends, is significantly smaller than N-PCL (about half of the N-PCL value, FIGURE 2.5F), and such a morphological character has been proven to boost mechanical performances when it gets below a given threshold which might be peculiar to the polymeric system but has been reported to be in the order of 400–500 nm [31,32].

Non-woven mats deformation is driven by a number of overlapping phenomena which are not always directly correlated to the polymer properties, such as non-homogenous distribution of the fibers direction, entanglements and bundling [2,33]. Following EQUATIONS 5 and 6 it was also possible to introduce two additional parameters useful to better define the material behaviour, as sketched in FIGURE 2.15A, and in particular:

1) the tangent line at the origin of the stress-strain curve, described by EQUATION 2.7:

$$\sigma_\varepsilon = E_0\varepsilon \qquad \text{EQUATION 2.7}$$

2) the line that best fit the linear trend of the stress-strain curve at high strain values, i.e. the tangent of the curve portion in linear region (Stage II), such as described in EQUATION 2.8:

$$\sigma_\varepsilon = E_{lin}\varepsilon + b \qquad \text{EQUATION 2.8}$$

The intersection of the two straight lines from EQUATIONS 2.7 and 2.8 provides the onset extrapolation of the slope change, i.e. a knee which can be used to represent the switch from the highest initial slope to the linear section of the stress-strain curve.
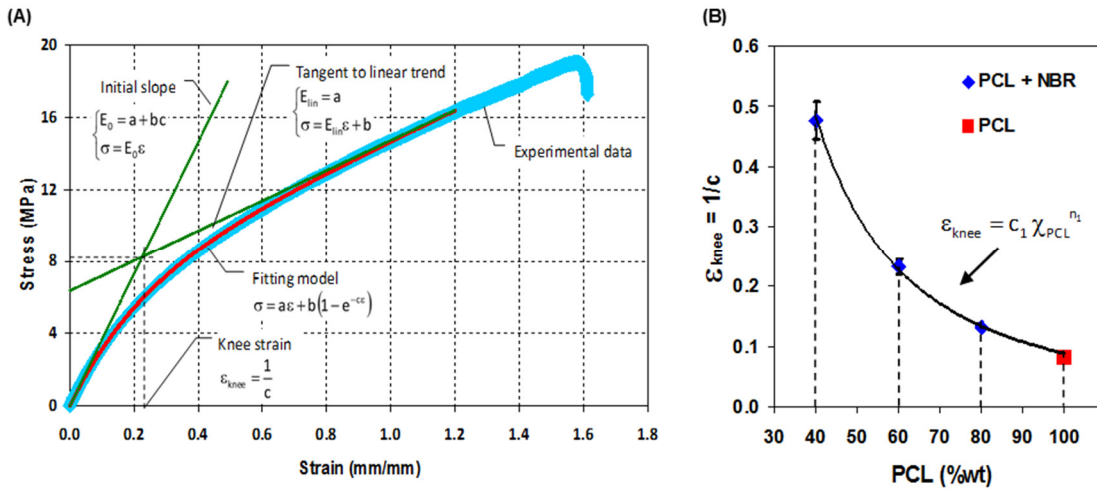
FIGURE 2.15 • A) Representation of the experimental data of the fitting model and of the two lines which describe the initial (E_0) and the linear (E_{lin}) range tangents to the curve, according to EQUATIONS 7 and 8. B) Plot of ε_{knee} as a function of the PCL weight fraction in the blends. The interpolating function relates the ε_{knee} to the PCL weight percentage (χPCL) and the best fitting constants are $c_1 = 440$ and $n_1 = -1.85$.

Moreover, it is possible to demonstrate that the strain at the intersection, ε_{knee}, equals $1/c$, where c is the parameter evaluated based on EQUATION 2.3 (see FIGURE 2.12). The evaluation of ε_{knee} from the experimental curves (see examples of FIGURE 2.16) shows a peculiar trend of such parameter when plotted as a function of PCL fraction in the blend, as displayed in FIGURE 2.15B.

Such a figure clearly highlights that, by increasing the content of NBR in the blend, the strain value at which the knee takes place increases.

While the initial lowering of stiffness might stem from the reorganization of fibers in the network, the reduction of intersections and the breaking of such fibers already bearing a load, asymptotic tendency of the stiffness could be mainly ascribed to fibers ordering along displacement direction. In the present case, both linear and non-linear E behaviours are affected in a similar way by the NBR addition to the nanofibrous mat, denoting a relevant effect of the liquid rubber to its mechanical behaviour throughout the entire deformation range, in agreement with the assumption that a stable thermoplastic elastomeric morphology has been obtained. The transition from one type of prevailing behaviour to the other is also influenced by the fiber thickness, their prevailing alignment and the presence of weld joints. This behaviour could stem from the fact that the initial non-linear behaviour, with higher stiffness, that was attributed

to deformation of the network complex system toward a more ordered one, is hampered by the presence of weld joints and plastic deformation induced by the NBR increasing content.
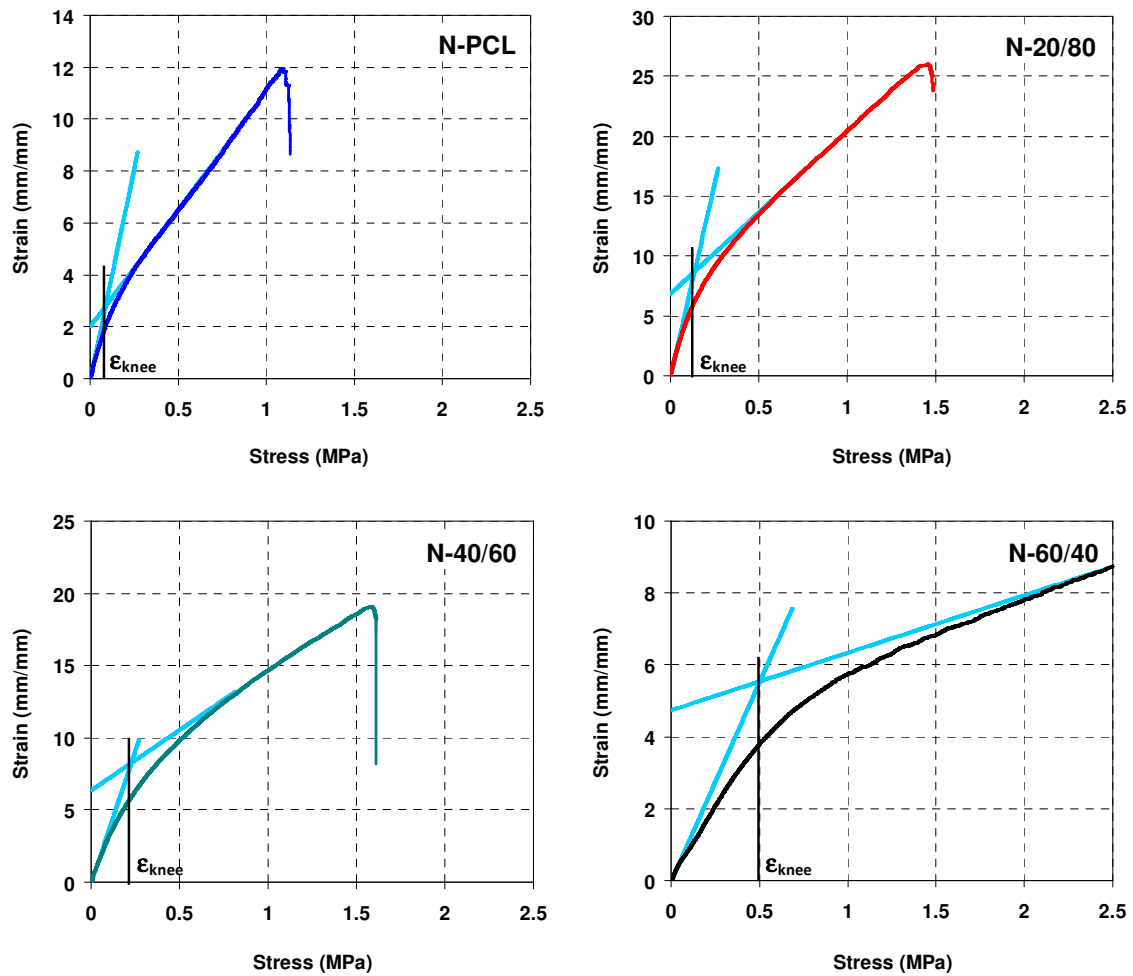
FIGURE 2.16 • Evaluation of ε_{knee} for the different tested samples as the intersection of the two straight lines from EQUATIONS 7 and 8. Curves displayed in the figure were selected to best fit the average values calculated for each batch of specimens.

2.2 • MATERIALS AND METHODS

2.2.1 • *Materials*

Carboxylated nitrile butadiene rubber (NBR) NIPOL 1072CGX was purchased from Zeon Chemicals [68%mol butadiene (Bu), 28%mol acrylonitrile (ACN), 4%mol methacrylic acid (MAA)]. Poly(ε-caprolactone) (PCL), M_w 70,000-90,000, was purchased from Sigma-Aldrich. Polymers were both used without any preliminary treatment. N,N-dimethylacetamide (DMAc), N,N-dimethylformamide (DMF), formic acid and chloroform (CHCl$_3$) were purchased from Sigma-Aldrich and used without further purifications.

2.2.2 • *Polymer solutions and blend preparation, viscosity measurements*

NBR solution (S-NBR, 10%wt) was prepared in DMAc (e.g. 1.0 g of polymer in 9.6 mL of solvent) under magnetic stirring at room temperature until formation of homogeneous solutions.

PCL solution (S-PCL, 10%wt) was prepared in CHCl$_3$/DMF 1:1wt (e.g. 1.0 g of polymer in 3.0 mL of CHCl$_3$ and 4.8 mL of DMF) under magnetic stirring at room temperature until formation of homogeneous solutions.

NBR/PCL blends were prepared by mixing together S-NBR and S-PCL solutions in different proportions (20, 40, 60, and 80%wt of S-NBR solution), according to TABLE 2.3. Polymer blends were stirred for minimum 2 h to ensure proper homogenization.

TABLE 2.3 • Relevant data of NBR, PCL and their mixed solution.

Solution/Blend	Polymer concentration[a]	Blend		Solvent system
		S-NBR solution	S-PCL solution	
	%wt	%wt	%wt	
S-NBR	10	100	0	DMAc
S-PCL	10	0	100	CHCl$_3$/DMF 1:1wt
S-20/80	10	20	80	DMAc, CHCl$_3$ and DMF[b]
S-40/60	10	40	60	DMAc, CHCl$_3$ and DMF[b]
S-60/40	10	60	40	DMAc, CHCl$_3$ and DMF[b]
S-80/20	10	80	20	DMAc, CHCl$_3$ and DMF[b]

[a] in case of blend, the value represents the total polymer concentration

[b] solvents proportions are determined by the ratio of the mixed solutions

Viscosity measurements were performed at 25 °C via rotational viscometer (Haake Viscotester 7 plus), equipped with R5 spindle at 200 rpm (except for the S-NBR and S-80/20, where R4 spindle was used to better comply the recommended viscosity ranges), using an adequate volume of solution.

2.2.3 • Solvent casting and spin coating films production

Films obtained via solvent casting were produced pouring an adequate amount of polymeric solution/blend into a Petri dish which is kept for 18 h in environmental conditions and finally moved in a desiccator under vacuum for 6 h (3 dynamical + 3 static vacuum) to ensure complete solvent removal.

Films obtained via spin coating (Delta 20 BM, B.L.E. Laboratory Equipment GmbH) were produced placing a few drops of solution on a 20 × 20 mm microscope slide and applying the following program: 60 s at 2,500 rpm, followed by 90 s at 3,500 rpm (acceleration/deceleration ramps of 20 s). Samples were finally moved in a desiccator under vacuum for 6 h (3 dynamical + 3 static vacuum) to ensure complete solvent removal.

2.2.4 • Nanofibrous mats production

Nanofibrous mats were produced using a Spinbow® electrospinning machine equipped with four 5 mL syringes. Needles (length 55 mm, internal diameter 0.84 mm) were joined to syringes via teflon tubing. Nanofibers were collected on a rotating drum covered with poly(ethylene)-coated paper at 50 rpm (tangential speed 0.39 m/s). Mats have final dimensions of approximately 30 × 40 cm. In TABLE 2.4 electrospinning process and environmental parameters for mats production are reported.

The electrospinning process was carried out until an adequate thickness of mat (ranging from 40 to 60 μm) was obtained. The mat thickness was measured using an analog indicator, applying a pressure of 360 g/m^2.

TABLE 2.4 • Electrospinning process parameters and nanofiber diameters of produced nanofibrous mats.

Nanofibrous mat	Electrospun Solution/Blend	Flow rate	Electric potential	Distance	Electric field[a]	Temperature	Relative humidity	Nanofiber diameter[b]
		mL/h	kV	cm	kV/cm	°C	%	nm
N-PCL	S-PCL	0.75	14.4	15.0	1.0	25-27	29-32	434 ± 196
N-20/80	S-20/80	0.70	17.0	13.0	1.3	22-25	23-25	238 ± 90
N-40/60	S-40/60	0.70	17.0	13.0	1.3	24-26	19-21	223 ± 56
N-60/40	S-60/40	0.55	18.3	13.0	1.4	22-24	20-22	253 ± 78
N-80/20	S-80/20	0.60	18.5	13.0	1.4	24-26	25-27	n.d.

n.d. = not detectable

[a] calculated as electric potential to distance ratio

[b] "as spun" nanofiber

2.2.5 • *Characterization of nanofibrous membranes*

Nanofibrous mats were analysed by Optical Microscopy with a Zeiss Axioscop and by scanning electron microscopy (SEM, Phenom ProX) to determine nanofibers morphology. All analysed surfaces were gold coated in order to make them conductive. The distribution of fibers diameters on the electrospun mat was determined via manual measurement of >100 single fibers by means of an acquisition and image analysis software (ImagePro Plus). Thermogravimetric (TGA) measurements were carried out using a TA Instrument SDT Q600 on 10 mg samples heating from Room Temperature (RT) up to 600 °C at 10 °C/min heating rate samples under inert atmosphere (nitrogen flow rate 100 mL/min), with a subsequent 30 min isotherm under oxidizing atmosphere (air flow rate 100 mL/min). Differential scanning calorimetry (DSC) measurements were carried out on a TA Instruments Q2000 DSC modulated apparatus equipped with RCS cooling system. In dynamic runs every sample (5 mg) was heated from 0 °C to 200 °C twice at 20 °C/min in nitrogen atmosphere, with an intermediate quench cooling. Wide-angle X-ray scattering (WAXS) were carried out at RT with a PANalytical X'Pert PRO diffractometer equipped with an X'Celerator detector (for ultrafast data collection). A Cu anode was used as X-ray source (K radiation: $\lambda = 0.15418$ nm, 40 kV, 40 mA), and 1/4° divergence slit was used to collect the data in 2θ range from 2° to 60°. Tensile tests of selected nanofibrous mats were made using a Remet TC-10 tensile testing machine equipped with a 100 N load cell, speed test 10 mm/min. Nanofibrous membranes were anchored in a paper frame (47 × 67 and 25 × 45 mm outer and inner

dimensions, respectively), pasted with cyanoacrylate glue for better handling (see CHAPTER 7, SECTION 7.4). Moreover, it guaranteed that all non-woven nanofibers were clamped in the machine fixtures. Effective specimen dimensions were 20 × 45 mm, (width) × (initial length), respectively. Paper frame was cut before the test started. After tensile test, the specimen was recovered and weighted for the stress (σ) calculation according to EQUATION 2.2. At least five specimens were tested for each nanofibrous mat type. The elastic modulus, maximum stress and elongation at break were evaluated. Tensile test data were analysed by means of a fitting model which enable the direct evaluation of elastic moduli (Young modulus and the linear trend for high deformations) of the material (see EQUATION 2.3).

2.3 • CONCLUSIONS

The ability to obtain electrospun nanofibrous mats based on homogeneous blends of liquid NBR rubber and PCL with a wide range of composition was here discussed and demonstrated. Such membranes show a single, low-temperature T_g and a surprisingly high PCL-like crystal phase content promoted by the presence of NBR.

This morphology well compares with the one of thermoplastic elastomers (TPE) and provides the membranes with excellent long-term stability (at least two years) without the need for a chemical rubber crosslinking. This morphology reflects also in a relevant mechanical performance which is improved with respect to the plain PCL nanofibers and thus shows promising properties that can be exploited in many fields, such as in composite modification. Additionally, these results were interpreted using a recently proposed phenomenological model, whose parameters are evaluated and explained taking into account nanofibers composition and morphology. While this is a preliminary model, whose terms' physical significance has still to be fully disclosed, the outstanding fitting ability validates its significance as a tool for the interpretation of nanofibrous mats mechanical behaviour.

Finally, the present formulation paves the way for implementing an easy additional crosslinking step to the present process, when in the presence of a convenient initiator system, leading to some easily obtained nanofibrous rubbery sponges, whose feature can be easily controlled.

2.4 • APPENDIX

2.4.1 • Evaluation of the solubility parameters for NBR and PCL and their miscibility

The solubility parameter δ, or Hildebrand solubility parameter, can be divided into three different components, the Hansen solubility parameters, according to EQUATION 2.2

$$\delta^2 = \delta_d^2 + \delta_p^2 + \delta_h^2 \qquad \text{EQUATION 2.2}$$

where δ_d is the factor accounting for dispersive forces, δ_p relates to polar forces and δ_h accounts for hydrogen bonding ability [12]. The Hansen solubility parameters can be evaluated according to the group contribution theory, summing up the contributions of each group composing the chemical structure of the material, in agreement with the following formulas, EQUATIONS 2.2-4

$$\delta_d = \frac{\sum_i F_{di}}{V} \qquad \text{EQUATION 2.3}$$

$$\delta_p = \frac{\sqrt{\sum_i F_{pi}^2}}{V} \qquad \text{EQUATION 2.4}$$

$$\delta_h = \sqrt{\frac{\sum_i E_{hi}}{V}} \qquad \text{EQUATION 2.5}$$

using values reported in the literature typical for each group's F_{di}, F_{pi}, E_{hi} and V [12,14].

One of the most common approaches, the one proposed by Hoftyzer and van Krevelen [34], states that each component (δ_d, δ_p and δ_h) can be evaluated for each polymer according to the groups' contribution theory, summing up the contributions of each group composing the compound and using values reported in the literature for the group's F_{di}, F_{pi}, E_{hi} and V [12,14].

While the evaluation of such parameter for copolymers might not be extremely precise, nonetheless the values obtained in TABLE 2.A2 for PCL and NBR respectively might help defining the relative miscibility of the two polymers, according to the following EQUATION 2.6

$$\overline{\Delta\delta} = \sqrt{(\delta_{\mathrm{d}PCL} - \delta_{\mathrm{d}NBR})^2 + (\delta_{\mathrm{p}PCL} - \delta_{\mathrm{p}NBR})^2 + (\delta_{\mathrm{h}PCL} - \delta_{\mathrm{h}NBR})^2}$$ EQUATION 2.6

A good miscibility occurs when $\overline{\Delta\delta}$ value is small, i.e. $\overline{\Delta\delta} < 5\mathrm{MPa}^{1/2}$, and partial miscibility could potentially be attained up to $10\mathrm{MPa}^{1/2}$ [14,15]. Evaluation of the Hansen solubility parameters for PCL was easily found in the literature [16], while a correct assessment of the solubility parameters for the actual carboxylated NBR polymer composition used in the present work was not available. Since it has been reported that variation of few percentage in the monomer composition could strongly affect the solubility parameters [17], such calculations were carried out for the specific polymer presently used, that is actually composed of three different repeating units derived from their related monomers, butadiene (Bu), acrylonitrile (ACN) and methacrylic acid (MAA).

For the present paper, the two polymers involved, NBR and PCL, can be represented according to the formulas reported in FIGURE 2.17.

n = 0.68
m = 0.28
l = 0.04
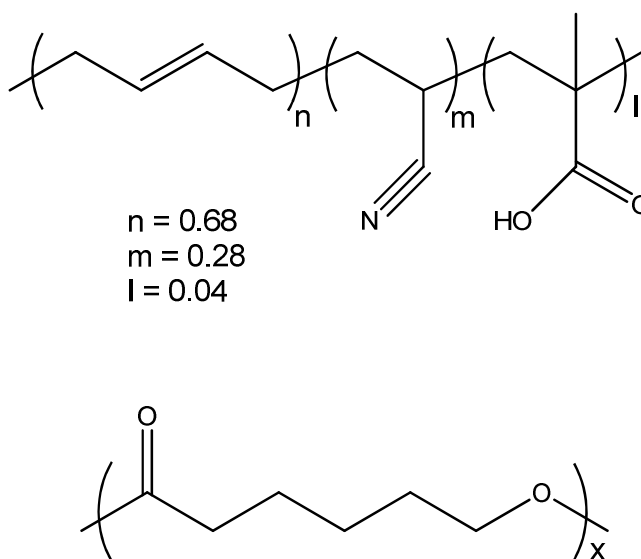
FIGURE 2.17 • NBR and PCL formulas

In this case V, the molar volume of the structural unit of the polymer NBR, has been evaluated according to the following EQUATION 2.7

$$V = \sum N_i V_i$$ EQUATION 2.7

In TABLE 2.5 are reported the values used for evaluating the Hansen solubility parameters for NBR, taken from the literature [14] according to the method of Hoftyzer and van Krevelen [14].

TABLE 2.5 • Parameters for NBR Hoftyzer and van Krevelen [35] groups contribution calculation

Group		V_i	F_{di}	F_{pi}	E_{hi}
		(cm^3/mol)	(J$^{1/2}$•cm$^{3/2}$•mol^{-1})	(J$^{1/2}$•cm$^{3/2}$•mol^{-1})	(J/mol)
Butadiene (n=0.68)					
-CH$_2$-	2x	15.55	270	0	0
=CH-	2x	13.18	200	0	0
Acrylonitrile (m=0.28)					
-CH$_2$-	1x	15.55	270	0	0
>CH-	1x	9.56	80	0	0
-CN	1x	23.1	430	1100	2500
Methacrylic Acid (l=0.04)					
-CH$_3$	1x	21.55	420	0	0
-CH$_2$-	1x	15.55	270	0	0
>C<	1x	3.56	-70	0	0
-COOH	1x	26.1	530	420	10000

The Hansen solubility parameters obtained according to EQUATIONS 2.3-5, together with those found in the literature for PCL [36], are finally reported in TABLE 2.6.

TABLE 2.6 • Hansen solubility parameters used for evaluation of NBR and PCL theoretical miscibility

	δ_d	δ_p	δ_h
NBR	13.2	10.6	4.5
PCL [36]	17.0	4.8	8.3

Based on the solubility parameter evaluation in TABLE 2.A2 and according to EQUATION 2.6, $\overline{\Delta\delta}$ value for the NBR/PCL pair was found to be 7.9MPa$^{1/2}$, a value that does not account for an easy miscibility of the two components, tending instead toward an immiscible system.

2.4.2 • *Application of the Nishi-Wang equation for the evaluation of melting point depression of miscible blends*

Nishi and Wang equation (EQUATION 2.8) for miscible blends of a crystallizable polymer with an amorphous (non-crystallizable) polymer [24] is applied to PCL/NBR blends:

$$\frac{1}{T^0_{m_{Blend}}} = \frac{1}{T^0_{m_{PCL}}} - \frac{R}{\Delta H^u_{PCL}} \frac{V^u_{PCL}}{V^u_{NBR}} \chi_{PCL,NBR} \phi^2_{PCL} \qquad \text{EQUATION 2.8}$$

where PCL represents the crystallizable polymer and NBR is the amorphous (non-crystallizable) polymer respectively, $T^0_{m_{Blend}}$ and $T^0_{m_{PCL}}$ are the equilibrium melting temperature of the blend and of the plain crystalline polymer respectively; ΔH^u_{PCL} is the repeating unit melting enthalpy for PCL, V is the repeating unit molar volume; ϕ^2_{PCL} is the PCL volume fraction and $\chi_{PCL,NBR}$ is the polymer-polymer Flory-Huggins interaction parameter.

The $T_{m_{Blend}}$ results (and not the $T^0_{m_{Blend}}$) are plotted in FIGURE 2.18 as the reciprocal melting temperature ($1/T_{m_{Blend}}$) as a function of the squared weight fraction (ϕ^2) of the crystallizable component, that is PCL.
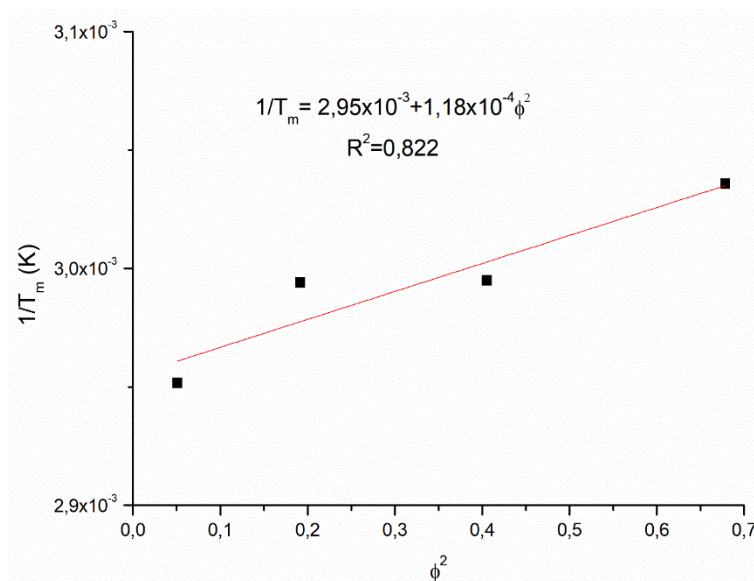
FIGURE 2.18 • Melting temperature ($1/T_m$, [K]) of N-X/Y blends nanofibers plotted according to EQUATION 2.3 for PCL crystal phase; in red is the linear regression line, whose equation is also reported on the graph.

Based on Flory-Huggins theory, it can be shown that negatives values for the $\chi_{PCL,NBR}$ are correlated to existence of interactions between the polymers, thus resulting in the miscibility of the system. A linear behaviour is expected if the above assumption is correct and if EQUATION 2.3 holds for this blend system. The correlation of the experimental data is pretty poor and the linear regression of the data yields the line drawn in the graph, with the equation reported. From the intercept of the line fitting the PCL melting data, the melting temperature of plain PCL can be extrapolated at T_m(Nishi-Wang) = 66°C, a value which is not too far from the experimental result (T_m (N-PCL) = 61°C in TABLE 2.1). Moreover, according to EQUATION 2.3, a positive slope of the regression line implies a negative value of the $\chi_{PCL,NBR}$ interaction parameter, which accounts some extent of miscibility. However, while the average trend is set in the direction of the miscibility of the two copolymers, the linearity expected when the Nishi-Wang equation is best fitted if far from the present situation ($R^2 = 0.822$); the poor correlation coefficient and the non-equilibrium condition that characterize the present approach suggest not to further use data extrapolated by the linear regression for calculating the $\chi_{PCL,NBR}$ interaction parameter value, in order to avoid misleading data.

References

[1]   J.H. Park, G.C. Rutledge, 50th Anniversary Perspective: Advanced Polymer Fibers: High Performance and Ultrafine, Macromolecules. 50 (2017) 5627–5642.

[2]   L. Mazzocchetti, T. Benelli, E. Maccaferri, S. Merighi, J. Belcari, A. Zucchelli, L. Giorgini, Poly-m-aramid electrospun nanofibrous mats as high-performance flame retardants for carbon fiber reinforced composites, Compos. Part B Eng. 145 (2018) 252–260.

[3]   S.S. Choi, J.P. Hong, Y.S. Seo, S.M. Chung, C. Nah, Fabrication and characterization of electrospun polybutadiene fibers crosslinked by UV irradiation, J. Appl. Polym. Sci. 101 (2006) 2333–2337. https://doi.org/10.1002/app.23764.

[4]   M. Tian, Q. Hu, H. Wu, L. Zhang, H. Fong, L. Zhang, Formation and morphological stability of polybutadiene rubber fibers prepared through combination of electrospinning and in-situ photo-crosslinking, Mater. Lett. 65 (2011) 3076–3079. https://doi.org/10.1016/j.matlet.2011.06.089.

[5]   A. Vitale, G. Massaglia, A. Chiodoni, R. Bongiovanni, C.F. Pirri, M. Quaglio, Tuning Porosity and Functionality of Electrospun Rubber Nanofiber Mats by Photo-Crosslinking, ACS Appl. Mater. Interfaces. (2019). https://doi.org/10.1021/acsami.9b04599.

[6]   X. Zhang, G.G. Chase, Electrospun elastic acrylonitrile butadiene copolymer fibers, Polymer (Guildf). 97 (2016) 440–448. https://doi.org/10.1016/j.polymer.2016.05.063.

[7]   R. Palazzetti, A. Zucchelli, Electrospun nanofibers as reinforcement for composite laminates materials – A review, Compos. Struct. 182 (2017) 711–727. https://doi.org/10.1016/j.compstruct.2017.09.021.

[8]   S. Park, J. Kim, M.-K. Lee, C. Park, H.-D. Jung, H.-E. Kim, T.-S. Jang, Fabrication of strong, bioactive vascular grafts with PCL/collagen and PCL/silica bilayers for small-diameter vascular applications, Mater. Des. 181 (2019) 108079. https://doi.org/10.1016/j.matdes.2019.108079.

[9]   A. Sensini, L. Cristofolini, Biofabrication of electrospun scaffolds for the regeneration of tendons and ligaments, Materials (Basel). 11 (2018) 1–43. https://doi.org/10.3390/ma11101963.

[10]   A. Doergens, J.A. Roether, D. Dippold, A.R. Boccaccini, D.W. Schubert, Identifying key processing parameters for the electrospinning of aligned polymer nanofibers, Mater. Lett. 140 (2015) 99–102. https://doi.org/10.1016/j.matlet.2014.10.150.

[11]   X. Wang, H. Zhao, L.S. Turng, Q. Li, Crystalline morphology of electrospun poly(ε-caprolactone) (PCL) nanofibers, Ind. Eng. Chem. Res. 52 (2013) 4939–4949. https://doi.org/10.1021/ie302185e.

[12]   A. Cipitria, A. Skelton, T.R. Dargaville, P.D. Dalton, D.W. Hutmacher, Design, fabrication and characterization of PCL electrospun scaffolds - A review, J. Mater. Chem. 21 (2011) 9419–9453. https://doi.org/10.1039/c0jm04502k.

[13]   P. Tipduangta, P. Belton, L.L. Fábián, L.Y. Wang, H. Tang, M. Eddleston, S. Qi, Electrospun Polymer Blend Nanofibers for Tunable Drug Delivery: The Role of Transformative Phase Separation on Controlling the Release Rate, Mol. Pharm. 13 (2016) 25–39. https://doi.org/10.1021/acs.molpharmaceut.5b00359.

[14]   D.W. Van Krevelen, K. Te Nijenhuis, Cohesive Properties and Solubility, in: Prop. Polym., 2009: pp. 189–227. https://doi.org/10.1016/b978-0-08-054819-7.00007-8.

[15]   M.T. Shaw, Preparation of Blends, in: Polym. Blends Mix., Springer Netherlands, 1985: pp. 57–67.

[16]   L.A. Chandler, E.A. Collins, Multiple glass transitions in butadiene-acrylonitrile copolymers, Rubber Chem. Technol. 43 (n.d.) 1465–1472.

[17]   H. Ono, H. Fujiwara, S. Nishimura, Nanoscale heterogeneous structure of polyacrylonitrile-co-butadiene with different molecular mobilities analyzed by spin–spin relaxation time, Polym. J. 45 (2013) 1027–1032.

[18] R. Chowdhury, M.S. Banerji, K. Shivakumar, Development of acrylonitrile-butadiene (NBR)/polyamide thermoplastic elastomeric compositions: Effect of carboxylation in the NBR phase, J. Appl. Polym. Sci. 100 (2006) 1008–1012.

[19] J. Brandrup, E.H. Immergut, E.A. Grulke, Polymer Handbook, 4th Ed., Wiley, 1999.

[20] D.J. Walsh, Polymer Blends, in: Compr. Polym. Sci. Suppl., Pergamon, 1989: pp. 135–154.

[21] L. Liu, S. Li, H. Garreau, M. Vert, Selective Enzymatic Degradations of Poly(l-lactide) and Poly(ε-caprolactone) Blend Films, Biomacromolecules. 1 (2000) 350–359.

[22] Y. Suzuki, H. Duran, W. Akram, M. Steinhart, G. Floudas, H.J. Butt, Multiple nucleation events and local dynamics of poly(ε-caprolactone) (PCL) confined to nanoporous alumina, Soft Matter. 9 (2013) 9189–9198.

[23] H. Bittiger, R.H. Marchessault, W.D. Niegisch, Crystal structure of poly-ε-caprolactone, Acta Crystallogr. Sect. B Struct. Crystallogr. Cryst. Chem. 26 (1970) 1923–1927.

[24] T. Nishi, T.T. Wang, Melting Point Depression and Kinetic Effects of Cooling on Crystallization in Poly(vinylidene fluoride)-Poly(methyl methacrylate) Mixtures, Macromolecules. 8 (1975) 909–915.

[25] J.D. Hoffman, J.J. Weeks, Melting process and the equilibrium melting temperature of polychlorotrifluoroethylene, J. Res. Natl. Bur. Stand. Sect. A Phys. Chem. 66A (1962) 13–28.

[26] G. Holden, Thermoplastic Elastomers and Their Applications, 2000.

[27] N.P. Cheremisinoff, Condensed Encyclopedia of Polymer Engineering Terms, 2001.

[28] A. Ridruejo, C. González, J. Llorca, Micromechanisms of deformation and fracture of polypropylene nonwoven fabrics, Int. J. Solids Struct. 48 (2011) 153–162. http://dx.doi.org/10.1016/j.ijsolstr.2010.09.013.

[29] S. Sinha-Ray, A.L. Yarin, B. Pourdeyhimi, Meltblown fiber mats and their tensile strength, Polymer (Guildf). 55 (2014) 4241–4247. http://dx.doi.org/10.1016/j.polymer.2014.05.025.

[30] K. Molnar, L.M. Vas, T. Czigany, Determination of tensile strength of electrospun single nanofibers through modeling tensile behavior of the nanofibrous mat, Compos. Part B Eng. 43 (2012) 15–21. http://dx.doi.org/10.1016/j.compositesb.2011.04.024.

[31] D. Papkov, Y. Zou, M.N. Andalib, A. Goponenko, S.Z.D. Cheng, Y.A. Dzenis, Simultaneously strong and tough ultrafine continuous nanofibers, ACS Nano. 7 (2013) 3324–3331. https://doi.org/10.1021/nn400028p.

[32] A. Baji, Y.W. Mai, S.C. Wong, Effect of fiber diameter on the deformation behavior of self-assembled carbon nanotube reinforced electrospun Polyamide 6,6 fibers, Mater. Sci. Eng. A. 528 (2011) 6565–6572.

[33] S. Backer, D.R. Petterson, Some Principles of Nonwoven Fabrics, Text. Res. J. 30 (1960) 704–711. https://doi.org/10.1177/004051756003000912.

[34] D.W. Van Krevelen, K. Te Nijenhuis, Cohesive Properties and Solubility, in: D.W. Van Krevelen, K.B.T.-P. of P. (Fourth E. Te Nijenhuis (Eds.), Prop. Polym., Elsevier, Amsterdam, 2009: pp. 189–227.

[35] A.F.M. Barton, Handbook of solubility parameters and other cohesion parameters (2nd edition), 1991.

[36] C. Bordes, V. Fréville, E. Ruffin, P. Marote, J.Y. Gauvrit, S. Briançon, P. Lantéri, Determination of poly(ε-caprolactone) solubility parameters: Application to solvent substitution in a microencapsulation process, Int. J. Pharm. 383 (2010) 236–243.

Chapter 3

Rubbery nanofibrous interleaves enhance fracture toughness and damping of CFRP laminates

Rubbery electrospun nanofibers may represent a smart way for hindering delamination and enhancing damping capacity in Carbon Fiber Reinforced Polymer (CFRP) laminates, which are two of the most serious drawbacks hampering their use.

In the present chapter, nanofibrous mats made of NBR/PCL blend (previously discussed in CHAPTER 2) with 20-40-60%wt of not crosslinked NBR, were interleaved in epoxy-based CFRPs to evaluate their effect on the final composite performance.

The interlaminar fracture toughness of laminates was assessed by Mode I and II loadings tests (evaluation of the energy release rate G_I and G_{II}, respectively), while the damping behaviour of laminates was investigated via dynamic mechanical analysis (DMA).

In FIGURE 3.1 is depicted a sketch of the work rationale.
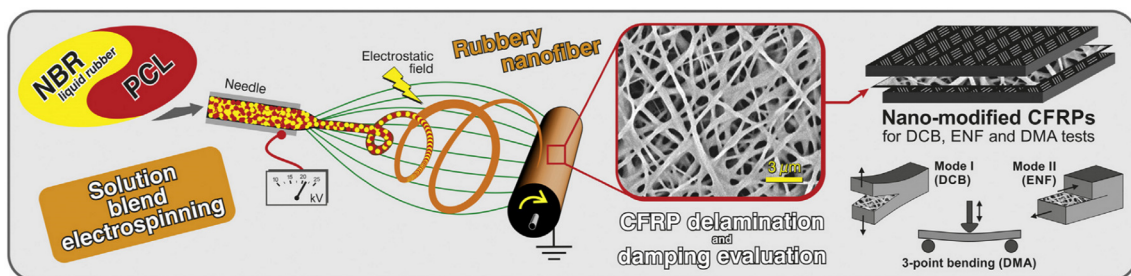
FIGURE 3.1 • Sketch of the work rationale: NBR/PCL blend nanofibers production by single-needle electrospinning process, mats integration in laminated CFRPs, and their testing for delamination, damping and thermomechanical properties evaluation.

3.1 • Results and Discussion

With the aim of obtaining room temperature mechanically stable nanofibrous mats of thermoplastic rubbery materials, which would not require crosslinking after deposition, the NBR liquid rubber component (i.e. a rubber prior its crosslinking stage) was blended with PCL via single-needle electrospinning. A firm nanofiber morphology was obtained, and a NBR content of 60%wt in the electrospun material appears to be the threshold for good quality stable nanofibers (Figure 3.2).
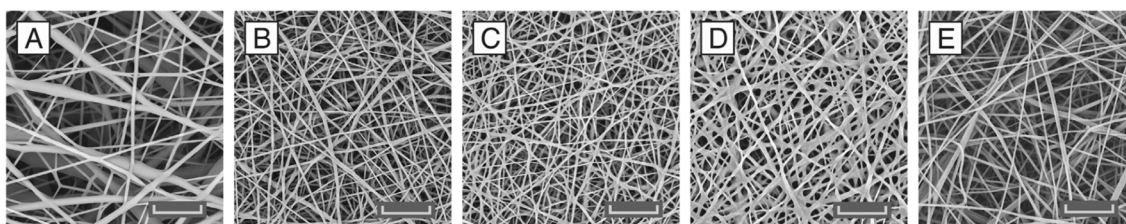
Figure 3.2 • SEM micrographs of nanofibrous mats interleaved in CFRP laminates: A) *n*-PCL, B) *n*-20/80, C) *n*-40/60, D) *n*-60/40 and E) *n*-NYL. Scale bar: 6 μm, 5,000×.

While NBR content up to 80%wt could be reached, the fibers were partially filmed (see Chapter 2, Figure 2.2) and the handling of the membrane was difficult, hence NBR content higher than 60%wt was intentionally discarded. All nanofibers have sub-micrometric diameters, roughly ranging from 200 to 400 nm (Table 3.5), and good mechanical properties as previously assessed (see Chapter 2, Section 2.1.5).

When nanofibers are included in CFRPs, they can affect dimension and weight of the composite differently from a bulk film. Indeed, fibrous mats are mainly made up of voids that can be impregnated by the resin precursors. In the present case, NBR/PCL blend fibers are expected to disappear upon curing since the fibers morphology is guaranteed solely by the presence of a PCL-like crystal phase that develops in the entire range of analyzed compositions and melts in the 55–65 °C range (see Chapter 2, Table 2.1), i.e. well below the laminate curing temperature (135 °C).

Little to no influence is expected, and indeed is not observed, on CFRP weight and dimensions with just a single interleaved membrane. A different behaviour is shown by composites where all the interlaminae are modified with nanofibers (Table 3.6). When CFRP panel density is taken into account (Figure 3.3A), addition of compact,

crystalline and dense nanofibers, such as Nylon 66, and to a certain extent PCL too, is observed to impart a small reduction in the composite density, while addition of a rubbery free-volume rich component, such as NBR liquid rubber, leads to a more significant density decrease.
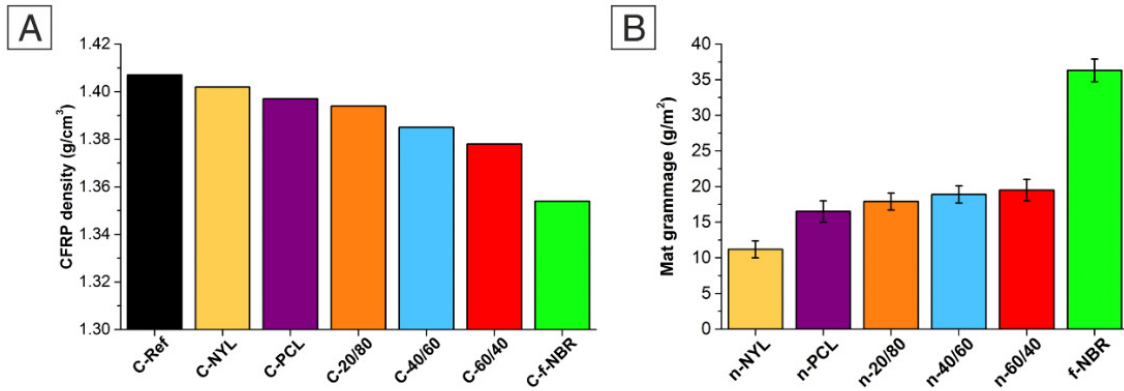
FIGURE 3.3 • A) CFRP density of the different composite panels produced for DMA measurements (10 plies) with or without 9 interleaved membrane (nanofibers and NBR film); B) Grammage of the interleaved membranes in CFRP panels for DCB, ENF and DMA tests.

The higher the NBR fraction in nanofiber blends, the lower the attained CFRP density. Further density decrease is observed with plain *f*-NBR film, though in this case the membrane grammage is almost double with respect to rubbery nanofibrous membranes (TABLE 3.5 and FIGURE 3.3B), as required to provide a minimum handling ability. While the grammage chosen for Nylon 66 mat is lower than the other nanofibrous mats (16.5–19.5 g/m^2, mean values) because it appears to be the limit for a complete mat impregnation with the prepreg resin.

3.1.1 • *Mode I and Mode II interlaminar fracture toughness evaluation of nano-modified CFRPs*

Laminate CFRP fracture resistance was determined under Mode I and Mode II loading configurations, via Double Cantilever Beam (DCB) and End-Notched Flexure (ENF) tests, respectively. While in the DCB test the specimen is subjected to a perpendicular load respect to the crack propagation plane (Mode I, opening), in the ENF test a bending deformation is imposed to simulate the sliding of the two constituent specimen beams (Mode II, sliding). For a better understanding of the results, the crack propagation (and

consequently the energy release rate, G, associated to) is split into two stages: the initiation stage (G_C), in which the delamination onset starts from the artificial crack, and the propagation stage (G_R). In propagation, the energy was evaluated considering a crack length (*a*) between 48 and 90 mm for Mode I, and the 32–42 mm range for Mode II tests. It is to underline that during DCB tests of CFRPs modified with rubber-containing layers, the designed crack plane (i.e. the central one) was not guaranteed to be the unique present, being possible the formation of an additional crack plane adjacent to this. If this occurred, the resulting $G_{I,R}$ was calculated by averaging only the points associated to the crack propagation in the modified interface to exclude any interference, reducing the abovementioned crack length range (TABLE 3.7).

Mode I and Mode II results (maximum load and calculated energy release rate) are listed in detail in TABLE 3.1.

TABLE 3.1 • Mode I (DCB test) and Mode II (ENF test) results: maximum load and energy release rate calculated both at initial ($G_{I,C}$ and $G_{II,C}$) and propagation ($G_{I,R}$ and $G_{II,R}$) stages.

CFRP	Maximum Load (N)		G_C (initial stage) (J/m^2)		G_R (propagation stage) (J/m^2)	
	Mode I	Mode II	Mode I	Mode II	Mode I	Mode II
C-Ref	48.9 ± 2.7	743.3 ± 14.7	373 ± 16	2806 ± 201	642 ± 166	3564 ± 291
C-PCL	51.7 ± 4.9	859.7 ± 32.5	314 ± 40	4352 ± 454	737 ± 87	4402 ± 203
C-20/80	75.4 ± 9.3	768.2 ± 26.0	1395 ± 238	3554 ± 222	2068 ± 311	3706 ± 179
C-40/60	93.8 ± 8.8	817.6 ± 49.7	1992 ± 88	3502 ± 290	2668 ± 472	3662 ± 145
C-60/40	100.2 ± 4.3	838.0 ± 34.9	2152 ± 188	3767 ± 246	2817 ± 347	4466 ± 365
C-*f*-NBR	96.3 ± 2.8	784.5 ± 16.3	2676 ± 106	3410 ± 162	3032 ± 332	4044 ± 320
C-NYL	65.0 ± 5.8	863.3 ± 15.8	1152 ± 263	3929 ± 262	1149 ± 137	4152 ± 334

FIGURE 3.4A shows the representative DCB load vs. displacement curves of the pristine sample (C-Ref) and of all the modified composite panels. The nano-modified laminates have a similar trend and slope of the corresponding reference until the first force drop occurs. However, the presence of the interleaved nanofibers, except for the PCL ones, clearly postpone the crack initiation and increase the maximum force.
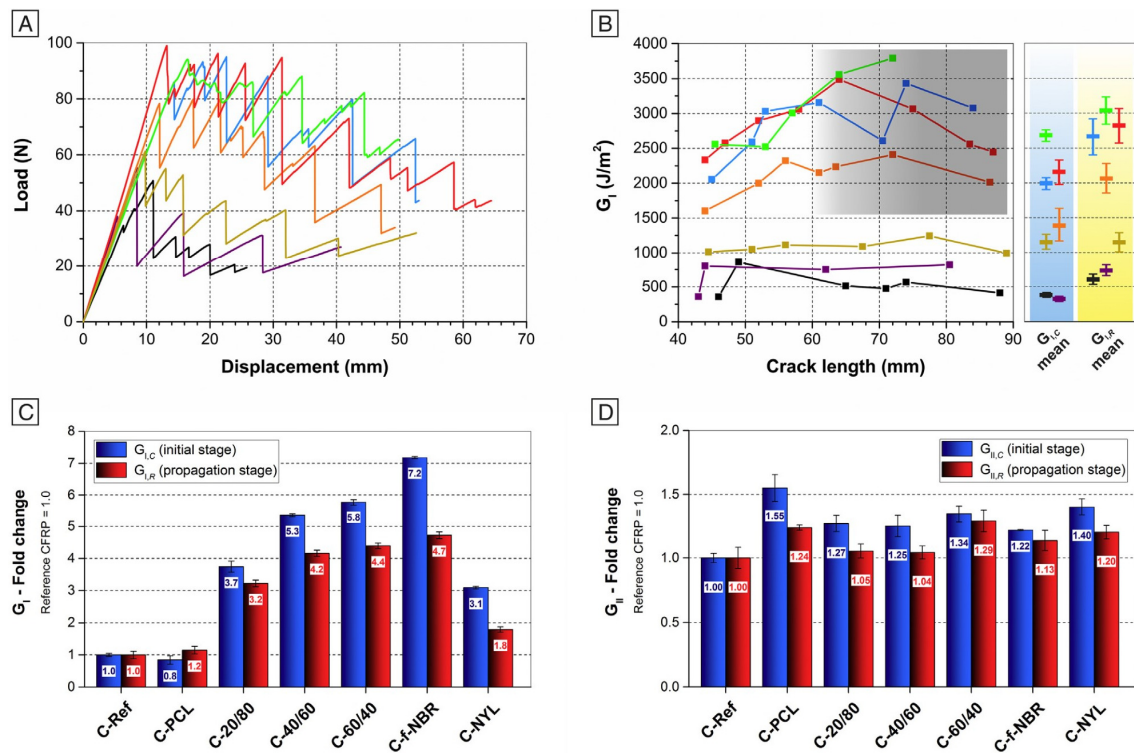
FIGURE 3.4 • DCB tests results: A) load-displacement curves; B) R-curves related to the same specimens displayed in A), besides the $G_{I,C}$ and $G_{I,R}$ average values. The shadow approximately indicates the crack range excluded for $G_{I,R}$ calculation of rubber-containing samples. Colours: black C-Ref, purple C-PCL, orange C-20/80, light blue C-40/60, red C-60/40, light green C-*f*-NBR, yellow C-NYL. C) average G_I fold change (initial and propagation stages). D) ENF test results: average G_{II} fold change (initial and propagation stages). Bars in C) and D) are expressed as the relative variation of the value with respect to the reference sample (C-Ref), whose value is set as 1.0.

Indeed, the average maximum load (FIGURE 3.5A) is significantly and statistically higher for the CFRPs interleaved with rubbery nanofibers: from +53% to +104% (C-20/80 and C-60/40, respectively), while a composition-related threshold at 40%wt of NBR appears, beyond which increasing the rubber fraction in the interleaved material does not correspond to a further performance enhancement. In fact, the use of pure rubber film (C-*f*-NBR) is not dramatically helping further the performance with respect to the blended nanofibers (FIGURE 3.5B), in spite of the grammage that for the film is almost double (TABLE 3.5 and FIGURE 3.3B).
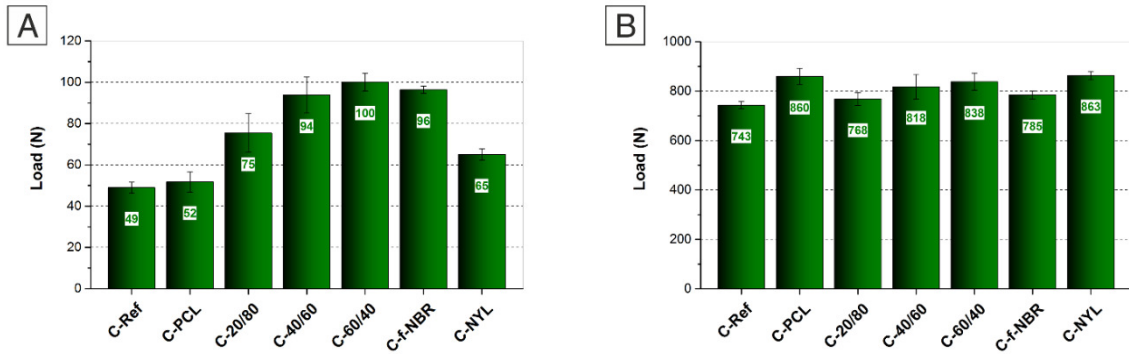
FIGURE 3.5 • Average maximum load recorded from DCB (A) and ENF (B) tests.

This behaviour is confirmed by the micrograph analysis of the crack path (see FIGURE 3.6).

In FIGURE 3.5B the R-curves (fracture toughness vs. crack length curves) resulting from the Mode I test are shown for the same representative specimens previously discussed. Their trends strengthen the hypothesis of a major hinder to CFRP delamination provided by NBR/PCL rubber nanofibers. Once again, the graph highlights two different "groups" of behaviour, i.e. with or without the rubber component in the composite. All the calculated G_I points (considering the test repetitions too) for rubbery-reinforced CFRPs, regardless of the NBR fraction, are above 1100 J/m^2, a value well higher than the performances of C-Ref, both in initial and propagation stages ($G_{I,C} = 373 \pm 16$ J/m^2 and $G_{I,R} = 642 \pm 75$ J/m^2). The lower limit jumps to 1900 J/m^2 when discarding the C-20/80 sample, supporting the idea of a NBR threshold in the blend nanofibrous mat above which only a slight increase in the mean values of both $G_{I,C}$ and $G_{I,R}$ can be found, as already observed for the maximum force behaviour. Assuming unitary the performances of the reference CFRP, the presence of NBR in the nanofibers in the 40–60%wt range dramatically affects the $G_{I,R}$ regardless of the actual liquid rubber content (increase of 320–340%, FIGURE 3C), while the $G_{I,C}$ is more sensitive to the NBR content in the whole studied composition range, displaying an increasing trend for increased NBR fractions (from +270% for C-20/80 to +620% for the rubber film). However, the use of pure NBR film brings a very limited further positive effect on the Mode I propagation stage (+370%) respect to C-60/40 (+340%), but at the cost of severe membrane handling issues during the lamination process, the impossibility to produce low-grammage films as previously explained, as well as significant drop in the thermomechanical properties, as discussed later in SECTION 3.2. The use of PCL nanofibers (*n*-PCL), on the contrary, leads to Mode I

delamination performance statistically comparable to the unmodified CFRP, thus suggesting that the presence of the rubbery component is the main responsible for such impressive boost in the delamination hampering ability. Such a toughening effect of the rubbery nanofibers is clearly displayed by the R-curves (FIGURE 3B), where CFRPs with blend nanofibers show a higher number of subsequent crack propagation, denoting a more efficient ability to hinder delamination. The obtained results will be later compared with literature data gathered in a previous review [1].
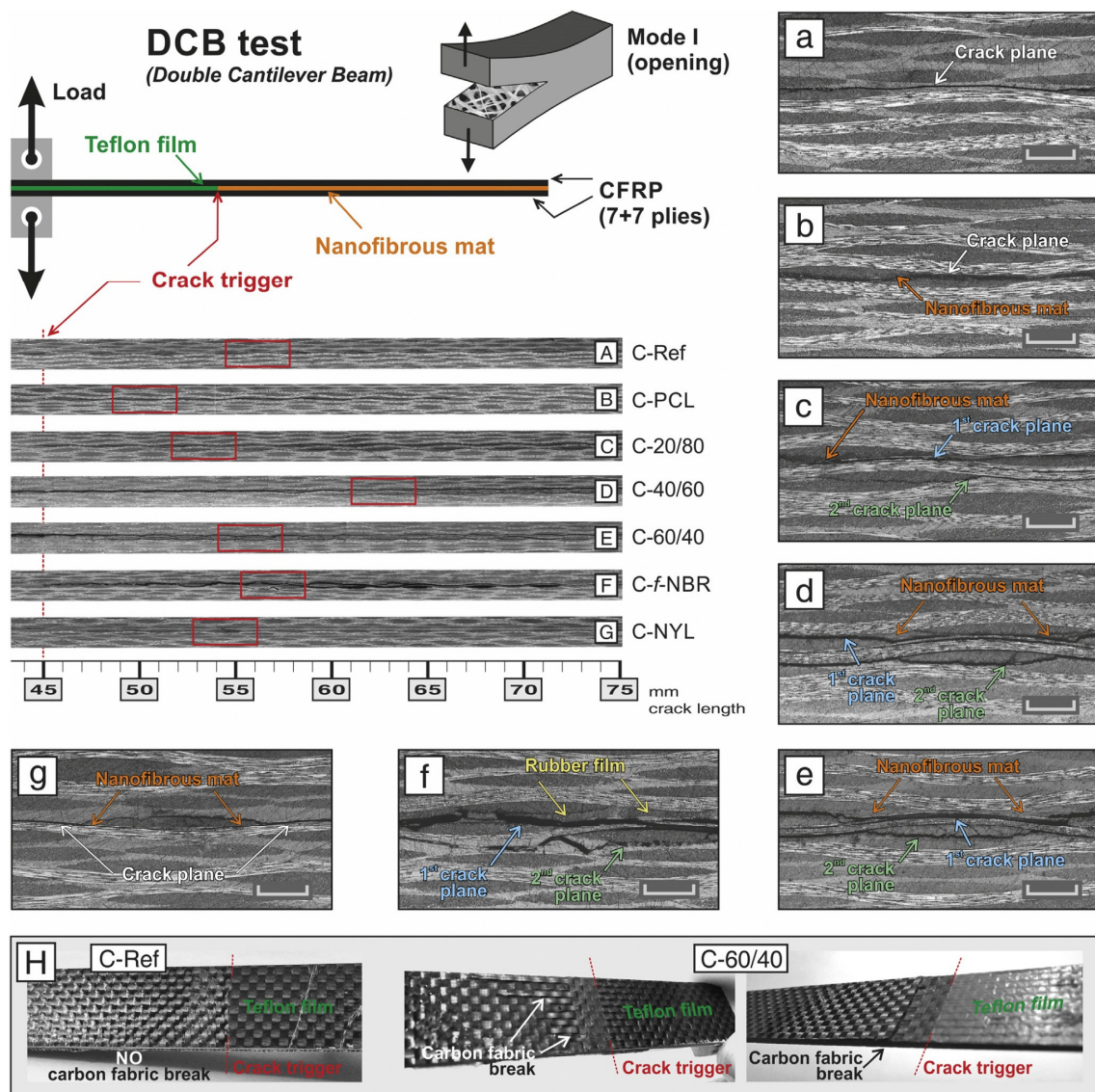
FIGURE 3.6 • Micrographs of DCB specimens after the delamination tests. a)-g): enlargements (5×, scale bar 500 μm) of the red squared regions highlighted in the respective DCB specimen sections A)-G). H) Digital camera photographs of the delamination surfaces after DCB test of one representative rubber modified composite (C-60/40) and of the unmodified CFRP (C-Ref).

The Mode I test results are confirmed by the micrograph analysis of the crack path (FIGURE 3.6).

Micrographs show an almost "linear" crack propagation in the central interface for unmodified C-Ref, as well as for C-PCL, while the CFRPs reinforced with rubbery nanofibers display a more complicated and an uneven crack path. This substantial change in the crack propagation behaviour is already present in the C-20/80 sample but becomes more evident starting from C-40/60 laminate. It is worth noting that the crack propagation occurs in the designed interlaminar plane (i.e. the central interface with the Teflon triggered crack), except for the rubbery modified samples where it extends also to the adjacent unreinforced interfaces. The crack, indeed, follows the path of least resistance and it is found to propagate across the very stiff woven carbon fabric, breaking it, instead of keep spreading along the initially designed fracture plane modified with the toughening layers (FIGURE 3.6c-f).

In FIGURE 3.7 SEM micrographs show the delamination surfaces of the previously discussed DCB specimens: while C-Ref displays the typical brittle fracture behaviour of epoxies characterized by wide flat planes (FIGURE 3.7A3), the addition of PCL leads to some toughening of the matrix, showing a more corrugated matrix region (FIGURE 3.7B3) and carbon fibers that tend to adhere more to the resin (FIGURE 3.7B2). Such a modification, however, is not enough to hamper delamination, as DCB tests proved.

In FIGURE 3.7C the delamination surface of the most representative composite with interleaved rubbery nanofibers, C-60/40, is reported: the very rough surface of the matrix (FIGURE 3.7C3), reminiscent of strong plastic deformation, can be considered a sign of considerable crack branching. Moreover, carbon fibers stay well embedded in the matrix (FIGURE 3.7C2), with no evidence of easy fiber pull out. An even rougher surface, that upon delamination presents also some spheres and holes morphology, is reported for the laminate with interleaved NBR film, where almost no naked carbon fibers can be detected (FIGURE 3.7D). These observations confirm the rubber toughening action toward the epoxy resin, which reflects on increased energy release rate as calculated by DCB tests. In the CFRP modified with Nylon 66 mat (FIGURE 3.7E), instead, no sign of matrix plasticisation is clearly detected, while nanofibers morphology is still evident, differently from all the previously discussed samples.
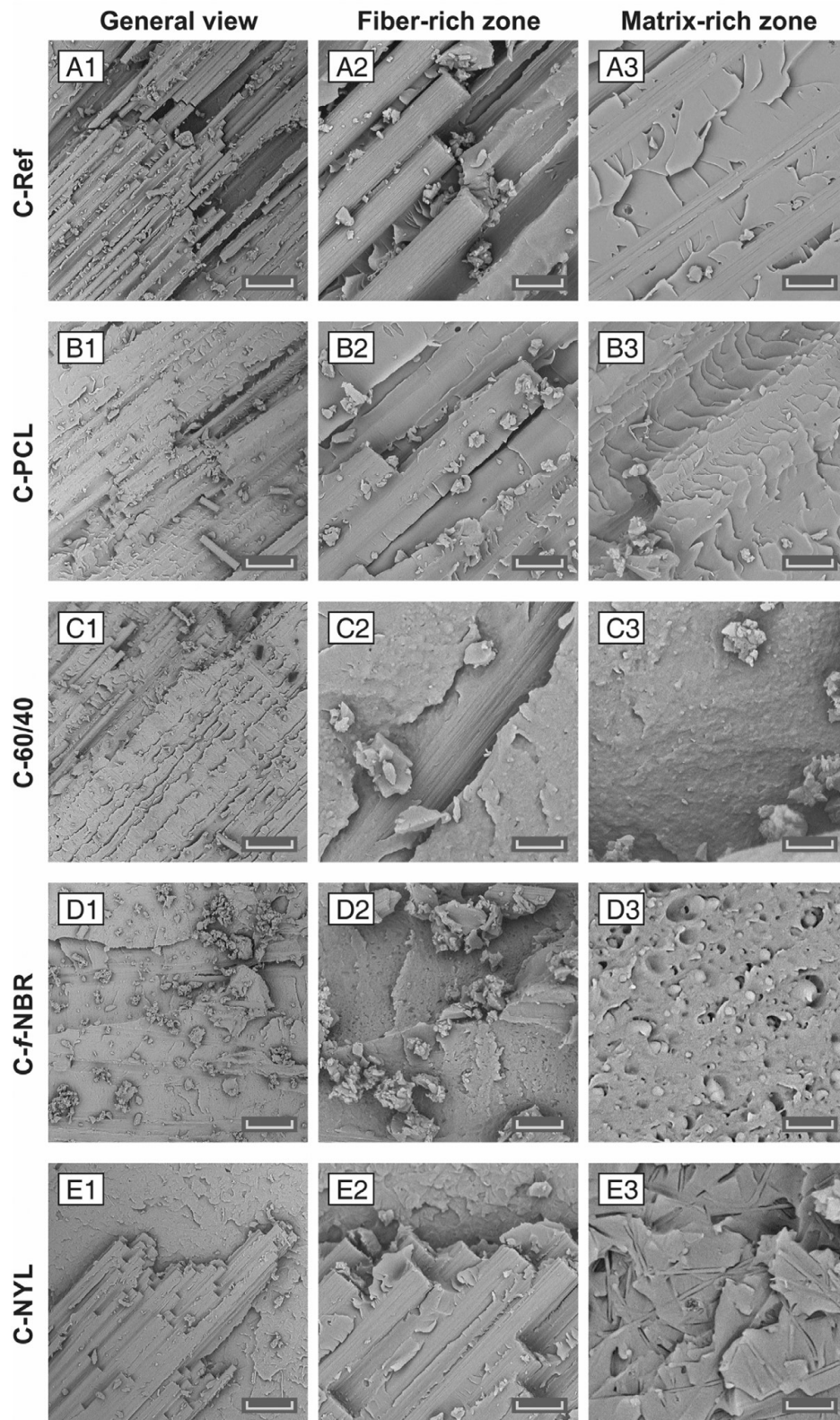
FIGURE 3.7 • SEM micrographs of delamination plane of DCB specimens after the tests: general view of the fracture plane (column 1, 1,000×, scale bar 50 µm), magnification of fiber-rich (column 2, 5,000×, scale bar 10 µm except for image C2, 10,000×, scale bar 5 µm) and matrix-rich (column 3, 5,000×, scale bar 10 µm except for image C3, 10,000×, scale bar 5 µm and for images D3-E3, 20,000×, scale bar 2.5 µm) zones.

This latter behaviour was however expected, based on the thermal properties of the different applied nanofibrous mats (the melting temperature of Nylon 66 is around 260 °C, see CHAPTER 7, FIGURE 7.8). In this case, the fracture toughening enhancement should be attributed to the fiber bridging mechanism.

While the enhancement on the Mode I interlaminar fracture toughness is impressive (up to 5.8 times the reference value), the action of rubbery nanofibrous mats on the Mode II fracture energy is not as relevant (FIGURE 3D and FIGURE 3.8).
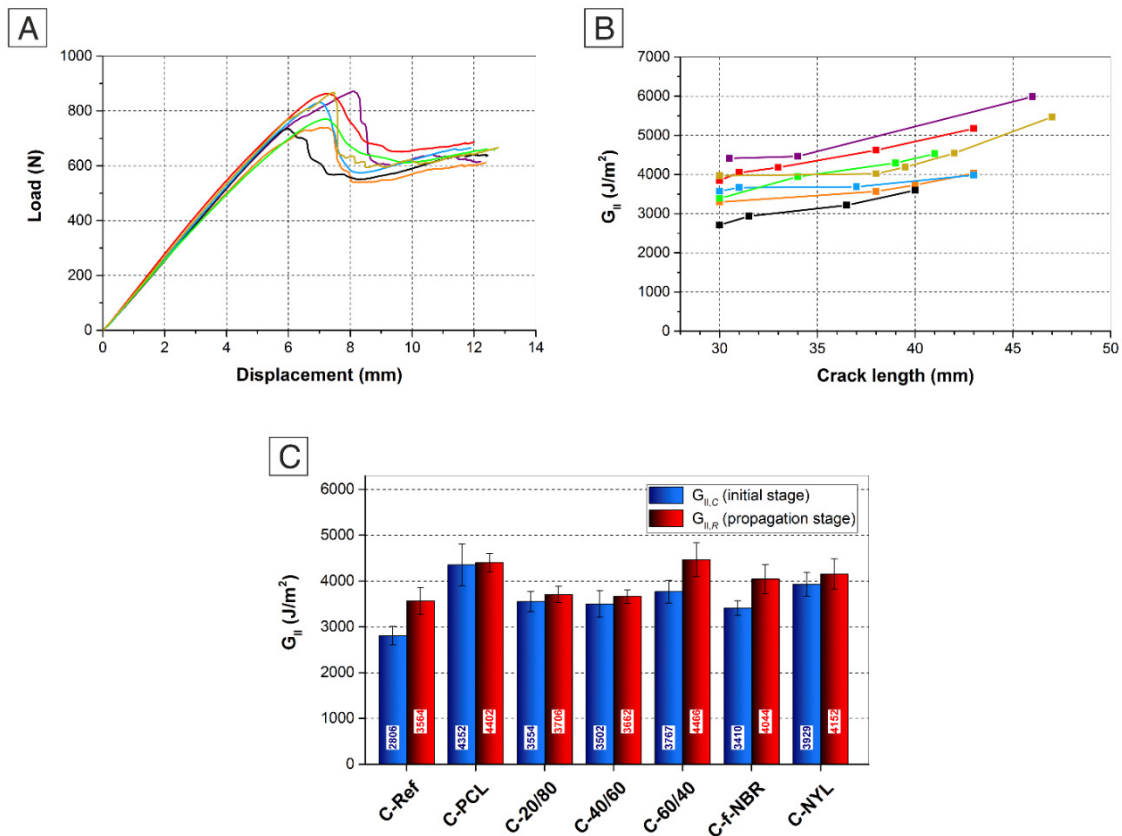
FIGURE 3.8 • ENF tests results: A) representative load-displacement curves; B) G_{II} vs. crack length trends related to the curves at point A); C) average G_{II} (initial and propagation) for the different analysed composite panels.

All the modified samples display an improvement in $G_{II,C}$ in the 20–60% range, while the impact on $G_{II,R}$ is less remarkable. Overall the NBR/PCL nanofiber modified CFRPs display a similar performance at low NBR contents (C-20/80 and C-40/60), with a slight increase in the action against delamination at the initial stage; the performance however improves in C-60/40 that displays $G_{II,C}$ similar to C-NYL and a higher $G_{II,R}$ comparable

to C-PCL (+34% and +29%, respectively, with respect to C-Ref). The latter, indeed, shows the best overall performances (+55% in $G_{II,C}$ and +24% in $G_{II,R}$).

These results well compare with the performance enhancements of many samples previously reported in the literature [1], as depicted in the graphs displayed in FIGURE 3.9.
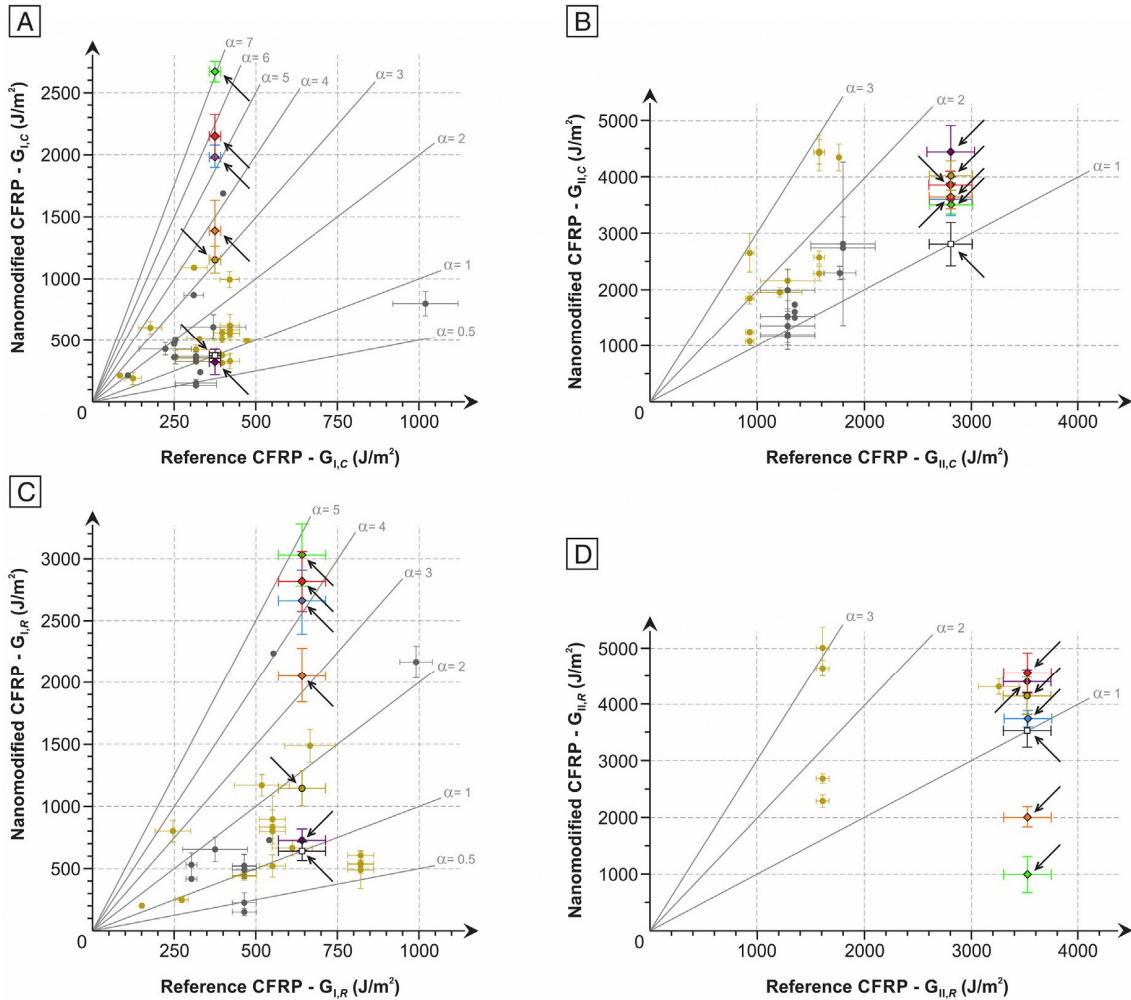
FIGURE 3.9 • Mode I (A, C) and Mode II (B,D) energy release rate of the tested composites (marked by arrows) compared to literature data [1] (yellow for CFRP modified with polyamide nanofibers, gray for "other" nanofiber types). Tested CFRPs: white C-Ref, purple C-PCL, orange C-20/80, light blue C-40/60, red C-60/40, light green C-f-NBR, yellow C-NYL. α represents the ratio between G nanomodified and G reference.

The proposed nano-modification of the interlayer, with rubbery nanofibers, has a dramatic impact on the composite delamination under Mode I loading, and in particular at the initiation stage ($G_{I,C}$), while in Mode II loading the G_{II} values are just slightly higher than the reference material in most of the cases. The effect of the rubber on the

Mode II delamination crack path, which again displays a jagged profile (FIGURE 3.10), is similar to the observed one in DCB micrographs after testing. However, in this case, no failure of carbon fiber fabric occurred.
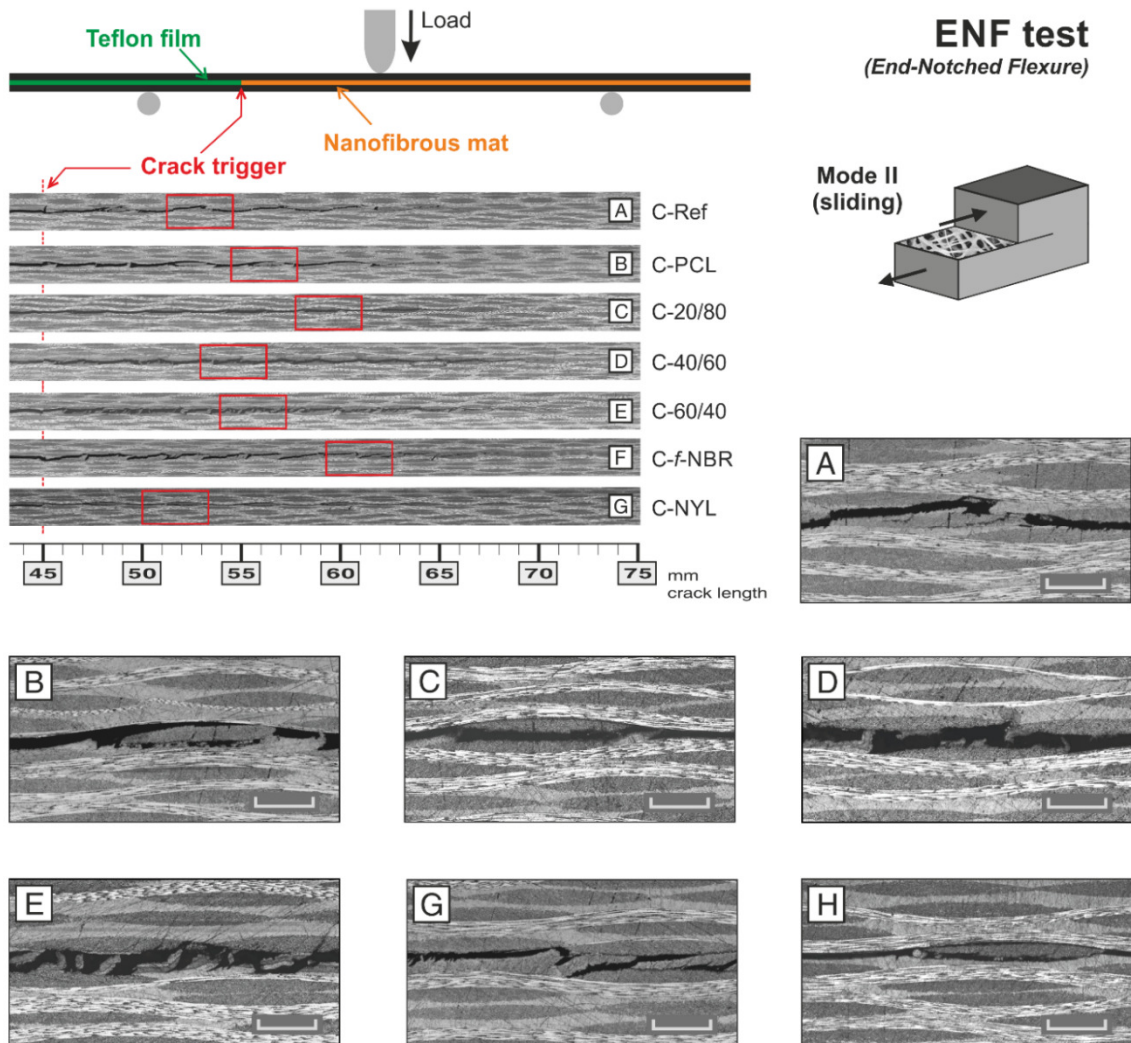
FIGURE 3.10 • Micrographs of ENF specimens after the delamination tests. a)-g): enlargements (5×, scale bar 500μm) of the red squared regions highlighted in the respective ENF specimen sections A)-G).

It is well known, and long since, that an increase of fracture toughness of the neat resin (in form of bulk without carbon fibers) has a lower effect on Mode II delamination fracture toughness than on Mode I when it is used on composite laminates [2]. This behaviour has been attributed to the different stress field distribution ahead of the crack tip for Mode I and II. In Mode I the stress at the crack tip is highly concentrated with a high gradient, therefore the presence of a tougher resin can help, by plasticizing, to blunt the crack tip and redistribute the stress. Differently, in Mode II the stress is

naturally redistributed ahead of the crack tip, thanks also to the laminar morphology of the composite, thus resulting in a less effect of a tougher resin on interlaminar fracture toughness. This behaviour was found in the laminates toughened with the present rubbery nanofibers too. It was also reported that the loss of fibrous morphology of the interleaved material, which is the case of "liquid" rubbery nanofibers, may detrimentally affect the composite performance in Mode II, while Mode I fracture toughness is not particularly sensitive to this phenomenon [3,4].

It can be concluded that by increasing the percentage of rubber in NBR/PCL blended nanofibers, the Mode I interlaminar fracture toughness increases ($G_{I,C}$ ranges between +270% and +480%, $G_{I,R}$ between +220% and +340%), while a slight variation (about +30%) of Mode II fracture toughness was observed for C-60/40.

3.1.2 • Thermomechanical properties and damping evaluation of nanomodified CFRPs via dynamic mechanical analysis (DMA)

The ability to viscoelastically deform might contribute to introduce some damping ability into the otherwise extremely stiff CFRP with the aim of hamper and delay crack triggering and, in turn, delamination. Several test methods are available to determine the damping of a material. DMA is a simple and fast way to assess the dynamic behaviour of materials: tanδ value, i.e. the ratio between E'' and E' (loss and storage moduli, respectively), is often addressed as "damping factor", and indeed accounts for the ability of the material to dissipate energy. Besides, DMA allows to determine the composite glass transition temperature (T_g), and the effective temperature region span of tanδ peak, all parameters useful to characterize the damping behaviour. Plain cross-linked NBR shows high damping at room temperature, thanks to its viscoelastic nature [5], PCL has some damping properties too, because they both are well above their glass transition, and thus able to dissipate energy via molecular rearrangements. By mixing NBR and PCL in different proportions, it may be possible to modulate the loss factor of the resulting blend, depending also on the extent of crystal phase present in it. In this case, however, a DMA evaluation of the performance of the pristine nanofibrous mat would be ineffective in terms of damping efficiency assessment, since in the composite the nanofibrous morphology is lost, as demonstrated by SEM micrograph (FIGURE 3.7B-C), and the polymers are found dispersed in the epoxy matrix, thus losing the dissipation

mechanism associated to the fibrous arrangement. Hence nanofibrous mats were directly integrated in CFRPs to evaluate their effect on dynamic-mechanical properties via DMA. Two very different configurations were tested, characterized by 10 CFRP plies with membranes interleaved only in the central interface and in all the interfaces, using the IMP503Z resin system, together with some laminate configurations with the IMP503Z-HT resin system (TABLE 3.8).

Besides the evaluation of the thermomechanical properties of the composite, the DMA is also useful to investigate nanofibers impact on the resin behaviour, contributing to better understand the blend/resin mixing process.

Unmodified CFRP (C-Ref) displays a single significant relaxation process, which can be safely attributed to the glass transition. Such a relaxation, clearly detected as a peak in the tanδ curve around 129 °C (T_α), is narrow and symmetrical, suggesting a good curing of the resin.

The lamination sequence with a single interleaved membrane provides a main significant relaxation T_α positioned at a comparable temperature (125–129 °C), and a conservative modulus (E') that is practically unaffected below T_g (TABLE 3.8 and FIGURE 3.11A).
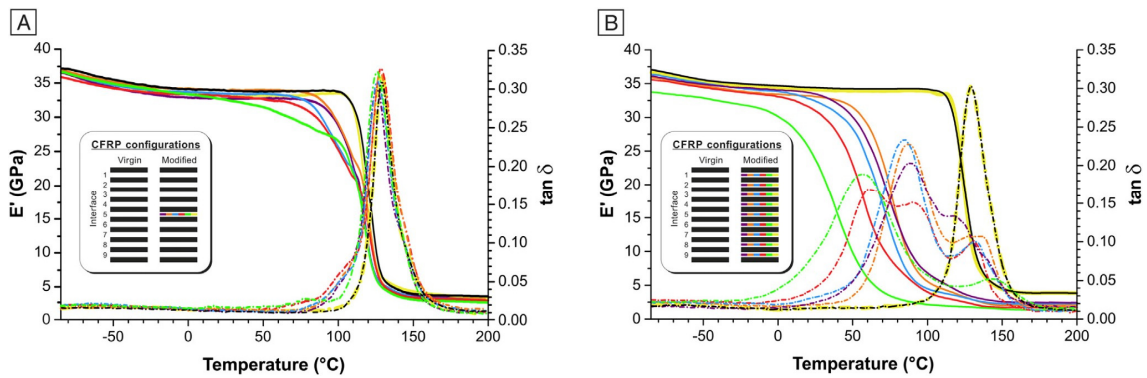
FIGURE 3.11 • E' (solid lines) and tanδ (dashed lines) representative curves of CFRP samples characterized by A) only the central interface modified and B) all the 9 interfaces modified. Colours: black C-Ref, purple C-PCL, orange C-20/80, light blue C-40/60, red C-60/40, light green C-f-NBR, yellow C-NYL. Inset box: tested CFRP configurations (thick lines: CFRP plies, thin lines: interleaved membranes, with colours as stated before).

However, just one modified interface with PCL or rubbery nanofibers impacts on the onset of the E' drop, which represents another way to determine the glass transition of a material: this is a more conservative approach for evaluating glass transition than

tanδ peak, being the E' onset the temperature extrapolation at which the storage modulus drop begins. The curves show the E' onset lowering becomes more important for increasing NBR fraction in the nanofibers (82 °C for C-60/40 instead of 116 °C of C-Ref), and 53 °C for the laminate with NBR film (C-*f*-NBR). Details are reported in TABLE 3.8.

Hence, to investigate the maximum membranes impact (at the considered grammage) on the CFRP thermomechanical properties, each ply interface but the external ones was modified with nanofibers, besides with NBR film (FIGURE 3.16B). The overall weight variation is in the 2–3%wt range, and roughly represents 5–10%wt with respect to the resin fraction. C-NYL displays a behaviour practically identical to C-Ref (FIGURE 3.11B): indeed, highly crystalline glassy nanofibrous mat does not affect the resin viscoelastic relaxation, and the limited weight fraction (about 2%wt) does not made the highly crystalline Nylon 66 glass transition detectable in the DMA spectrum.

Such a behaviour well compares with the observations drawn upon analysing fracture surfaces of the DCB tested samples, where no signs of resin plasticization were evidenced. C-PCL shows, instead, a different behaviour. Although the storage modulus (E') seems to display a single relaxation, the width of such transition is wider and begins at a decisively lower temperature than C-Ref and C-NYL. Moreover, the tanδ shows a complex multipeaked profile with a high-T shoulder matching the epoxy resin T_α and a lower-T peak at 89 °C that, by both the intensity and the position, cannot be ascribed to the sole PCL fraction crystal melting (2–3%wt overall PCL content, melting temperature 60 °C, see CHAPTER 2, TABLE 2.1). The C-*f*-NBR composite displays a somehow similar profile with respect to C-PCL, showing once again a less intense high-T peak corresponding to the epoxy T_α and an even lower-T (58 °C) main relaxation phenomenon. Both composites display a main intense relaxation in a position that does not belong to their respective glass transitions (which are in both cases well below 0 °C, see CHAPTER 2, TABLE 2.1), neither to the PCL crystal phase melting, as previously observed in phase separated epoxy/PCL samples [6].

While, indeed, a wealth of papers [6–8] reports reaction-induced phase separation in both epoxy/PCL and epoxy/NBR systems, this does not appear to be the case. Instead, a phase separated system would display in DMA spectra an intense α relaxation due to the resin glass transition and some less intense phenomena due to the main thermal

transition of the minor component(s), being it PCL or NBR. On the other side, when a component of plasticizing ability is mixed with a polymer it is renown that a broadening of its α-peak occurs. The lack of such different characters in the tanδ spectra in favor of an intermediate behaviour in between the two extreme components (with a prevalence of the epoxy resin, as expected) accounts thus for some miscibility in both systems. This view is supported by some recent literature [3,9] that reports core-shell nanofibers with the outer shell based on PCL to allow for thermoplastic melting and diffusion within the epoxy, leading to some positive toughening action. Composites modified with NBR/PCL nanofibrous mats show a behaviour similar to the one of C-PCL for compositions up to 40%wt NBR, while further increase of the rubbery fraction (60%wt) leads to the appearance of an additional relaxation positioned at a temperature comparable with C-*f*-NBR low-T phenomenon. Assuming that the polymers from nanofibers melt (PCL) and diffuse (PCL and NBR) into the epoxy matrix during curing cycle, the latter formulation (C-60/40) seems to display two different phases reminiscent of the previously discussed epoxy/PCL and epoxy/NBR blends. The presence of the highly damping NBR component further widens the energy dissipation window of the composites down to below room temperature and might also promote some phase separation with a mixed composition, that would explain the appearance, in the fracture surface, of the observed globular morphology.
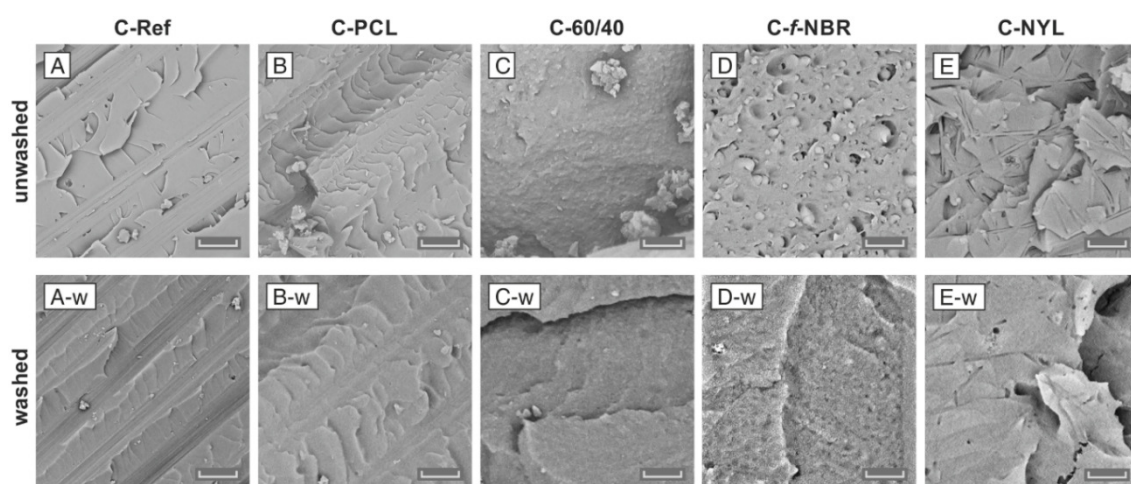
Figure 3.12 • SEM micrographs of delamination plane of DCB specimens after the tests: before (A-E) and after washing in suitable solvents (A-w – E-w) (A, B images: 5,000×, scale bar 10μm; C, D, E images: 20,000×, scale bar 2.5 μm).

The latter hypotheses are strengthened by the aspect of the delamination surfaces previously discussed (FIGURE 3.7) after the attempt at washing them with chloroform, in order to remove soluble polymeric fractions. Literature indeed reports extremely peculiar spherical of interpenetrated morphologies of the phase separated component that can be easily highlighted upon selective removal of one component. Such peculiar morphologies do not appear in the present samples (FIGURE 3.12), with the exception of the one modified with NBR film, where the small spheres seem to be removed, leaving some holes.

Damping capacity of the same CFRP samples was thus investigated in isothermal conditions (25, 35 and 45 °C), under a wide range of testing frequencies (1 - 2.5 - 5 - 10 - 20 - 33.3 - 50 Hz). Results are summarized in FIGURE 3.13, showing the trend of relative variation of nanomodified CFRPs with respect to C-Ref sample, while in TABLE 3.2 tanδ values of tested samples for various conditions are reported.
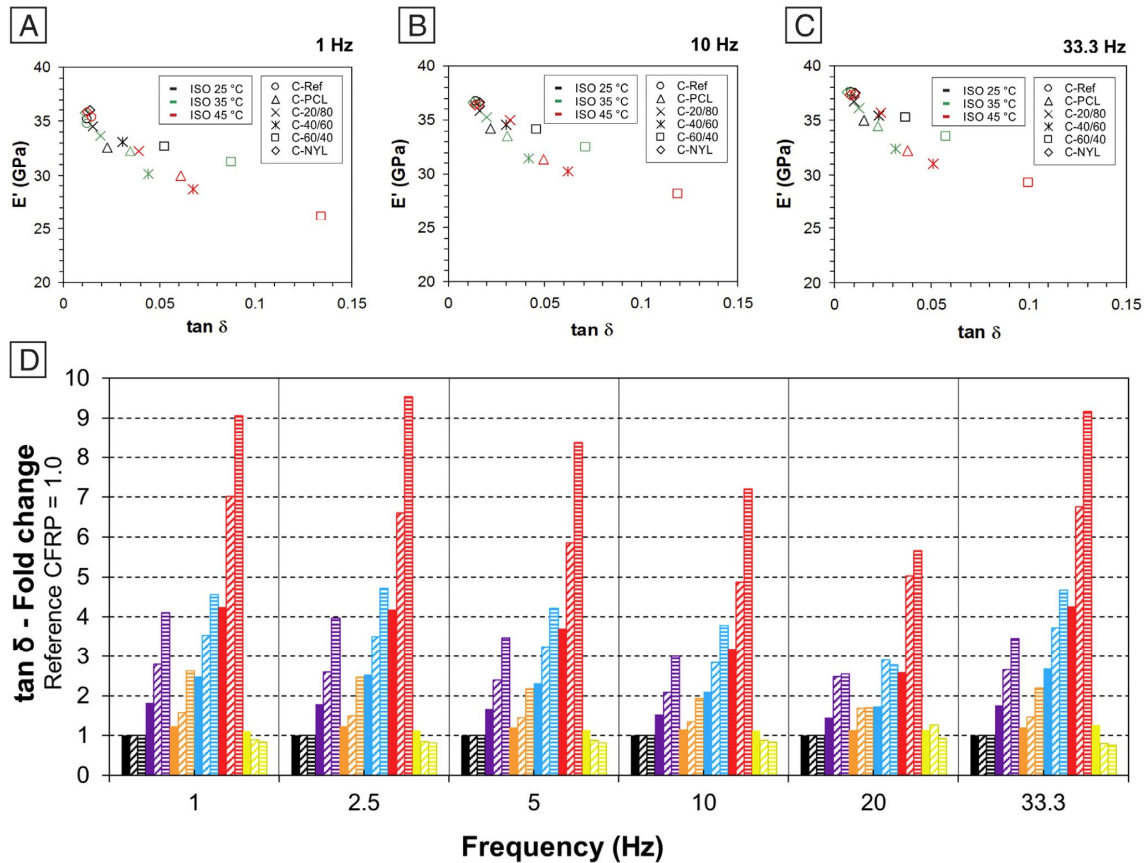
FIGURE 3.13 • E' vs tanδ graphs for CFRPs tested under isothermal conditions at 1 Hz (A), 10 Hz (B) and 33.3 Hz (C). D) Relative variation of tanδ for different CFRPs at various frequencies and isothermal temperatures (solid bar 25 °C; oblique dashed bar 35 °C; horizontal dashed bar 45 °C). Colours: black C-Ref, purple C-PCL, orange C-20/80, light blue C-40/60, red C-60/40, yellow C-NYL. 50 Hz data are not displayed because of no positive tanδ values detected for C-Ref at this frequency.

TABLE 3.2 • Tanδ values from DMA tests in isothermal conditions at 25, 35 and 45 °C.

CFRP sample	Testing frequency	ISO 25		ISO 35		ISO 45	
		tanδ	Normalized tanδ [a]	tanδ	Normalized tanδ [a]	tanδ	Normalized tanδ [a]
	Hz	10^{-3} MPa/MPa		10^{-3} MPa/MPa		10^{-3} MPa/MPa	
C-Ref [c]	1.0	12.4 ± 0.2	1.0	12.5 ± 0.2	1.0	14.8 ± 0.3	1.0
	2.5	11.4 ± 0.2	1.0	12.1 ± 0.2	1.0	13.8 ± 0.2	1.0
	5.0	12.5 ± 0.2	1.0	12.8 ± 0.1	1.0	14.9 ± 0.1	1.0
	10.0	14.3 ± 0.1	1.0	14.6 ± 0.1	1.0	16.4 ± 0.1	1.0
	20.0	19.2 ± 0.7	1.0	14.1 ± 0.8	1.0	19.8 ± 0.8	1.0
	33.3	8.5 ± 1.1	1.0	8.5 ± 1.5	1.0	10.8 ± 1.5	1.0
	50.0	(b)	—	(b)	—	(b)	—
C-PCL [d]	1.0	22.6 ± 0.3	1.8	34.8 ± 0.6	2.8	60.9 ± 0.2	4.1
	2.5	20.5 ± 0.3	1.8	31.3 ± 0.2	2.6	55.0 ± 0.2	4.0
	5.0	21.0 ± 0.2	1.7	30.7 ± 0.2	2.4	51.9 ± 0.2	3.5
	10.0	21.8 ± 0.3	1.5	30.5 ± 0.1	2.1	49.3 ± 0.1	3.0
	20.0	27.9 ± 0.4	1.4	35.0 ± 0.6	2.5	50.5 ± 0.5	2.6
	33.3	15.0 ± 0.9	1.8	22.5 ± 1.4	2.7	37.5 ± 0.9	3.5
	50.0	3.0 ± 1.3	"LOW"	9.4 ± 1.4	"HIGH"	24.3 ± 1.2	"HIGH"
C-20/80 [e]	1.0	15.2 ± 0.1	1.2	19.6 ± 0.4	1.0	39.0 ± 0.3	1.0
	2.5	14.0 ± 0.1	1.2	18.0 ± 0.2	1.0	34.2 ± 0.2	1.0
	5.0	14.9 ± 0.2	1.2	18.5 ± 0.3	1.0	32.6 ± 0.2	1.0
	10.0	16.4 ± 0.2	1.1	19.6 ± 0.2	1.0	31.8 ± 0.3	1.0
	20.0	21.7 ± 0.4	1.1	23.7 ± 0.6	1.0	33.7 ± 1.0	1.0
	33.3	10.2 ± 1.0	1.2	12.5 ± 1.2	1.0	23.8 ± 1.0	1.0
	50.0	(b)	—	(b)	—	9.3 ± 1.2	"HIGH"
C-40/60 [f]	1.0	30.8 ± 0.2	2.5	44.1 ± 0.2	3.5	67.7 ± 0.3	4.6
	2.5	28.9 ± 0.1	2.5	42.4 ± 0.1	3.5	65.3 ± 0.2	4.7
	5.0	29.0 ± 0.1	2.3	41.6 ± 0.1	3.3	63.0 ± 0.1	4.2
	10.0	30.0 ± 0.1	2.1	41.7 ± 0.1	2.8	62.2 ± 0.1	3.8
	20.0	33.3 ± 0.6	1.7	41.0 ± 0.8	2.9	55.1 ± 0.9	2.8
	33.3	23.0 ± 0.3	2.7	31.7 ± 1.2	3.7	50.7 ± 0.6	4.7
	50.0	10.7 ± 1.0	"HIGH"	21.7 ± 0.9	"HIGH"	38.6 ± 0.3	"VERY HIGH"
C-60/40 [g]	1.0	52.8 ± 0.2	4.3	87.6 ± 0.4	7.0	134.3 ± 0.4	9.1
	2.5	47.9 ± 0.1	4.2	79.6 ± 0.3	6.6	132.0 ± 0.5	9.5
	5.0	46.4 ± 0.1	3.7	74.9 ± 0.3	5.9	125.0 ± 0.6	8.4
	10.0	45.8 ± 0.1	3.2	71.2 ± 0.3	4.9	118.5 ± 0.6	7.2
	20.0	50.0 ± 0.7	2.6	70.9 ± 0.6	5.0	111.9 ± 0.5	5.7
	33.3	36.4 ± 1.2	4.3	57.4 ± 1.6	6.8	99.4 ± 1.8	9.2
	50.0	21.7 ± 1.0	"HIGH"	42.1 ± 1.0	"VERY HIGH"	80.7 ± 0.9	"VERY HIGH"
C-NYL [h]	1.0	13.8 ± 0.2	1.1	11.2 ± 0.4	0.2	12.4 ± 0.4	0.8
	2.5	12.9 ± 0.1	1.1	10.2 ± 0.3	0.1	11.3 ± 0.5	0.8
	5.0	14.3 ± 0.1	1.1	11.2 ± 0.3	0.2	12.2 ± 0.6	0.8
	10.0	16.2 ± 0.1	1.1	12.8 ± 0.3	0.2	13.7 ± 0.6	0.8
	20.0	22.0 ± 0.7	1.1	18.0 ± 0.6	0.7	18.2 ± 0.5	0.9
	33.3	10.8 ± 1.2	1.3	6.8 ± 1.6	0.8	8.2 ± 1.8	0.8
	50.0	(b)	—	(b)	—	(b)	—

[a] respect to C-Ref. The value is the ratio between the considered tanδ value and the tanδ value of C-Virgin at the same combination of temperature/frequency

[b] tanδ value was zero or a slightly negative number.

[c] effective temperature: ISO 25 at 25.4 °C, ISO 35 at 35.0 °C, ISO 45 at 45.0

[d] effective temperature: ISO 25 at 25.0 °C, ISO 35 at 35.2 °C, ISO 45 at 45.1

[e] effective temperature: ISO 25 at 25.4 °C, ISO 35 at 35.0 °C, ISO 45 at 45.0

[f] effective temperature: ISO 25 at 25.3 °C, ISO 35 at 35.3 °C, ISO 45 at 45.0

[g] effective temperature: ISO 25 at 25.2 °C, ISO 35 at 35.2 °C, ISO 45 at 45.0

[h] effective temperature: ISO 25 at 25.0 °C, ISO 35 at 35.2 °C, ISO 45 at 45.1

The data clearly show that temperature strongly affects the damping factor. The higher the temperature, the higher the tanδ value is for a considered frequency and CFRP type. In particular, the effect is higher for composites with high NBR fractions in mats. Also testing frequency influences tanδ value (FIGURE 3.14).
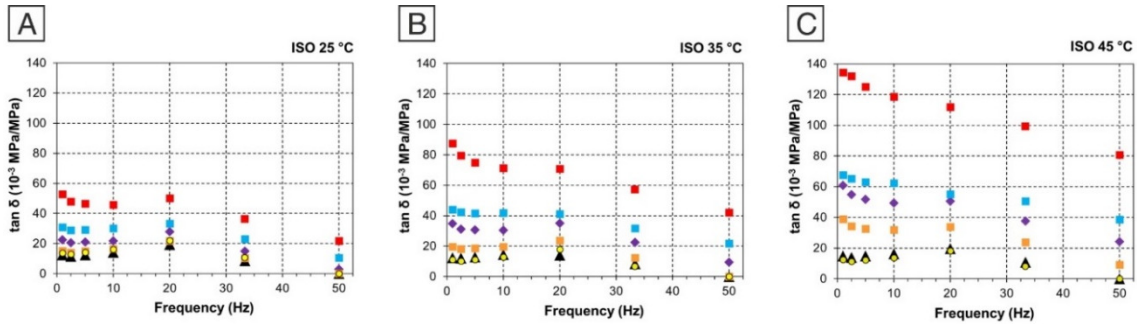
FIGURE 3.14 • Tanδ values of CFRPs determined at A) 25 °C, B) 35 °C and C) 45 °C (isothermal conditions).

At 25 °C (FIGURE 3.14A) all samples, except C-60/40, have the maximum damping capacity at 20 Hz (C-60/40 has a slightly better tanδ value at 1 Hz). At 35 °C (FIGURE 3.14B) the damping behaviour of CFRP sample is similar to that observed at 25 °C: C-60/40 composite shows a better damping capacity at low frequencies, in particular at 1 Hz. At 45 °C (FIGURE 3.14C) C-Ref, C-20/80 and C-PCL have a trend similar to that showed at 25 °C and 35 °C, while C-40/60 and C-60/40 show a downward trend with increasing frequencies (with some exception for C-40/60). It is worth to notice that, contrarily to C-Ref, almost all nano-modified CFRPs (with the exception of C-20/80 at 25 and 35 °C) show damping capacity also at the highest tested frequency (50 Hz, see TABLE 3.2).

FIGURE 3.13A-C reports stiffness-loss maps [10] evaluated at different frequencies and temperatures. This way of representing mechanical performances of the CFRPs highlights the effect that different additive systems have on mechanical behaviour and how, with the present approach, it is possible to tune and tailor the performance of the final laminates.

The main drawback of the widespread use of such rubbery nanofibers in CFRPs resides in the lowering of E' onset (TABLE 3.8), which may strongly limit the use of toughened laminates. Of course, all the applications which involve low service temperature are not affected by this problem. On the contrary, composites may benefit from reduced matrix

brittleness, which makes more difficult the microcracks formation and propagation [11]. However, one of the advantages of using nanofibrous membranes to toughen the composites is the fact that they can be conveniently positioned, during lamination, in the critical regions, without modifying the whole mass of the object. They can be applied for tailored and localized modification only in critical areas where interlaminar stresses are mostly concentrated due to geometric discontinuities, such as free edges, holes, ply-drops and adhesive bonding [12]. Contrarily to the use of bulk toughened matrix, the mat interleaving approach allows to preserve the average thermomechanical properties of the whole component.

Moreover, both the grammage and the matrix characteristics may be accurately chosen to tailor the laminate properties in terms of storage modulus, T_g, damping and delamination performance, depending on the application requirements.

With the aim of better understanding the impact of such rubbery nanofibers on the CFRP thermomechanical properties, some additional CFRP panels were produced using a different resin (a "High Temperature" HT epoxy, IMP503Z-HT resin system) for evaluating the effect on a hosting material with different properties. In this case, the most promising mat candidate (*n*-60/40) for what concerns the CFRP fracture toughness and damping improvement, but also the most problematic one because of the lowering of CFRP T_g, was selected.
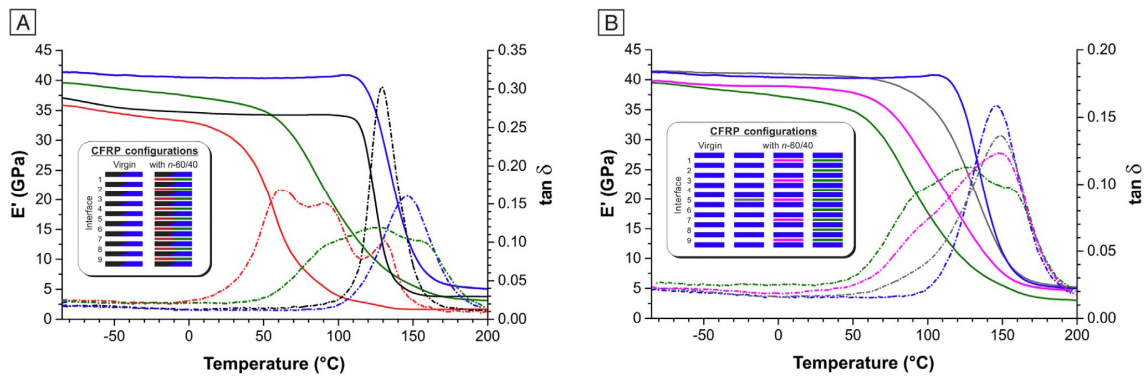
FIGURE 3.15 • A) DMA of unmodified CFRP (C-Ref with IMP503Z resin system and a reference with the "High Temperature" HT resin, black and blue curves, respectively) and CFRP with 9 membranes *n*-60/40 interleaved (red curves IMP503Z resin, green curves with IMP503Z-HT resin. B) Comparison of different configurations of CFRPs with the "HT" resin system: unmodified CFRP (blue), and with interface 5 (gray), interfaces 1-3-5-7-9 (magenta) and all interfaces (green) modified.

The *n*-60/40 mat was used to modify, again, all the interfaces and just the central one (FIGURE 3.15, green curves, and FIGURE 3.15B, gray curves, respectively) of a 10 plies CFRP panel. Moreover, an additional panel was produced with 5 nanofibrous membranes positioned at the 1-3-5-7-9 interlayers (FIGURE 3.15B, magenta curves).

A direct comparison of the effect of *n*-60/40 mat on the two applied epoxy resin systems demonstrates a very similar effect: FIGURE 3.15A displays the behaviour of the two reference unmodified composites (C-Ref and C-Ref-HT) with the relative 9-membrane-interleved ones (C-60/40 and C-60/40-HT_9).

While the HT resin has a slightly higher glass transition temperature (T_α = 150 °C, E' onset at 122 °C), the effect of the NBR-rich nanofibers (C-60/40-HT_9) is highly reminiscent of the C-60/40 sample: in both cases a high-T relaxation typical of the unmodified epoxy is still present together with two low-T peaks that, according to the previous interpretation might be due to the PCL-rich and NBR-rich regions. This behaviour is also observed to a minor extent in composites with a lower amount of modification. In particular, the placement of 5 interleaved membranes leads to a lesser widening of the tanδ peak toward low-T (C-60/40-HT_5). This trend holds in the single membrane modified CFRP (C-60/40-HT_1). It is worth noting that even if the E' onset moves toward lower temperature when increasing the number of nano-modified interfaces, the reached T_g temperature (E' onset) depends also on the properties of the hosting matrix. While the addition of only one *n*-60/40 mat in the resin system IMP503Z determines a shift of the E' onset from 116 °C to 82 °C, in presence of the HT resin version the same mat causes a drop at 103 °C, starting from 122 °C of the unmodified laminate (C-Ref-HT). A similar trend is observed when all the interfaces are nano-modified: E' onset at 40 °C for the IMP503Z resin and 61 °C for the HT resin. The CFRP with 5 mats interleaved displays an intermediate behaviour with respect to the two extreme CFRP configurations (E' onset of 72 °C). These observations point at demonstrating an important role of the hosting resin system too on the resulting laminate thermomechanical properties, in addition to all the other presented variables, i.e. NBR percentage in the nanofiber and number of modified interfaces, but also the extreme versatility of the rubbery nanofibrous membranes that are able to significantly modify different matrices.

3.2 • MATERIALS AND METHODS

3.2.1 • Materials

Carboxylated nitrile butadiene rubber (NBR) NIPOL 1072CGX was purchased from Zeon Chemicals [68%mol butadiene (Bu), 28%mol acrylonitrile (ACN), 4%mol methacrylic acid (MAA)]. Poly(ε-caprolactone) (PCL), M_w 70,000-90,000, was purchased from Sigma-Aldrich. Nylon 66 Zytel E53 NC010, kindly provided by DuPont, was dried in a stove at 110 °C for minimum 6 h before use. N,N-dimethylacetamide (DMAc), N,N-dimethylformamide (DMF), formic acid and chloroform ($CHCl_3$) were purchased from Sigma-Aldrich and were used without any preliminary treatment. Plain weave carbon fabric (200 g/m^2) in epoxy matrices with two different glass transition temperatures (GG204P IMP503Z and "High Temperature" GG204P IMP503Z-HT) prepregs for composite lamination were supplied by G. Angeloni s.r.l. (Venezia, Italy).

3.2.2 • Nanofibers and CFRP panels production

Nanofibrous mats were produced via single-needle electrospinning, as described in CHAPTER 2. A Spinbow® electrospinning machine equipped with four 5 mL syringes was used. Needles (length 55 mm, internal diameter 0.84 mm) were joined to syringes via teflon tubing. Fibers were collected on a rotating drum covered with poly(ethylene)-coated paper at 60 rpm (0.39 m/s tangential speed) to avoid a prevalent fiber orientation direction. Mats have final dimensions of approximately 30 × 40 cm. The plain NBR solution was electrospun to obtain a film, taking advantage of the rubber low glass transition temperature that allows nanofibers to coalesce, forming a film. A higher grammage of the membrane was reached (TABLE 3.5 and FIGURE 3.3B), due to some restraints in the membrane handling ability: it was indeed impossible to process *f*-NBR films and transfer them onto prepregs during lamination, when the same grammage of the other nanofibrous mats was used. Hence the membrane used in the present work represent the minimum processing grammage to provide transferability from the paper support during CFRP lamination.

NBR solution (S-NBR, 10%wt) was prepared in DMAc (e.g. 1.0 g of polymer in 9.6 mL of solvent) under magnetic stirring at room temperature until formation of homogeneous solutions. PCL solution (S-PCL, 10%wt) was prepared in $CHCl_3$/DMF 1:1wt (e.g. 1.0 g of polymer in 3.0 mL of $CHCl_3$ and 4.8 mL of DMF) under magnetic stirring at room temperature until formation of homogeneous solutions. NBR/PCL blends were prepared by mixing together S-NBR and S-PCL solutions in different proportions (20, 40, 60%wt of S-NBR solution), according to TABLE 3.3. Polymer blends were stirred for minimum 2 h to ensure proper homogenization.

TABLE 3.3 • Details of NBR and PCL solutions, and of their blend.

| Solution/Blend | Polymer concentration[a] | Blend | | Solvent system |
| | | S-NBR solution | S-PCL solution | |
	%wt	%wt	%wt	
S-NBR	10	100	0	DMAc
S-PCL	10	0	100	$CHCl_3$/DMF 1:1wt
S-20/80	10	20	80	DMAc, $CHCl_3$ and DMF[b]
S-40/60	10	40	60	DMAc, $CHCl_3$ and DMF[b]
S-60/40	10	60	40	DMAc, $CHCl_3$ and DMF[b]
S-80/20	10	80	20	DMAc, $CHCl_3$ and DMF[b]

[a] in case of blend, the value represents the total polymer concentration

[b] solvents proportions are determined by the ratio of the mixed solutions

Nylon 66 solution 10%wt was prepared in formic acid/$CHCl_3$ 45:55wt (e.g. 1.0 g of polymer in 3.3 mL of formic acid and 3.3 mL of $CHCl_3$).

In TABLE 3.4 electrospinning process and environmental parameters for mats production are reported.

TABLE 3.4 • Process and environmental electrospinning parameters of mats integrated in CFRP panels.

Electrospun mat	Flow rate	Electric potential	Distance	Electric field[(a)]	Temperature	Relative humidity
	mL/h	kV	cm	kV/cm	°C	%
n-PCL	0.75	14.4	15.0	1.0	25-27	29-32
n-20/80	0.70	17.0	13.0	1.3	22-25	23-25
n-40/60	0.70	17.0	13.0	1.3	24-26	19-21
n-60/40	0.55	18.3	13.0	1.4	22-24	20-22
f-NBR	0.75	18.0	13.0	1.4	23-25	21-23
n-NYL	0.30	20.0	17.0	1.2	25-27	31-34

[(a)] calculated as electric potential to distance ratio

Nanofibrous mats were analysed by scanning electron microscopy (SEM, Phenom ProX) to determine nanofibers morphology. All analysed surfaces were cold sputter-coated with gold in order to avoid electrostatic surface charging.

Nanofibers of NBR/PCL blends with different composition (labelled as n-X/Y, where n stands for "nanofibrous mat", X is the NBR weight fraction in the nanofiber and Y the PCL counterpart), as well as of plain Nylon 66 (labelled as n-NYL) and PCL (labelled as n-PCL) were obtained. A plain NBR compact film derived from the coalesced nanofibers (f-NBR, where f stands for "film") was produced.

TABLE 3.5 • Laminated panels intended for DCB, ENF, DMA tests, and main membranes characteristics.

CFRP for DCB / ENF	CFRP for DMA		Interleaved membrane			
14 plies - IMP503Z resin 1 central mat + Teflon trigger	10 plies - IMP503Z resin 1 central mat / 9 mats	10 plies IMP503Z-HT resin	Membrane label	NBR fraction	Membrane grammage [a)]	Nanofiber diameter [b)]
				%wt	g/m²	nm
C-Ref	C-Ref	C-Ref-HT	—	—	—	—
C-PCL	C-PCL	—	n-PCL	0	16.5 ± 1.5	402 ± 174
C-20/80	C-20/80	—	n-20/80	20	17.9 ± 1.2	247 ± 76
C-40/60	C-40/60	—	n-40/60	40	18.9 ± 1.2	216 ± 63
C-60/40	C-60/40	C-60/40-HT_m [c)]	n-60/40	60	19.5 ± 1.5	259 ± 72
C-f-NBR	C-f-NBR		f-NBR	100	36.3 ± 1.6	—
S-NYL	S-NYL	10	n-NYL	—	11.2 ± 1.2	275 ± 69

[a)] Average values derived from at least 5 measurements in different membrane regions

[b)] Average values derived from at least 100 diameter measurements, manually done on single nanofibers by means of the Photoshop measurement tool

[c)] Various CFRP configurations: mats positioned in interface 5 (central), in 1-3-5-7-9 interfaces, and in all the interfaces (refer to TABLE 3.8 and FIGURE 3.15B)

In TABLE 3.5 the produced membranes are reported, as well as the nanofibers diameter and the grammage of the mats, while the average membrane thickness is reported in

TABLE 3.6. The mat thickness was measured using an analog indicator, applying a pressure of 360 g/m^2.

TABLE 3.6 • Characteristics of the CFRP panels for 10-ply DMA samples.

CFRP	Nanofibrous mat	Mat grammage[a]	Mat thickness[a]	Total mat thickness in CFRP	CFRP thickness	CFRP thickness increase[b]	CFRP thickness variation[b]	Mats compaction degree[c]	CFRP density	CFRP density variation[b],[d]
		g/m^2	μm	mm	mm	mm	%	%	g/cm^3	%
C-Ref	—	—	—	—	2.583	—	—	—	1.407	—
C-PCL	n-PCL	16.5 ± 1.5	80 ± 4	0.72	2.709	0.126	+ 4.9	83	1.397	-0.7
C-20/80	n-20/80	17.9 ± 1.2	65 ± 4	0.59	2.767	0.184	+ 7.1	69	1.394	-0.9
C-40/60	n-40/60	18.9 ± 1.2	57 ± 3	0.51	2.792	0.209	+ 8.1	59	1.385	-1.6
C-60/40	n-60/40	19.5 ± 1.5	46 ± 3	0.41	2.847	0.264	+ 10.2	36	1.378	-2.1
C-f-NBR	f-NBR	36.3 ± 1.6	37 ± 3	0.33	2.886	0.303	+ 11.7	9	1.354	-3.8
C-NYL	n-NYL	11.2 ± 1.2	52 ± 4	0.47	2.606	0.023	+ 0.9	95	1.402	-0.4

[a] Average mat grammage and thichness values derive from at least 5 and 15 measurements, respectively

(b) respect to C-Virgin

(c) in the composite. It is calculated as (Total mat thickness – CFRP thickness increase)/ (Total mat thickness)

[d] CFRP density was calculated from DMA panels before specimen cutting, discarding the edge zones (laminates dimensions approximately 55x35 mm^2)

Specimens for the interlaminar fracture toughness evaluation (DCB and ENF tests) were prepared via hand lay-up in air-conditioned room (22-24 °C, 24-26% of relative humidity), stacking 14 prepreg plies (GG204P IMP503Z), interleaving a single nanofibrous mat in the central interface, and adding a Teflon film (FIGURE 3.16) to allow the trigger for specimen delamination. All the nanofibrous membranes (and NBR film) were directly applied with their paper substrate onto the prepreg during lamination process. Prior to the application of additional prepreg plies, as required by the followed stacking sequence, the paper substrate was removed. Corresponding reference panels without nanofibrous membrane were also produced for the sake of comparison.
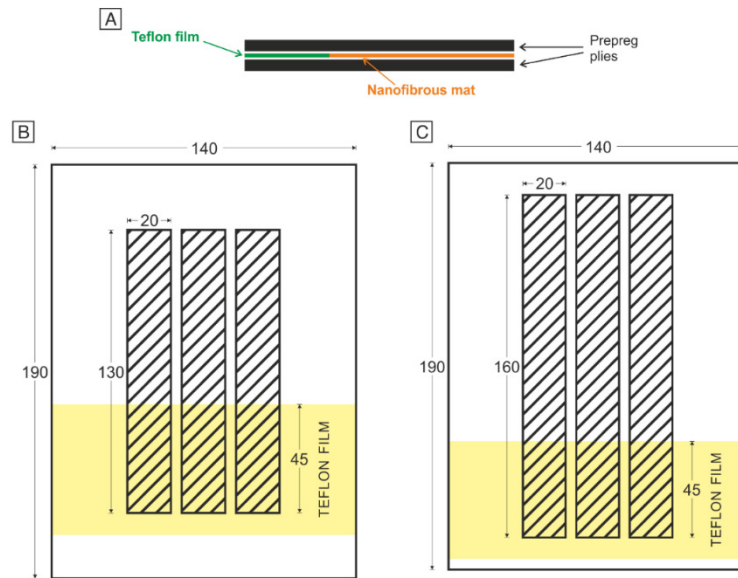
FIGURE 3.16 • Samples for characterization of delamination performance: section view (A) and dimensions (in mm) of CFRP panel and specimens for DCB (B) and ENF (C).

Composite panels are labelled as C-Z, where C stands for "composite" and Z represents just the composition of the abovementioned interleaved nanofibrous mat (*n*-X/Y, *n*-PCL, *n*-NYL). When NBR film (*f*-NBR) is used, the label of the composite keeps such indication (C-fNBR) for better clarity. The unmodified composite, used as reference material, is labelled C-Ref. Uncured panels underwent a preliminary treatment of 2 h at 45 °C under vacuum for better nanofibers impregnation prior curing cycle in autoclave (2 h at 135 °C, under vacuum, 6 bar external pressure, heating/cooling ramp 2 °C/min).

For DCB and ENF tests, CFRP panels (140 × 190 mm) constituted by 14 plies in total were produced via hand lay-up and consolidated applying the same preliminary treatment and cure cycle as reported above for the DMA samples. The specimens were obtained by cutting out the CFRP panel, discarding the edge parts (at least 15 mm) for avoiding any inhomogeneity. Specimens thickness range from 3.5 to 3.7 mm.

DCB specimens had the following final dimensions: 130 mm total length (*L*), 20 mm width (*b*), 45 mm crack length (*a*), and were tested under a 3.0 mm/min crosshead separation rate. Aluminium blocks were fixed with epoxy resin glue on the tip for the application of the load.

ENF specimens had the following dimensions: 160 mm total length, 20 mm width (b), 45 mm crack length, and were tested under a 1.0 mm/min crosshead separation rate. ENF tests were carried out with 100 mm span ($2L$) between supports, and the specimen placed in the 3-point bending geometry as following: 50 mm specimen half-span (L) and 30 mm delamination length (a_0).

In propagation, the energy release rate was evaluated considering a crack length between 48 and 90 mm for Mode I ($G_{I,R}$), and the 32-42 mm range for Mode II tests ($G_{II,R}$). In particular, for DCB tests of rubber-containing layers, a specific crack length range for the $G_{I,R}$ calculation was considered for each sample type, averaging only the points associated to the crack propagation in the modified interface. Details about the specific samples crack length range considered for the $G_{I,R}$ calculation for each sample is reported in TABLE 3.7.

TABLE 3.7 • Crack length range considered for $G_{I,R}$ calculation for each CFRP sample.

DCB sample	Crack length range
	mm
C-Ref	48-90
C-PCL	48-90
C-20/80	48-72
C-40/60	48-66
C-60/40	48-58
C-f-NBR	48-67
C-NYL	48-90

CFRP panels for DMA tests (FIGURE 3.17) were produced stacking 10 plies of GG204P IMP503Z prepregs. When the case, the membranes listed in TABLE 3.5 were placed within each ply, for a total of 9 integrated membranes, and also only in the central one (between interface 5 and 6, FIGURE 3.17A).
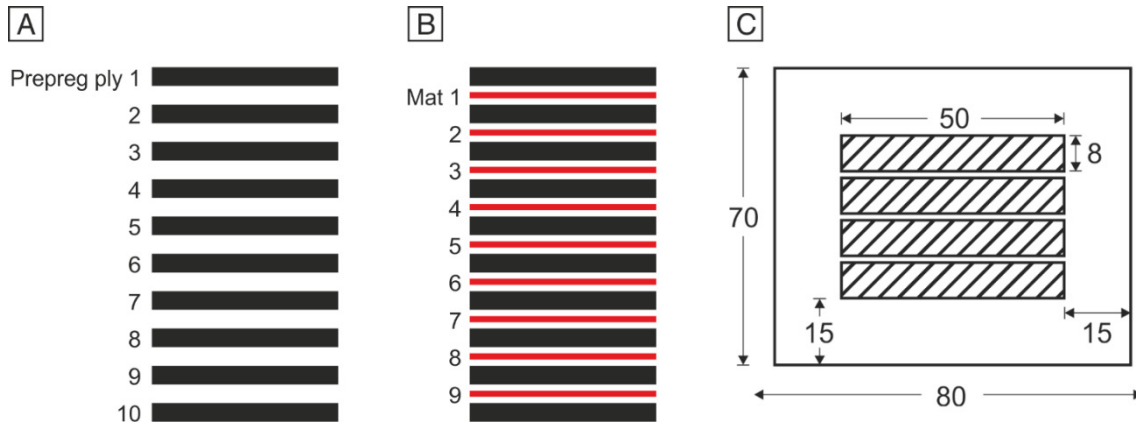
FIGURE 3.17 • Stacking sequence of plies/mats for panel production: (A) unmodified and (B) 9 nano-modified interfaces CFRP (laminates with a different number of integrated mats were produced too). (C) Dimensions (in mm) of CFRP panel and DMA samples.

An unmodified reference panel for the sake of comparison (C-Ref) was produced too. Samples with a different number and a different positioning of *n*-60/40 mat were also produced with prepreg GG204P IMP503Z-HT (C-60/40HT_*m*, where "*m*" accounts for the different number of the interleaved interfaces, as reported in detail in TABLE 3.8), together with an unmodified panel (C-Ref-HT). Specimens for DMA were 50 × 8 mm, obtained by cutting out 70 × 80 mm CFRP panels (FIGURE 3.17C). To ensure CFRP homogeneity, edge parts of panel (about 15 mm) were discarded. Specimen thickness ranges from 2.6 to 2.9 mm, as reported in detail in TABLE 3.6.

TABLE 3.8 • Laminated CFRP tested via DMA and their thermomechanical properties.

CFRP	Interleaved membrane	10 plies CFRP - 1 central mat - IMP503Z resin			10 plies CFRP - 9 mats - IMP503Z resin				10 plies CFRP - IMP503Z-HT resin		
		E' below E' onset [a]	E' onset	T_α [b]	E' below E' onset [a]	E' at 25 °C	E' onset	T_α [b]	E' below E' onset [a]	E' onset	T_α [b]
		GPa	°C	°C	GPa	GPa	°C	°C	GPa	°C	°C
C-Ref	—	34.5 ± 1.1	116 ± 1	129	34.7 ± 1.2	34.5 ± 1.1	116 ± 1	129	—	—	—
C-Ref-HT	—	—	—	—	—	—	—	—	41.2 ± 0.9	122 ± 2	150
C-PCL	C-Ref	32.9 ± 0.9	97 ± 2	125	33.4 ± 1.0	33.2 ± 1.1	51 ± 1	89	—	—	—
C-20/80	C-PCL	33.5 ± 1.2	92 ± 2	128	32.5 ± 1.2	32.2 ± 1.2	59 ± 2	87	—	—	—
C-40/60	C-20/80	33.1 ± 1.3	84 ± 1	127	32.8 ± 0.9	32.3 ± 1.2	49 ± 1	84	—	—	—
C-60/40	C-40/60	33.3 ± 1.3	82 ± 2	127	32.3 ± 1.1	31.0 ± 1.1	40 ± 2	63	—	—	—
C-60/40-HT_1 [c]	C-60/40	—	—	—	—	—	—	—	40.7 ± 1.2	103 ± 2	151
C-60/40-HT_5 [c]	C-60/40	—	—	—	—	—	—	—	38.2 ± 1.2	72 ± 2	151
C-60/40-HT_5 [c]	C-60/40	—	—	—	—	—	—	—	36.3 ± 1.1	61 ± 2	130
C-*f*-NBR	C-*f*-NBR	32.4 ± 1.2	53 ± 2	126	32.2 ± 1.0	25.7 ± 1.5	15 ± 1	58	—	—	—
S-NYL	S-NYL	33.4 ± 1.3	112 ± 1	129	34.0 ± 1.1	34.0 ± 1.1	117 ± 1	129	—	—	—

[a] E' below E' onset was evaluated at 25 °C for CFRPs with only the central interface modified and for laminates with IMP503Z-HT, while for CFRPs with 9 mats interleaved at 0 °C (except for C-f-NBR at −25 °C)

[b] T_α corresponds to the main peak in tanδ curve, so it does not necessarily represent the tanδ peak positioned at the highest temperature. The standard deviation is not reported because it is lower than 1 °C for all the cases

[c] Various CFRP configurations: mats positioned in interface 5 (C-60/40-HT_1), in 1-3-5-7-9 interfaces (C-60/40-HT_5), and in all the interfaces (C-60/40-HT_1)

3.2.3 • Characterization of CFRPs

DCB and ENF tests were carried out using an Instron 5966 universal testing machine equipped with a 10 kN load cell, at room temperature (20 °C). DCB specimens were tested at 3.0 mm/min crosshead separation rate, while ENF at a displacement rate of 1.0 mm/min. At least 3 specimens for each CFRP material/delamination mode were tested.

DCB tests were performed in order to evaluate the energy release rate for Mode I loading (G_I, in J/m^2), both at the initial and propagation stages ($G_{I,C}$ and $G_{I,R}$, respectively), using the following formula [13]:

$$G_I = \frac{3P\delta}{2ba} 1000 \qquad \text{EQUATION 3.1}$$

where P is the load (in N), δ the crosshead displacement (in mm), a the crack length (in mm), b the specimen width (in mm).

ENF tests were carried out for evaluating the fracture toughness in Mode II loading (G_{II}, in J/m^2), both at the initial and propagation stages ($G_{II,C}$ and $G_{II,R}$, respectively), using the following formula [14]:

$$G_{II} = \frac{9P\delta a^2}{2b(\frac{1}{4}L^3 + 3a^3)} 1000 \qquad \text{EQUATION 3.2}$$

where P is the load (in N), δ the crosshead displacement (in mm), a the crack length (in mm), b the specimen width (in mm) and L the span length between supports (in mm).

Dynamic mechanical analysis (DMA) was carried out with a Netzsch DMA 242 E Artemis instrument in three-point bending deformation mode, using a 40 mm fixed span. DMA analysis in temperature ramp were carried out in the −85 +200 °C range at 3 °C/min heating rate, 1 Hz frequency, amplitude 20 μm, static force / dynamic force ratio = 1.5. DMA analyses in isothermal conditions were performed at 25, 35 and 45 °C, with temperature variations lower than 0.1 °C once stability was reached during tests. Instrument parameters were left all unchanged, but the testing frequencies, which in isothermal conditions are 1, 2.5, 5, 10, 20, 33.3 and 50 Hz. Tanδ values were obtained upon averaging 7 consecutive points recorded by the machine every 100 s (total time span about 12 min), after reaching temperature stability.

3.3 • CONCLUSIONS

The interleave of NBR/PCL blend nanofibrous mats during CFRP lamination proved to be a powerful tool to hinder delamination of epoxy-based CFRP laminates via localized resin toughening without significantly affecting weight and dimension of the laminate. A dramatic increase of the energy release rate (G) at the initiation and propagation stages (up to 5.8× and 4.4× the reference values, respectively) is observed. Acting on the hinder of crack initiation represents a major safety parameter since, once a crack starts, the laminate is already compromised and unrepairable. Nonetheless, reducing crack propagation helps to increase the safety and lifetime of the component. Rubbery nanofibers demonstrated the ability to significantly impact Mode I delamination (up to +480% of G_I), while in Mode II the improvement is limited (up to +34% of G_{II}). The rubbery mats are also able to blend with the epoxy matrix during curing, providing a significant modification of the damping ability. By increasing the NBR content, the composite damping increases, but at the expenses of a decreased maximum operating temperature (lowering of E' onset, T_g). The system proved to be easily tailorable, depending on the specific application, simply acting on the percentage of rubber in the fiber in order to best compromise between damping and maximum operating temperature.

Such promising results pave the way to the application of rubbery nanofibrous mats for localized modification of laminates in critical spots, such as free edges, holes, ply-drops and adhesive bonding, providing a flexible and easy system to be integrated in the composite during the lamination process.

Another important parameter, which could affect tanδ, E' onset (T_g) and fracture toughness, is the grammage of the interleaved mat, which should be explored in the future for a thoroughly evaluation of the rubbery nanofibers effect on laminate thermomechanical properties.

References

[1]   R. Palazzetti, A. Zucchelli, Electrospun nanofibers as reinforcement for composite laminates materials – A review, Compos. Struct. 182 (2017) 711–727. https://doi.org/10.1016/j.compstruct.2017.09.021.

[2]   Application of Fracture Mechanics to Composite Materials, Elsevier, 1989. https://doi.org/10.1016/B978-0-444-89079-5.50001-5.

[3]   L. Daelemans, N. Kizildag, W. Van Paepegem, D.R. D'hooge, K. De Clerck, Interdiffusing core-shell nanofiber interleaved composites for excellent Mode I and Mode II delamination resistance, Compos. Sci. Technol. 175 (2019) 143–150. https://doi.org/10.1016/j.compscitech.2019.03.019.

[4]   G.W. Beckermann, K.L. Pickering, Mode i and Mode II interlaminar fracture toughness of composite laminates interleaved with electrospun nanofibre veils, Compos. Part A Appl. Sci. Manuf. 72 (2015) 11–21. https://doi.org/10.1016/j.compositesa.2015.01.028.

[5]   Z.D. Xu, Y.X. Liao, T. Ge, C. Xu, Experimental and theoretical study of viscoelastic dampers with different matrix rubbers, J. Eng. Mech. 142 (2016) 1–12. https://doi.org/10.1061/(ASCE)EM.1943-7889.0001101.

[6]   A. Cohades, E. Manfredi, C.J.G. Plummer, V. Michaud, Thermal mending in immiscible poly(ϵ-caprolactone)/epoxy blends, Eur. Polym. J. 81 (2016) 114–128. https://doi.org/10.1016/j.eurpolymj.2016.05.026.

[7]   R.J.J. Williams, B.A. Rozenberg, J. Pascault, Reaction-induced phase separation in modified thermosetting polymers, 1997. https://doi.org/10.1007/3-540-61218-1_7.

[8]   G. Vanden Poel, S. Goossens, B. Goderis, G. Groeninckx, Reaction induced phase separation in semicrystalline thermoplastic/epoxy resin blends, Polymer (Guildf). 46 (2005) 10758–10771. https://doi.org/10.1016/j.polymer.2005.09.013.

[9]   L. Daelemans, W. Van Paepegem, D.R. D'hooge, K. De Clerck, Excellent Nanofiber Adhesion for Hybrid Polymer Materials with High Toughness Based on Matrix Interdiffusion During Chemical Conversion, Adv. Funct. Mater. 29 (2019) 1–10. https://doi.org/10.1002/adfm.201807434.

[10]   M. Brodt, R.S. Lakes, Composite Materials Which Exhibit High Stiffness and High Viscoelastic Damping, J. Compos. Mater. 29 (1995) 1823–1833. https://doi.org/10.1177/002199839502901402.

[11]   T. Takeda, W. Fan, Q.P. Feng, S.Y. Fu, F. Narita, Y. Shindo, Cryogenic mechanical properties of woven glass/epoxy composites modified with multi-walled carbon nanotube and n-butyl glycidyl ether under tensile static and cyclic loadings, Cryogenics (Guildf). 58 (2013) 33–37. https://doi.org/10.1016/j.cryogenics.2013.09.005.

[12]   T.K. O'Brien, Delamination of Composite Materials, Compos. Mater. Ser. 4 (1991) 181–198. https://doi.org/10.1016/B978-0-444-70507-5.50009-3.

[13]   D5528-01 2001. Standard Test Method for Mode I Interlaminar Fracture Toughness of Unidirectional Fiber-Reinforced Polymer Matrix Composites, Am. Soc. Test. Mater. (2014) 1–13. https://doi.org/10.1520/D5528-13.2.

[14]   BS EN 6033:2015, BS EN 6034 : 2015 BSI Standards Publication Aerospace series — Carbon fibre reinforced plastics — Test method — Determination of interlaminar fracture toughness energy — Mode I —, BSI Stand. Publ. (2015) 14.

Chapter 4

DAMPING AND MECHANICAL BEHAVIOUR OF COMPOSITE LAMINATES INTERLEAVED WITH RUBBERY NANOFIBERS

The development of composite components with superior damping capacity is welcome in fields like automotive and aerospace for improving comfort and reducing composite damages. In this chapter, a nanomodified structural composite with improved damping is presented. Vibration hampering is achieved by interleaving electrospun Nitrile Butadiene Rubber / poly(ϵ-caprolactone) (NBR/PCL) blend nanofibrous mats into epoxy unidirectional Carbon Fiber Reinforced Polymer (CFRP) prepregs. Three sample configurations were produced using rubbery nonwoven layers with different thicknesses (5, 10 and 20 µm) for evaluating the effect of grammage layer on CFRP damping and mechanical properties. Damping behaviour was evaluated by single cantilever beam vibration tests using the advanced Modified-Coulomb-Model (MCM).
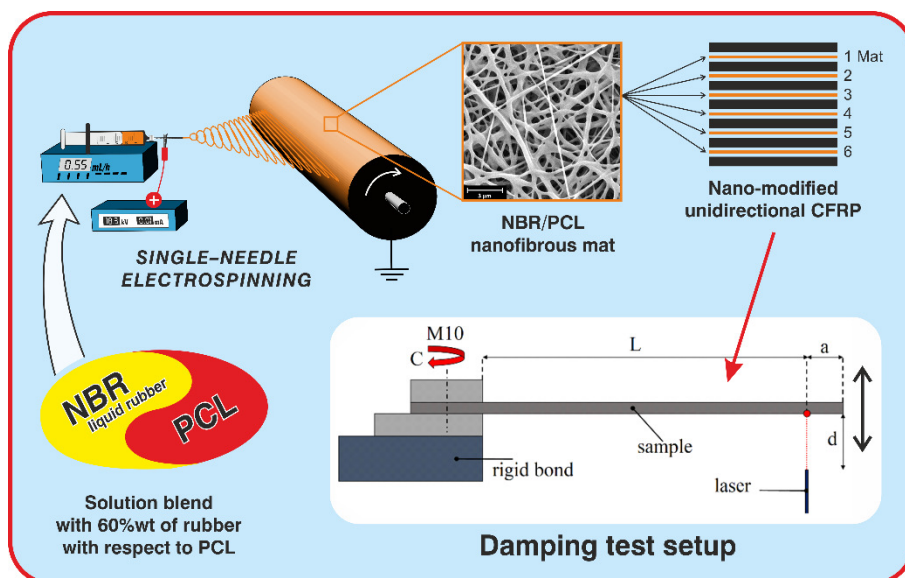
4.1 • RESULTS AND DISCUSSION

4.1.1 • Thermomechanical characterization

An overview of the overall thermomechanical properties of the different laminate configurations was evaluated via DMA. In FIGURE 4.1 the storage modulus (E′) and loss factor (tanδ) versus temperature are plotted. The laminates int. 5 and int. 10 show an E′ trend similar to the reference one. The storage modulus is comparable to the one displayed by the unmodified CFRP, while the E′ onset slightly lowers (107 °C vs 113 °C for the ref.). By contrast, int. 20 shows a first E′ onset at 55 °C, and a main E′ drop characterized by an onset at 99 °C. Their first onset can be attributed to the melting of the PCL crystalline fraction, while the second drop is due to the glass transition of the toughened epoxy resin. The behaviour of the last sample is similar to what evidenced by rubbery-modified CFRPs reported in CHAPTER 2.
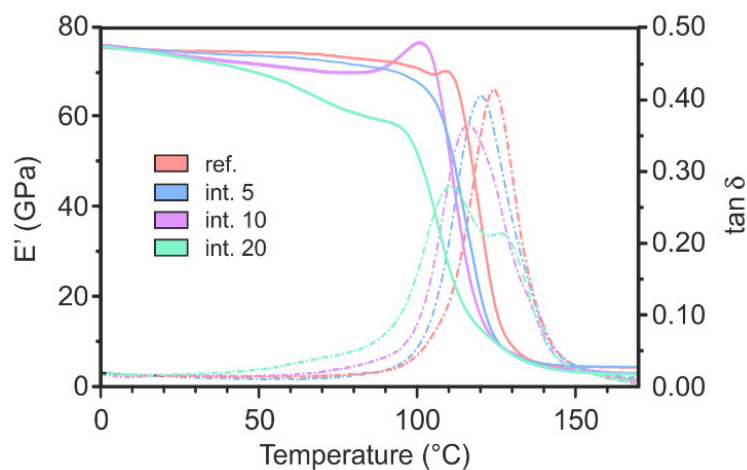
FIGURE 4.1 • DMA analyses of the different laminate configurations.

Regarding the tanδ, the peaks do not show relevant shifts for increasing grammage of interleaved mats, except for int. 20 configuration (main peak at 111 °C vs 124 °C for the ref. one). Besides, the shape of the curve is different, displaying two peaks. The first peak accounts for the toughened epoxy resin thanks to mixing with NBR/PCL blend, while the second one, at 128 °C, is due to the unmodified resin fraction. It is to underline that in almost all the modified laminates, the presence of the NBR/PCL blend

widens the window dissipation energy of the composite to lower temperature, indicating a potentially damping enhancement also at room temperature.

4.1.2 • *Mechanical tests and fracture analysis*

The influence of both interleaved mat grammage and temperature was more deeply investigated via destructive 3PB analyses. Flexural elastic modulus and strength of the different sample configurations do not evidence significant differences at RT (FIGURE 4.2), which stay near 100 GPa and 1100 MPa, respectively. However, with increasing temperature, the effect of the nanomat becomes more noticeable, especially for higher mat grammages. Indeed, at 80 °C the int. 20 configuration shows a reduction of 13 % in elastic modulus and 20 % in flexural strength compared to the ref. configuration. These results are in good accordance with the overall performance of E' identified by the DMA tests.
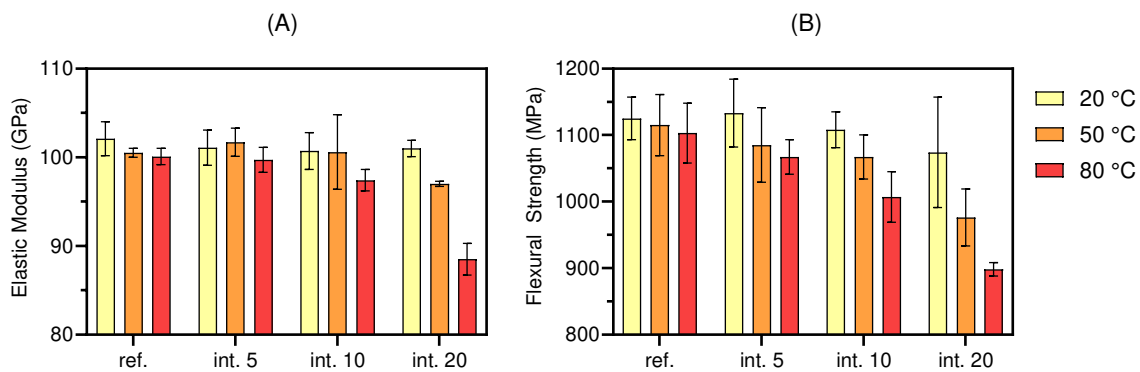
FIGURE 4.2 • (A) Flexural elastic modulus and (B) flexural strength for different sample configurations and temperatures.

The variation of laminate elastic modulus upon temperature was deeply elucidated carrying out 3PB cyclic loading-unloading tests. FIGURE 4.3 shows the flexural modulus as a function of temperature. As can be noticed, the elastic modulus shows a significant reduction only when high temperatures (> 80°C) and high grammages (> 5 g/m^2, int. 10) are combined. However, during the life-cycle of common composite components, these high temperatures are rarely reached, except for special applications.

Although the qualitative trends of E′ and flexural modulus are similar, the numerical values shown in FIGURE 4.3 are much more reliable than those obtained from the DMA, where E′ is strongly influenced by the specific specimen loading region (e.g. local

fiber/matrix ratio under solicitation). On the contrary, since the imposed deformation in 3PB test is macroscopic, the local effects become negligible because the stressed volume is increased.
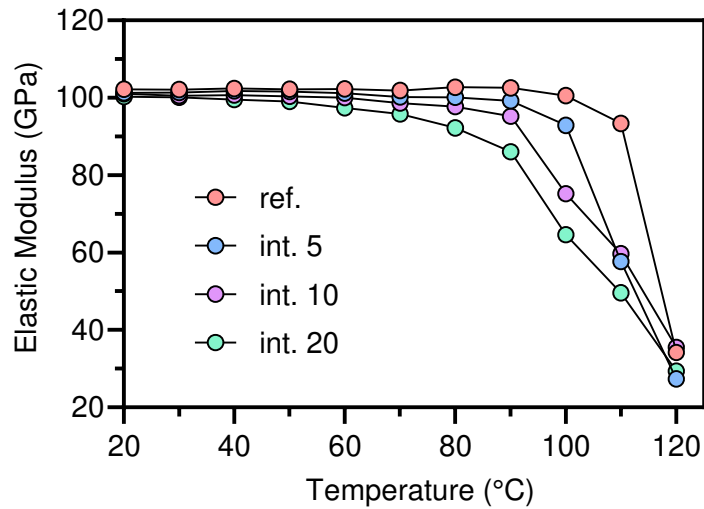
FIGURE 4.3 • Temperature dependence of flexural modulus.

In FIGURE 4.4 are displayed the perpendicular and parallel views of the fracture surfaces of 3PB specimens tested up to failure at RT for each laminate configuration. In this way, it was possible to observe both pulled out fibers (in blue in the sketch of FIGURE 4.4) and fibers broken in correspondence of the fracture surface of the specimen (in red). Moreover, int. 20 was analysed also at 50 and 80 °C.

The fracture surfaces of the ref. laminate appear sharp and brittle, with a marked fiber/matrix debonding (perpendicular view) and naked pulled out carbon fibers (parallel view). This behaviour is typical of low-toughened thermosetting polymers.

For nano-interleaved laminates, it can be noticed that the nanofibrous morphology is completely lost. Indeed, as previously observed in FIGURE 4.4, during the curing cycle the NBR/PCL blend mixed with the epoxy resin, leading to toughened matrix. As a matter of fact, by increasing the grammage of interleaved mat, the fracture surfaces become more irregular with more pronounced indented markings, meaning a greater ductile deformation. Moreover, a higher adhesion between carbon fibers and toughened epoxy matrix (perpendicular view) is found, and the matrix remains attached to the pulled out fibers (parallel view). This effect is maximized in int. 20, particularly when the testing temperature is increased from RT to 50 and 80 °C.
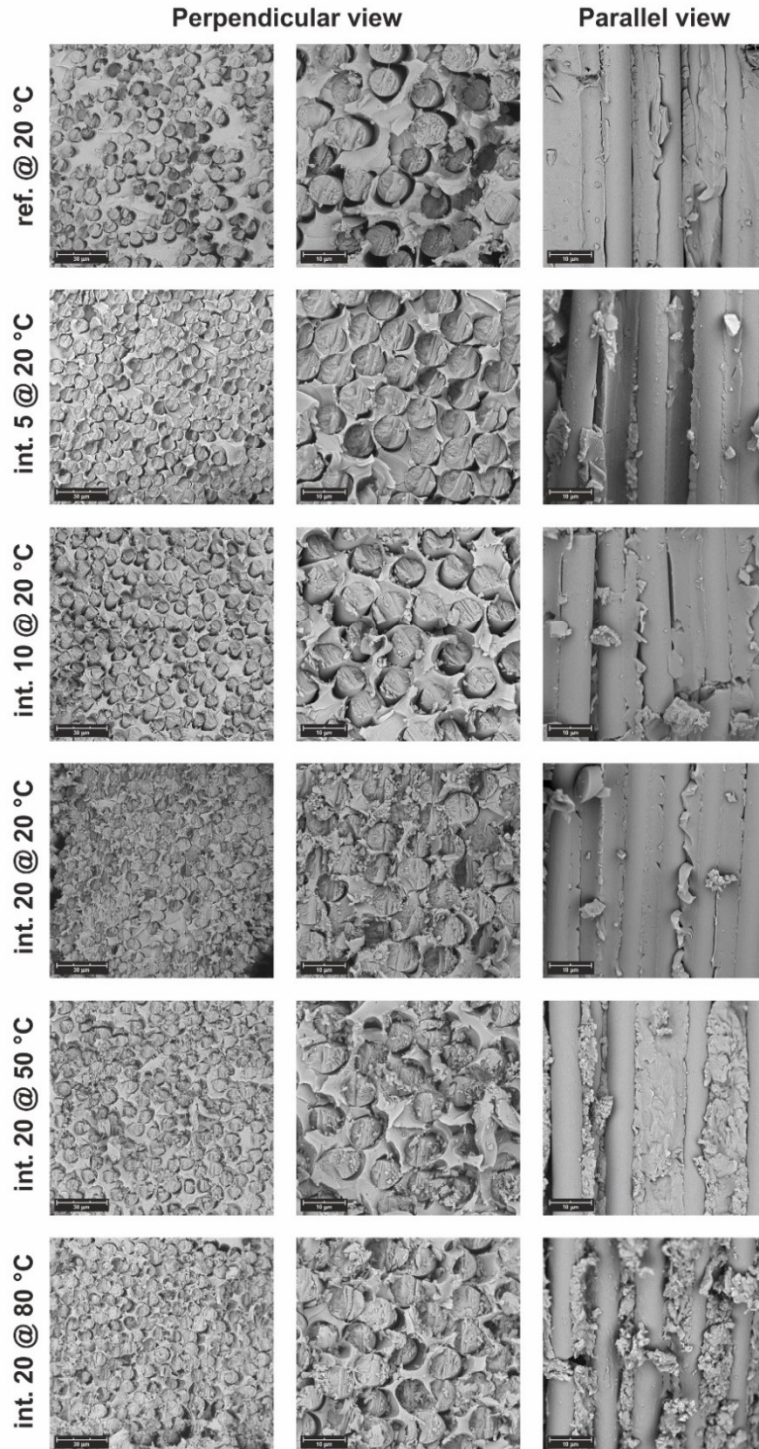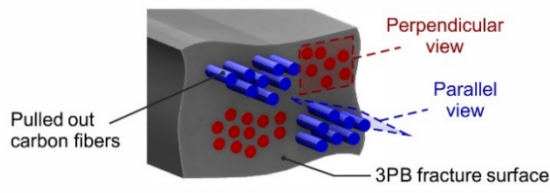
FIGURE 4.4 • SEM micrographs of fracture surfaces after destructive 3PB tests. Scale bar: 30 µm first column (2,000×), 10 µm second and third columns (5,000×).

4.1.3 • Damping analysis

Regarding damping tests, the fitting of the experimental signal with MCM has always guaranteed a $R^2 \geq 0.99$. It was therefore possible to calculate the normalized material damping value for each configuration by excluding the contribution of both the air and the joint. This method was adopted because the damping effect of the air is predominant compared to the material one.

The material damping factor ranges from $1.75 \cdot 10^{-3}$ to $3.10 \cdot 10^{-3}$ for the ref. and int. 20 configurations, respectively (FIGURE 4.5A). FIGURE 4.5B shows the material damping enhancement versus the laminate weight variation for the different configurations. It is interesting to note that as the grammage of the nanofibrous membranes increases an exponential trend is observed in material damping. The major damping enhancement was obtained with the int. 20 configuration, achieving an improvement of 77% for a laminate weight increment of 1.5% only.
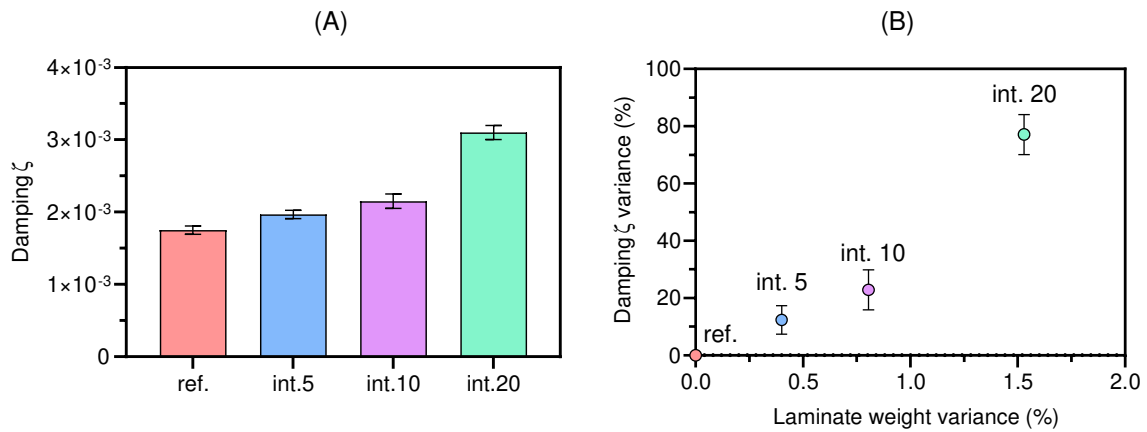
FIGURE 4.5 • (A) Material damping of the different sample configurations and (B) material damping percentage variation as a function of the laminate percentage weight variance.

4.2 • MATERIALS AND METHODS

4.2.1 • Electrospinning

Carboxylated nitrile butadiene rubber (NBR) NIPOL 1072CGX was purchased from Zeon Chemicals (68%mol butadiene, 28%mol acrylonitrile, 4%mol methacrylic acid). Poly(ε-caprolactone) (PCL), M_w 70,000-90,000, was purchased from Sigma-Aldrich. Polymers were both used without any preliminary treatment. N,N-dimethylacetamide (DMAc), N,N-dimethylformamide (DMF) and chloroform ($CHCl_3$) were purchased from Sigma-Aldrich and used without further purifications.

Rubbery NBR/PCL nanofibrous mats were prepared following the method proposed in CHAPTER 2, SECTIONS 2.2.2 and 2.2.4. The electrospinning process parameters and environmental condition for producing nanofibrous mats with 60%wt of NBR are reported in TABLE 4.1.

TABLE 4.1 • Electrospinning process parameters and nanofiber diameter.

Nanofibrous mat	Flow rate mL/h	Electric potential kV	Distance cm	Electric field[a] kV/cm	Temperature °C	Relative humidity %	Nanofibers diameter[b] nm
n-60/40	0.55	18.3	13	1.4	22-24	20-22	268 ± 43

[a] calculated as electric potential to distance ratio
[b] as spun nanofiber

To assess the thickness of the nanofibrous layers, a digital comparator (Alpa MegaRod) was used. To calculate the mat grammage (i.e. the mat weight per square meter), the nanofibrous layers were weighted by a scale with a resolution of 0.01 mg (Radwag AS 60/220.R2).

Nanofiber morphology (FIGURE 4.6) was observed through a Scanning Electron Microscope (SEM, Phenom ProX).
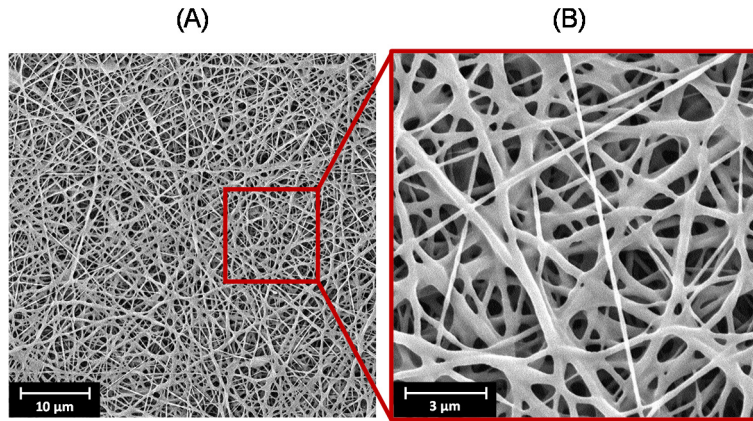
FIGURE 4.6 • SEM micrographs of NBR/PCL rubbery nanofibrous mat (n-60/40) at (A) 5,000×
magnification and (B) 20,000× magnification.

4.2.2 • Laminates and specimens fabrication

The carbon fiber epoxy unidirectional prepreg was T700S-24K/DT210 epoxy-based resin provided by Deltapreg (Toray group, Italy), with Vf = 53% and 350 g/m^2 of carbon fibers.

Four laminate configurations, reported in TABLE 4.2 were fabricated. All the laminates configurations were fabricated by staking 7 layers of unidirectional prepreg oriented at 0°. A reference configuration composed of only prepreg plies without interleaved layers (named ref.) and three nano-structured ones with 5 μm, 10 μm, and 20 μm thick nanofibrous layers interleaved at each prepreg interface (named int. 5, int. 10, and int. 20, respectively) were produced.

TABLE 4.2 • Sample laminate configurations of produced.

Configuration	Mat thickness	Mat grammage
	μm	g/m^2
ref.	-	-
int. 5	5	2.5
int. 10	10	5.1
int. 20	20	9.6

Laminates were cured with vacuum bag technology in autoclave at 130 °C for 2 hours and 6 bar pressure. The resulting laminates thickness was 2.6 mm without significant difference among laminates configurations. For each configuration, the specimens for thermomechanical (DMA), mechanical (3PB) and dynamic (damping) tests were extracted from the same laminate. Their dimensions, defined according to ASTM D7264, ISO 6721-1 and ASTM E756-05, are reported in TABLE 4.3.

TABLE 4.3 • Specimens geometry.

Test	Length mm	Width mm	Thickness mm
DMA	50	7.5	2.6
3PB	110	15	2.6
Damping	280	25	2.6

4.2.3 • Thermomechanical, mechanical, and damping tests

Overall thermomechanical properties of CFRPs were evaluated via DMA, using a Netzsch DMA 242 E Artemis instrument in a three-point bending configuration with a fixed span of 40 mm. DMA analyses were carried out with a heating ramp from 0 to 170 °C, 3 °C/min heating rate, 1 Hz oscillating frequency, 20 µm amplitude and a static / dynamic force ratio of 1.5. For each laminate configuration 3 specimens were tested.

Flexural tests were carried out to assess the effect of the nanofibrous rubbery membranes on the mechanical properties of the different laminate configurations. Two different types of flexural tests under different conditions were performed: i) the destructive one, carried up to failure, to evaluate the elastic modulus and the flexural strength at three different temperatures (20, 50, and 80 °C) and ii) a dynamic test performed in the elastic regime at a frequency of 1 Hz to evaluate the elastic modulus degradation as a function of the temperature. Regarding type i) 3PB test, the aforementioned temperatures were chosen because 20 °C is the reference RT, 50 °C because it is slightly lower than the melting of the PCL crystalline fraction of the rubbery blend, and 80 °C because it is enough above the PCL melting temperature.

Type ii) 3PB test, despite similar to the DMA one, allowed a more precise assessment of the flexural modulus as a function of the temperature. In fact, since UD CFRP laminates exhibit a very high flexural stiffness, the evaluation of conservative modulus (E') by the DMA may be not accurate. 3PB tests were performed on Instron Model 8033 equipped with a climatic chamber using a 2 kN load cell. The destructive tests were conducted at a crosshead speed of 2 mm/min. The dynamic ones were sinusoidally load between 0.15% and 0.30% flexural strain amplitude. A total of 12 3PB specimens were tested for each laminate configuration.

The dynamic tests for damping evaluation were performed according to ASTM E756-05 in a cantilever beam configuration with a laser sensor (optoNCDT 1402 - Micro-Epsilon) pointed at the specimen tip, as shown in FIGURE 4.7. The specimen was excited by preloading its tip and then instantaneously releasing it. For each laminate configuration, 3 specimens were tested and for each one 5 repetitions were performed. The setup parameters, depicted in FIGURE 4.7, were L = 255 mm, d = 105 mm, C = 25 Nm, a = 5 mm.
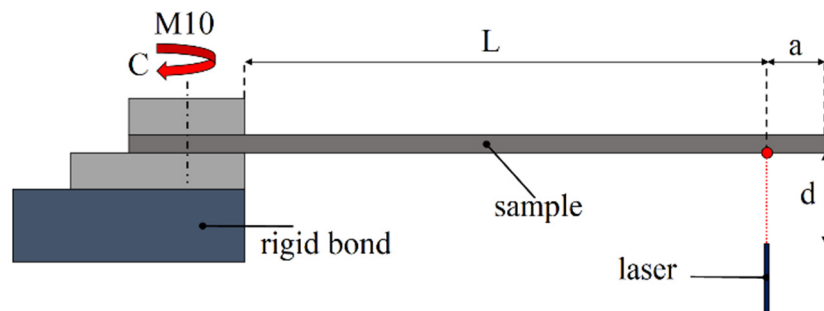
FIGURE 4.7 • Damping test setup scheme.

The tip displacement measured by the laser was acquired at 2 kHz by ADC converter (NI-9215 National Instruments) and processed by a MATLAB custom software based on MCD model. First, the signal was cut with a 10 s time window (FIGURE 4.8A). Subsequently, the Short Time Fourier Transform (STFT) was performed to obtain the spectrogram of the signal. In FIGURE 4.8B each curve represents the amplitude vs frequency for a specific time segment of the signal. The STFT was performed in MATLAB by using the spectrogram function. The signal was cut into time segments 0.1 s long, by using the Hamming window function. Then, each signal segment was

extended on 1 s time span by using the zero-padding technique, in order to increase the frequency resolution of the Fast Fourier Transform (FFT). A high signal segment overlap of 15/16 was chosen to have a high time resolution. The aforementioned parameters have been experimentally optimized for the specific type of signal analysed in this work.
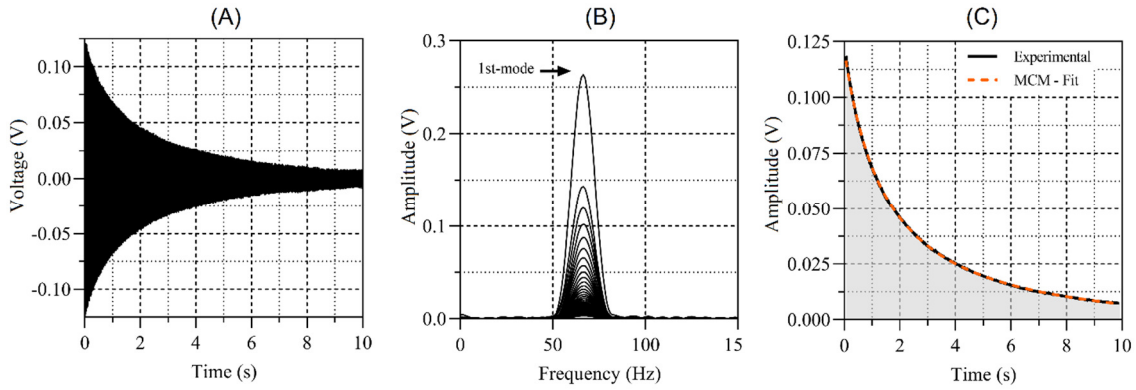
FIGURE 4.8 • (A) Original signal acquired by laser sensor; (B) Short Time Fourier Transform (STFT) of the signal; (C) Experimental amplitude decay as a function of time and fitting with the Modified-Coulomb-Damping (MCD) model.

Then, for each amplitude vs frequency curve of the STFT of FIGURE 4.8B, the maximum amplitude of the first resonance frequency was extracted and expressed as function of time (FIGURE 4.8C). In this way, it was possible to find the amplitude decay curve in the time domain.

According to the Modified Coulomb Damping (MCD) model [1] the time varying amplitude can be defined as:

$$\dot{y}(t) = -c - by(t) - ay(t)^2 \qquad \text{EQUATION 4.1}$$

where t is the time and a, b and c are coefficients accounting for viscous (air), material (structural or hysteretic) and Coulomb (friction) damping contributions, respectively. Solving the first-order EQUATION 4.1, under the assumption that the Coulomb damping is not dominant (i.e. $4ac < b^2$), the amplitude can be expressed as:

$$y(t) = \frac{b(p-1) + r(p+1)}{2a(1-p)} \qquad \text{EQUATION 4.2}$$

where $r = (b^2 - 4ac)$, $\alpha = 2ay_0 + b - r$, $\beta = 2ay_0 + b + r$, $p = {^\alpha/_\beta}\, e^{-rt}$ and y_0 the initial amplitude. EQUATION 4.2 was fitted on the experimental amplitude decay curve using the robust regression with least absolute residuals weight function. In this way it was possible to separate the material damping contribution (coefficient b) from the air and friction ones.

An equivalence with the well-known classic damping ratio ζ can be done assuming that the material damping contribution is dominant. Hence, the MCD time varying amplitude (EQUATION 4.1) can be simplified as $\dot{y}(t) = -by(t)$. The solution of this first-order equation is:

$$y(t) = y_0 e^{-bt} \qquad \text{EQUATION 4.3}$$

In the same manner, it is possible to express the response of the well-known single-degree of freedom mass-springer-damper model (given by $m\ddot{x}(t) + c\dot{x}(t) + kx(t) = 0$) as $x(t) = x_0 e^{-\zeta\omega_n t} \cos(\omega_n\sqrt{1 - \zeta^2})$ or in terms of amplitude as:

$$y(t) = y_0 e^{-\zeta\omega_n t} \qquad \text{EQUATION 4.4}$$

where ω_n is the resonance frequency. Finally, matching the amplitude of the MCD model (EQUATION 4.3) with the one of the classical single-degree of freedom mass-spring-damper model (EQUATION 4.4), it is possible to express the equivalent damping ratio as:

$$\xi = \frac{b}{\omega_n} \qquad \text{EQUATION 4.5}$$

4.3 • CONCLUSIONS

In this work a structural composite was prepared by interleaving rubbery NBR/PCL nanofibrous layers between unidirectional CFRP prepreg laminates.

Thermomechanical properties were experimentally evaluated using 3PB tests and DMA. Flexural tests show no significant differences at room temperature in elastic modulus and flexural strength between reference and nano-modified configurations. Only for the highest grammage and for temperatures over 50 °C, the effect of the nanomat becomes noticeable. In particular, when 80 °C are reached, the int. 20 configuration shows a reduction of 13% in elastic modulus and 20% in flexural strength compared to the ref. one. These results are in good accordance with DMA ones, which shows an E' onset drop from 113 °C to 55 °C. The morphology of the fracture surfaces as well appears to be affected by the amount of interleaved rubbery nanofibers, becoming more irregular and ductile.

Damping behaviour was evaluated by single cantilever beam vibration tests. Thanks to the advanced Modified-Coulomb-Damping (MCD) model, an accurate measurement of the material damping was obtained excluding the air and joint contributions.

The interleaved NBR/PCL nanofibrous mats greatly improved the composite damping capacity with a maximum increase of 77% in the composite loss factor, with a negligible influence on flexural strength and modulus below E' onset temperature. Moreover, no significant impact on laminate weight and thickness, respect to reference samples without nano-reinforcement, were found.

Hence, this type of nano-modified composite material is suitable for all those applications that require high energy dissipation ensuring at the same time high mechanical performance even at intermediate in-service temperature. The integration of nanofibrous rubbery membranes interspersed between the composite laminae overcomes the limits related to the use of bulk viscoelastic layers, which could negatively affect the laminate weight and integrity, even increasing its fracture toughness. This technique may allow engineers to design advanced composite components with high damping capacity by ultra-low grammage rubbery nanofibrous layers addition.

Reference

[1]   Clarence W. de Silva, Vibration and Shock Handbook, 2005.

Chapter 5

Sᴇʟꜰ-ᴀꜱꜱᴇᴍʙʟʏ NBR/NOMEX NANOFIBERS AS LIGHTWEIGHT RUBBERY NONWOVENS FOR HINDERING DELAMINATION IN EPOXY CFRPꜱ

Still today, concerns regarding delamination strongly limit the widespread use of high-performance composite laminates, like Carbon Fiber Reinforced Polymers (CFRPs), in replacement of metals. Nanofibrous mat interleaving is a well-established approach to reduce delamination. In 2020, for the first time, the Author proposed the use of not-crosslinked Nitrile Butadiene Rubber / poly(ε-caprolactone) (NBR/PCL) rubbery nanofibers for hindering delamination and enhancing damping in CFRPs, achieving excellent results. However, the nano-modifications may affect the laminate thermomechanical properties. Here, this limitation is entirely overcome by using rubbery NBR/Nomex nanofibers: no laminate stiffness nor glass transition temperature (T_g) lowering occurs upon CFRP nano-modification. Stable not-crosslinked nanofibers with up to 60%wt of NBR were produced via single-needle electrospinning, then morphologically, thermally, spectroscopically and mechanically characterized. NBR and Nomex disposition in the nanofiber was investigated too via selective removal of the sole rubber fraction, revealing the formation of particular self-assembly structures that resembles core-shell nanofibers or fibrillated hierarchical structures, depending on the imposed electrospinning solution flow rate. Mode I and II loading tests show a significant improvement of interlaminar fracture toughness of rubbery-modified CFRPs, especially G_I (up to +180%), while G_{II} enhancement is less pronounced. By contrast, pure Nomex nanofibers dramatically worsen the delamination resistance (G_I drop near 60%). While the integration of rubbery materials often causes a lowering of the laminate thermomechanical properties, this is not the case. Indeed, both the original laminate stiffness and glass transition temperature (T_g) are maintained, paving the way to extensive and reliable use of such rubbery mats in composite laminates for improving delamination resistance without affecting other relevant properties.

5.1 • RESULTS AND DISCUSSION

Single-needle electrospinning of rubbery blends is currently almost the only way to produce dimensionally stable NBR rubbery nonwoven mats without additional steps, such as rubber crosslinking, during or after the electrospinning process. Indeed, pure "liquid" NBR nanofibers production is prevented by the low T_g of rubber, which, instead, leads to film formation (see CHAPTER 2, SECTION 2.1.1). As demonstrated in CHAPTER 1, the use of a semi-crystalline thermoplastic polymer with suitable characteristics, like low-T_g and melting temperature above room temperature, can be exploited to produce a nanofibrous morphology with elastomeric behaviour. The obtained structure, made of NBR blended with poly(ε-caprolactone) (PCL), is similar to a thermoplastic elastomer (TPE) which comprises at least two interconnected polymer phases. PCL crystal regions act as hard domains at room temperature, giving mechanical strength and, as a consequence, dimension stability, while the PCL/NBR blended regions represent the soft domain, leading to the overall elastomeric behaviour of the nanofibrous structure, thus overcoming the detrimental rubber cold flow.

5.1.1 • *Miscibility evaluation of NBR/Nomex pair and electrospinning*

The blending approach proved to be a smart way to simply obtain nanofibers with tailored characteristics. Virtually, any type of polymer can be mixed together, given an electrospinnable solution. Also immiscible polymers (from a thermodynamic point of view) like the pair NBR/poly(ε-caprolactone), can be blended and processed through electrospinning without phase separation phenomena, thanks to the rapid solvent evaporation (see CHAPTER 1). According to the approach proposed by Hoftyzer and van Krevelen [1], the miscibility of a polymer pair can be evaluated considering the thermodynamic solubility parameter δ, or Hildebrand solubility parameter, which in turn derives from three different contributions, the Hansen solubility parameters ($\delta^2 = \delta_d^2 + \delta_p^2 + \delta_h^2$).

The relative miscibility of the two polymers can be thus evaluated according to the following equation:

$$\overline{\Delta\delta} = \sqrt{(\delta_{dNomex} - \delta_{dNBR})^2 + (\delta_{pNomex} - \delta_{pNBR})^2 + (\delta_{hNomex} - \delta_{hNBR})^2}$$ EQUATION 5.1

When the difference between the δ parameter ($\overline{\Delta\delta}$) for the polymer pair is below 5 MPa$^{1/2}$ there is good miscibility, while 5< $\overline{\Delta\delta}$ >10 may account for partial miscibility [1,2].

Upon evaluation of the solubility parameters as explained in APPENDIX 5.4, NBR/NX pair shows a $\overline{\Delta\delta}$ = 5.8 MPa$^{1/2}$. This value is slightly higher than the abovementioned threshold, placing the rubber/polyaramid pair into the partial miscibility zone. However, it is worth mentioning that also in this thermodynamically unfavourable situation, blending may be still possible. In our previous work regarding NBR/PCL nanofibers, their full blending was demonstrated even if the calculated $\Delta\delta$ value was 7.9 MPa$^{1/2}$, denoting low miscibility. In CHAPTER 1 it was shown that the electrospinning process can promote the formation of a polymeric blend whose existence is prevented from a thermodynamic point of view. Indeed, kinetic factors may decisively contribuite to obtain a blend, since the very fast solvent evaporation occurring during electrospinning may be able to "freeze" a partially miscible pair in a single-phase material [2].

FIGURE 5.1 shows the produced nanofibers, characterized by diameters ranging from 160 to 630 nm. The process parameters are reported in TABLE 5.3. The nanofibers show a smooth surface, without defects like beads, while fiber bundling may occur. To have an isotropic interlayer reinforcement, it is fundamental to obtain mats with random oriented nanofibers. Given the important role played by the relative humidity, which at high values favours the aligned disposition of fibers [3], a precise humidity control was done during electrospinning, keeping the RH $\leq$ 35%. This allows obtaining random deposition of nanofibers as much as possible. The produced rubbery nanofibers are expected to be solvent-free, even when the high-boiling solvent DMAc is used, thanks to the ability of the electrospinning process at inducing rapid and effective solvent evaporation.

To investigate the disposition of the polymers inside the nanofiber, selective removal of the rubber fraction was done via mats washing in chloroform, which is a non-solvent for the polyaramide. A peculiar morphology was found, as visible in FIGURE 5.1. In particular, the *s*-60/40 solution leads to different morphologies depending on the process conditions, especially on the selected flow rate (the working distance was however changed in the case of *n*-60/40_*c* to obtain a stable electrospinning process).
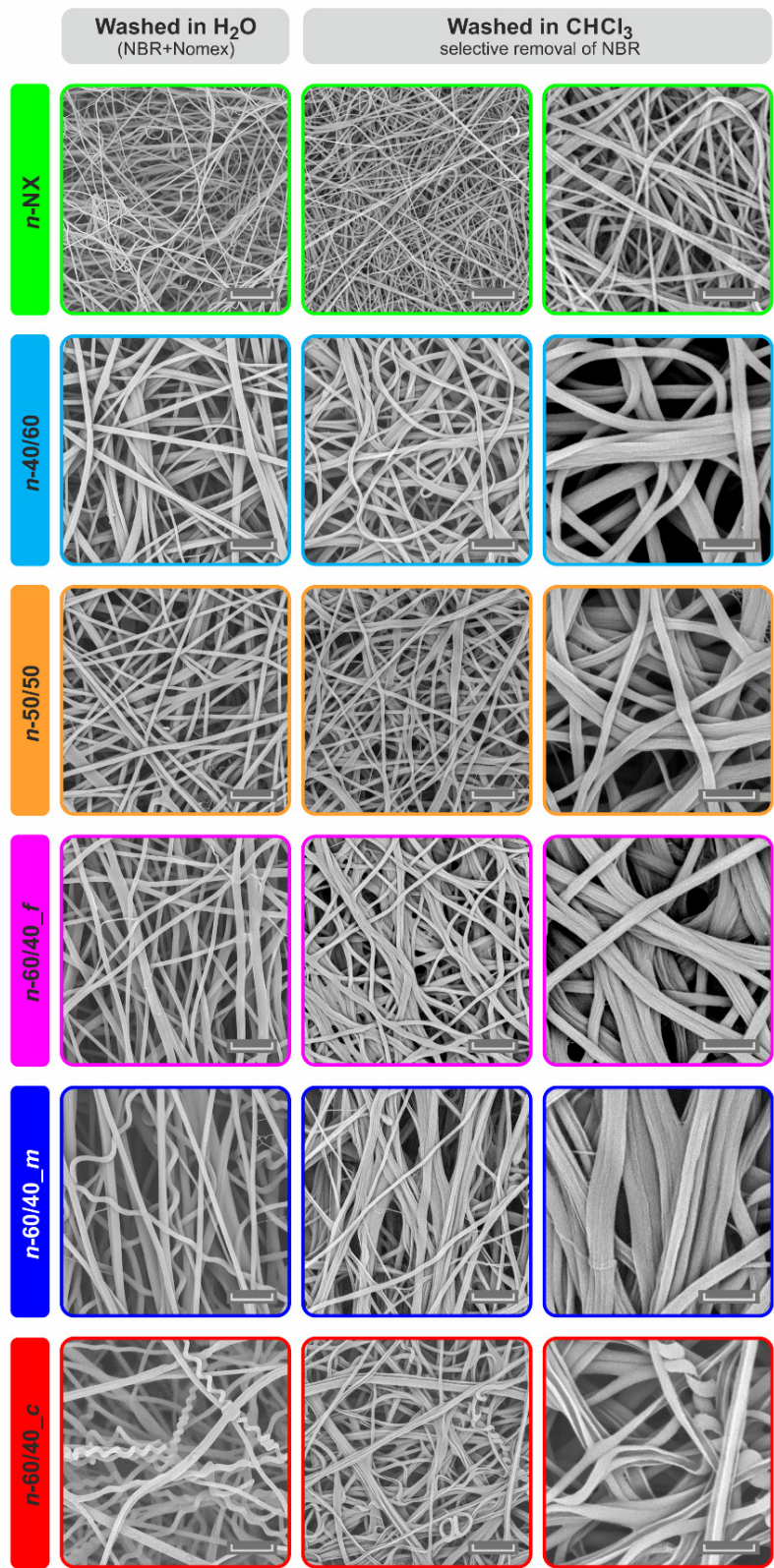
FIGURE 5.1 • SEM micrographs of produced nanofiber after washing in water for LiCl removal (1st column) and after chloroform to eliminate NBR (2nd and 3rd columns). 1st and 2nd columns 10,000×, scale bar 5 μm; 3rd column 30,000×, scale bar 2 μm.

As low as 0.20 mL/h flow rate gives a "fibrillated" nanofiber, where it is possible to distinguish a sort of ultra-low fiber bundle of Nomex in the inner, and the NBR fraction around it. When increasing the flow rate to 0.35 mL/h, the fibrillated morphology is not the unique present: a different one characterized by a completely different relative polymer fraction disposition occurs. This morphology resembles a *quasi* core-shell structure, with the NBR in the inner, and the Nomex in the outer (FIGURE 5.1). By setting a significantly higher flow rate of 1.10 mL/h, the so-called *quasi* core-shell morphology is the only present (FIGURE 5.1).

5.1.2 • Tensile test of nanofibrous mats

Mechanical behaviour of rubbery nonwovens, as well as Nomex nanofibrous mat, were investigated via tensile testing. Since the mechanism of action of these NBR/Nomex nanofibrous nonwovens against delamination should be a combination of both matrix toughening and "bridging effect", the evaluation of the mat mechanical resistance is relevant. While NBR, mixing with the epoxy, acts as resin toughner, Nomex maintains its original shape even after the curing cycle, providing a three-dimensional thread that helps to hamper microcracks formation and propagation [4]. The effectiveness of the so-called "bridging effect" should also be correlated to the mechanical properties of the nanostructured interleaf, leading to potentially higher reinforcement for increased mechanical performances, provided a good adhesion between epoxy resin and nano-reinforcement occurs.

In FIGURE 5.2A,B stress-strain curves representative of each sample are reported. The effect of rubber is clearly evident. All NBR/Nomex nonwovens display a ductile behaviour, with maximum strain in the 66-87% range (FIGURE 5.2C), while Nomex mat (*n*-NX) has a more fragile behaviour, characterised by a lower elongation capacity (ε_{max} = 31%). As expected, also the toughness is significantly higher for rubbery mats, which is from 1.7 to 2.7 times the *n*-NX (FIGURE 5.2D). The presence of the rubber component also affects the mats elastic modulus (FIGURE 5.2E), which results lower than the polyaramide nonwoven one (1219 ± 60 MPa). However, the mat stiffness does not appear to be sensitive to the actual rubber fraction present in the nanofibers, being the modulus in the 650-750 MPa range in much cases, at least in the investigated 40-60%wt NBR range. Only *n*-60/40_*c* represents an exception: its

Young's modulus (388 ± 64 MPa) is significantly lower than the other rubbery mats, suggesting an important role of the nanofibrous morphology on this aspect.
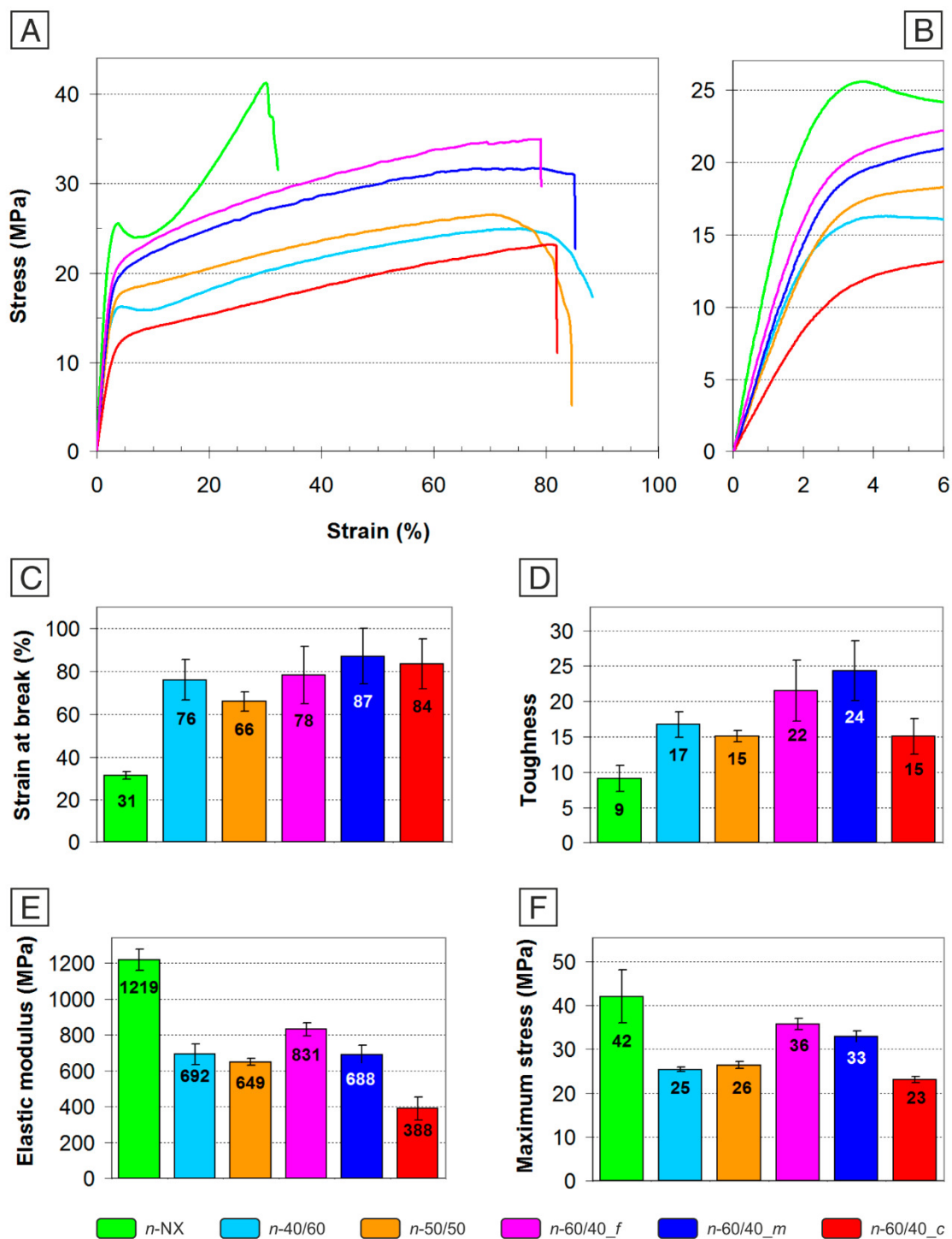

FIGURE 5.2 • Tensile test results: A) stress-strain curves of representative nanofibrous mats; B) enlargement of the 0-6% strain region; C) strain at break; D) toughness; E) elastic modulus evaluated as the slope of the linear regression in the 0-1% strain; F) maximum stress. Stress was calculated according to EQUATION 5.2.

A similar behaviour is found analysing the maximum stress, which is the highest for Nomex nanofibers (42 ± 6 MPa) and, again, quite similar for the blend ones, with the n-60/40_c showing the lowest value (23 ± 1 MPa, FIGURE 5.2F). It is worth pointing out that the found mechanical behaviours are highly reliable, given the application of the mass-based normalisation of load, which exclude errors eventually introduced by voids and mat thickness measurement (see CHAPTER 8).

5.1.3 • Mode I and Mode II interlaminar fracture toughness evaluation of nano-modified CFRPs

The interlaminar fracture resistance of CFRPs was assessed via Double Cantilever Beam (DCB) and End-Notched Flexure (ENF) tests, where the laminate is solicited in Mode I and Mode II loading modes, respectively. In the first case, the specimen beams are subjected to a perpendicular load with respect to the crack propagation plane, while in the second one a bending deformation is imposed to simulate the sliding of the two constituent beams. The calculated energy release rate (G), resulting from the delamination tests, can be associated to two different crack propagation stages: the initiation stage (G_C), in which the delamination onset starts from the artificial crack, and the propagation stage (G_R). The G_R was evaluated considering a crack length range between 48 and 80 mm of length for Mode I and 32-45 mm range for Mode II tests.

Representative load vs. displacement curves deriving from DCB tests are shown in FIGURE 5.3A. Laminates with interleaved blend nanomats present the same trend and slope of the corresponding reference until the first force drop occurs, but the crack initiation is postponed and the maximum force raised (up to +60%). On the contrary, 100% Nomex nanofibers clearly promote delamination phenomena, being the maximum force significantly lower than the reference (-27%), besides a *quasi*-continuous crack propagation, as highlighted by the load-displacement profile characterised by frequent and low-entity load drops. The presence of NBR seems to be able not only to counterbalance the lousy performance of Nomex nanofibers, but also to impart an overall positive action toward delamination.
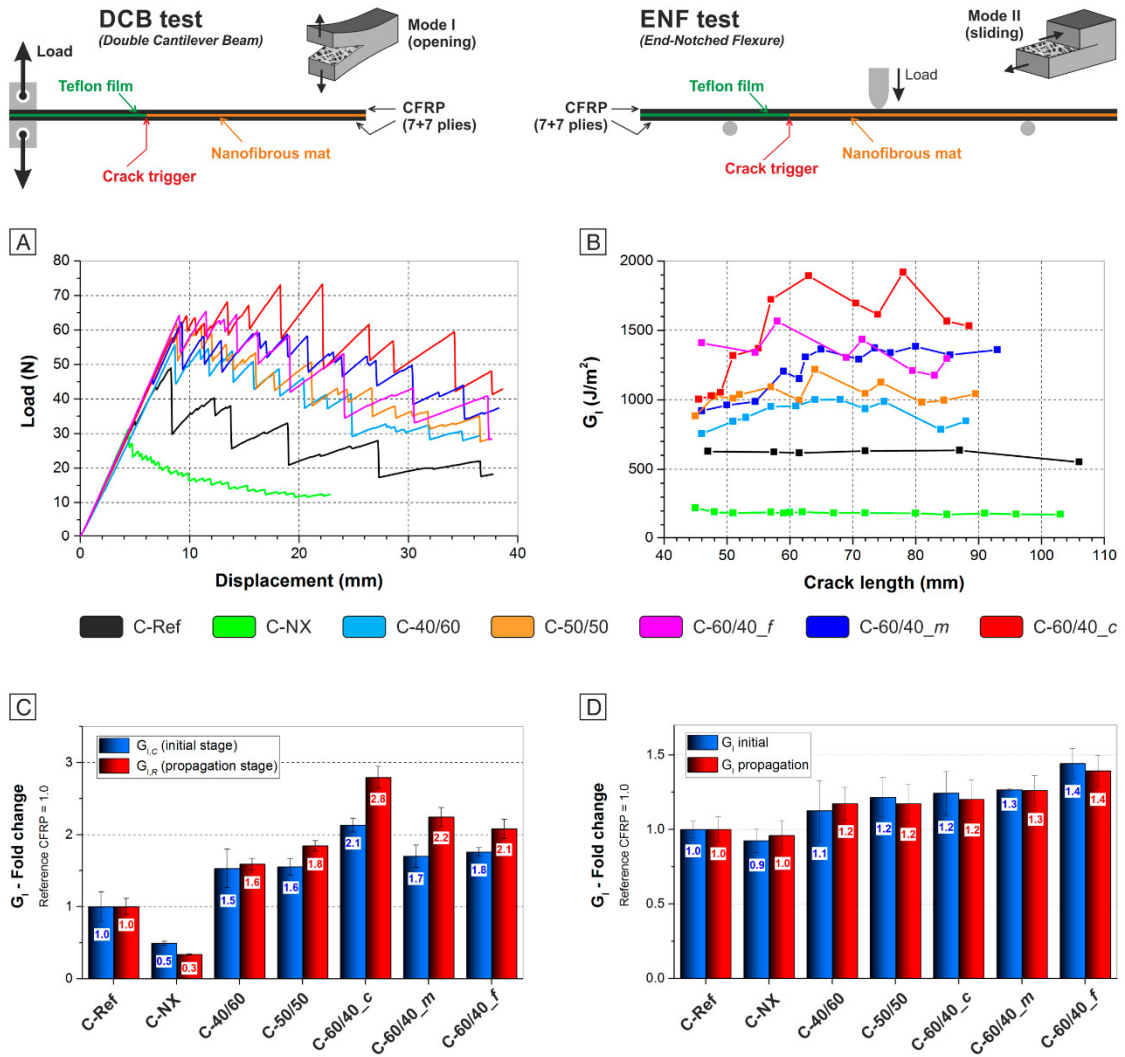
FIGURE 5.3 • DCB tests results: A) load-displacement curves; B) *R*-curves related to the same specimens displayed in A); C) average G_I fold change (for initial and propagation stages). D) ENF test results: G_{II} average fold change (initial and propagation stages). Bars in C) and D) are expressed as the relative variation of the value with respect to the reference sample (C-Ref), whose value is set as 1.0.

R-curves (fracture toughness vs. delamination length curves) calculated from the Mode I tests are shown in FIGURE 5.3B. As for the maximum load, G_I trends show a relevant ability of NBR/Nomex nanofibrous mats to hinder the delamination, being the energy required for the crack propagation significantly higher respect to the unmodified reference (up to +180%). A 40%wt of rubber in the nanofiber raises the G_I of 50-60%, both at initiation and propagation stages (C-40/60). Increasing the NBR content (C-50/50) leads to further enhancement of the $G_{I,R}$ (+84% respect C-Ref), while the $G_{I,C}$ is similar to the C-40/60 one (+55%). Moving to nanofibers with a prevalent rubber fraction (60%wt of NBR), the laminate toughening is even better, also showing a G dependence from the

nanofiber morphology. In particular, the mat constituted by *quasi* core-shell nanofibers (C-60/40_*c*) enables the best overall CFRP performance: +113% of $G_{I,C}$ and +179% of $G_{I,R}$ compared to unreinforced C-Ref. Instead, the other two morphologies (fibrillated nanofibers, mix of fibrillated and *quasi* core-shell nanofibers) have a quite similar impact toward delamination resistance, whose modified CFRPs (C-60/40_*f* and C-60/40_*m*) show an increase in both $G_{I,C}$ and $G_{I,R}$ in the range +70-75% and +108-124%, respectively.

Comparing these results with our previous nano-modified CFRPs with NBR/PCL nanofibrous mats, it appears evident that the enhancement is less strong (up to +180% vs. +480). However, as will be illustrated in SECTION 5.3.4, adding NBR/Nomex nanofibers do not cause any significant T_g lowering nor stiffness reduction of the laminate, as demonstrated by dynamic mechanical analysis.

Nomex nanofibrous mat worsens the overall delamination performance, lowering the interlaminar fracture toughness. A significant reduction of both $G_{I,C}$ (–51%) and $G_{I,R}$ (–67%) is observed, precluding the use of *meta*-aramidic nanofibers as epoxy composite tougheners, which act very similar to a bulk film with poor adhesion with the matrix. This bad result may be due to a lower epoxy resin crosslinking when present Nomex nanofibers (see SECTION 5.1.4 and REF. [5]) and to possible low interaction with the polyaramide.

5.1.4 • *Thermomechanical properties of nano-modified CFRPs*

The evaluation of the laminate thermomechanical properties is of paramount importance to thoroughly define the behaviour of the material, and consequently its application field. In fact, stiffness and/or T_g lowering represents a common drawback which can afflict laminates modified with a low mechanical and thermal properties material, like rubbery nanofibers. Also in our previous work, in the face of a relevant damping improvement (up to 9 times the reference), NBR/PCL nanofibers can significantly affect the laminate thermomechanical properties, particularly the T_g. Therefore, a careful evaluation of the nano-modification extent was suggested to meet the best compromise between damping and mechanical properties, as presented in SECTION 3.1.2 CHAPTER 3. In the present case, the dynamic mechanical analysis (DMA) reveals a very slight mat impact on the nano-modified composites (FIGURE 5.4 and TABLE 5.1).
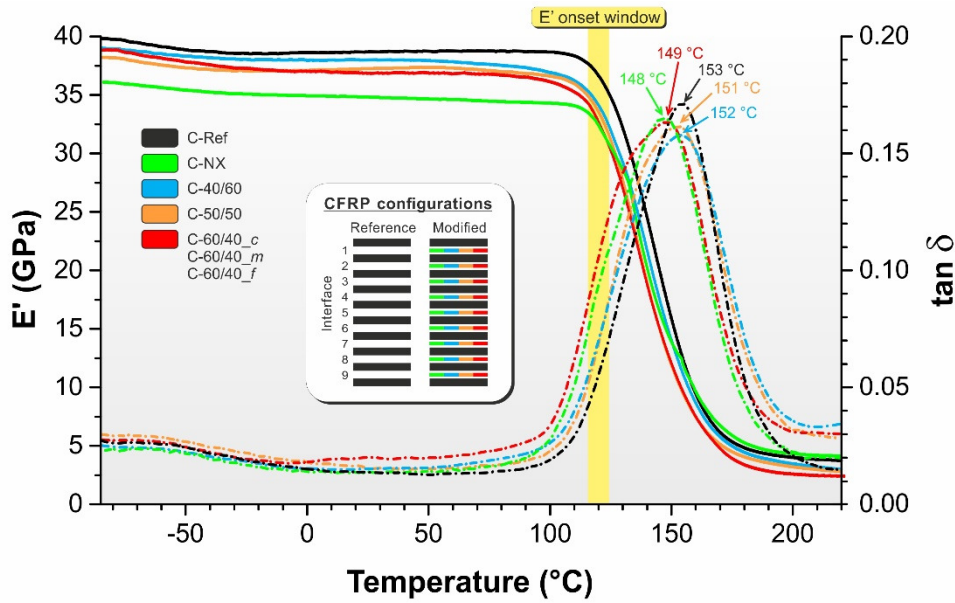
FIGURE 5.4 • E' (solid lines) and tanδ (dashed lines) representative curves of CFRP samples from –85 °C to 220 °C, heating rate 3.0 °C/min, 1 Hz. The inset graphic shows the CFRPs configurations tested by DMA. Only one curve for C-60/40_c, C-60/40_m and C-60/40_f is displayed for better clarity (all CFRPs modified with mats containing 60%wt of NBR behave in the same way).

TABLE 5.1 • Laminated CFRP tested via DMA and their thermomechanical properties

CFRP	Interleaved mat	E' @ 25 °C	E' onset	T_α
		GPa	°C	°C
C-Ref	—	39.7 ± 1.2	122 ± 1	153
C-NX	n-NX	35.2 ± 1.1	115 ± 1	148
C-40/60	n-40/60	38.5 ± 1.2	121 ± 1	152
C-50/50	n-50/50	37.3 ± 1.3	120 ± 1	151
C-60/40_c	n-60/40_c	37.5 ± 1.0	118 ± 2	149
C-60/40_m	n-60/40_m	36.8 ± 1.3	118 ± 2	149
C-60/40_f	n-60/40_f	37.1 ± 1.2	118 ± 1	150

Nomex nanofibers have a negative effect on the composite thermomechanical properties, causing the E' lowering at 25 °C from 39 GPa of unmodified CFRP to 35 GPa, without providing any improvement of the other tested mechanical properties. This happens even if the polyaramid is about 250 °C below its T_g; in this situation, no influence on CFRPs stiffness should take place, as happens with interleaved Nylon 66

nanofibrous mat (see SECTION 3.1.2 of CHAPTER 3). The behaviour found is probably ascribable to the polyaramide influence on the epoxy crosslinking kinetics, which is somehow hampered [5]; hypothesis also confirmed by the shift toward a lower temperature of the CFRP tanδ peak (148 °C vs 153 of the C-Ref).

All rubbery modified CFRPs, even with 60%wt of NBR, maintain almost all the composite original stiffness (E' below T_g of 37-38 GPa vs. 39 GPa of C-Ref), while the T_g evaluated at E' onset is only slightly lowered (–5 °C in the worst case of C-60/40_c). Therefore, the material maximum operating temperature stays practically unchanged, allowing the modified CFRPs to be used in the same application fields of the unmodified commercial CFRP. Laminate modified by NBR/PCL nanofibrous mats resulted highly sensitive to the rubber percentage in the nanofiber, causing an important lowering of the material T_g. In the case of NBR/Nomex blend nanofibers, the presence of the thermal resistant Nomex instead of the low-T_g ($\approx$ –60 °C) and low-T_m ($\approx$ 60 °C) PCL counterpart appears to be fundamental to the retention of CFRP thermomechanical properties.

The analysis of tanδ is useful for damping evaluation, since it accounts for the material ability to hamper vibration via energy dissipation. Tanδ values reveal about a +50% in the 20-100 °C temperature range for C-60/40, regardless of the particular nanofiber morphology. A small NBR content leads to lower effects. All the tanδ curves of rubber-modified CFRPs display a single relaxation associated to the glass transition, with a tanδ peak (T_α = 149-152 °C) very close to the C-Ref one (153°C). The relaxations display broader peaks due to the plasticizing effect caused by the nano-modification. Rubbery nanofibers add some plasticization thanks to the NBR fraction mixing with the resin, while in the case of pure Nomex nanofibers the plasticizing effect, even present, is probably due to the already mentioned influence on the epoxy crosslinking.

DMA demonstrates that the integration of NBR/Nomex nanofibrous mats does not reduce the laminate stiffness nor its T_g, which stay practically unchanged with respect to the unmodified CFRP. All the original laminate thermomechanical properties are maintained, with the benefitting of an excellent improvement of the interlaminar fracture toughness.

5.2 • MATERIALS AND METHODS

5.2.1 • Materials

Carboxylated nitrile butadiene rubber (NBR) Nipol 1072CGX was purchased from Zeon Chemicals [68%mol butadiene (Bu), 28%mol acrylonitrile (ACN), 4%mol methacrylic acid (MAA)].

Poly(*m*-phenylene isophtalamide) (PMIA, Nomex) and lithium chloride (LiCl), Sigma-Aldrich, were dried before use (in an oven at 110 °C for 3 and 24 h, respectively). *N,N*-dimethylacetamide (DMAc) and chloroform (CHCl₃) were purchased from Sigma-Aldrich and were used without any preliminary treatment. Plain weave carbon fabric (200 g/m²) in epoxy matrix (GG204P IMP503Z-HT) prepreg for composite lamination were supplied by G. Angeloni s.r.l. (Venezia, Italy).

5.2.2 • Solution/blends preparation, nanofibrous mats production and their characterization

NBR solution for blends preparation (*s*-NBR_*b*, 10%wt) was prepared in CHCl₃ (e.g. 1.0 g of polymer in 6.0 mL of solvent) under magnetic stirring at 50 °C heating for at least 4 hours until formation of homogeneous solutions.

Nomex solution for blends preparation (*s*-NX_*b*, 10%wt) was prepared in DMAc in presence of 3.5%wt of LiCl, calculated respect to the polyaramide fraction (e.g. 1.0 g of polymer, 0.35 g LiCl in 9.6 mL of solvent). The salt was dissolved in DMAc under magnetic stirring for at least 2 h at 80 °C before adding Nomex staples; then the mixture was stirred at maximum 80-90 °C until complete polymer dissolution.

Solution for plain Nomex electrospinning (*s*-NX, 10%wt) was prepared via dilution with CHCl₃ of a 14%wt Nomex solution, LiCl 3.5%wt, in DMAc (*s*-NX_*conc*, e.g. 1.4 g of polymer, 0.35 g LiCl in 14.5 mL of DMAc, then addition of 2.7 mL of CHCl₃). The concentrated Nomex solution was prepared as described above for *s*-NX_*b*. After CHCl₃ addition, the resulting mixture was stirred for at least 1 h before electrospinning. The *s*-NX solution was not directly prepared in the DMAc/CHCl₃ solvent system

because chloroform is a non-solvent for the polyaramide, thus its dissolution does not completely occur, with mostly polymer swelling.

Nitrile Butadiene Rubber/Nomex (NBR/Nomex) blends were prepared by mixing together *s*-NBR_*b* and *s*-NX_*b* solutions in different proportions (40, 50 and 60%wt of *s*-NBR_*b* solution). Polymer blends were stirred for minimum 2 h before electrospinning to ensure proper homogenization.

Blend nanofibrous mats are labelled as *n*-X/Y, where *n* stands for "nanofibrous mat", X and Y the percentage weight fraction of NBR and Nomex, respectively, in the nanofiber. In case of mats with 60%wt of NBR, the additional final letter indicates the nanofiber morphology: *quasi* core-shell nanofiber (*c*), fibrillated nanofiber (*f*), and a mix of the two morphologies (*m*). Details of solutions and blends composition are reported in TABLE 5.2.

TABLE 5.2 • Composition details of NBR, Nomex solution and of their blends.

Solution/Blend	Polymer concentration [a]	NBR content	LiCl [b]	Solvent system
	%wt	%wt	%wt	
S-NBR_*b*	10.0	10.0	–	$CHCl_3$
S-NX_*b*	10.0	–	2.5	DMAc
S-NX_*conc*	14.0	–	3.5	DMAc
S-NX	10.0	–	2.5	$CHCl_3$/DMAc 77:23wt (84:16v/v)
S-40/60	10.0	4.0	1.5	$CHCl_3$/DMAc 40:60wt (24:56v/v)
S-50/50	10.0	5.0	1.3	$CHCl_3$/DMAc 50:50wt (38:62v/v)
S-60/40	10.0	6.0	1	$CHCl_3$/DMAc 60:40wt (49:51v/v)

[a] in case of blend, the value represents the total polymer concentration

[b] LiCl content is calculated respect to the Nomex fraction

Nanofibrous mats were produced using a 4-needles electrospinning machine (Spinbow®) equipped with 5 mL syringes. Needles (internal diameter 0.51 mm, length 55 mm) were joined to syringes via teflon tubing. Nanofibers were collected on a 50 rpm rotating drum (tangential speed 0.39 m/s), covered with poly(ethylene)-coated paper. Mats have final dimensions of approximately 30 × 40 cm.

Electrospinning process and environmental parameters for mats production are reported in TABLE 5.3.

TABLE 5.3 • Electrospinning process parameters and nanofiber diameters of produced nanofibrous mats.

Nanofibrous mat	Electrospun solution/blend	NBR content in nanofiber	Flow rate	Electric potential	Distance	Electric field [a]	Temperature	Relative humidity
		%wt	mL/h	kV	cm	kV/cm	°C	%
n-NX	S-NX	0	0.25	18.0	8.5	2.1	24-25	29-33
n-40/60	S-40/60	40	0.80	22.0	8.0	2.8	24-25	30-34
n-50/50	S-50/50	50	0.25	18.0	8.5	2.1	24-26	28-31
n-60/40_*c*	S-60/40	60	1.10	25.0	11.0	2.3	22-24	32-34
n-60/40_*m*	S-60/40	60	0.35	24.0	17.5	1.4	23-25	32-34
n-60/40_*f*	S-60/40	60	0.20	25.0	17.5	1.4	23-25	31-33

[a] calculated as electric potential to distance ratio

Nanofibrous mats were analyzed by scanning electron microscopy (SEM, Phenom ProX) to determine nanofibers morphology. To investigate the NBR and Nomex disposition in the nanofiber, selective removal of the sole NBR fraction in the blend nanofibers was carried out via two consecutive washes in $CHCl_3$ (1 + 1 h) on a small piece of mat in a Petri dish, changing the solvent between each wash. All analyzed surfaces were gold coated in order to make them conductive.

DSC measurements were carried out on a TA Instruments Q2000 DSC Modulated apparatus equipped with RCS cooling system. NBR/NX nanofibrous mat samples (10 mg) were first heated to 100 °C for 15 minutes to remove humidity, then cooled down to –85 °C and then heated at 20 °C/min to 300 °C in nitrogen atmosphere. Nomex, both in staple and nanofiber form, was analyzed with the same conditions, except for the maximum temperature (375 °C), while NBR just heating from –85 to 200 °C. Tensile tests of nanofibrous mats were made using a Remet TC-10 testing machine equipped with a 100 N load cell, speed test 10 mm/min. Nanofibrous mat specimens for tensile testing (20 × 45 mm, width and gage length, respectively) were prepared as reported in SECTION 7.2.4 of CHAPTER 7). Tensile test data were normalised by means of a reliable method, which is based on specimen mass normalization of load instead of its section area according to the following equation:

$$\sigma = \rho \frac{F}{m} L \qquad \text{EQUATION 5.2}$$

where ρ is the material density (not the apparent membrane density), m is the specimen mass, L is the specimen initial length, F is the force and σ is the stress. In the present case, ρ has been evaluated as the weighted average value of the two pure polymeric components density, according to nanofiber specific composition. For each sample type at least 5 specimens have been tested. Detail about load normalization and data fitting model can be found in CHAPTER 8.

5.2.3 • CFRPs production and characterization

Nanofibrous mats were washed at room temperature in distilled water before their integration in CFRPs to remove LiCl salt. Mats were immersed twice in water for 10 + 10 minutes, changing water between each wash, and allowing their drying at room temperature. Effective salt removal was assessed via EDX (Energy Dispersive X-ray) analysis.

Specimens for the interlaminar fracture toughness evaluation (DCB and ENF tests) were prepared via hand lay-up, stacking 14 prepreg plies (GG204P IMP503Z-HT), interleaving a single nanofibrous mat in the central interface, and adding a Teflon film as a trigger for specimen delamination (see SECTION 3.2 of CHAPTER 3 for details). Reference panels without nanofibrous mat were also produced for the sake of comparison.

Specimens for DMA tests were produced stacking 10 plies of prepregs (refer to SECTION 3.2 of CHAPTER 3 for details). All the interfaces (except for the external ones) were nano-modified, for a total of 9 interleaved mats. An unmodified one was also produced as a reference.

Composite panels are labelled as C-Z, where C stands for "composite" and Z represents the composition of the abovementioned nanofibrous mat (X/Y, NX). The unmodified composite is labelled C-Ref. Uncured panels underwent a preliminary treatment of 2 h at 45 °C under vacuum for better nanofibers impregnation prior curing cycle in autoclave (2 h at 135 °C, under vacuum, 6 bar external pressure, heating/cooling ramp 2 °C/min).

Details of the laminates production and of CFRP panels/specimens dimensions are reported in SECTION 3.2 of CHAPTER 3. In TABLE 5.4 CFRPs produced are listed, as well as the grammage of the interleaved nanofibrous mats.

TABLE 5.4 • CFRP panels intended for DCB, ENF and DMA tests

| CFRP | Interleaved nanofibrous mat | |
	Mat label	NBR fraction
		%wt
C-Ref	—	—
C-NX	*n*-NX	0
C-40/60	*n*-40/60	40
C-50/50	*n*-50/50	50
C-60/40_*c*	*n*-60/40_*c*	60
C-60/40_*m*	*n*-60/40_*m*	60
C-60/40_*f*	*n*-60/40_*f*	60
C-60/40_*f*-2	*n*-60/40_*f*	60

DCB and ENF tests were carried out using a two-column hydraulic universal testing machine (Instron 8033) equipped with a 1 kN load cell. DCB specimens were tested at 3.0 mm/min crosshead separation rate, while ENF at 1.0 mm/min. At least 3 specimens for each CFRP sample/delamination mode were tested.

DCB tests were performed for evaluating the energy release rate for Mode I loading (G_I, in J/m^2), both at the initial and propagation stages ($G_{I,C}$ and $G_{I,R}$, respectively), using EQUATION 5.3 [6]:

$$G_I = \frac{3P\delta}{2ba}1000 \qquad \text{EQUATION 5.3}$$

where P is the load (in N), δ the crosshead displacement (in mm), a the crack length (in mm), b the specimen width (in mm).

ENF tests were carried out for evaluating the fracture toughness in Mode II loading (G_{II}, in J/m^2), both at the initial and propagation stages ($G_{II,C}$ and $G_{II,R}$, respectively), using EQUATION 5.4 [7]

$$G_{II} = \frac{9P\delta a^2}{2b(\frac{1}{4}L^3 + 3a^3)}1000 \qquad \text{EQUATION 5.4}$$

where P is the load (in N), δ the crosshead displacement (in mm), a the crack length (in mm), b the specimen width (in mm) and L the span length between supports (in mm).

Dynamic mechanical analysis (DMA, Netzsch DMA 242 E Artemis) was performed in three-point bending deformation mode, using a 40 mm fixed span support. DMA analyzes were carried out in the −85 +220 °C range at 3 °C/min heating rate, 1 Hz frequency, amplitude 20 µm, static force / dynamic force ratio = 1.5.

5.3 • CONCLUSIONS

The efficacy of rubbery nanofibers interleaving for improving delamination resistance of composites is confirmed. Solution blends made of Nitrile Butadiene Rubber (NBR) and the high-performance Nomex polyaramide were produced and successfully processed via single-needle electrospinning, after careful optimization of solution and process parameters. Dimensionally stable NBR/Nomex nanofibers with up to 60%wt of rubber were obtained and thoroughly characterized. The disposition of NBR and Nomex in the nanofiber was investigated via selective removal of the sole NBR fraction, revealing the formation of particular self-assembly structures that resembles core-shell nanofibers or fibrillated hierarchical structures. The imposed solution flow rate determines which of the very different morphology is obtained, making it easy to switch from one to another. Tensile tests of rubbery mats revealed a good improvement of both strain at break and toughness compared to Nomex one, and the retention of sufficient strength also when a 60%wt of NBR is present. Mode I and Mode II loading tests show a significant improvement of interlaminar fracture toughness, especially G_I (up to +180%). It was also established the use of pure Nomex nanofibers dramatically worsen the delamination resistance, with a G_I drop of 50-70%. While the integration of rubbery materials (particularly if not-crosslinked like in the present study) often causes a lowering of the laminate thermomechanical properties, this is not the case. Indeed, both original laminate stiffness and glass transition temperature (T_g) are maintained, paving the way to extensive and reliable use of such rubbery mats in composite laminates for improving delamination resistance without affecting other relevant properties.

5.4 • APPENDIX

5.4.1 • *Evaluation of the solubility parameters for NBR and Nomex and their miscibility*

TABLE 5.5 • Parameters for PMIA and NBR Hoftyzer and van Krevelen groups' contribution calculation

Group		V_i (cm³/mol)	F_{di} (J$^{1/2}$•cm$^{3/2}$•mol^{-1})	F_{pi} (J$^{1/2}$•cm$^{3/2}$•mol^{-1})	E_{hi} (J/mol)
Butadiene (n=0.68)					
-CH$_2$-	2x	15.55	270	0	0
=CH-	2x	13.18	200	0	0
Acrylonitrile (m=0.28)					
-CH$_2$-	1x	15.55	270	0	0
>CH-	1x	9.56	80	0	0
-CN	1x	23.1	430	1100	2500
Methacrylic Acid (l=0.04)					
-CH$_3$	1x	21.55	420	0	0
-CH$_2$-	1x	15.55	270	0	0
>C<	1x	3.56	-70	0	0
-COOH	1x	26.1	530	420	10000

Group		V_i (cm³/mol)	F_{di} (J$^{1/2}$•cm$^{3/2}$•mol^{-1})	F_{pi} (J$^{1/2}$•cm$^{3/2}$•mol^{-1})	E_{hi} (J/mol)
PMIA					
-C=O	2x	28.3	290	770	2000
-N-H	2x		160	210	3100
-CH$_{ar}$ (4x)	2x	13.42x4	1270	110	0
-C$_{ar}$ (2x)		7.42x2			

The Hansen solubility parameters obtained for the two polymers are finally reported in TABLE 5.6.

TABLE 5.6 • Hansen solubility parameters used for evaluation of NBR and PCL theoretical miscibility

	δ_d	δ_p	δ_h
NBR	13.2	10.6	4.5
PMIA	17.8	8.3	7.2

Values from TABLE 5.6 are used for the evaluation of the $\overline{\Delta\delta} = 5.8\text{MPa}^{1/2}$ according to EQUATION 5.1:

$$\overline{\Delta\delta} = \sqrt{(\delta_{dNomex} - \delta_{dNBR})^2 + \left(\delta_{pNomex} - \delta_{pNBR}\right)^2 + (\delta_{hNomex} - \delta_{hNBR})^2} \qquad \text{EQUATION 5.1}$$

References

[1]   D.W. Van Krevelen, K. Te Nijenhuis, Cohesive Properties and Solubility, in: Prop. Polym., 2009: pp. 189–227. https://doi.org/10.1016/b978-0-08-054819-7.00007-8.

[2]   P. Tipduangta, P. Belton, L.L. Fábián, L.Y. Wang, H. Tang, M. Eddleston, S. Qi, Electrospun Polymer Blend Nanofibers for Tunable Drug Delivery: The Role of Transformative Phase Separation on Controlling the Release Rate, Mol. Pharm. 13 (2016) 25–39. https://doi.org/10.1021/acs.molpharmaceut.5b00359.

[3]   L. Mazzocchetti, T. Benelli, E. Maccaferri, S. Merighi, J. Belcari, A. Zucchelli, L. Giorgini, Poly-m-aramid electrospun nanofibrous mats as high-performance flame retardants for carbon fiber reinforced composites, Compos. Part B Eng. 145 (2018) 252–260. https://doi.org/10.1016/j.compositesb.2018.03.036.

[4]   R. Palazzetti, A. Zucchelli, Electrospun nanofibers as reinforcement for composite laminates materials – A review, Compos. Struct. 182 (2017) 711–727. https://doi.org/10.1016/j.compstruct.2017.09.021.

[5]   S. Merighi, E. Maccaferri, J. Belcari, A. Zucchelli, T. Benelli, L. Giorgini, L. Mazzocchetti, Interaction between polyaramidic electrospun nanofibers and epoxy resin for composite materials reinforcement, 2017. https://doi.org/10.4028/www.scientific.net/KEM.748.39.

[6]   D5528-01 2001. Standard Test Method for Mode I Interlaminar Fracture Toughness of Unidirectional Fiber-Reinforced Polymer Matrix Composites, Am. Soc. Test. Mater. (2014) 1–13. https://doi.org/10.1520/D5528-13.2.

[7]   BS EN 6033:2015, BS EN 6034 : 2015 BSI Standards Publication Aerospace series — Carbon fibre reinforced plastics — Test method — Determination of interlaminar fracture toughness energy — Mode I —, BSI Stand. Publ. (2015) 14.

Chapter 6

Self-sensing hybrid composite laminate by piezoelectric nanofibers interleaving

One of the most critical aspects of composite materials is their vulnerability to impact loadings. In recent years, Structural Health Monitoring (SHM) systems have been developed to continuously watch over on the event of an impact and so monitor the health status of the structure. However, this technique needs the integration of sensors in the composite laminate, like Fiber Bragg Grating or piezoelectric ceramic transducers, which often can dramatically reduce the inherent strength of the hosting material.

In this chapter, the integration of a nanostructured piezoelectric sensor made by poly(vinylidenefluoride-trifluoroethylene) (PVDF-TrFE) nanofibers into a composite laminate with aluminium sheets as electrodes is proposed. Structurally, the resulting composite is a hybrid laminate consisting of aluminium sheets alternatively bonded to glass-fiber reinforced plastics (GFRP) prepreg layers and interleaved with PVDF-TrFE nanofibrous mats. Such lay-up belongs to a special class of hybrid laminates known as Glass Laminate Aluminum Reinforced Epoxy (GLARE), well known for its superior impact strength. Moreover, nanofibrous mat interleaving is a consolidated technique used to increase the delamination toughness and impact strength of composite laminates without affecting the overall stiffness. Hence, the resulting nanostructured hybrid laminate constitutes itself a piezoelectric sensor capable of detecting an impact load on its whole surface, with potentially superior impact resistance compared to pristine ones.

Non-destructive impact tests were performed using an instrumented drop-weight tower to investigate the real-time electrical response of the self-sensing laminate. A lumped electric model was applied to study and optimize the electrical circuit parameters. Then, the self-sensing laminate performance was evaluated in terms of linearity and spatial uniformity.

6.1 • RESULTS AND DISCUSSION

6.1.1 • Characterization of the embedded piezoelectric nanofibers

Morphology

The integration of the GLARE laminate with the piezoelectric nanofibrous mat was investigated by optical micrograph (FIGURE 6.1a) and SEM (FIGURE 6.1b,c) analyses of the cross-section.
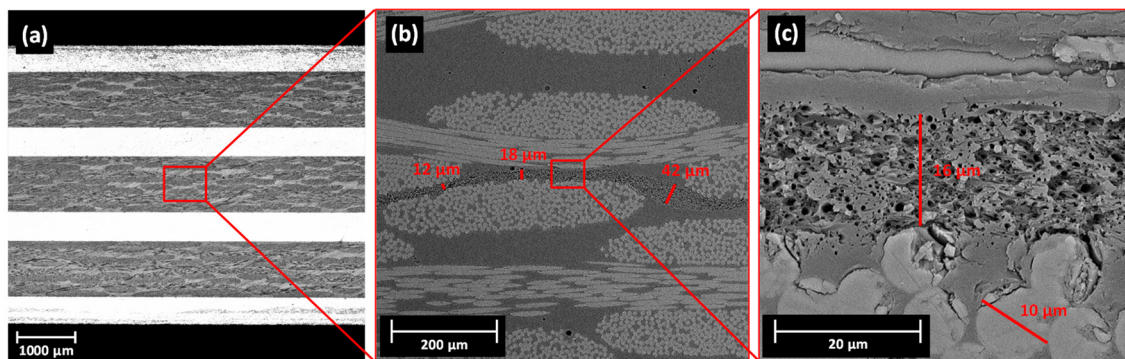

FIGURE 6.1 • Cross-section micrograph analysis of the piezoelectric nanofibrous mat integrated with GLARE laminate at different magnifications: (a) full laminate cross-section, (b) piezoelectric nanofibrous mat interlayer and (c) nanofibers.

In FIGURE 6.1a the resulting stacking sequence of the self-sensing laminate can be observed, with the aluminium sheets, appearing as the white layers, interspersed with GFRP woven plies. Focussing on the laminate mid-plane (see FIGURE 6.1b,c), the piezoelectric nanofibrous mat embedded in the epoxy matrix can be observed. It is worth noting that PVDF-TrFE was removed by flushing the laminate in acetone, to help pointing out the empty traces left by the nanofibers, that clearly stand out from the matrix in the SEM micrographs. FIGURE 6.1b clearly shows that the nanofibrous mat completely fills the matrix-rich interlayer between the upper and lower glass plies, by varying its thickness from 12 to 44 µm, to adapt to the weave of the fiberglass fabric. In the composite matrix, few voids can be observed, with a maximum diameter of 10 µm. However, their dimension did not compromise the poling process. Moreover, FIGURE 6.1c shows that the nanofibrous mat is completely impregnated and integrated with the epoxy matrix. Generally, it can be noted that the

contribution in volume and thickness of the piezoelectric nanofibrous mat on the GLARE laminate is negligible.

Crystallinity

While PVDF homopolymer has several polymorphs including four known chain conformations, with the most common crystalline phase that shows no significant piezoelectric behaviour, in PVDF-TrFE copolymer, on the contrary, the presence of the TrFE co-monomer helps the natural formation of the ferroelectric β crystalline phase, independently of the processing method [1,2]. The β-phase is, indeed, the one exhibiting the highest dipole moment and hence the most active piezoelectric phase. While the developed crystal phase (β-phase) is process-insensitive, the crystallinity degree χ_c and the average size of the crystallites, instead, may depend on the processing conditions, i.e. the cooling rate [3].
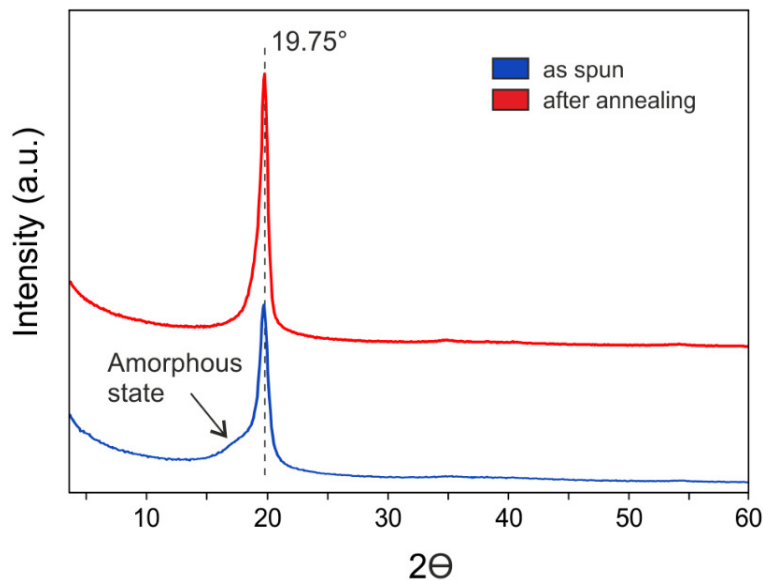
FIGURE 6.2 • WAXS diffractograms of PVDF-TrFE nanofibers: as-spun (blue) and after annealing at 150 °C for 1h (red) and cooling at 2 °C/min.

The Wide-angle X-ray scattering (WAXS) analysis was carried out in order to assess the actual crystal phase type and content in the obtained nanofibers: the diffraction pattern recorded for the "as-spun" PVDF-TrFE (blue curve, FIGURE 6.2) shows a reflection positioned at $2\Theta = 19.75°$, typical of sole electroactive β-phase crystal lattice [4]. Moreover, the as-spun nanofibers present a shoulder associated with a relevant

amorphous phase fraction. Indeed, the high evaporation rate occurring during the electrospinning process can act similarly to a high cooling rate for the polymeric melt (a similar shoulder is found in quenched PVDF-TrFE [4]). The annealing at 150 °C for 1h (red curve) significantly modifies the diffraction pattern of the nanofibrous membrane, with the crystal lattice 19.75° reflection that increases in intensity and definition and a contemporary reduction of the broad amorphous shoulder, denoting an improvement of the β-phase. The crystallinity degree, as calculated from the diffractograms deconvolution, also account for such an increase in β-phase content, with χ_c, that increases from 33% for as-spun nanofibers up to 52% for the annealed ones.

Note that the annealing conditions applied to the fibers are chosen to replicate the thermal condition at which the nanofibrous mat embedded in the composite are subjected during the curing cycle (see FIGURE 6.10). Therefore, it can be assumed that the nanofibers embedded in the self-sensing laminate present an enhanced β-phase compared to as spun ones.

6.1.2 • *Piezoelectric response to impact*

Shielding vs triboelectricity

During an impact, when the two colliding objects come into contact, a current flow may occur in between them. The current flow can be caused by the different electric potential between the two objects or the triboelectric charging generated by their friction [5]. This electric discharge, even if low, can interfere with the low voltage and high impedance piezoelectric signal. Moreover, the internal electrodes, due to the large area of the laminate, can behave as an antenna and collect the external electromagnetic interferences, thus disturbing the piezoelectric signal.

In the graphs of FIGURE 6.3 the laminate electric response (red curve) was compared to the contact force measured by the impactor load cell (blue curve). In the top row is shown the Reference laminate behaviour while in the bottom row the Piezo one, with the external electrodes floating (left column) and grounded (right column). Theoretically, the reference laminate (GLARE without nanofibers) should be electrically inert, however, in the floating configuration a signal is recorded when the two colliding objects come into contact, which could be erroneously attributed to the

contact force. Nevertheless, the signal does not fit the contact force curve and its shape, magnitude and sign were noticed to be random for multiple impacts with similar conditions. When the two external electrodes are grounded, instead, the signal is reduced by 3 orders of magnitude. This proves that the signal is generated by electrical disturbs and the external electrodes can shield them. Regarding the self-sensing laminate (Piezo), when the external electrodes are floating the piezoelectric signal is remarkably disturbed by the similar magnitude external electric noise. Instead, when the external electrodes are grounded, the interference is shielded and the piezoelectric signal faithfully reproduces the contact force.
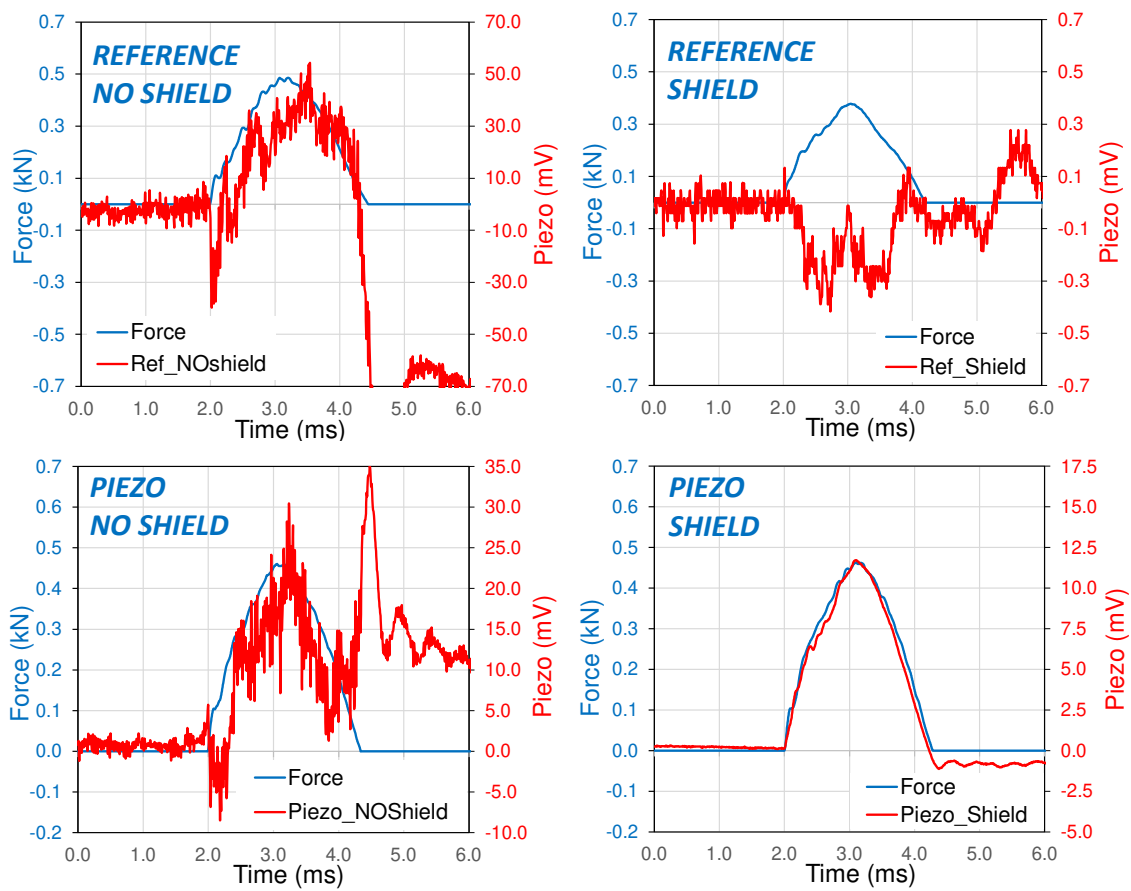

FIGURE 6.3 • Electric response (red curve) compared to the contact force measured by the impactor load cell (blue curve), for the Reference laminate (top row) and Piezo one (bottom row), with the external electrodes floating (left column) and grounded (right column) and a shunt resistance of 100 MΩ.

Signal proportionality vs shunt resistance

When the self-sensing laminate is subjected to impact, an electric charge proportional to the force magnitude is developed in the piezoelectric element (composed by the nanofibers embedded in the GFRP and the two aluminium electrodes) [6]. By virtue of the element capacitance this charge is stored in the element and is prevented from leaking away, by the high leakage resistance of the piezoelectric element. However, the impedance of the piezo element and the instrument amplifier input is not really infinite. Moreover, a shunt resistance is necessary to discharge the time accumulated electric charges, coming from ambient noise. Hence over time charges leak away and the piezoelectric signal loses its proportionality with the force magnitude.

In FIGURE 6.4 the piezoelectric response of the self-sensing laminate (continuous red curve) generated during impact is reported and compared to the contact force measured by the impactor commercial load cell (blue curve), for different shunt resistance values.
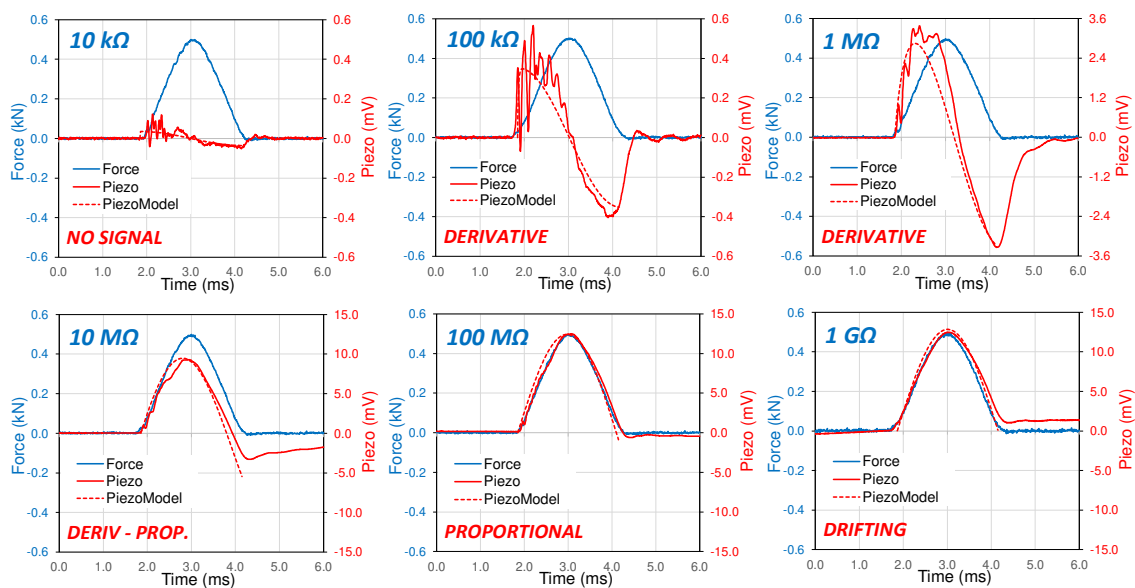
FIGURE 6.4 • Piezoelectric response of the self-sensing laminate (continuous red curve) compared to the contact force measured by the impactor load cell (blue curve) and the piezoelectric model estimated response (dotted red curve), for different shunt resistance values.

With 1 kΩ resistor the piezoelectric signal is too low to be distinguished from the electric noise. By raising the resistance to 100 kΩ and then to 1 MΩ, the piezoelectric signal magnitude increases and becomes detectable. However, the piezoelectric signal does not follow the contact force trend, while it seems to be more proportional to its

slope (time derivate). By further increasing the shunt resistance value from 1 MΩ to 1000 MΩ, the piezoelectric signal trend changes from semi-derivative to fully proportional, fitting better and better to the contact force curve. However, with a 1000 MΩ resistor the signal starts to drift (visible as a signal offset). Indeed, when the shunt resistance is too high, the electric charges coming from ambient noise cannot be dissipated. Therefore, a shunt resistance of 100 MΩ was chosen as the best compromise between signal proportionality and drifting.

6.1.3 • *Electric model for the impact response of the self-sensing laminate*

In FIGURE 6.5 is shown the equivalent electric circuit of the self-sensing laminate connected to the voltage amplifier.
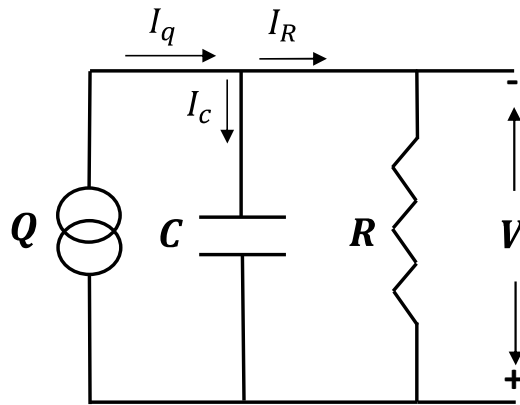
FIGURE 6.5 • Equivalent electric circuit of the self-sensing laminate connected to the voltage amplifier.

In the circuit, the piezoelectric element can be modelled as a charge source Q_p, in parallel with a capacitor C_p and a very high internal leakage resistance which can be neglected [7]. The cable capacitance C_c is in parallel with the sensor one, while the low cable resistance can be neglected. The shunt resistor R_s is connected in parallel to the circuit. The impedance of the amplifier is, instead, high enough to be neglected. Therefore, according to Kirchhoff's law, the equivalent capacitance C is the sum of the piezo and cable capacitances in parallel ($C = Cp + Cc$), while the equivalent resistance R can be reduced to the shunt resistance R_s. A capacitance of 182 pF and 19 pF was measured for the piezo element and the signal cable, respectively.

By applying Kirchhoff's laws and expressing the relationships of the electric components in complex form ($I_Q = dQ/dt = d_{33} \, dF/dt$; $I_C = V \, J\omega C$; $I_R = V/R$), the circuit equation can be simply written as:

$$V(t) = \frac{R}{j\omega RC + 1} \, d_{33} \frac{dF(t)}{dt} \qquad \text{EQUATION 6.1}$$

being the electric charges Q generated by the piezoelectric element proportional to the applied stress [6] and hence, in this case, to the impact force: $Q = d_{33}F$, with d_{33} the piezoelectric coefficient.

Under the assumption that non-linearities (indentation, membrane stiffness, damage) and mass of the laminate would be negligible, the impact can be modelled as a simple single degree of freedom spring-mass system [8], in which the impact force response is a half-sine wave: $F(t) = F \sin(\omega t)$, with $\omega = 2\pi/T$ and T equal to two times the impact duration.

Therefore, by solving EQUATION 1 in Laplace domain for a sine wave load and then anti transforming it back to the time domain, the piezoelectric voltage output for an impact load can be expressed as:

$$V(t) = \frac{Fd_{33}\omega R}{\omega^2 R^2 C^2 + 1}\left(-e^{-\frac{t}{RC}} + \cos(\omega t) + \omega RC \sin(\omega t)\right) \qquad \text{EQUATION 6.2}$$

EQUATION 2 is composed of a transient component (exponential term) and a steady-state one (harmonic terms). It can be observed that for high time constant values ($\tau = RC$) compared to the impact time duration ($\omega = 2\pi/T$), the transient term and the first steady-state one can be neglected and the expression can be reduced to:

$$V(t) = \frac{F \, d_{33}}{C} \sin(\omega t) \qquad \text{EQUATION 6.3}$$

EQUATION 3 shows that for high time constant values compared to the impact time duration, the piezoelectric voltage output becomes proportional to the contact force, confirming what was qualitatively observed in the graphs of FIGURE 6.4. Moreover, the sensitivity (signal voltage / impact force ratio) of the self-sensing laminate results to be

proportional to the piezoelectric coefficient d_{33}, independent by the resistance and inversely proportional to the capacitance C.

The unknown d_{33} coefficient was derived from the impact test results depicted in FIGURE 6.4 for 100 MΩ resistance (high time constant value), by expressing EQUATION 3 as a function of it. An equivalent piezoelectric coefficient of $5.12 \cdot 10^{-3}$ pC/N was so obtained for the self-sensing laminate, which is 3 orders of magnitude lower than the one reported by the supplier for the pure PVDF-TrFE (22 pC/N). The remarkably lower value may be attributed to the piezoelectric nanofibers integration into the composite (see FIGURE 6.1). In fact, being the laminate remarkably stiffer than the PVDF-TrFE polymer, the impact load directly transferred to the nanofibers is reduced and thus the generated electric charges.

In the graphs of FIGURE 6.4 the piezoelectric voltage output estimated by the model (dotted red lines) for an impact duration of 2.35 ms, is compared to the experimental results (continuous red lines), for different shunt resistance values. As can be observed, the model curves have a similar trend to the experimental ones up to the impactor rebound because after that moment the impact force drop to zero, while the model hypothesized that the force after the initial transient continues as a steady state sine wave.
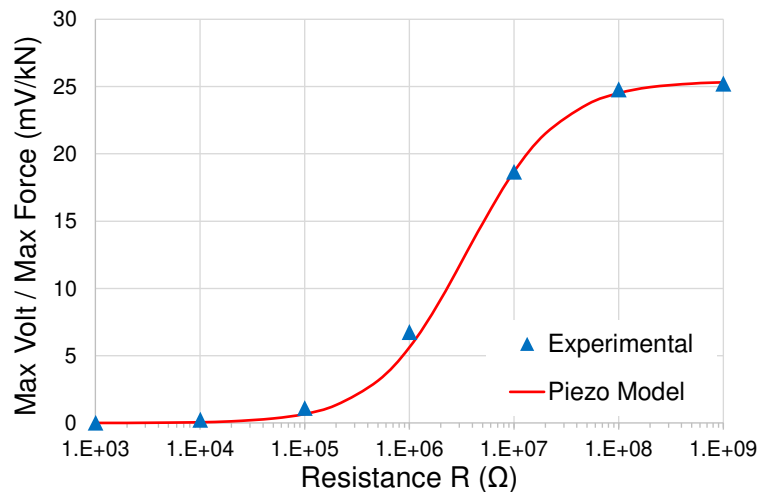

FIGURE 6.6 • Maximum output voltage – force ratio estimated by the electric model as function of the shunt resistance (red curve), compared to the ones obtained in the experimental tests of SECTION 6.1.2 (blue triangles).

In FIGURE 6.6 the blue triangles represent the ratio between maximum voltage generated by the self-sensing laminate and the maximum force recorded during impact, for different shunt resistance values (experimental tests of FIGURE 6.4), while the red curve is the ratio estimated by the piezoelectric model. As can be observed, the model fits the experimental results with good approximation. Moreover, the experimental results confirm what observed for EQUATION 3, that for high time constant values the sensitivity becomes independent of the resistance value.

As previously mentioned, according to EQUATION 3, the sensitivity is inversely proportional to the capacitance and, being the capacitance proportional to the laminate area, the latter is limited by the signal-to-noise ratio. Considering a noise level of 0.1 mV of the measuring chain and a resolution target of 0.1 kN, the maximum allowable area of the self-sensing laminate is 0.25×0.25 m^2. Over this value the electrodes, i.e. the internal aluminium sheets, have to be separated and the signals acquired independently. The multiple signals can be then conveyed to a common spot by cutting the internal aluminium sheets, mimicking the tracks of a PCB board. Moreover, the electrodes subdivision may be exploited for impact localization.

Sensor performance: linearity and spatial uniformity

Electrical performances of the self-sensing laminate were evaluated in terms of linearity (piezoelectric signal versus impact force) and spatial uniformity (sensor sensitivity versus impact position).

The sensor linearity has been evaluated by recording the piezoelectric voltage peak and contact force peak for impacts performed at different magnitude levels. Results are reported in the scatter plot of FIGURE 6.7 and interpolated with a linear regression model with 95% of probability confidence bands computed using the likelihood method as reported in ASTM E739.

The sensitivity of the self-sensing laminate turns out to be 25.2 ± 1.7 mV/kN with a coefficient of determination R^2 equal to 0.999. It must be mentioned that the observed remarkable linearity (R^2) is quite common in piezoelectric sensors and also in a wide force range. The detected lower limit of the sensor sensitivity was of 0.05 kN and was attributed mostly to the inherent noise in the measurement chain (electrodes, cables and

amplification circuit). The measured sensitivity results to be adequate to detect an impact that can damage the composite, being generally in the kN scale. However, for the localization of the impact spot by triangulation, the sensitivity should be optimized (e.g., by varying the piezoelectric nanofibrous mat and GFRP thicknesses) in order to be able to detect elastic wave propagations into the laminate.
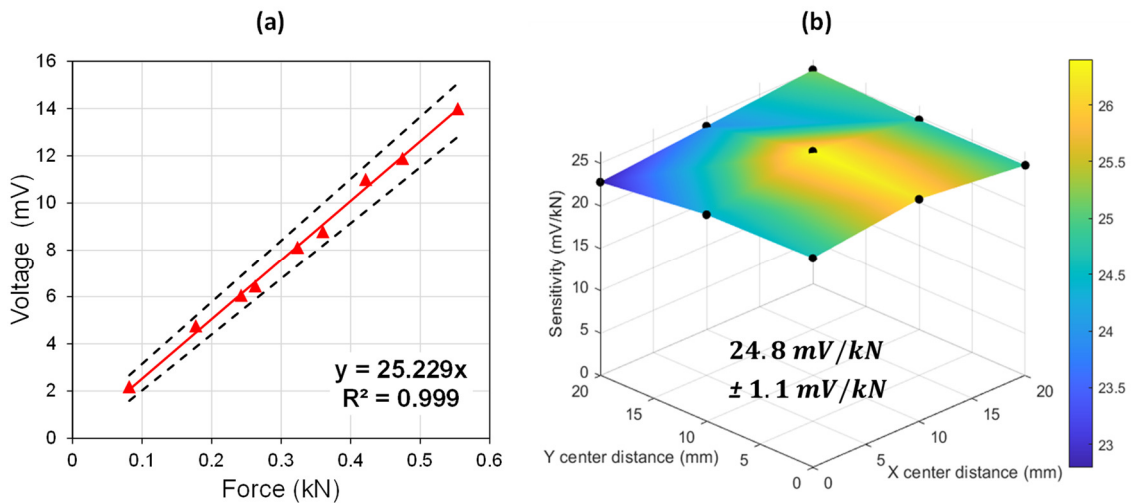

FIGURE 6.7 • (a) Sensor linearity: piezoelectric voltage peak versus contact force peak for impacts performed at different magnitude levels. (b) Spatial uniformity: sensitivity of the self-sensing laminate impacted at different points on its surface.

The self-sensing laminate should have the capability to detect an impact event on its whole surface for structural health monitoring purposes. Moreover, to provide a reliable response on the impact magnitude, and hence the consequent damage, the sensitivity should be as much homogeneous as possible on its surface. For this reason, the laminate was impacted with a magnitude of 0.5 kN at different points on its surface with a grid pattern of 3 × 3, 10 mm step between each point and origin in the laminate center. The measured sensitivity for each impact point is reported in the three-dimensional scatter plot of FIGURE 6.7b. The calculated sensitivity has a confidence interval of ± 1.1 mV/kN with 95% confidence level, which corresponds to a relative error of ± 4.6% and should be acceptable for structural health monitoring purposes. The measured relative error can be considered representative for larger laminates because the grid tested area is bigger than the unit dimensions of the glass fiber fabric texture and nanofibrous one.

By performing low-velocity impact tests, damage evolution can be experimentally correlated to the maximum impact force and therefore to the linear piezoelectric response of the self-sensing laminate. Hence, the SHM system can be alerted when the piezoelectric signal overcomes a certain threshold value [9,10].

6.2 • MATERIALS AND METHODS

6.2.1 • *Fabrication process of the self-sensing laminate*

Piezoelectric polymer and electrospinning

The piezoelectric nanofibrous non-woven mat was fabricated by electrospinning method (FIGURE 6.8a) and nanofibers were made of PVDF-TrFE 70:30 %mol copolymer (Solvene® 300 EAP, courtesy of Solvay S.p.A. Milan). The copolymer shows a Curie temperature (T_c) of 103 °C and a melting temperature (T_m) of 145 °C, measured by Differential Scanning Calorimetry (DSC) analysis. As will be clarified afterwards, these specific thermal features are crucial both for the fabrication and poling of the piezoelectric composite laminate.

The copolymer was dissolved at 20 %wt in a mixture of 55:45wt of acetone (AC) and dimethylformamide (DMF). The non-woven nanofibrous mat was fabricated with a four-needle with drum collector electrospinning machine (Lab Unit, Spinbow®). Electrospinning process was carried out under the following optimized conditions: 0.8 ml/h flow rate per nozzle, 18 kV electric potential, 18 cm needle to collector distance, 0.2 m/s tangential speed, 20-24 °C temperature at 40÷50% of relativity humidity (RH). The process was carried out for 8 hours to obtain an A3 size randomly oriented nanofibrous mat. In FIGURE 6.8a,b Scanning Electron Microscope (SEM) micrographs of the cross-section and morphology of the nanofibrous mat so obtained are shown, respectively.
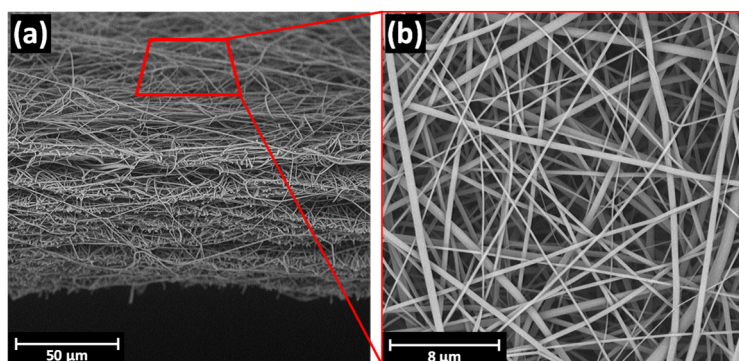

FIGURE 6.8 • SEM micrographs of the piezoelectric nanofibrous mat: (a) cross-section, (b) morphology.

The measured mat thickness was 50 μm (evaluated with a digital indicator having a measuring pressure of 100 g/cm^2), while the areal weight was 16 g/m^2. The average fiber diameter, evaluated on 100 different fibers, was 340 ± 120 nm. The electrospinning process was stable and it has the potential to be scaled up at industrial level (e.g. by needleless technology), reducing the fabrication time by one or two orders of magnitude [11].

Stacking sequence and curing

The self-sensing laminate is composed of thin layers of aluminium (Al 2024-T3, $60 \times 70 \times 0.5$ mm), interspersed with layers of woven Glass Fiber Reinforced Polymer (GFRP) prepreg (E-glass 8H Satin 300g/m^2 - epoxy matrix, VV300S - DT121H-34 DeltaPreg, $80 \times 90 \times {\sim}0.22$ mm) and the piezoelectric nanofibrous mat interleaved at the laminate midplane ($80 \times 90 \times {\sim}0.05$ mm). The resulting stacking sequence is $[Al_1/(GFRP\text{-}0°)_4/\ Al_1/(GFRP\text{-}0°)_2/Nano_1]_s$, as depicted in FIGURE 6.9.
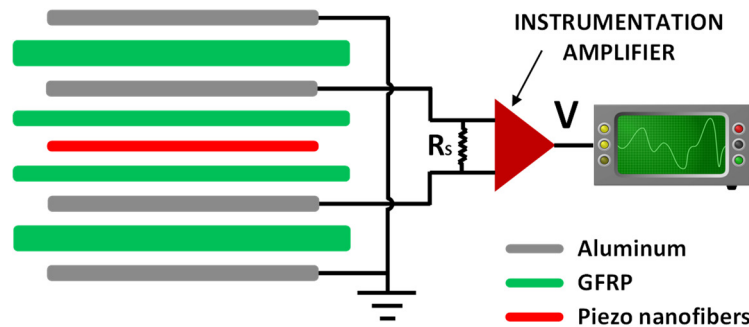
FIGURE 6.9 • Stacking sequence of the self-sensing GLARE laminate and electric connections.

The aluminium sheets, in addition to the structural function of increasing the impact resistance as occurs in standard GLARE laminates, have the electrical function of collecting the piezoelectric signal and shielding the sensor. For the sake of comparison, a laminate with the same stacking sequence of the self-sensing one (hereafter named Piezo) but lacking the nanofibrous mat (hereafter named Reference) was also fabricated.

Before stacking, the aluminium sheets were subjected to surface treatment by chemical etching in sulfuric acid/ferric sulfate solution (P-2 Etching according to ASTM D2651), to improve the adhesion with the epoxy matrix of the GFRP plies. Moreover, signal

cables (430-FST, Micro-Measurements), coated with a Teflon jacket, to withstand the high temperatures of the composite curing cycle, were soldered on the aluminium sheets with a Sn/Cu 97/3 soldering paste specific for aluminium (Flux SN35). If difficulties in placing the signal cable should arise, due to the needs of trimming and/or constraining the edges of the composite structure, the cables can be let to come out from the laminate surface by making a small incision on the prepreg and aluminium sheets at the laminate edge, as proposed in [12].

After stacking, both Piezo and Reference laminates were cured in autoclave with a vacuum bag pressure of -850 mbar and external pressure of 6 bar, using a custom 3 steps cure cycle (see graph of FIGURE 6.10) made up of: (i) a 30 min isotherm @ 50 °C, (ii) a 120 min isotherm @ 100 °C, and (iii) a 60 min isotherm @ 150 °C, with 2 °C/min heating and cooling ramps.
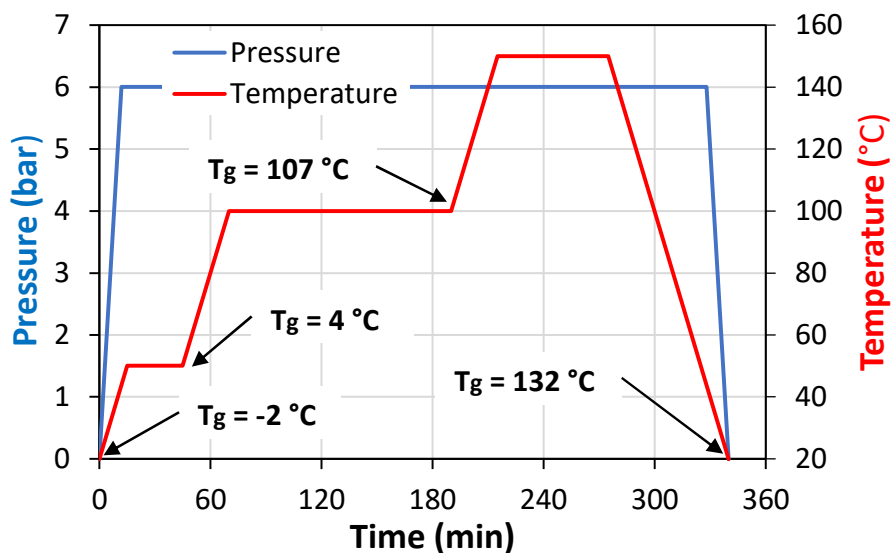
FIGURE 6.10 • Cure cycle of the self-sensing GLARE laminate.

Step (i) was introduced to promote the impregnation of the nanofibrous mat, by decreasing the viscosity of the epoxy resin without significantly triggering the cross-linking. The second step (ii) allows the gradual cross-linking of the epoxy matrix in mild conditions, trying to avoid exotherm-triggered temperature overshot that might outgrow the melting temperature of the polymeric nanofibers, thus helping to preserve their morphology. The third step (iii) completes the cross-linking of the epoxy resin and brings the glass transition temperature (T_g) over the Curie one (T_c). Despite the

step (iii) temperature is above the melting temperature of PVDF-TrFE, the nanofiber morphology is preserved because the surrounding epoxy matrix has already a sufficient cross-linking degree to act as a mold. Note that in FIGURE 6.10 the T_g reached by the resin at each step are also reported. The resulting final thickness of the cured laminate was 4.6 ± 0.05 mm.

Poling

Despite the ferroelectric nanofibrous mat could be self-polarized by the strong electric field employed in the electrospinning process [13] the preferential dipole orientation is lost during the subsequent curing of the composite laminate, which is carried out above the Curie temperature. Therefore, after curing, the self-sensing laminate with the embedded PVDF-TrFE nanofibrous mat was poled by applying an electric field of 6 kV/mm between the two inner electrodes (aluminium plies) at a temperature of 110 °C for 30 minutes and then cooling it down to room temperature at 2 °C/min, keeping the electric field on to stabilize the polar alignment. Finally, to remove any residual electrostatic charge induced by the electrospinning and poling processes, the laminate was left at 60 °C for 72 hours with short-circuited electrodes.

The polarization temperature of 110 °C was selected because is higher than the PVDF-TrFE Curie temperature ($T_c = 103$ °C), but at the same time lower than the glass transition temperature of the laminate epoxy matrix ($T_g = 132$ °C). Indeed, the mobility of the electric dipoles above Curie temperature increases and as a consequence they can be aligned by applying a significantly lower poling electric field than the one necessary at room temperature (150 kV/mm as suggested by the supplier), reducing the risk of electrical breakdown. At the same time, the poling temperature was kept lower than the T_g temperature, above which the electric permittivity of the epoxy matrix would rapidly decrease [14], with consequent increases of the conductivity and, in turn, risk of electrical breakdowns. Another critical aspect in the poling process is the presence of voids which can trigger electrical discharges. Indeed, in preliminary samples cured out of autoclave, poling was not possible due to electrical discharges caused by a high void content.

The poling step represents the most critical aspect in the fabrication of the self-sensing laminate because of the risk of electric breakdowns. However, if the poling temperature is kept between the Curie and Tg temperatures and composite voids are minimized (as

in this case by using prepreg and autoclave technology), the piezoelectric nanofibers can be successfully polarized.

Signal conditioning

As shown in the diagram of FIGURE 6.9, the electrical charges generated by the nanofibrous piezoelectric mat are collected by the two internal electrodes (aluminium sheets) of the laminate. At the same time, the two external aluminium plies of the laminates are connected to ground, to shield the sensor from triboelectric noise and external electromagnetic interferences.

The piezoelectric sensor, composed by the nanofiber embedded in the GFRP and the two aluminium electrodes, acts as a capacitor in parallel with a very high internal leakage resistance (thanks to the high permittivity of the GFRP). Therefore, the high impedance signal output of the piezoelectric sensor has to be converted by a pre-amplifier to a low impedance signal, suitable for the direct transmission to the acquisition system. The voltage amplifier is composed of an instrumentation amplifier (INA 118, Texas Instruments) with an impedance input of 10 GΩ and an interchangeable shunt resistor (varied from 1 kΩ to 1 GΩ) connected in parallel to the circuit, to tune the electric sensor response.

6.2.2 • Low-Velocity Impact test

Non-destructive low-velocity impact tests were performed to investigate and optimize the electrical response of the self-sensing laminate to impact. For this purpose, a drop-weight tower was employed, built according to the ASTM D7136 standard, as showed in FIGURE 6.11.

The impactor had a total mass of 1.3 kg and a 12.7 mm diameter hemispherical steel tip, instrumented with a piezoelectric commercial load cell (208C05, PCB Piezotronics). The laminate was placed on a plane with a 60 x 50 mm pit (smaller than the standard one) and clamped with two harmonic steel strips, to avoid rebounds. The signal generated by the self-sensing laminate and the contact force measured by the impactor load cell were synchronously acquired at 100 kHz by means of an ADC converter (NI cDAQ 9171 combined with NI 9215, National Instrument).
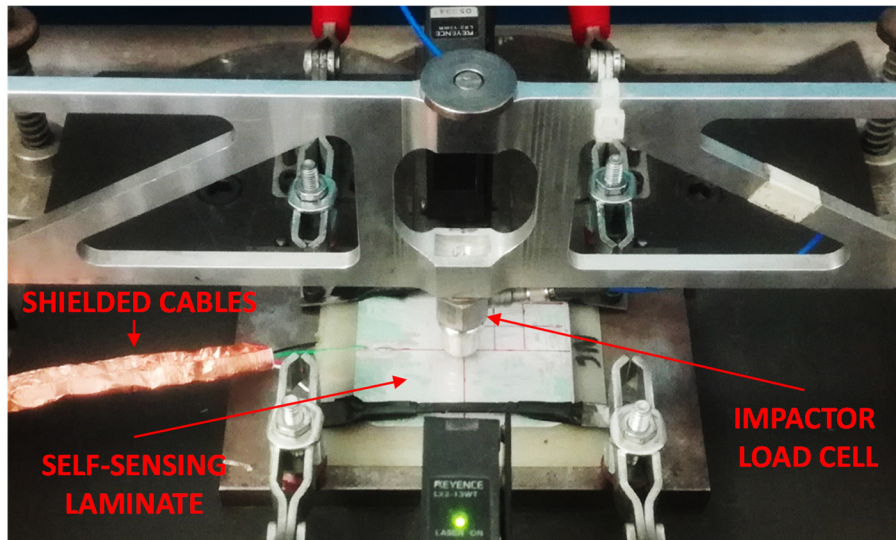
FIGURE 6.11 • Low velocity impact test set-up.

The electrical response of the laminate was investigated for different shunt resistances and with or without shielding. For this purpose, laminates were impacted multiple times, keeping the maximum impact force lower than 0.5 kN to avoid damaging the laminate.

6.3 • CONCLUSIONS

In this work, the integration of a nanostructured piezoelectric sensor, made of PVDF-TrFE nanofibers, into a composite laminate with aluminium sheets as electrodes has been achieved. Structurally, the resulting composite is a hybrid laminate known as Glass Laminate Aluminum Reinforced Epoxy (GLARE), consisting of aluminium sheets alternatively bonded to GFRP prepreg layers, functionalized with PVDF-TrFE interleaved nanofibrous mats. Such a nanostructured hybrid laminate becomes itself a piezoelectric sensor, capable of detecting on its whole surface an impact load. This concept overcomes the issues related to the mechanical performance reduction due to the embedding of an extrinsic commercial sensor, which acts as damage triggering. The self-sensing laminate stacking sequence was designed to reduce the triboelectric and ambient noise. Moreover, a simple and compact electronic circuit, based on an instrumentation amplifier and a shunt resistance, was realized for the conditioning of the piezoelectric signal.

Non-destructive impact tests were performed using an instrumented drop-weight tower to investigate the real-time electrical response of the self-sensing laminate. A lumped electric model was applied to study and optimize the electrical circuit parameters. The piezoelectric signal response was studied for different shunt resistance values, and an optimized resistance value was found as the best compromise between signal proportionality and drifting. The sensor linearity, defined as sensor signal versus impact force, is of 0.99. While the spatial uniformity response, i.e. the sensor sensitivity versus different impact positions, showed a relative error of 4.6%.

Future studies will focus on the evaluation of the impact strength of the self-sensing hybrid laminate functionalized by piezoelectric nanofibrous mat interleaving.

References

[1]   P. Martins, A.C. Lopes, S. Lanceros-Mendez, Electroactive phases of poly(vinylidene fluoride): Determination, processing and applications, Prog. Polym. Sci. (2014). https://doi.org/10.1016/j.progpolymsci.2013.07.006.

[2]   R.G. Kepler, R.A. Anderson, Ferroelectric polymers, Adv. Phys. (1992). https://doi.org/10.1080/00018739200101463.

[3]   E. Maccaferri, L. Mazzocchetti, T. Benelli, T.M. Brugo, A. Zucchelli, L. Giorgini, Rubbery nanofibers by co-electrospinning of almost immiscible NBR and PCL blends, Mater. Des. 186 (2020) 108210. https://doi.org/10.1016/j.matdes.2019.108210.

[4]   W. Xia, Z. Xu, Q. Zhang, Z. Zhang, Y. Chen, Dependence of dielectric, ferroelectric, and piezoelectric properties on crystalline properties of p(VDF-co-TrFE) copolymers, J. Polym. Sci. Part B Polym. Phys. (2012). https://doi.org/10.1002/polb.23125.

[5]   Z.L. Wang, A.C. Wang, On the origin of contact-electrification, Mater. Today. (2019). https://doi.org/10.1016/j.mattod.2019.05.016.

[6]   Piezoelectric sensorics: force, strain, pressure, acceleration and acoustic emission sensors, materials and amplifiers, Choice Rev. Online. (2002). https://doi.org/10.5860/choice.40-0924.

[7]   M. Serridge, T.R. Licht, Piezoelectric accelerometers and Vibration Preamplifiers - Theory and Application Handbook, Bruel & Kjaer, 1987.

[8]   S. Abrate, Impact on Composite Structures, 1998. https://doi.org/10.1017/cbo9780511574504.

[9]   H. Fu, Z. Sharif Khodaei, M.H.F. Aliabadi, An Event-Triggered Energy-Efficient Wireless Structural Health Monitoring System for Impact Detection in Composite Airframes, IEEE Internet Things J. (2019). https://doi.org/10.1109/JIOT.2018.2867722.

[10]   H. Fu, Z. Sharif Khodaei, M.H. Aliabadi, An energy efficient wireless module for on-board aircraft impact detection, in: 2019. https://doi.org/10.1117/12.2513534.

[11]   H. Niu, T. Lin, Fiber generators in needleless electrospinning, J. Nanomater. 2012 (2012). https://doi.org/10.1155/2012/725950.

[12]   T. Feng, D. Bekas, M.H. Ferri Aliabadi, Active health monitoring of thick composite structures by embedded and surface-mounted piezo diagnostic layer, Sensors (Switzerland). (2020). https://doi.org/10.3390/s20123410.

[13]   D. Mandal, S. Yoon, K.J. Kim, Origin of piezoelectricity in an electrospun poly(vinylidene fluoride-trifluoroethylene) nanofiber web-based nanogenerator and nano-pressure sensor, Macromol. Rapid Commun. (2011). https://doi.org/10.1002/marc.201100040.

[14]   W. Jilani, N. Mzabi, O. Gallot-Lavallée, N. Fourati, C. Zerrouki, R. Zerrouki, H. Guermazi, Dielectric relaxations investigation of a synthesized epoxy resin polymer, Eur. Phys. J. Plus. (2015). https://doi.org/10.1140/epjp/i2015-15076-6.

Chapter 7

Morphology, thermal, mechanical properties and ageing of Nylon 66/graphene nanofibers as Nano² materials

Nylon 66 nanofibers loaded with different graphene amounts were successfully produced with stable process and good fiber quality. Graphene addition is found to significantly affect diameter but not thermal behaviour of nanofibers. A new phenomenological model is applied for the interpretation of nanofibrous mat, trying to take into account the nanofibrous morphology. The model highlights a graphene contribution to mechanical properties that mainly affects the initial steps of deformation where fibers stretch, slide, twist and re-orient. Finally, the nanofibers were analysed after 20 months ageing, showing no significant alteration with respect to the pristine ones.

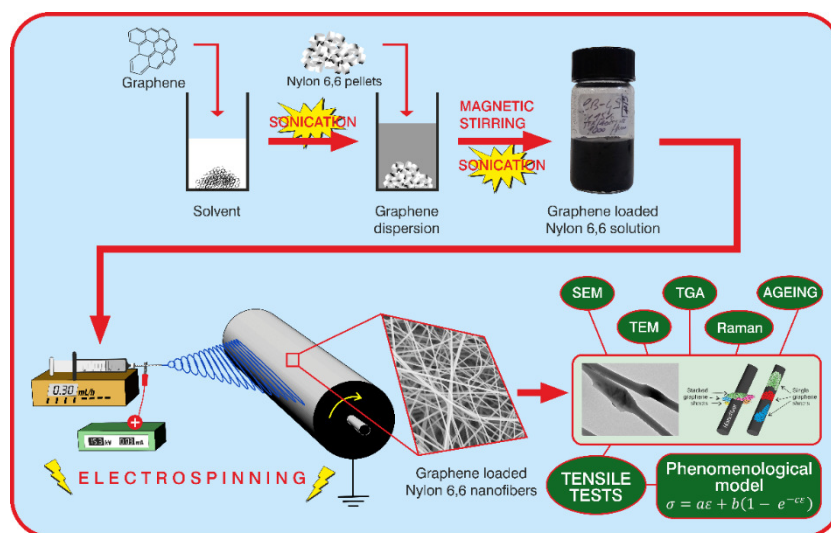In FIGURE 7.1 is depicted a sketch of the work rationale.

FIGURE 7.1 • Sketch of the paper rationale: preparation of Nylon 66 plus graphene solution to be electrospun and graphene nanoreinforced mat characterization.

7.1 • INTRODUCTION

Nanoscale reinforcements, such as nanofibers [1], nanoparticles [2] and carbon based nano-reinforcements [3,4], represent a versatile tool for modifying polymer and polymer composite properties. While carbon-based nano-additives may exploit different allotropic forms of C [5,6], Graphene and Related Materials (GRMs), i.e. Graphene (G), Graphene Oxide (GO) and reduced Graphene Oxide (rGO), where carbon atoms are prevalently arranged in two-dimensional monolayer of sp^2 hybridized carbon atoms positioned in a hexagonal lattice [4], are very promising candidates. Although the single graphene sheet is just a few angstrom thick, the bidimensional layer can easily extend up to hundreds of microns in width; however, it can be reduced to nanoscale dimensions, allowing the creation of the so-called graphene nanoplatelets (GNPs), useful in the preparation of nanocomposites with outstanding properties [7]. In this frame, two-dimensional substrates, not necessarily carbon-based, can also be modified in order to provide additional beneficial properties [5,6,8], without appreciable size and weight penalties [9]. GRMs can be thus effectively used to enhance the mechanical behaviour of polymers. In literature, several examples are reported, applying to the widest range of polymeric materials, with gain in both moduli and ultimate properties at break [10–14]. Moreover, thanks to their overall nano-dimensions, GRMs are even suitable for incorporation in polymeric nanofibers, thus creating nano-reinforced nanobjects (Nano^2) [15]. Polymeric nanofibers are technologically useful, low-cost, and high surface area materials successfully applied as filtration media, as drug delivery carriers, in tissue engineering as scaffolds for cell growth, they are highly sensitive sensor media and they are reinforcing elements in composites [16,17]. In most cases, nanofibers are themselves used as nano-reinforcements, and the addition of GRMs may be a convenient way to improve the nanofiber properties or to add peculiar properties to nanofibers [18]. It has been indeed proved that nanofibers can positively affect functional and mechanical properties of composites [19] and, when embedded in carbon fiber/epoxy resin composites, the interlaminar fracture toughness and delamination onset fatigue behaviour definitely increase, without a significant impact on the overall dimension of the final composite [16]. While the aspects of the reinforcing effect are still under debate, two main actions are envisaged: the bridging action of the

submicrometric filaments keeping together the diverging composites sections and the ability to deviate the crack path, thus enhancing the overall fracture propagation energy [1]. In the field of the delamination toughening, the mechanical performance of the nanofiber membrane plays a crucial role, and Nylon 66 (PA 66) presently represents a popular composite modifier, owing to its low cost, and high melting temperature allowing it to stay in the nanofibrous form during the curing step of many matrices [1]. The improvement of thermal and mechanical behaviour of PA 66 nanofibrous membranes with the use of GNPs looks, thus, an attractive perspective for application in composite delamination toughening and many other industrial fields such as, for example, filtration media. Nevertheless, it is recognized that evaluation of nanofibrous mats mechanical performances can be tricky, since mechanisms of deformation in nonwoven fabrics are based on both fibers and fiber-entanglements deformations [20], and a correct assessment can be hard to achieve. Indeed, while the greatest part of the literature has been focussed on the evaluation of the nanofibers functional properties, to the best of the Author's knowledge, only few works [21,22] investigate the mechanical properties of electrospun PA 66 nanofibers reinforced with plain GNPs. Among them, one reports 0.5, 1.0 and 1.5%wt of graphene addition leading to an improvement on both elongation at break and toughness (up to +73% and +50%, respectively), with a concomitant detrimental effect on either Young's modulus or tensile strength (up to −53% and −35%, respectively) of the mat. The second paper accounts for a continuously increasing storage modulus of the fibers with 0.1, 0.5 and 1.0%wt G content: however, in this case fibers are highly aligned and mechanical properties are evaluated only on the basis of DMA measurements; hence no ultimate tensile strength or elongation are investigated. Moreover, no literature at all was found regarding the behaviour of GRMs modified nanofibers upon ageing, in particular when the polymer matrix is crystallizable, such as PA 66. Hence, in the present work PA 66 nanofibers loaded with various amount of graphene are produced, and both thermal and mechanical properties are analysed. A broad range of graphene fractions, ranging from very low (500 ppm) to very high (15%wt) content, are considered and investigated. While in many cases graphene based nanocomposite nanofibers are produced thanks to surface modification of carbon nanotubes (CNTs), G or GO, to help the dispersion of the carbonaceous additive [23], one of the purposes of the present work is to provide a simple solvent system for dispersing both the polymer and the graphenic derivative

without chemical modification of the latter. In order to obtain graphene loaded electrospun membranes, a solvent system suitable for both suspending graphene and dissolving PA 66 is presented and, for the first time, used for electrospinning purposes. The produced nanofibers are then characterized to determine their morphological, thermal and mechanical properties, in order to provide a thorough overview of the obtained product. Moreover, the properties of the nanofibrous mats was investigated both as produced and after 20 months, with the aim of establishing the effects of the carbonaceous additive on the thermal and mechanical properties upon ageing. In this context, a mathematical model has been put forward, to provide help in understanding mechanical behaviour of the electrospun fibers. The model, used to fit the experimental data, would attempt at proposing an easy and simplified interpretation of the complex and multifaceted aspects affecting the mechanical response of a nanofibrous membrane.

7.2 • RESULTS AND DISCUSSION

7.2.1 • Graphene loaded solutions and electrospinning process

Electrospinning needs a homogeneous and process-compatible solution (e.g. acceptable viscosity, sufficient conductivity, adequate solvent system volatility) to be successfully carried out. Graphene loaded solutions, on the other side, require a good stability in terms of time, to guarantee that well exfoliated graphenic sheets do not reaggregate before being interleaved with polymer chains upon polymer solution mixing with GRM suspensions. Hence, the choice of a solvent system which would address both PA 66 solution and graphene suspension is a key factor in the production of high-quality nanofibers.

Formic acid and chloroform/formic acid mixtures are commonly used for dissolving PA 66 in preparation of solutions for electrospinning purposes [24–26]; TFE/formic acid is also a suitable solvent system [27]. A recent work [28] shows the use of TFA/acetone as a good and promising solvent system for the production via solvent casting of GNPs loaded PA 66 films that exhibit smooth surfaces and improved mechanical/electrical properties. Moreover, it is reported that the prepared solutions have good stability in terms of GNPs. suspension. Nevertheless, this solvent system has never been used in electrospinning process of PA 66 solutions.

In order to assess the stability of GNPs in different solvent media, several dispersions were produced using the same Nylon 66 provided by DuPont. Preliminary tests for graphene dispersion stability (1,000 ppm) were made in sonicator bath (type AC 14, Uniset), performing two sonication cycles (6 hours each, 15 hours rest period in between); solvents and solvent mixtures tested are reported in TABLE 7.1.

TABLE 7.1 • Graphene dispersions for stability tests in various solvents.

Dispersion	Graphene content	Solvent
DISP-1	1,000 ppm	TFE
DISP-2	1,000 ppm	TFE/formic acid 7:3 v:v
DISP-3	1,000 ppm	formic acid
DISP-4	1,000 ppm	chloroform
DISP-5	1,000 ppm	chloroform/formic acid 1:1 v:v
DISP-6	1,000 ppm	TFA/acetone 1:1 v:v

After 6 hours sonication they all appear well homogeneous, as showed in FIGURE 7.2A, with no visible differences between them. After 15 hours of rest (FIGURE 7.2B) it is evident the effect of dispersion media.
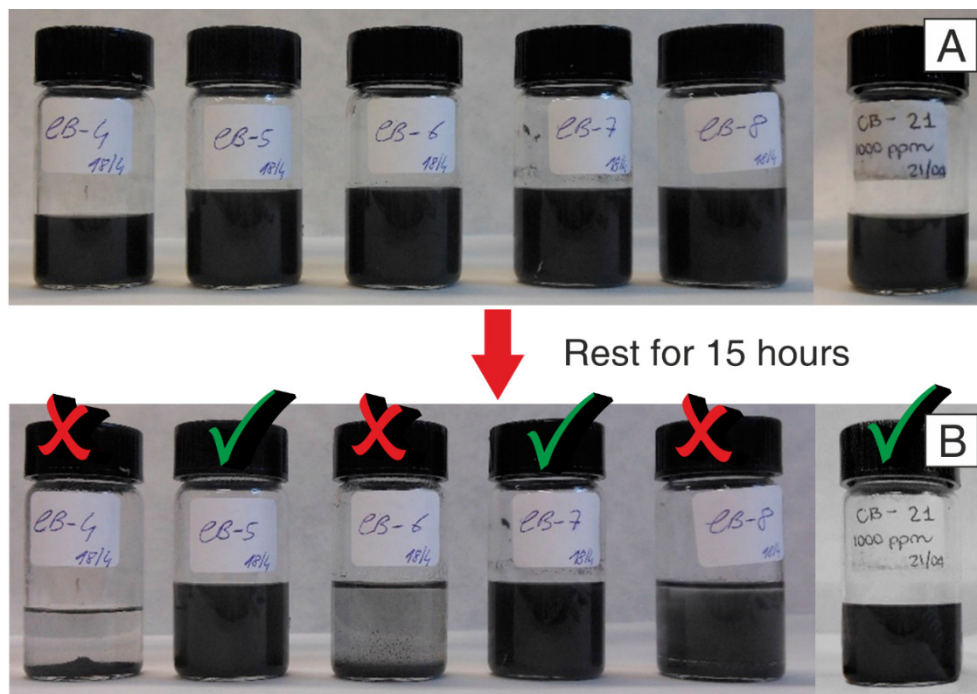

FIGURE 7.2 • Dispersions stability tests: (A) after 6 hours of sonication, (B) after 15 hours of rest. From left to right: DISP-1, DISP-2, DISP-3, DISP-4, DISP-5, DISP-6.

The most stable graphene dispersions are those based on TFE/formic acid (DISP-2), chloroform (DISP-4) and TFA/acetone (DISP-6), which are still perfectly dispersed after 15 hours. However, chloroform is not a good solvent for PA 66, and requires addition of formic acid for solubilizing the polymer; however, the mixture chloroform/formic acid shows poor stability in terms of graphene suspension. A second cycle of sonication (6 hours) does not improve the quality of dispersions.

Stable graphene loaded suspensions were obtained both using TFE/formic acid and TFA/acetone mixtures; hence, a first attempt at mixing them with a PA 66 solution of convenient concentration has been attempted using both solvents combinations. The process was carried out applying sonication in three subsequent steps for achieving the best dispersing action: sonication of plain graphene/solvent system in sonicator bath, followed by sonication with tip sonicator, and, finally, sonication of the complete polymer-containing solution. The first step is useful to provide a gross separation of the

graphene aggregates to make more effective the subsequent steps processed via tip sonicator. The intermediate step favours the graphene dispersion, since the highly efficient tip-sonication is more effective in a low viscosity medium than in a highly viscous one, like the polymer-containing solution. However, the presence of a viscoelastic material, like a polymer, may then positively affect the dispersing effect of sonication [29], acting as a surfactant and avoiding graphene sheets reaggregation. Thus, the final sonication step, occurring upon PA 66 solution addition, provides good overall homogeneity of the polymeric solution. A 15%wt PA 66 concentration represents a balanced choice in terms of viscosity, attained fiber diameters and processability when processing the solution via electrospinning. A lower concentration (10%wt) provides an insufficient viscosity, resulting in a less stable electrospinning process with solution drops that fall from the syringe needle provoking the formation of widespread holes in the mat, associated to a lower productivity owing to the lower polymer concentration and lower applicable flow rate (0.10 mL/h). By contrast, a concentration of 18%wt leads to the formation of fibers characterized by micrometric diameters. Solutions with higher concentrations tend to form a gel within few hours (FIGURE 7.3).

FIGURE 7.3 • Effect of the polymer concentration on the behaviour of solution with 1,000 ppm of graphene: 10%wt, stable solution (left); 20%wt, gel formation (right).

Upon different tests, TFA/acetone mixture was proven to lead to the best fibers quality (diameters down to 260 nm, high flow rate up to 0.70 mL/h, absence of beads) and improved electrospinning process stability over the time. Moreover, TFA/acetone 1:1 vol represents the best solvent ratio: indeed, an increase in the TFA fraction determines an undesired discontinuity in the electrospinning process, while its decrease hampers

polymer dissolution (a ratio 3:7 vol only induces the swelling of PA 66 pellet). The processing conditions should not be able to degrade the polymer; hence no modification of the starting molecular weight is expected. The presence of graphene does not affect significantly the solution electrospinnability, even at very high graphene concentrations. The electrospinning process is stable, without neither drops expulsion nor needle obstruction, and can be thus positively carried out, once the process parameter optimization has been tailored on the very specific solution characteristics (TABLE 7.5). The obtained nanofibrous mats, as reported in TABLE 7.5, will be labelled as NanoNY-XG, where X represents the weight fraction of graphene in the electrospun fibers.

7.2.2 • *Morphological and structural characterization of electrospun mats*

Electrospun nanofibrous mats were assessed via scanning electron microscopy to investigate the morphology and arrangement of the fibers. FIGURE 7.4 displays a panoramic micrograph of the overall membrane aspect, with magnification focussed on the fiber morphology of the different graphene containing formulations produced from the TFA/acetone 1:1 solution. It is clearly observed that fibers do not exhibit any evidence of macroscopic defects, showing instead regular and smooth surfaces. At the highest graphene load values, i.e. 8%wt and 15%wt, and to a smaller extent even at 5%wt and 2%wt, some protrusion can be detected along the fibers, whose presence, however, does not seem to interrupt the seamless fiber continuity. All nanofibers are obtained with a random arrangement, with no significant prevailing orientation neither morphologic defects like beads.
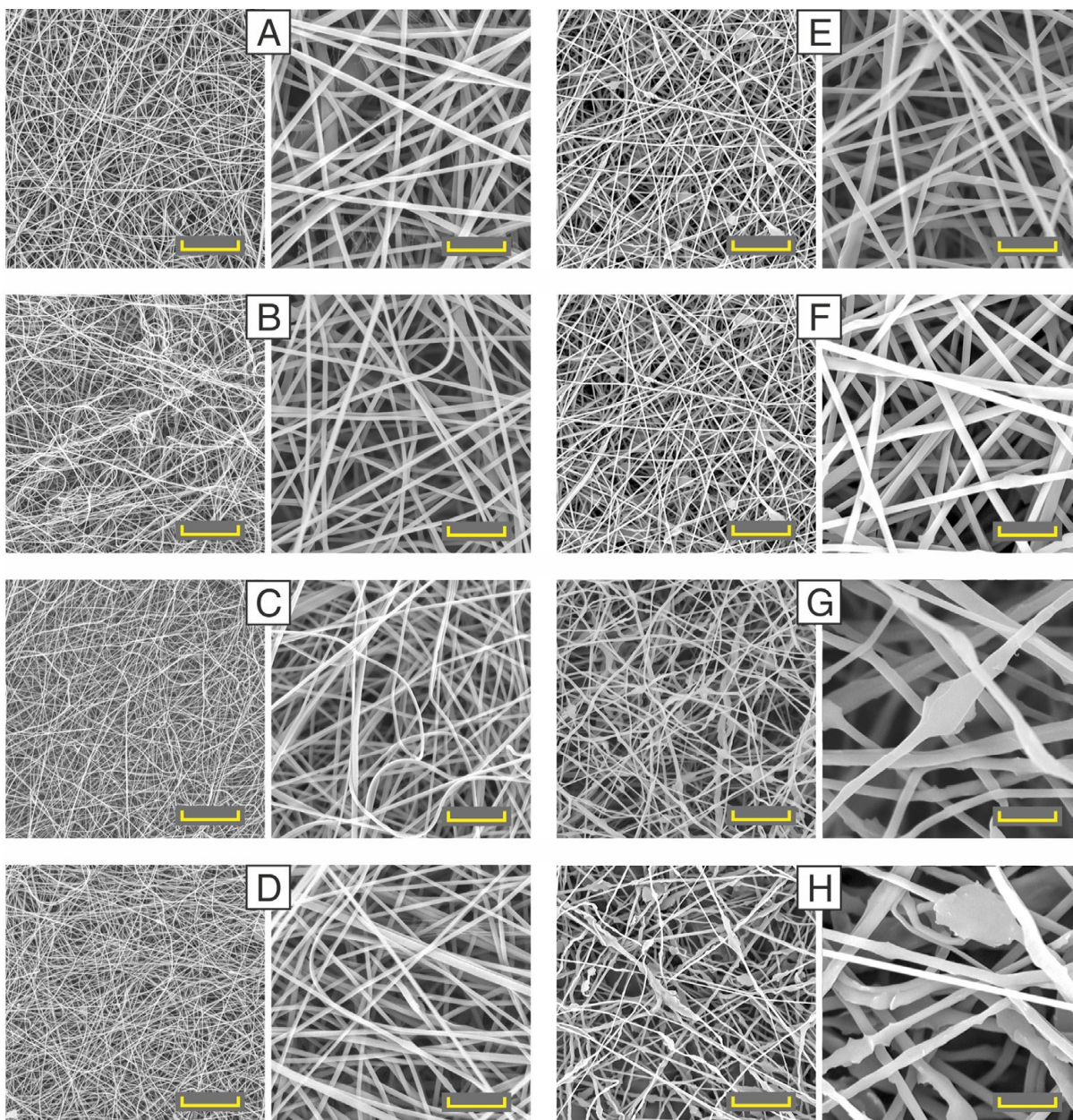
FIGURE 7.4 • Electrospun nanofibrous mats at different magnification, left 3,000×, right 15,000×: (A) NanoNY-0G, (B) NanoNY-0.05G, (C) NanoNY-0.1G, (D) NanoNY-1.5G, (E) NanoNY-2G, (F) NanoNY-5G, (G) NanoNY-8G, (H) NanoNY-15G. Scale bar: left (3,000×) 20 μm, right (15,000×) 4 μm.

While the average diameter of nanofibers stays well below the micrometre threshold, the presence of different graphene loads in the starting solutions affects the fibers thickness, particularly at low graphene fractions (FIGURE 7.5).
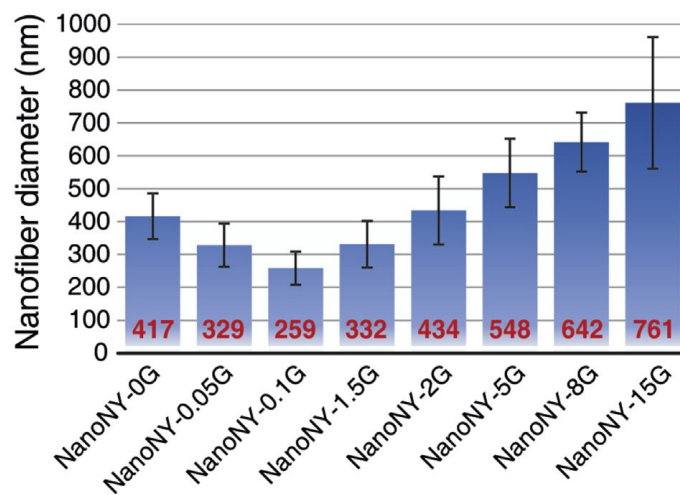
FIGURE 7.5 • Nanofiber diameters of produced mats.

A clear trend is observed, where a very small amount of graphene, up to 0.1%wt (1,000 ppm), determines a decrease in diameter which lowers the average value of about 40%; a further increase in G percentage causes, instead, the fibers average size to start increasing again, up to +80% with respect to plain PA 66; +190% with respect to the thinnest 1,000 ppm graphene containing fibers (NanoNY-0.1G). This behaviour could stem from the synthesis of two concomitant phenomena with contrasting effects, namely the raise of both solution conductivity and viscosity induced by the addition of G. Indeed, the first effect favours the stretching of the polymer jet, being the jet itself more sensitive to the electrostatic field; the second, contrarily, hinders the jet stretching, since the presence of G sheets favour chain mobility hindrance, hampering the ability of the single chain to untie and elongate. The trend showed in FIGURE 7.5 is therefore explained as such: up to 1,000 ppm of graphene content the raise in conductivity predominates the increment in viscosity, at 2%wt the two effects are perfectly counterbalanced with respect to the plain solution, while for higher G percentages the raise in viscosity is the prevailing result. Nanofibers with low amount of graphene (up to 1.5%wt) have very smooth surfaces; on the contrary, highly graphene loaded nanofibers have less smooth surfaces and the presence of graphene platelets protrusions is detected.

As already pointed out, in SEM images displayed in FIGURE 7.4, graphene sheets protrusions are clearly observed even at not so high magnification (15,000×), starting from nanofibers with 2%wt of nano-reinforcement (NanoNY-2G). As graphene content

increases, nanofibers with high graphene content (NanoNY-8G and NanoNY-15G) not only show lumps caused by the inclusion of wide graphene sheets, but also sudden changes in the single fiber direction linearity, a feature that uncommonly appears in electrospun fibrous membranes. While in principle, the average size distribution of graphene sheets should be the same for all the electrospun solutions, hence expecting thinner diameters to highlight such protruding graphenic sheets far more than thicker ones, this behaviour has not been observed at all up to NanoNY-1.5G. Accurate search of defects in samples up to 1.5%wt G content does not display evidence of defects along the fiber. A TEM investigation of such defects, reported in FIGURE 7.6 for NanoNY-5G and NanoNY-15G, highlights some interesting features. It is worth to point out that the average nanofiber thickness is almost beyond the threshold for electron transparency (200–300 nm), hence the investigation focussed on the thinnest fibers in the mat to allow for the detection of some internal morphology. In FIGURE 7.6A, the coupling in the same picture of two NanoNY-5G adjacent fibers highlights two significant behaviours: in the upper fiber, the darkening in the colour where the fiber slightly bends and displays some outer protrusion can be associated to some graphenic aggregates coalesced during the processing. This morphological aspect, however, accounts for an almost full inclusion of the carbon-based additive within the fiber boundaries.
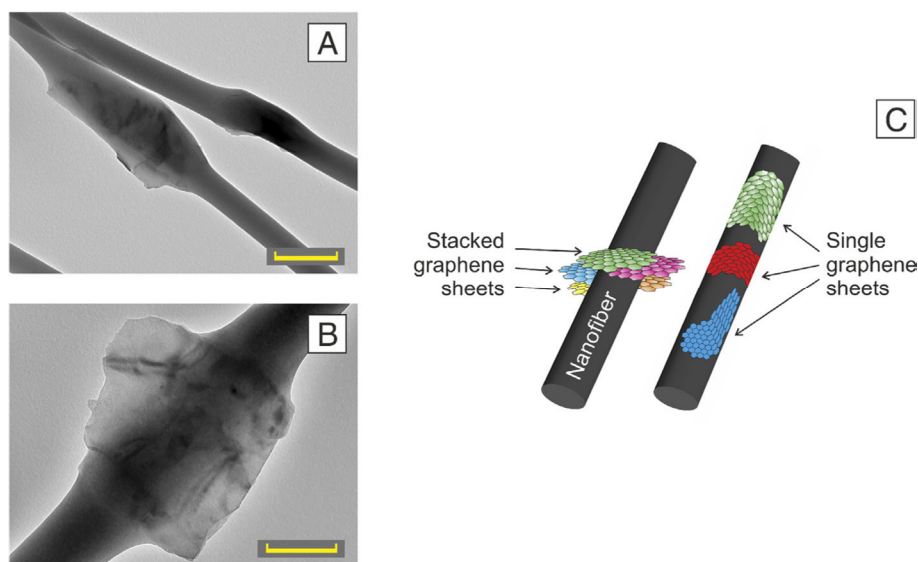

FIGURE 7.6 • TEM images of nanofibrous mats loaded with (A) 5%wt of G, scale bar 500 nm, and (B) 15%wt, scale bar 300 nm. (C) Sketch of graphene disposition along the nanofiber.

The lower fiber in FIGURE 7.6A displays, instead, a bigger lump characterized by wider external lips and by lighter shadows that seem to suggest the stacking of graphenic sheets with concomitant fiber thinning. This observation is confirmed in the TEM micrograph of NanoNY-15G (FIGURE 7.6B), where a clearly identifiable squared item protrudes out of the fiber, displaying some morphological feature accounting for G sheet stacking, with some wrinkles in the spread platelets. Such piled aggregates might stem from the very high G-concentration in the starting solution and they might be too rigid to bend and comply with the fiber morphology, as it happens, for example, in the upper fiber in FIGURE 7.6A.

The Raman spectrum recorded on the morphologically relevant protruding features (FIGURE 7.7) is indeed typical of multilayered graphenic sheets [30], with 2D band accounting for at least 5 layers stacking, together with a signal ascribed to the polymeric fiber component. It is worth to point out that Raman spectra recorded on fibers with G content lower than 1.5%wt display only bands typical of the polyamide fraction that reasonably envelops the carbonaceous additive within the fiber boundary (FIGURE 7.7).
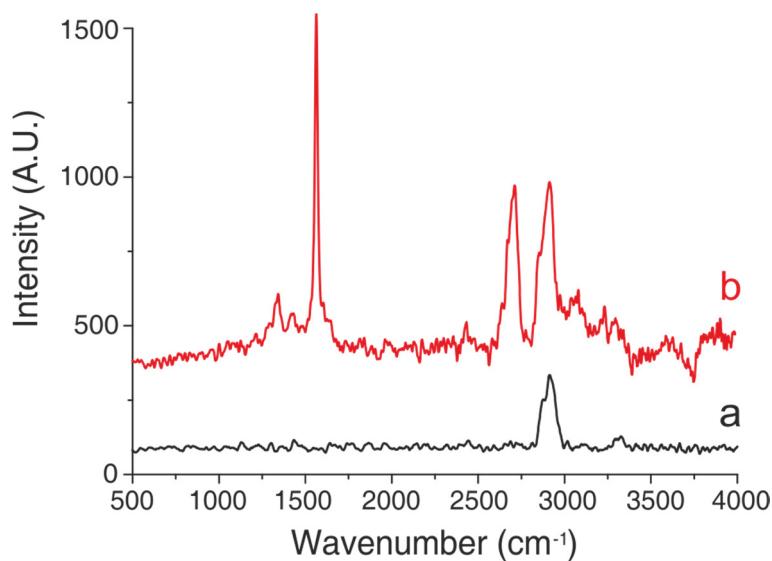

FIGURE 7.7 • Raman spectra of (A) NanoNY-0G, (B) NanoNY-15G.

7.2.3 • Thermal characterization of nanofibrous mats

The nanofibrous membranes were investigated via DSC, in order to assess the effect of the carbonaceous nano-additive on the thermal properties of the polymer (FIGURE 7.8).
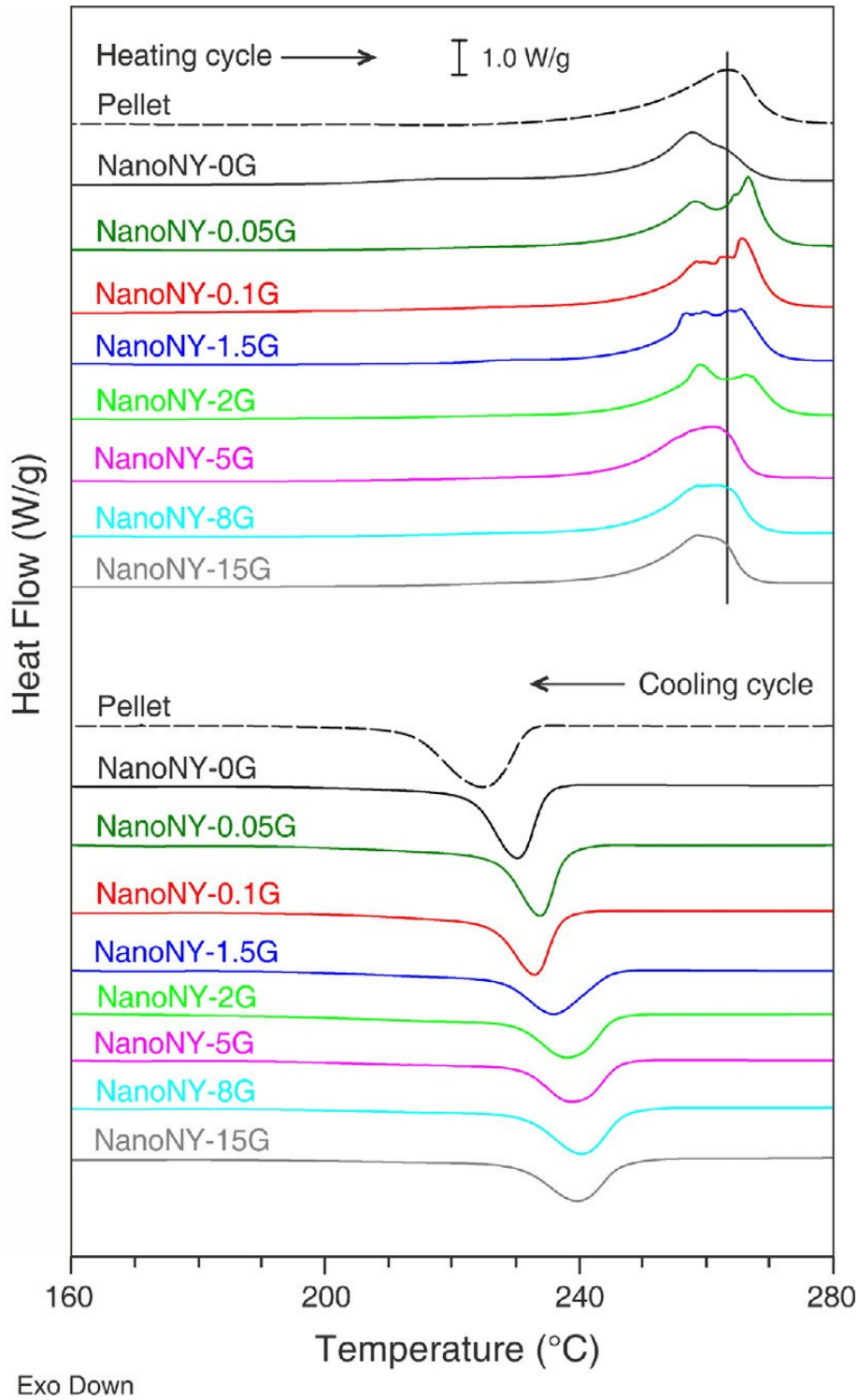

FIGURE 7.8 • DSC curves of NanoNY-X mats, heating and cooling scans.

All of the investigated samples display, during the first heating scan, an endothermic peak accounting for the melting of the semicrystalline polymer. It is clearly observed that the electrospun PA 66 shows a multiple endotherm centered at T lower than the pellet since, as expected, the processing conditions affect Nylon ability to crystallize with respect to the bulk pellet situation. This behaviour could be related to an average smaller size of the crystallites due to the processing conditions. It has been reported in the literature that molecular orientation and crystallinity of electrospun fibers can be strongly affected by many concomitant factors such as concentration, applied voltage, solvents, polymer molecular properties and others. It has been indeed proved that electrospun PA 66 nanofibers modify their crystallinity depending on the solvent used, (use of formic acid solution does not lead to any multiple endotherm [31], while chloroform/formic acid 50/50 partially does [32]) as well as on the nanofiber size [31]. This latter parameter is reported to affect also mechanical properties, which are strongly increased below a given diameter, that Baji *et al.* reported to be lower than 450 nm [31]. Such an effect onto mechanical behaviour however does not infer a concurrent increase in the polymer crystal phase content. In the present case, the average diameter of the obtained nanofiber is at the threshold for a strong contribution of the nanometric dimension of the fibers to the mechanical properties. The addition of graphene to the solution to be electrospun seems to slightly affect the high G-loaded nanofibers (above 2%wt G content in the nanofibers), which display a single melting endotherm, that is however located at a slightly lower T than the PA 66 pellet (FIGURE 7.8). On the contrary, for smaller ranges of graphene loads (below 2%wt G content in the nanofibers), the electrospinning process seems to highly affect the melting peak with respect to the behaviour of pelletized PA 66, either in the shape and/or in its maximum/maxima position. In particular, the presence of multiple peaks is observed in these cases, with appearance of a higher temperature peak with respect to the corresponding pellet and plain PA 66 (FIGURE 7.8). It is worth to point out that plain PA 66, with no graphene addition, does not display the peak splitting just upon electrospinning processing. The high T peak appearance, however, has been known for a long time in PA 66 fibers [33] and, even when observed in nanofibers, it is ascribed to the drawing process, where the applied conditions lead to a "more perfect planar zig-zag conformation in the extended chain crystal structures under the influence of applied tensile stress" as found by Gazzano *et al.* [32], ruling out any

difference in the crystal structure [34]. Under the latter assumption, for each sample it has been possible to evaluate the degree of crystallinity (χ_c) of nanofibrous mats according to the following equation:

$$\chi_c = \frac{\Delta H_m}{\Delta H_{m,100\%}} \cdot 100 \qquad \qquad \text{EQUATION 7.1}$$

where ΔH_m is the melting enthalpy of the sample, $\Delta H_{m,100\%}$ is the melting enthalpy of a hypothetical 100% crystalline PA 66 (196 J/g [35]). ΔH_m used for the calculation refers to the real content of polymer in the nanofiber, thus discarding the graphene presence which does not contribute to the PA 66 crystal melting.
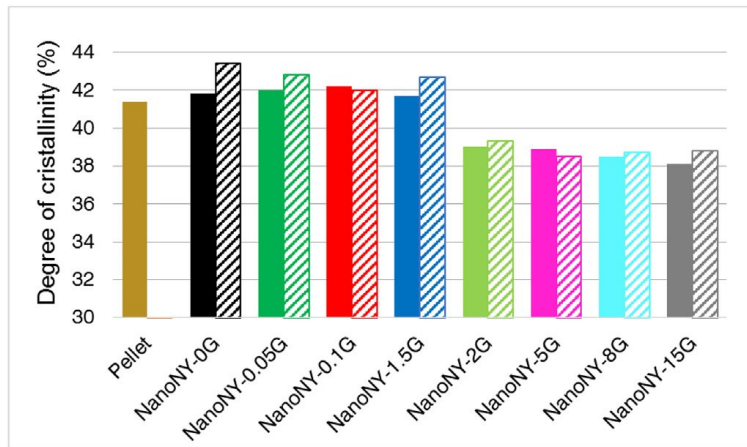

FIGURE 7.9 • Degree of crystallinity of PA 66 nanofibrous mats "As spun" (solid bars) and "Aged" (dashed bars) and comparison with PA 66 pellet. Data calculated from DSC curves.

Besides the previously discussed effects of the electrospinning process, thermograms in FIGURE 7.8 and data reported in FIGURE 7.9 display that a graphene content up to 1.5%wt does not affect significantly the nanofiber degree of crystallinity, which is similar to plain PA 66 nanofibers and pellets. A lower amount of G (NanoNY-0.05G) promotes the high T_m peak without a relevant effect on the overall amount of crystallinity. While it has been reported that G tends to act as a nucleant promoting polymer ability to crystallize, the electrospinning is known to slightly hamper the process. Concurrently, it has been reported that smaller diameter nanofibers have usually undergone higher draw ratio, which tends to hamper the formation of bigger and more perfect crystals [31]. The higher nucleating effect of graphene can contrast this behaviour and promote the larger crystal formation. An increase in the graphene

content, however, would cause a confinement effect hampering the formation of large crystals. The high T_m peak, indeed, lowers in intensity until it disappears in NanoNY-5G, where the low T_m endothermal transition remains in a position which corresponds to the lower T_m of the nanofibers with low to no graphenic content, and is located at a slightly lower temperature than plain PA 66 pellet, accounting for the presence of smaller and less perfect crystallites. The effect of the higher drawing ratios in the thinnest nanofibers is confirmed also by the slightly higher T_g observed in these samples (FIGURE 7.10).
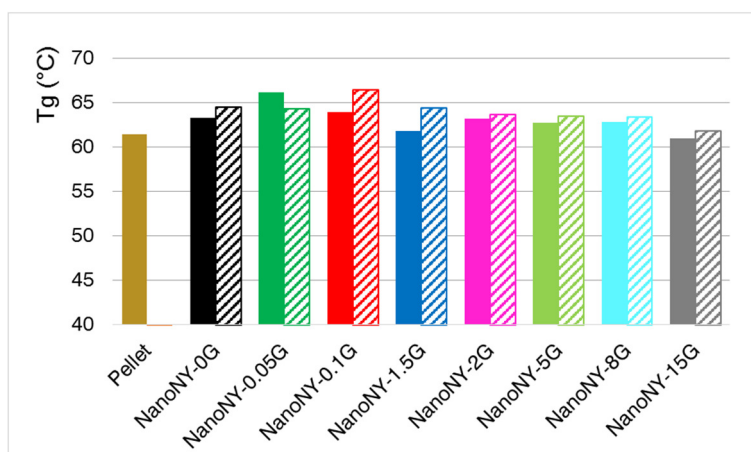

FIGURE 7.10 • Transition temperature of PA 66 nanofibrous mats "As spun" (solid bars) and "Aged" (dashed bars) and comparison with PA 66 pellet. Data calculated from DSC curves.

While the nucleating effect of graphene can be somehow eclipsed by the opposite tendency of thinner nanofiber to hinder crystallization, this feature can be clearly detected in the DSC cooling scans (FIGURE 7.8). In this case, the nanometric size of the fibers should have been removed upon the first melting, and the nucleating action of graphene promotes crystallization at higher temperature, the higher is the G content. This trend reaches almost a *plateau* for the highest G loads. The nanofibrous mats thermal behaviour is stable over the time: after 20 months from their production the degree of crystallinity is practically unchanged (dashed bars in FIGURE 7.9).

7.2.4 • Tensile test of PA 66 nanofibrous mats

While the above discussed thermal features would straightforwardly transfer into modification of the mechanical properties when dealing with bulk materials, the way

graphene affects the behaviour of the nanofibrous mats is on the contrary difficult to draw. Selected nanofibrous mats (NanoNY-0G, NanoNY-0.05G, NanoNY-0.1G and NanoNY1.5G) have been tested to evaluate their mechanical behaviour both as spun and after ageing. The obtained raw results, displayed as load-displacement curves in FIGURE 7.11, show that in the case of graphene loaded samples the maximum load and the displacement at the maximum load are greater than the plain PA 66 samples.
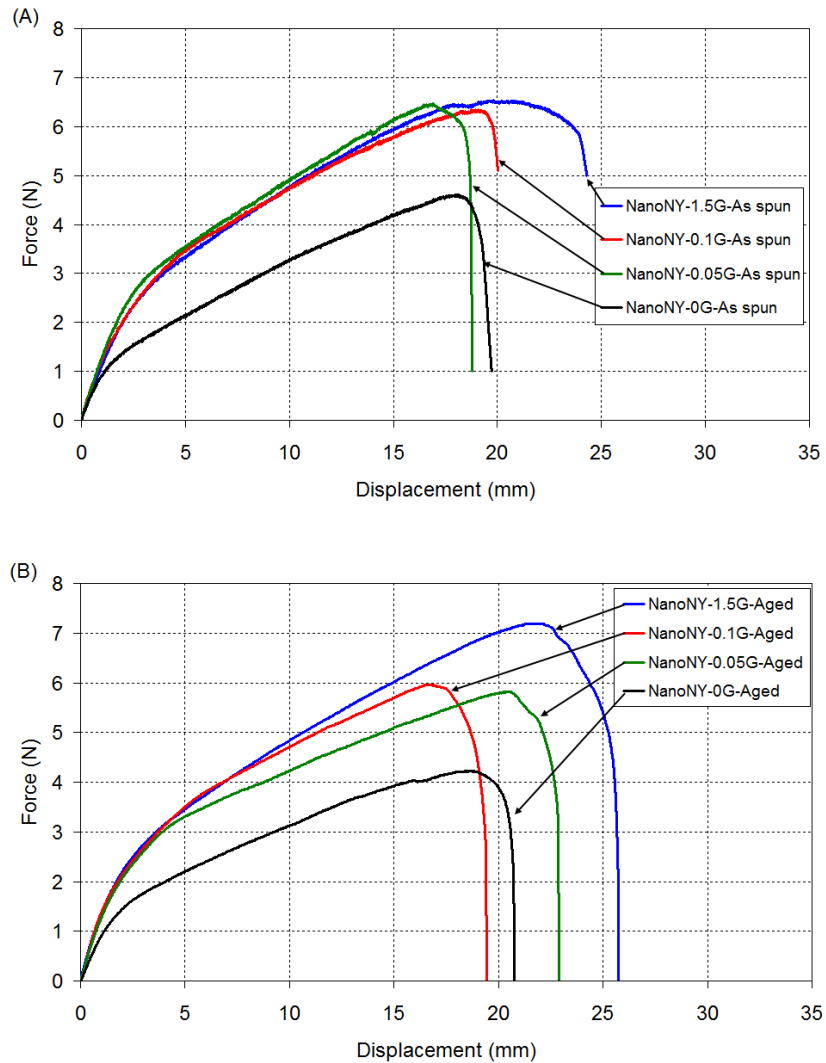
FIGURE 7.11 • Raw Load-vs-Displacement curves recorded for "As spun" (A) and "Aged" (B) nanofibrous mats: for each batch of NanoNY-0G, NanoNY-0.05G, NanoNY-0.1G and NanoNY-1.5G, either "As spun" and "Aged" one selected curve is plotted, which is the closest to the average behaviour of the overall batch.

Nevertheless, the corresponding stress-strain curves must be calculated and analysed to provide reliable data to be discussed. The standard approach to deal with mechanical

properties is based on the force normalization with respect to the cross-section area, while the displacement is converted in strain normalizing with respect to the initial length. Using this approach, the cross section of each specimen has been calculated by means of the width and the thickness of mat samples, where the thickness has been estimated with a mechanical micrometer on an area of about 30 mm^2 applying a low preload (100 g), in order to reduce the modifications of the mat nanofibrous structure. In FIGURE 7.12 examples of the stress-strain curves of "As spun" and "Aged" samples, calculated according to the previous classic approach, are displayed.

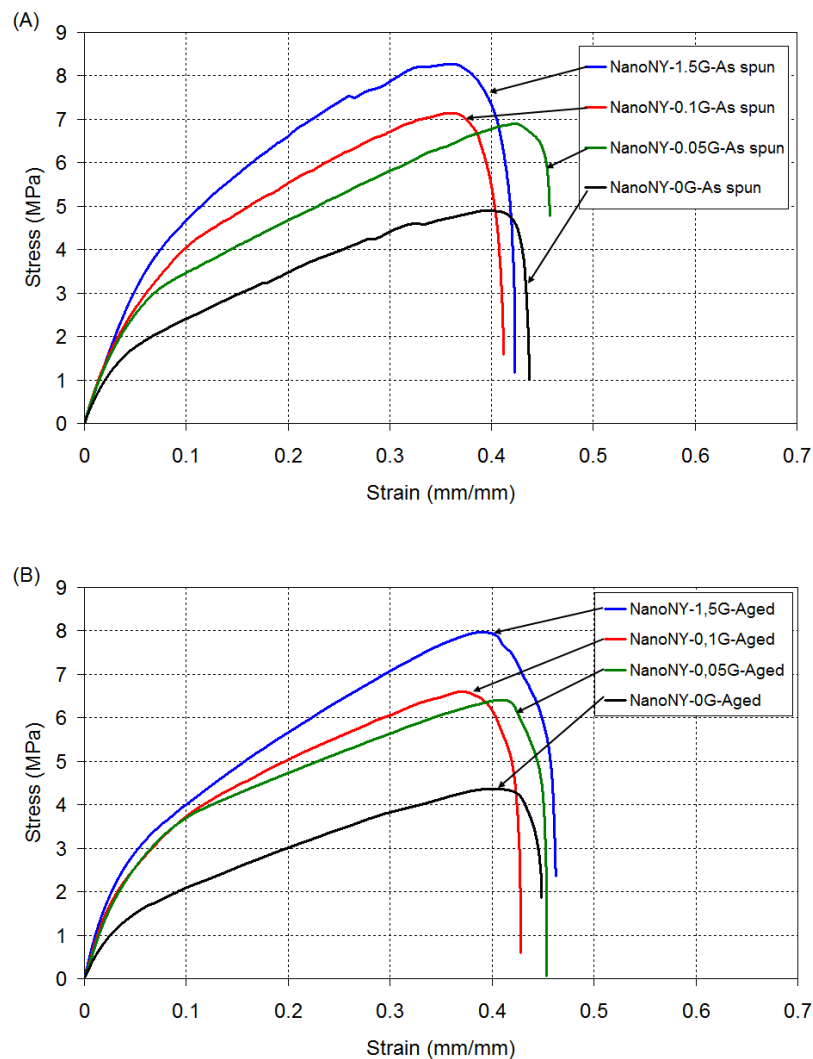FIGURE 7.12 • Stress-vs-Strain curves calculated with the classic approach for "As spun" (A) and "Aged" (B) nanofibrous mats: for each batch of NanoNY-0G, NanoNY-0.05G, NanoNY-0.1G and NanoNY-1.5G, either "As spun" and "Aged" one selected curve is plotted, which is the closest to the average behaviour of the overall batch.

In FIGURE 7.13 the three main obtained parameters are summarized in bar-chart form: Young's modulus (E), maximum value of stress (σ_{max}) and the strain at which the maximum stress is obtained ($\varepsilon_{\sigma\ max}$). The obtained results show that both E and σ_{max} values are significantly influenced by the graphene content, while $\varepsilon_{\sigma\ max}$ is not.
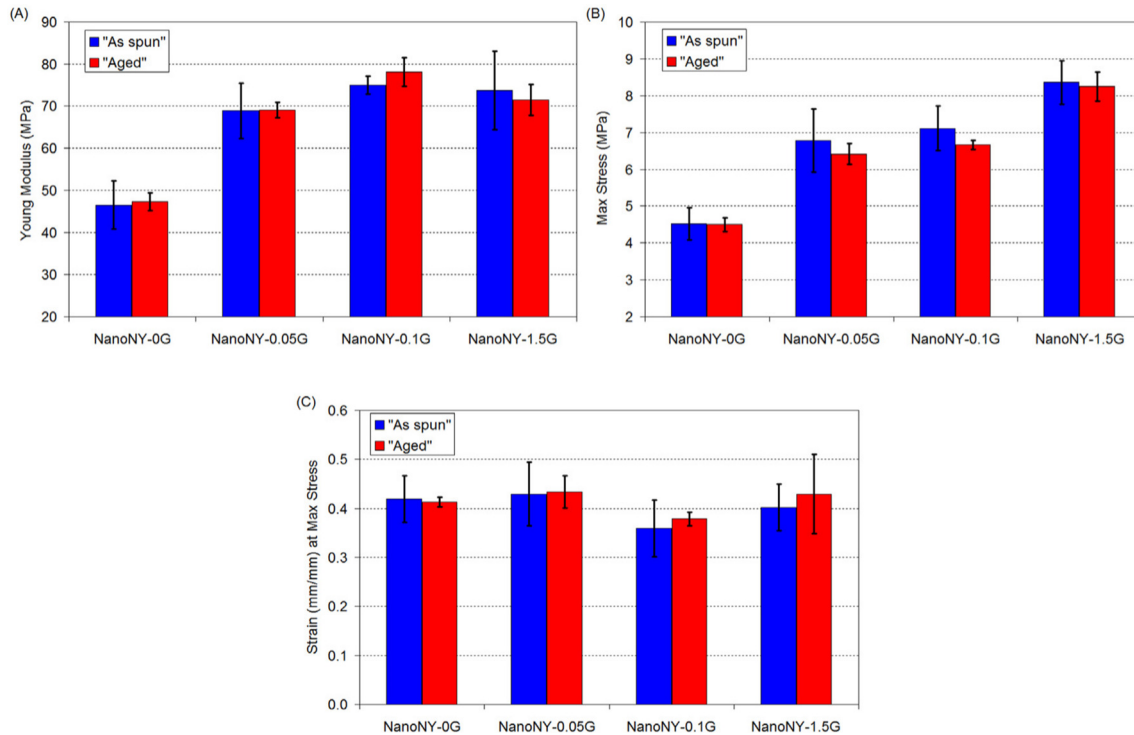
FIGURE 7.13 • Results data synthesis according to classic evaluation of the mechanical properties of nanofibrous mats in terms of (A) Young's modulus, (B) maximum stress and (C) strain corresponding to the maximum value of stress.

The Young's modulus increases by increasing graphene content and a 50–60% increment (see TABLE 7.2) can be observed in graphene loaded samples with respect to the pure PA 66, with the maximum increase (61%) in the case of 1,000 ppm of G.

Graphene contributes to the σ_{max} (TABLE 7.2) with increment ranging from 50 to 85% with respect to virgin samples, with the maximum performance obtained in the case of 15,000 ppm G content. Finally, assessment of the aged samples does not highlight a significant change in mechanical performance.

While the above discussed results might well compare with previous literature [21,22] in term of G efficiency in improving mechanical properties, there may still be some methodological concern regarding the data analysis and manipulation in the case of

nanofibrous specimen: a first topic concerns the stress calculation, while another issue regards the evaluation of the Young's modulus.

TABLE 7.2 • Variation of Young's modulus and maximum value of stress in graphene loaded samples respect to pure PA 66 nanofibrous mat according to evaluation of mechanical properties based on a classic approach.

	Young's modulus %	σ_{max} %
500 ppm vs. Virgin	+48	+50
1,000 ppm vs. Virgin	+61	+57
15,000 ppm vs. Virgin	+59	+85

Stresses acting on a nanofibrous mat sample under tension are indeed difficult to be exactly calculated because each fiber and the fibers architecture in the mat (fiber orientation, fiber crosses and fiber welds) influence the force distribution in the sample and consequently its mechanical behaviour. The classical approach used in the literature to calculate the stress, based on the evaluation of the cross-section area upon simple measurement of specimen macroscopic width and thickness, is a very rough way to estimate the stress itself. This approach does not account for the fibrous morphology, in particular for fibers number and diameter and, at the same time, with the previous "classic" approach, the free volume among fibers is wrongly assumed to be filled by the same fiber material as it would be for a bulk object (FIGURE 7.14).
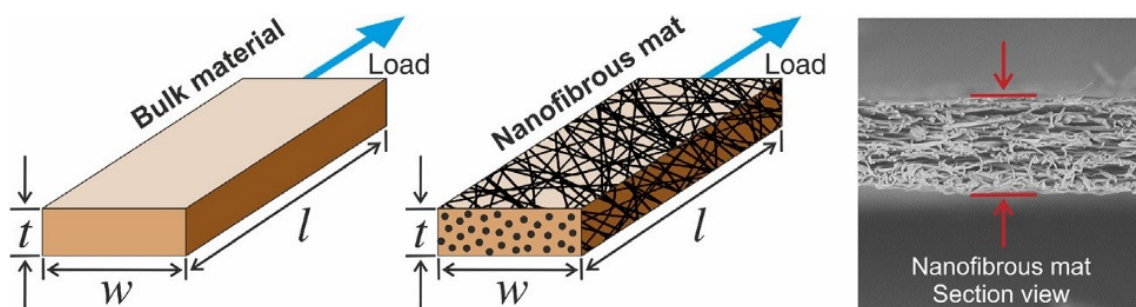

FIGURE 7.14 • Schematic representation of bulk versus nanofibrous materials for highlighting the problems in the definition of the cross-section area.

For discarding the bias induced by the complex thickness measurement, the experimental raw data (such as FIGURE 7.11) were re-analysed by applying the

following EQUATION 7.2 that describes the stress as a function of simple and easy to measure quantities (detailed description in CHAPTER 8):

$$\sigma = \rho \frac{F}{m} L \qquad \text{EQUATION 7.2}$$

where "m" is the specimen mass (measured in mg), "ρ" is the material density, "L" is the specimen initial length (in mm), F is the force (measured in N) and σ is the stress expressed in MPa. While ρ evaluation should take into account any additive fraction, such as graphene content, in the present case it is assumed to be equal to plain PA 66 density, i.e. 1.14 mg/mm^3, owing to the fact the presence of G would affect the overall values by roughly 1% at the outmost. However, appropriate calculation of such a parameter becomes crucial if a significant additive fraction is used. The idea underlying the proposed formula (EQUATION 7.2) is that the mass of the sample is redistributed in an ideal sample which has the length of the tested sample but with an ideal cross-section area where there is no free volume between fibers. Based on EQUATION 7.2, the tensile test results in terms of force-displacement have been re-calculated; in FIGURE 7.15 examples of the new curve are reported.
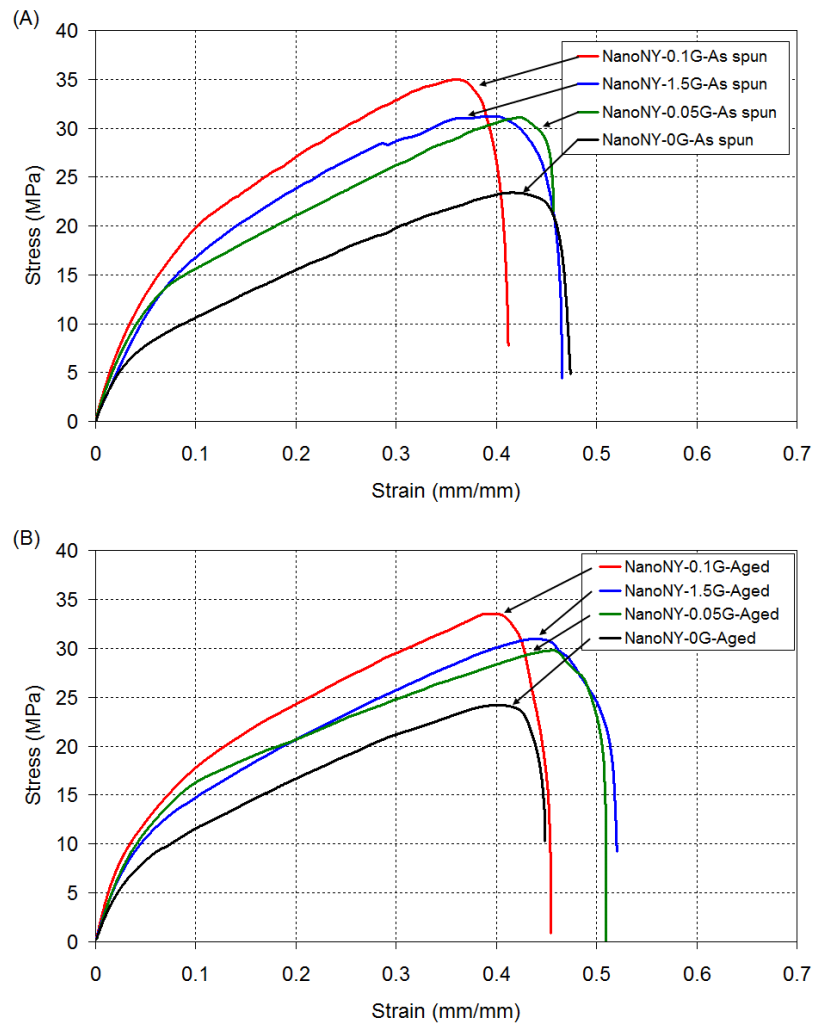
FIGURE 7.15 • Stress-vs-Strain curves where stress has been calculated by means of the equivalent area approach (EQUATION 2) for approach for "As spun" (A) and "Aged" (B) nanofibrous mats: for each batch of NanoNY-0G, NanoNY-0.05G, NanoNY-0.1G and NanoNY-1.5G, either "As spun" and "Aged" one selected curve is plotted, which is the closest to the average behaviour of the overall batch.

The results obtained applying this new approach are summarized in FIGURE 7.16. It can be noted that values of stress are considerably higher with respect to those calculated with the classic approach, and this fact is due to the evaluation of the equivalent cross-section area calculated by the specimen mass introduced in EQUATION 7.2 that is somehow able to discard the contribution of the voids in the cross-section. Comparing bar charts in FIGURE 7.13A–B with those in FIGURE 7.16A–B, it can be pointed out that E and σ_{max} values statistical dispersion is reduced by the implementation of EQUATION 7.2 in the calculations. In particular, the average coefficient of variation (defined as the ratio between the standard deviation and the mean value of the data) for Young's modulus

and maximum stress calculated with "classic" approach are both around 10%, while, considering the results obtained using EQUATION 7.2, both values drop around 5%.
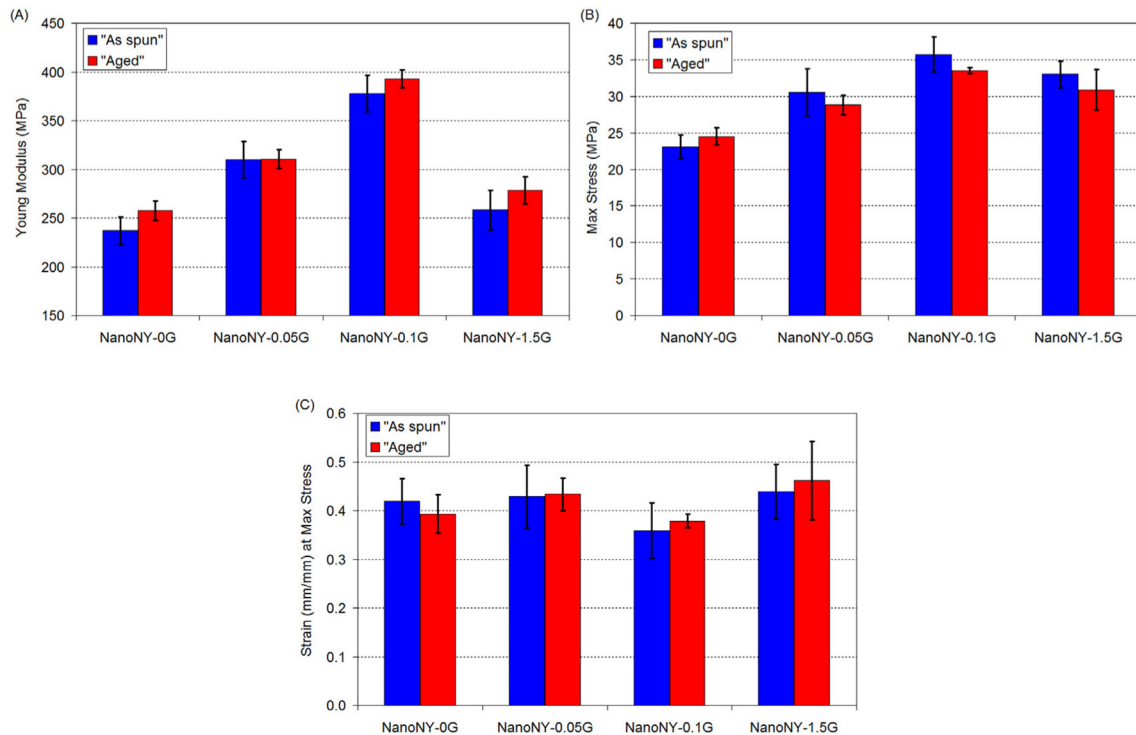
FIGURE 7.16 • Results data synthesis from stress calculated by means of equivalent area; (A) Young's modulus, (B) maximum stress and (C) strain corresponding to the maximum value of stress.

The reduced dispersion on results can be related to the more reliable evaluation of stress based on the latter approach. From a physical point of view, the new analysis procedure confirmed that the ageing did not impact the mechanical behaviour of the materials, while such a new approach supports the idea that graphene just slightly affects $\varepsilon_{\sigma\ max}$ values. The overall trend (TABLE 7.3) show that NanoNY-0.1G (1,000 ppm G) sample displays the most relevant variation of both E (+59%) and σ_{max} (+55%), with respect to the reference NanoNY-0G.

It was indeed previously observed that the best σ_{max} result obtained by classic analysis of data is represented by NanoNY-1.5G (15,000 ppm of G, TABLE 7.2) while implementation of EQUATION 7.2 provides overall results which better agree with the previously discussed data trends on morphology (average diameter, FIGURE 7.5) and thermal behaviour (degree of crystallinity, FIGURE 7.9).

TABLE 7.3 • Variation of Young's modulus and maximum value of stress in graphene loaded samples respect to pure PA 66 nanofibrous mat based on data analysed with EQUATION 7.2.

	Young's modulus %	σ_{max} %
500 ppm vs. Virgin	+31	+32
1,000 ppm vs. Virgin	+59	+55
15,000 ppm vs. Virgin	+9	+43

The discrepancy in the two results can be explained by the different way used to evaluate the stress values: the implementation of EQUATION 7.2 in the calculations enables a more realistic evaluation of stress with respect to the application of cross-section normalization of the force, where a great amount of the area value is actually composed of voids (FIGURE 7.14).

Once the concerns regarding a convenient evaluation of the stress have been cleared with the implementation of EQUATION 7.2 in the calculations, the issues regarding Young's modulus estimation have been approached. The standard procedure based on the linear regression of the stress-strain data at the early strain stage (from 0.005 mm/mm to 0.015 mm/mm) is considered very well established in literature.

However, it is to highlight that the material stiffness variations described in FIGURE 7.12 and FIGURE 7.15 are more complex.
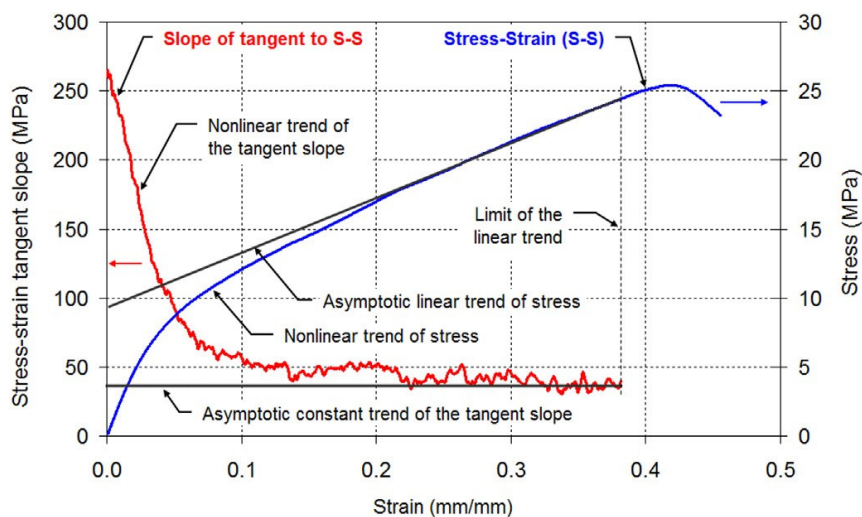

FIGURE 7.17 • Example of stress-strain curve (on the right scale) and slope of tangent to stress-strain curve (on the left) where the nonlinear and the asymptotic constant trends are in evidence.

In fact, as displayed in FIGURE 7.17, the material stiffness, calculated as the slope of the tangent to the stress-strain curve, decreases from an initial value down to an asymptotic constant trend. Such a behaviour is peculiar of this type of fibrous materials when they are subjected to tension (see REFS. [29,36,37] where similar stress-strain curves are reported) and it is related to the peculiar nature of the nonwoven structure, which is ascribed to phenomena such as non-homogenous distribution of the fibers, voids, entanglements and twinning of single fibers (bundles). The initial stiffness exhibited by a membrane made of randomly oriented nanofibers subjected to tension, is due to the complexity of fibers network (fibers entanglements, potential adhesion at fibers crosses, fibers bundling, friction between fibers) and to the number of fibers which are aligned along the displacement direction. The initial nonlinear behaviour, with the stiffness lowering, can thus be attributed to the reorganization of fibers in the network, the reduction of intersections and the breaking of those fibers which initially are already under tension. The asymptotic constant trend of the stiffness is the result of the ordered fibers which are, finally, prevalently aligned to the displacement direction. Based on this observation, it was introduced a new mathematical model for the fitting of the stress-strain experimental results. The model, reported in EQUATION 7.3, is considered as the superimposition of two stress contributions, one linear and one nonlinear (σ_1 and σ_2 respectively), as also sketched in FIGURE 7.18A:

$$\sigma(\varepsilon) = \sigma_1(\varepsilon) - \sigma_2(\varepsilon) = (a\varepsilon + b) - (be^{-c\varepsilon}) = a\varepsilon + b(1 - e^{-c\varepsilon}) \qquad \text{EQUATION 7.3}$$

EQUATION 3 can be used to calculate the slope of the tangent to the stress-strain curve by simple derivation of stress respect strain:

$$\frac{d\sigma}{d\varepsilon} = E(\varepsilon) = a + bce^{-c\varepsilon} \qquad \text{EQUATION 7.4}$$

where here E(ε) is used to indicate the function that describes the slope of the tangent and can be interpreted as the local material stiffness or Young's modulus.

Using EQUATION 7.4 two main features of the model can be obtained:

- the initial material stiffness (or initial Young's modulus, E_0)

$$E_0 = \lim_{\varepsilon \to 0} E(\varepsilon) = a + bc \qquad \text{EQUATION 7.5}$$

- the asymptotic constant stiffness (or the Young's modulus of the linear trend of stress-strain curve, E_{lin})

$$E_{lin} = \lim_{\varepsilon \to \infty} E(\varepsilon) = a \qquad \text{EQUATION 7.6}$$
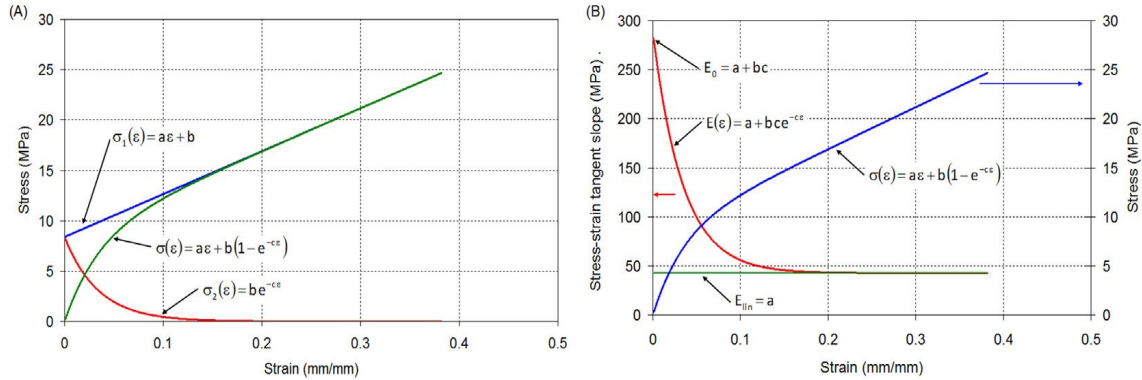
FIGURE 7.18 • Graphical sketch (A) of linear (blue) and nonlinear (red) stress terms together with the full model (green) obtained by their combination according to EQUATION 7.3, and representation (B) of stress and stiffness mathematical models with the two main parameters E_0 and E_{lin}.

The EQUATIONS 7.3 and 7.4 are all sketched in FIGURE 7.18B. The model has been used to fit stress-strain results using last square algorithm with excellent results (FIGURE 7.19 shows an example of the accuracy of the model fitting to real data, displaying a mean square error of the fitted model of 0.015 MPa^2).
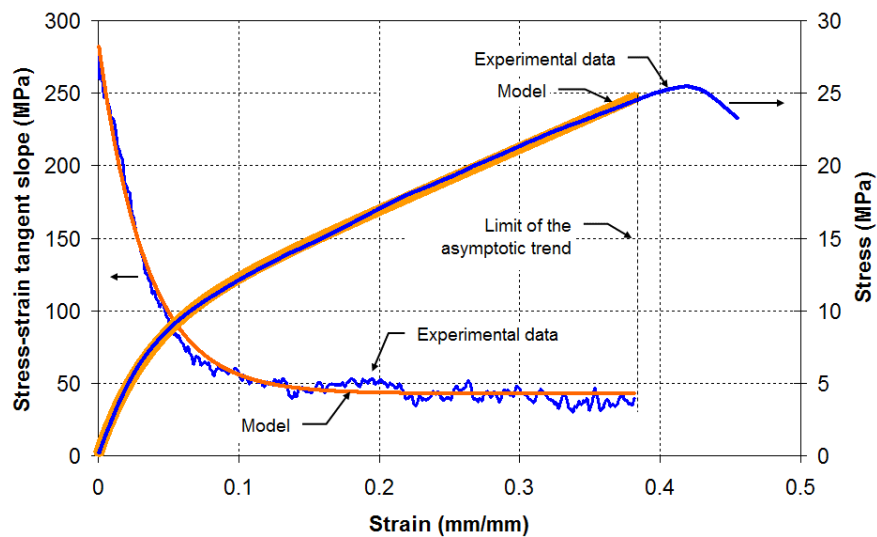
FIGURE 7.19 • Example of stress and stiffness models fitting of experimental data obtained by least square algorithm (a = 42.63 MPa, b = 8.38 MPa, c = 29.23, mean square error = 0.015 MPa^2).

The application of the data fitting model allows to calculate the two main parameters, E_0 and E_{lin}, for both "As spun" and "Aged" specimens (see FIGURE 7.20).

FIGURE 7.20 • Bar charts of the initial (A) and of the linear (B) Young's modulus in the case of both "As spun" "Aged" nanofibrous mat.

Results obtained by means of model fitting confirm that the ageing does not affect the main material properties. Data obtained using the model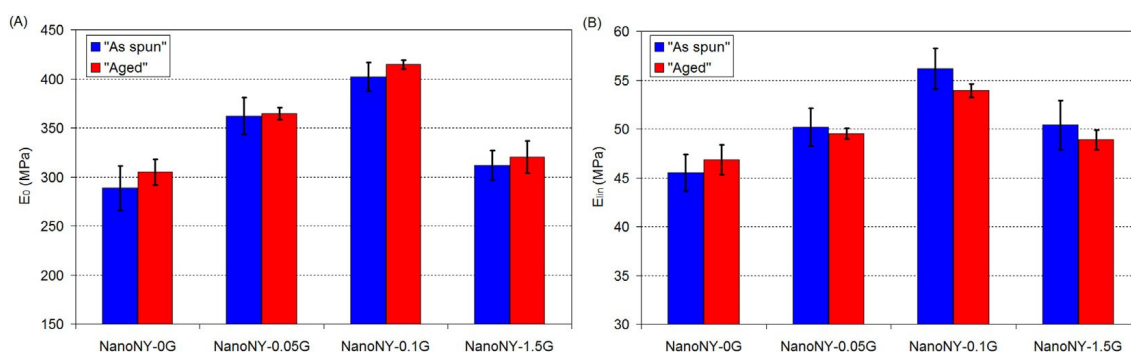 fitting previously proposed show that the initial Young's moduli of G modified nanofibrous mats are greater than that of plain PA 66 non-wovens (FIGURE 7.20A), with NanoNY-0.1G (1,000 ppm) providing the best results. The analysis of the linear portion of the stress-strain curves, represented by the asymptotic constant Young's modulus (E_{lin}), further confirms the benefits provided by integration of G, in particular when in limited amount, showing that in the case of 1,000 ppm G there is an increment, respect to virgin samples, of about 20% of the value. In this frame, the obtained results demonstrate that the presence of G does not alter the linear contribution to the mechanical properties, but, on the contrary, affects the way the nanofibers behave within the complex structure of the mat. Hence there is an initial step where fibers stretch, slide one onto each other, twist and reorient and this is the parameter which the presence of graphene affects the most: indeed, beside an align increase in the crystalline content of the Nylon, G mainly contributes to the thinning of the spun materials that indeed, keeping constant the volume, produces longer fibers more able to entangle, twist and become interconnected. While these results still confirm the benefits of G addition, the differences highlighted in the G actual effect when switching from the classic method (that well compared with the literature data in terms of extent of the mechanical properties improvements) to the new overall mechanical behaviour approach point out that the nanofiber morphology provides a more challenging substrates for the graphenic additive to express its

reinforcing ability at a "bulk material" level. Indeed, the similarity between the size of the nanofibers and of the G sheets dimension (both in the range of few hundreds nanometers) might well be at the limit of an efficient dispersion and interaction of G with polymeric chains for expressing the mechanical reinforcement at its maximum potential (i.e. hindrance of polymer chain mobility, increasing stiffness and strength, preventing cracking, *etc*).

7.3 • MATERIALS AND METHODS

7.3.1 • Materials

PA 66 (Nylon 66 Zytel E53 NC010 kindly provided by DuPont) was dried in a stove at 110 °C for minimum 6 h before use. Trifluoroacetic acid (TFA), acetone, 2,2,2-trifluoroethanol (TFE), formic acid and chloroform, all reagent grade, were purchased from Sigma-Aldrich. Solvents were used without further purifications. Graphene nanoplatelets (PURE G+, DirectaPlus) was kindly provided by Reglass s.r.l. Minerbio (Bologna).

7.3.2 • Preparation of PA 66/graphene solutions

PA 66 (Nylon 66) solutions (15%wt) were prepared in TFA/ acetone 1:1 vol mixture. Pristine solution was made dissolving PA 66 pellets under magnetic stirring and mild heating (maximum 50 °C) until complete polymer dissolution.

Graphene loaded solutions were prepared according to the following method: 1) graphene/solvents mixture sonication via bath sonicator for 30 minutes; 2) graphene/solvents mixture sonication via tip sonicator for 3 h (instrument settings: amplitude 30%, pulse on 9 s, pulse off 1 s); 3) polymer addition to the graphene dispersion, keeping the mixture under magnetic stirring for minimum 1 hour, and in any case until complete dissolution; 4) mixture sonication via tip sonicator for 4 h (instrument settings: amplitude 38%, pulse on 9 s, pulse off 1 s). Sonicator bath (type AC 14, Uniset) and tip sonicator (type VCX 750, Sonics, 750W, microtip diameter 3 mm) were used for graphene dispersion.

The obtained solutions will be labelled as NY-XG, where X represents the weight fraction of graphene with respect to the polymer in the solution. In TABLE 7.4 the list of the solutions prepared for electrospinning is reported.

TABLE 7.4 • PA 66 solutions prepared for nanofibrous mats production.

Solution	Polymer concentration %wt	Graphene content [a] ppm (%wt)	Solvent system
NY-0G	15	- - -	TFA/acetone 1:1 v:v
NY-0.05G	15	500 (0.05)	TFA/acetone 1:1 v:v
NY-0.1G	15	1,000 (0.1)	TFA/acetone 1:1 v:v
NY-1.5G	15	15,000 (1.5)	TFA/acetone 1:1 v:v
NY-2G	15	20,000 (2.0)	TFA/acetone 1:1 v:v
NY-5G	15	50,000 (5.0)	TFA/acetone 1:1 v:v
NY-8G	15	80,000 (8.0)	TFA/acetone 1:1 v:v
NY-15G	15	150,000 (15.0)	TFA/acetone 1:1 v:v

[a] referred to the sum of polymer and graphene weights

7.3.3 • *Nanofibrous mats production*

Nanofibrous mats were produced via electrospinning technique. A Spinbow® electrospinning machine equipped with four 5 mL syringes was used. Needles (length 55 mm, internal diameter 0.84 mm) were joined to syringes via teflon tubing. Fibers were collected on a rotating drum covered with poly(ethylene)-coated paper at 60 rpm. Mats have final dimensions of approximately 20 × 40 cm. The obtained nanofibrous mats will be labelled as NanoNY-XG, where X represents the weight fraction of graphene in the electrospun fibers. The electrospinning process was carried out until an average thickness of mat of 50 μm was obtained. The mat thickness was measured using an analog indicator, applying a pressure of 360 g/m^2.

In TABLE 7.5 the parameters for optimized electrospinning of nanofibrous mats are reported.

TABLE 7.5 • Electrospinning parameters used for mats production.

Nanofibrous mat	Electrospun solution	Graphene content [a]	Flow rate	Electric potential	Distance	Electric field [b]	Temperature	Relative humidity
		ppm (%wt)	mL/h	kV	cm	kV/cm	°C	%
NanoNY-0G	NY-0G	—	0.32	20.0	17.0	1.2	26-28	38-40
NanoNY-0.05G	NY-0.05G	500 (0.05)	0.23	20.8	18.0	1.2	26-28	43-45
NanoNY-0.1G	NY-0.1G	1,000 (0.1)	0.25	21.0	18.0	1.2	25-26	54-45
NanoNY-1.5G	NY-1.5G	15,000 (1.5)	0.17	18.0	18.0	1.0	26-27	39-31
NanoNY-2G	NY-2G	20,000 (2.0)	0.50	16.7	15.0	1.1	23-24	33-35
NanoNY-5G	NY-5G	50,000 (5.0)	0.70	17.3	15.0	1.2	24-26	28-30
NanoNY-8G	NY-8G	80,000 (8.0)	0.30	15.1	20.0	0.8	24-26	24-26
NanoNY-15G	NY-15G	150,000 (15.0)	0.50	20.0	15.0	1.3	22-24	31-33

[a] referred to the sum of polymer and graphene weights

[b] calculated as electric potential to distance ratio

7.3.4 • *Characterization of nanofibrous mats*

Nanofibrous mats were analysed by scanning electron microscopy (SEM, Phenom ProX) to determine nanofibers morphology. All analysed surfaces were gold coated in order to make them conductive. The distribution of fiber diameters on the electrospun mat was determined through the measurement of approximately 50 fibers by means of an acquisition and image analysis software (ImagePro Plus), and the results were given as the average diameter ± standard deviation. Graphene nanoplatelets dispersion in nanofibers was investigated by transmission electron microscopy (TEM): images were acquired by a TEM/STEM FEI Tecnai F20 working at 200 kV. The samples were prepared by direct transfer of fibers on a multifoil-carbon film supported on a copper grid. Raman spectra were recorded with an Ar^{+} laser light source (514.5 nm). The Raman spectrometer is also equipped with a Leica DMLM Renishaw 1000 RAMAN Micro-Spectrometer equipped with microscope (objectives 5×, 20×, and 50×), a rejection filter (notch or edge), a monochromator (1200 lines/mm) and a charge-coupled device thermoelectrically cooled (203 K) detector. DSC measurements were carried out on a TA Instruments Q2000 DSC Modulated apparatus equipped with RCS cooling system. In dynamic runs every sample (5 mg) was heated from 0 °C to 120 °C, cooled to 0 °C, then heated to 290 °C (heating/cooling rate 20 °C) in nitrogen atmosphere.

Tensile tests of selected nanofibrous mats were made using a Instron 5966 universal testing machine equipped with a 100 N load cell, speed test 10 mm/min. Nanofibrous membranes were anchored in a paper frame (47 × 67 and 25 × 45 mm outer and inner dimensions, respectively), pasted with cyanoacrylate glue, for better handling (FIGURE 7.21). Moreover, it guaranteed that all non-woven nanofibers were clamped in the machine fixtures. Effective specimen dimensions were 20 × 45 mm. Paper frame was cut before test started. Measurements are repeated after 20 months ageing.
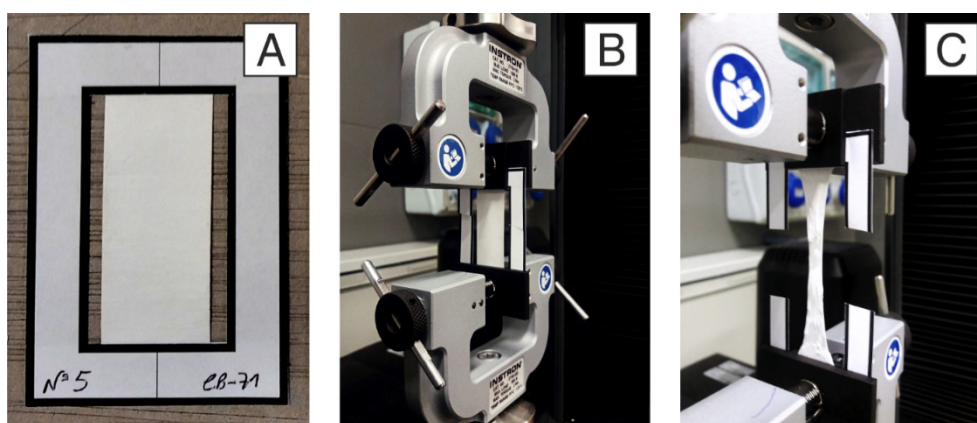
FIGURE 7.21 • (A) Nanofibrous mat specimen. Tensile test: (B) before start, (C) during test.

Seven specimens were tested for each nanofibrous mat type. The elastic modulus, maximum load, elongation at break are expressed as the mean value ± standard deviation.

According to both the classical-approach-based calculations and to the new proposed method based on EQUATION 7.2, the Young's modulus has been calculated by means of linear regression of stress-strain data in the strain range from 0.005 mm/mm to 0.015 mm/mm for all specimens. The selection of this specific strain range was based on the minimization of the linear fitting error.

Nanofibrous mats for thermal and mechanical properties characterization after 20 months from the production have been kept at ambient conditions without temperature and humidity control.

7.4 • CONCLUSIONS

PA 66 nanofibrous mats loaded with different amounts of G were successfully produced with a stable process and good fiber quality, thanks to the optimization of the solvent system. It was then demonstrated that G content strongly affects the fiber diameter in particular at very low amounts of nano-reinforcement. It was also demonstrated that the presence of the carbonaceous additive helps crystal formation, even when the thinning of the fibers and the electrospinning process would hamper it. Moreover, a new phenomenological model has been put forward for the interpretation of the mechanical behaviour of such nanofibrous mats: in this frame a contribution of G has been observed, that affects the initial steps of deformation where fibers stretch, slide one onto each other, twist and re-orient. While this is a preliminary model, whose terms' physical significance is still under investigation, the outstanding fitting performance ability corroborates its significance as a tool for the interpretation of the mechanical behaviour of nanofibrous mats. Finally, the nanofibers were also thermally and mechanically analysed after 20 months ageing, showing no significant alteration with respect to the pristine ones, thus confirming the stability of the process and the lack of detrimental effect in time due to G addition.

References

[1]   R. Palazzetti, A. Zucchelli, Electrospun nanofibers as reinforcement for composite laminates materials – A review, Compos. Struct. 182 (2017) 711–727. https://doi.org/10.1016/j.compstruct.2017.09.021.

[2]   S.K. Kumar, V. Ganesan, R.A. Riggleman, Perspective: Outstanding theoretical questions in polymer-nanoparticle hybrids, J. Chem. Phys. 147 (2017). https://doi.org/10.1063/1.4990501.

[3]   Y. Zhang, K.Y. Rhee, D. Hui, S.-J. Park, A critical review of nanodiamond based nanocomposites: Synthesis, properties and applications, Compos. Part B Eng. 143 (2018) 19–27. https://doi.org/10.1016/j.compositesb.2018.01.028.

[4]   D.G. Papageorgiou, I.A. Kinloch, R.J. Young, Mechanical properties of graphene and graphene-based nanocomposites, Prog. Mater. Sci. 90 (2017) 75–127. https://doi.org/10.1016/j.pmatsci.2017.07.004.

[5]   Y. Zhang, J.R. Choi, S.-J. Park, Thermal conductivity and thermo-physical properties of nanodiamond-attached exfoliated hexagonal boron nitride/epoxy nanocomposites for microelectronics, Compos. Part A Appl. Sci. Manuf. 101 (2017) 227–236. https://doi.org/10.1016/j.compositesa.2017.06.019.

[6]   Y. Zhang, K.Y. Rhee, S.-J. Park, Nanodiamond nanocluster-decorated graphene oxide/epoxy nanocomposites with enhanced mechanical behavior and thermal stability, Compos. Part B Eng. 114 (2017) 111–120. https://doi.org/10.1016/j.compositesb.2017.01.051.

[7]   L. Mazzocchetti, T. Benelli, E. D'Angelo, S. Ligi, G. Minak, E. Poodts, F. Tarterini, V. Palermo, L. Giorgini, Managing heat phenomena in epoxy composites production via graphenic derivatives: Synthesis, properties and industrial production simulation of graphene and graphene oxide containing composites, 2D Mater. 4 (2017) 1–14. https://doi.org/10.1088/2053-1583/4/1/015020.

[8]   T. Benelli, L. Mazzocchetti, E. D'Angelo, M. Lanzi, F. Saraga, L. Sambri, M.C. Franchini, L. Giorgini, New nitrogen-rich heterocycles for organo-modified bentonites as flame retardant fillers in epoxy resin nanocomposites, Polym. Eng. Sci. 57 (2017) 621–630. https://doi.org/10.1002/pen.24565.

[9]   L. Mazzocchetti, T. Benelli, E. Maccaferri, S. Merighi, J. Belcari, A. Zucchelli, L. Giorgini, Poly-m-aramid electrospun nanofibrous mats as high-performance flame retardants for carbon fiber reinforced composites, Compos. Part B Eng. 145 (2018) 252–260. https://doi.org/10.1016/j.compositesb.2018.03.036.

[10]   S. Vadukumpully, J. Paul, N. Mahanta, S. Valiyaveettil, Flexible conductive graphene/poly(vinyl chloride) composite thin films with high mechanical strength and thermal stability, Carbon N. Y. 49 (2011) 198–205. https://doi.org/10.1016/j.carbon.2010.09.004.

[11]   O.M. Istrate, K.R. Paton, U. Khan, A. O'Neill, A.P. Bell, J.N. Coleman, Reinforcement in melt-processed polymer-graphene composites at extremely low graphene loading level, Carbon N. Y. 78 (2014) 243–249. https://doi.org/10.1016/j.carbon.2014.06.077.

[12]   M. El Achaby, F.Z. Arrakhiz, S. Vaudreuil, E.M. Essassi, A. Qaiss, Piezoelectric β-polymorph formation and properties enhancement in graphene oxide - PVDF nanocomposite films, Appl. Surf. Sci. 258 (2012) 7668–7677. https://doi.org/10.1016/j.apsusc.2012.04.118.

[13]   S. Kashyap, S.K. Pratihar, S.K. Behera, Strong and ductile graphene oxide reinforced PVA nanocomposites, J. Alloys Compd. 684 (2016) 254–260. https://doi.org/10.1016/j.jallcom.2016.05.162.

[14]   B. Mayoral, E. Harkin-Jones, P.N. Khanam, M.A. AlMaadeed, M. Ouederni, A.R. Hamilton, D. Sun, Melt processing and characterisation of polyamide 6/graphene nanoplatelet composites, RSC Adv. 5 (2015) 52395–52409. https://doi.org/10.1039/C5RA08509H.

[15] L. Sisti, J. Belcari, L. Mazzocchetti, G. Totaro, M. Vannini, L. Giorgini, A. Zucchelli, A. Celli, Multicomponent reinforcing system for poly(butylene succinate): Composites containing poly(l-lactide) electrospun mats loaded with graphene, Polym. Test. 50 (2016) 283–291. https://doi.org/10.1016/j.polymertesting.2016.01.022.

[16] T.M. Brugo, G. Minak, A. Zucchelli, H. Saghafi, M. Fotouhi, An Investigation on the Fatigue based Delamination of Woven Carbon-epoxy Composite Laminates Reinforced with Polyamide Nanofibers, Procedia Eng. 109 (2015) 65–72. https://doi.org/10.1016/j.proeng.2015.06.208.

[17] J. Zhang, T. Yang, T. Lin, C.H. Wang, Phase morphology of nanofibre interlayers: Critical factor for toughening carbon/epoxy composites, Compos. Sci. Technol. 72 (2012) 256–262. https://doi.org/10.1016/j.compscitech.2011.11.010.

[18] B. Li, H. Yuan, Y. Zhang, Transparent PMMA-based nanocomposite using electrospun graphene-incorporated PA-6 nanofibers as the reinforcement, Compos. Sci. Technol. 89 (2013) 134–141. https://doi.org/10.1016/j.compscitech.2013.09.022.

[19] T. An, B. Pant, S.Y. Kim, M. Park, S.-J. Park, H.-Y. Kim, Mechanical and optical properties of electrospun nylon-6,6 nanofiber reinforced cyclic butylene terephthalate composites, J. Ind. Eng. Chem. 55 (2017) 35–39. https://doi.org/10.1016/j.jiec.2017.06.044.

[20] S. Backer, D.R. Petterson, Some Principles of Nonwoven Fabrics, Text. Res. J. 30 (1960) 704–711. https://doi.org/10.1177/004051756003000912.

[21] M. Goodarz, S.H. Bahrami, M. Sadighi, S. Saber-Samandari, The influence of graphene reinforced electrospun nano-interlayers on quasi-static indentation behavior of fiber-reinforced epoxy composites, Fibers Polym. 18 (2017) 322–333. https://doi.org/10.1007/s12221-017-6700-3.

[22] F. Navarro-Pardo, G. Martínez-Barrera, A. Martínez-Hernández, V. Castaño, J. Rivera-Armenta, F. Medellín-Rodríguez, C. Velasco-Santos, Effects on the Thermo-Mechanical and Crystallinity Properties of Nylon 6,6 Electrospun Fibres Reinforced with One Dimensional (1D) and Two Dimensional (2D) Carbon, Materials (Basel). 6 (2013) 3494–3513. https://doi.org/10.3390/ma6083494.

[23] F. Navarro-Pardo, A.L. Martinez-Hernandez, C. Velasco-Santos, Carbon Nanotube and Graphene Based Polyamide Electrospun Nanocomposites: A Review, J. Nanomater. 2016 (2016) 1–16. https://doi.org/10.1155/2016/3182761.

[24] Y. Huang, D.R. Paul, Effect of MolecularWeight and Temperature on Physical Aging of ThinGlassy Poly(2,6-dimethyl-1,4-phenylene oxide) Films, J. Polym. Sci. Part B Polym. Phys. 45 (2007) 1390–1398. https://doi.org/10.1002/polb.

[25] Y. Liang, G. Zheng, W. Han, C. Liu, J. Chen, Q. Li, B. Liu, C. Shen, X. Peng, Nano-hybrid shish-kebab: Isotactic polypropylene epitaxial growth on electrospun polyamide 66 nanofibers via isothermal crystallization, Mater. Lett. 65 (2011) 653–656. https://doi.org/10.1016/j.matlet.2010.11.034.

[26] F. Hajiani, A.A.A. Jeddi, A.A. Gharehaghaji, An investigation on the effects of twist on geometry of the electrospinning triangle and polyamide 66 nanofiber yarn strength, Fibers Polym. 13 (2012) 244–252. https://doi.org/10.1007/s12221-012-0244-3.

[27] N.-M. Barkoula, B. Alcock, N.O. Cabrera, T. Peijs, Fatigue Properties of Highly Oriented Polypropylene Tapes and All-Polypropylene Composites, Polym. Polym. Compos. 16 (2008) 101–113. https://doi.org/10.1177/096739110801600203.

[28] E.L. Papadopoulou, F. Pignatelli, S. Marras, L. Marini, A. Davis, A. Athanassiou, I.S. Bayer, Nylon 6,6/graphene nanoplatelet composite films obtained from a new solvent, RSC Adv. 6 (2016) 6823–6831. https://doi.org/10.1039/C5RA23647A.

[29] A. Ridruejo, C. González, J. Llorca, Micromechanisms of deformation and fracture of polypropylene nonwoven fabrics, Int. J. Solids Struct. 48 (2011) 153–162. http://dx.doi.org/10.1016/j.ijsolstr.2010.09.013.

[30] A.C. Ferrari, J.C. Meyer, V. Scardaci, C. Casiraghi, M. Lazzeri, F. Mauri, S. Piscanec, D. Jiang, K.S. Novoselov, S. Roth, A.K. Geim, Raman Spectrum of Graphene and Graphene Layers, Phys. Rev. Lett. 97 (2006) 187401. https://doi.org/10.1103/PhysRevLett.97.187401.

[31]   A. Baji, Y.-W. Mai, S.-C. Wong, Effect of fiber diameter on the deformation behavior of self-assembled carbon nanotube reinforced electrospun Polyamide 6,6 fibers, Mater. Sci. Eng. A. 528 (2011) 6565–6572. https://doi.org/10.1016/j.msea.2011.05.012.

[32]   M. Gazzano, C. Gualandi, A. Zucchelli, T. Sui, A.M. Korsunsky, C. Reinhard, M.L. Focarete, Structure-morphology correlation in electrospun fibers of semicrystalline polymers by simultaneous synchrotron SAXS-WAXD, Polymer (Guildf). 63 (2015) 154–163. https://doi.org/10.1016/j.polymer.2015.03.002.

[33]   J.P. Bell, P.E. Slade, J.H. Dumbleton, Multiple melting in nylon 66, J. Polym. Sci. Part A-2 Polym. Phys. 6 (1968) 1773–1781. https://doi.org/10.1002/pol.1968.160061007.

[34]   T. Hasegawa, T. Mikuni, Higher-order structural analysis of nylon-66 nanofibers prepared by carbon dioxide laser supersonic drawing and exhibiting near-equilibrium melting temperature, J. Appl. Polym. Sci. 131 (2014) n/a-n/a. https://doi.org/10.1002/app.40361.

[35]   M. Inoue, Studies on Crystallization of High Polymers by Differential Thermal Analysis, J. Polym. Sci. Part A. 1 (1963) 2697–2709.

[36]   S. Sinha-Ray, A.L. Yarin, B. Pourdeyhimi, Meltblown fiber mats and their tensile strength, Polymer (Guildf). 55 (2014) 4241–4247. http://dx.doi.org/10.1016/j.polymer.2014.05.025.

[37]   K. Molnar, L.M. Vas, T. Czigany, Determination of tensile strength of electrospun single nanofibers through modeling tensile behavior of the nanofibrous mat, Compos. Part B Eng. 43 (2012) 15–21. http://dx.doi.org/10.1016/j.compositesb.2011.04.024.

Chapter 8

HOW NANOFIBERS CARRY THE LOAD: TOWARDS A UNIVERSAL AND RELIABLE APPROACH FOR TENSILE TESTING OF POLYMERIC NANOFIBROUS MEMBRANES

Nanofibrous nonwovens show high versatility and outstanding properties, with reduced weight. The porous morphology and the high material flexibility and deformability make complex their mechanical testing, severely affecting results reliability.

This chapter presents an accurate, systematic, and critical study concerning tensile testing of nonwovens, using electrospun Nylon 66 random nanofibrous mats as case study. Nanofibers diameter and specimen geometry were investigated to thoroughly describe the nanomat tensile behaviour, also considering the polymer thermal properties, and the nanofibers crossings number as a function of the nanofibers diameter. Stress-strain data were analysed using a phenomenological data fitting model to interpret the tensile behaviour better.
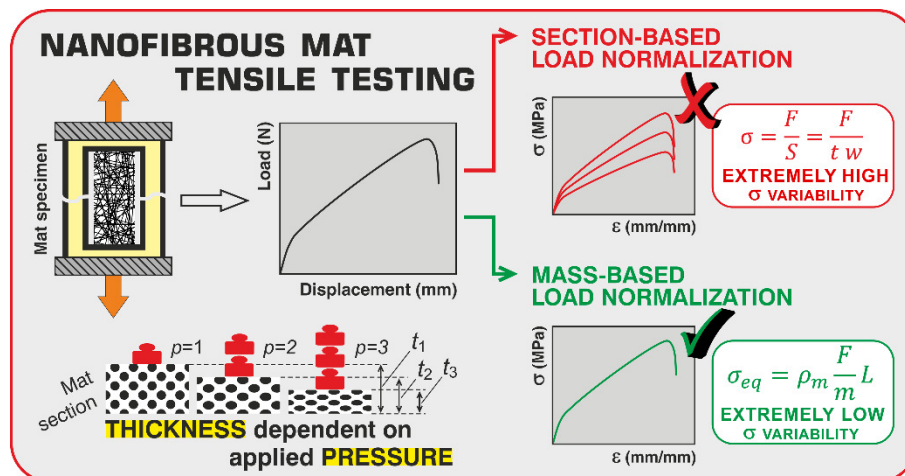
8.1 • INTRODUCTION

Nonwoven fabrics are structures where fibers are not arranged in a specific pattern (e.g. warp and weft) while still maintaining the aspect and most of the properties of a woven textile. These materials have a lot in common with textiles, paper and some polymeric products. Nonetheless, they also display some peculiarities: in place of weaving of textiles, the fibers in the form of staple or continuous filaments are kept together by frictional forces through entanglements or adhesive forces between fibers, with or without the use of binders [1], as a consequence of chemical, mechanical, heat or solvent treatment. The fibers can be natural or man-made and characterized by any diameter [1], but usually are in the micrometer range. It is not a simple task to define "nonwovens", so that in the years various definitions were proposed (and amended) by different organizations for taking into account the multifaceted aspects which characterize this class of materials [2]. BS EN ISO 9092:2019 defines nonwoven as "engineered fibrous assembly, primarily planar, which has been given a designed level of structural integrity by physical and/or chemical means, excluding weaving, knitting or papermaking". Structural integrity, as specified by the standard, means a "measurable level of added tensile strength", namely the nonwoven should possess some mechanical strength derived from the fiber assembly structure, highlighting the importance of (tensile) mechanical properties.

Nowadays, nonwovens find use in a wide variety of applications, often with high added value, like medical devices, filters, technical clothes, home and industrial furniture, thermal and acoustic insulation, and engineered materials [3]. Several properties are dependent on the diameter size, such as porosity and pore dimension [4], which in turn impact, for example, filtering capacity [4]. Mechanical properties, in particular, are significantly enhanced moving from micrometer to nanometer scale [5]. In the last two decades, indeed, nonwoven fabrics made of nanofibers gained increasing attention, thanks to their high surface to volume ratio and outstanding properties. Besides the application as highly efficient filters [6], nanofibrous nonwoven mats are successfully used in tissue engineering [7,8], sensor [9,10], catalysis [11], adhesive bonded joints [12] and composite materials with enhanced mechanical performances [13] (see also CHAPTER 3) and/or peculiar properties [14]. In most applications, the assessment of mat

mechanical properties is fundamental for evaluating effective applicability, and tensile testing is commonly performed. However, the highly porous morphology, together with the overall high material flexibility and deformability, strongly limit the results reliability. Nanofibrous mats are usually very thin and delicate, making them difficult to be handled. For this reason, usually, the mats are handled with their original support substrate until their final usage. Therefore, the specimen preparation for tensile testing requires particular attention for avoiding mat damage, pre-tensioning, or fibers slipping from the grips during testing. The use of a paper frame to be cut before testing is a valid solution (see CHAPTER 7, SECTION 7.2.4), helping to handle and positioning the specimen, and to better measure the gauge length. However, even when all cautions are taken to run the test, evaluation of the cross-section area, required to normalize recorded load data to calculate the stress (σ), is still troublesome in particular in terms of thickness determination. Indeed, while thickness measurement of non-porous "bulk" materials is simple, it may be tricky for porous and "low-stiffness" ones. Being nanofibrous mats characterized by high porosity, with values close to 90%, the measured thickness is surely affected by the measurement itself. since nonwovens are very thin and the cross-section area is directly proportional to the thickness, the normalized load values (i.e. stress, σ) may be particularly affected by this drawback. Within this frame, testing of materials is ruled by technical standards published by national and international standards organizations, such as ASTM International, ISO, BSI, UNI, with the aim of obtaining comparable results. However, there are only a few standards for the testing of nonwovens, such as ISO 9073 and BS EN 29073, with a lack of specific indication for nanofibrous nonwovens, making them practically not applicable to nanometric fibrous systems. As an example, BS EN 29073-3:1992 (ISO 9073-3:1989), related to the "determination of tensile strength and elongation" of nonwovens, prescribes to prepare a rectangular specimen 50 mm width and, possibly, 200 mm length (gauge length), for "avoiding risks due to local heterogeneity of nonwovens or to undue cutting of long-fibre nonwovens". As a matter of fact, due to the previously discussed difficult handling of nanofibrous mats, the preparation of specimens with these characteristics is practically precluded in most cases. Furthermore, the reason why such a specimen size is prescribed clearly suggests that the considered fibers are not nanometric. It is worth noting that in the cited standard the breaking strength is to be expressed in newtons (N), so actually, it represents the breaking load rather than a "real" strength (σ at break).

Again, this is to underline that neither here nor in other standards regarding nonwovens (excluding geotextiles nonwovens [15], and paper [16,17], which are not considered a nonwoven according to its definition [1]) a method is reported to evaluate the elastic modulus (in MPa) and the strength (load per unit area of cross-section, in MPa) of this type of engineered materials. These tensile properties require σ calculation and, in turn, the evaluation of the mat thickness. The lack of an indication on how to determine tensile properties stems probably from the difficulty in measuring thickness, and in defining uniquely *the* thickness. Even if there is a standard for the determination of "conventional" nonwovens thickness [18], it appears not applicable to nanofibrous nonwovens, since this standard refers to "thicker" nonwovens respect to nanofibrous ones (mm vs μm scale). Besides, the discussed test apparatus is quite complex and not available to common laboratories for routinely procedures. However, the thickness dependency from the applied pressure during measurement surely affects the measured thickness also in "conventional" nonwovens, since BS EN ISO 9073-2 specifies the measuring pressure to be adopted. Also the standard for paper thickness determination [19] seems to be not helpful, since the paper is made by cellulose fibers consolidated via pressure during calendering. Consequently, the thickness measurement is less dependent on the measuring pressure, and therefore, the related problem is not as important as in nanofibrous nonwovens. The well-known standard for tensile testing of bulk plastics (ASTM D638) is not useful too.

The mat thickness dependency on the way it is assessed makes a real comparison of mechanical performances of nanofibrous nonwovens a difficult task, especially when comparing mats tested by different laboratories. The knowledge of the thickness measurement conditions (mainly the applied pressure) should help, but usually, this information is missing [20–32]. The underestimation of this aspect, affecting almost all the studies about tensile testing of nanofibers, prevents in fact any reliable comparison.

Presently, a technical standard that establishes a method and the technical criteria to carry out tensile testing of nonwoven nanofibrous mats is not available. To the best of the Authors' knowledge, not even studies concerning data reliability of tensile testing of nanofibrous nonwovens exist. However, given the tremendous boost in the use of nanofibrous nonwovens, searching for a reliable and simple way to tensile test this type of materials is of primary importance.

In this work is presented an accurate, systematic and critical study concerning tensile testing of nonwoven mats, using electrospun Nylon 66 nanofibrous mats as a case study. The "classical" approach to normalization of load by means of specimen cross-section area is compared to a mass-based normalization one, as well as a normalization based on the mat grammage (areal density). A viable way to convert tensile data of previously tested mats is presented too. Nanofibrous mat characteristics, such as fibers diameter, grammage, and specimen geometry (width and gauge length) are deeply investigated to thoroughly describe the tensile behaviour of nonwovens. Mats mechanical performances were discussed taking into account polymer properties (degree of crystallinity and glass transition temperature), and the number of potential nanofibers crossings as a function of the nanofiber diameter. Experimental stress-strain data are then analysed using a phenomenological data fitting model to better understand the tensile behaviour.

8.2 • RESULTS AND DISCUSSION

8.2.1 • *Membrane thickness evaluation and "classical approach" to tensile test*

The accurate evaluation of the thickness is a key factor to characterize several materials properties. This measurement is quite simple when dealing with bulk materials, but it may be very tricky in case of porous and "low-stiffness" materials, since the measurement procedure itself affects the measured thickness value. Nonwovens, to which electrospun nanofibers clearly belong, are surely affected by this drawback.
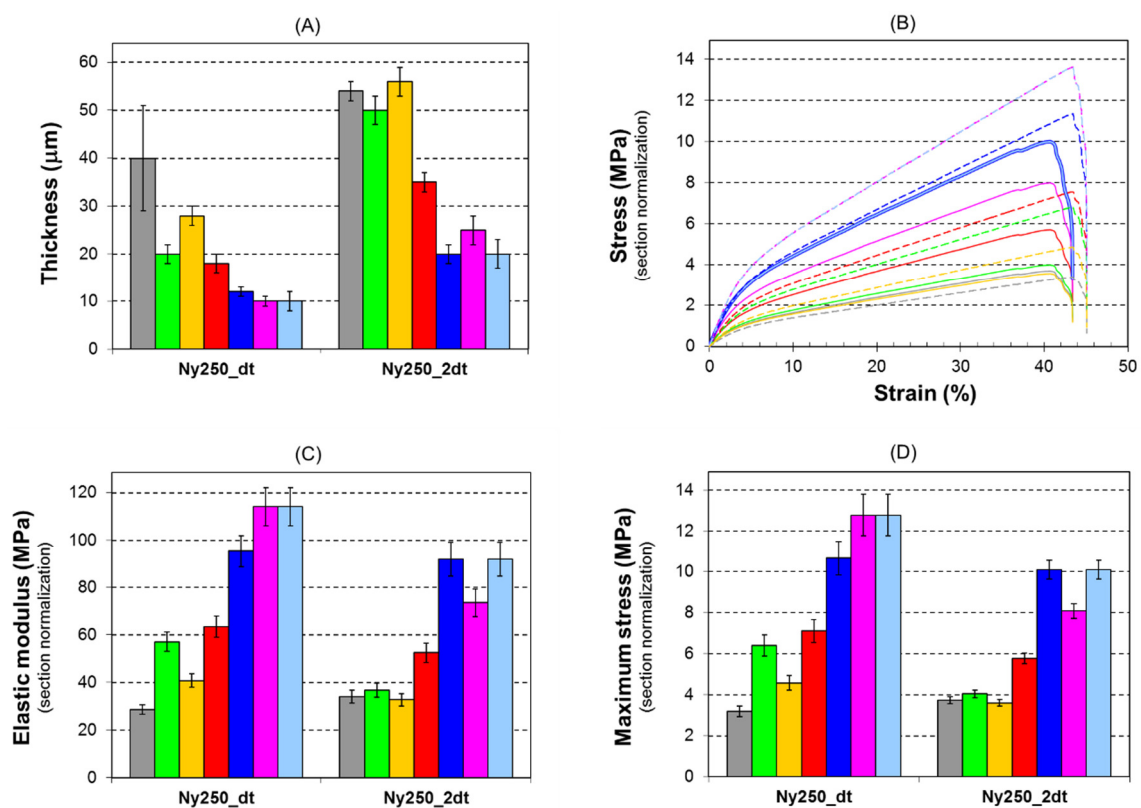

FIGURE 8.1 • (A) Thickness measurements on the two distinct Ny250 nanofibrous mats, using different measurement tools. (B) Comparison of stress-strain curves of the tensile tests performed on Ny250_dt (dashed lines) and Ny250_2dt (solid lines) obtained from the application of the "classical approach" as per EQUATION 8.1, using the different thicknesses reported in (A). (C) Elastic modulus and (D) maximum stress derived from the analysis of stress-strain curves in (B). The colours are coherent with the ones adopted for the identification of the measurement instruments.

To demonstrate it, two Ny250 membranes, named Ny250_dt and Ny250_2dt, were electrospun for a deposition time one twice the other (dt and 2dt), to assess the thickness of each membrane, evaluated in a limited area, where the nanofiber deposition is expected to be homogeneous. The histograms in FIGURE 8.1A show the thickness measured on the two different Ny250 membranes using the measurement tools reported in TABLE 8.4.

The measured thickness is strongly affected by the peculiar tool used for its evaluation, resulting in very different values, with a maximum observed discrepancy of about 300% within the same area. It can be surely affirmed that overall Ny250_dt mat is thinner than Ny250_2dt (provided that the comparison is done using the same instrument), but it is not possible to define *the* mat thickness uniquely, as the measurement tool influences the recorded value as a function of the applied pressure.

The use of different thickness values may, in turn, affect enormously tensile test results. The recorded load-displacement data, which do not consider dimensions and geometry of the specimen, require normalization to obtain comparable stress-strain curves. The classical approach used for stress evaluation (σ, in MPa) requires the specimen thickness (t, in mm) for evaluating the cross-section area (S, in mm^2) normal to the applied load direction, as shown by the following equation:

$$\sigma = \rho \frac{F}{m} L$$

<div align="right">EQUATION 8.1</div>

where F is the force N and w the specimen width mm. Clearly, any variation in t significantly affects σ, being the section S directly proportional to it.

Tensile tests were performed on two specimens with a dimension of 20 × 45 mm sampled from the analysed region of Ny250_dt and Ny250_2dt. For each specimen, stress values were calculated according to EQUATION 8.1, using the thicknesses reported in FIGURE 8.1A, obtaining the multiple stress-strain curves represented in FIGURE 8.1B. The curves display significantly different profiles, while they should be in principle overlapped or, at least, highly resembling one each other. As a consequence, both elastic modulus (E) and maximum stress (σ_{max}) assume completely different values, ranging from 35÷100 MPa and 4÷14 MPa, respectively (FIGURE 8.1C-D). It is, therefore, demonstrated that the thickness measurement methodology deeply affects the results. Moreover, it is worth mentioning that even using the same tool, different stress-strain

curves are obtained for the two considered specimens, though in theory the result should be the same. Indeed, the lower the thickness of the nanofibrous mat to be measured, the greater the relative error, since the dimension of the mat is evaluated as the difference between the overall thickness of the mat and the supporting paper minus the one of the paper alone.

Such scattered results are obviously unacceptable, pointing at the impossibility of making any reliable comparison of nanofibrous mats tensile properties made by different research groups. Curves can be reliably compared only within the same type of nanofibrous mats measured with the same instrument and in the same conditions. Nonetheless, even under these assumptions, stress-strain curves may not be comparable when dealing with "extremely low" thickness, as the measurement error compares to the actual measurement value. E and σ_{max} should, instead, be unaffected by the particular specimen geometry, being these values characteristics of the material. Finally, besides all the above considerations on the correct thickness evaluation, an additional issue arises when trying to follow EQUATION 8.1, since the nanofibrous mat is wrongly considered as a bulk material: the voids among nanofibers are assumed to be filled by the polymeric material, leading to a significant underestimation of σ and of all related properties.

8.2.2 • Tensile test data normalized with respect to nanofibrous mat grammage

A general, simple, and reliable method to normalize the load-displacement data for obtaining more comparable stress-strain curves is highly needed. The use of nanofibrous mat grammage (G, in g/m^2, defined as per EQUATION 8.2), which involves the mat mass measurement and its surface area (A, in m^2), may be a viable solution. Hereafter mathematical steps are reported to express stress (σ, in MPa) as a function of grammage (EQUATION 8.3).

$$\sigma = \frac{F}{S}$$

$$\sigma_{eq} = \frac{F}{S_{eq}}$$

$$G = \frac{m}{A} = \frac{m}{L\,w} \qquad\qquad \text{EQUATION 8.2}$$

$$\rho_m = \frac{m}{V_{eq}} = \frac{m}{L\,w\,t_{eq}}$$

$$t_{eq} = \frac{m}{\rho_m L\,w} = \frac{G}{\rho_m}$$

$$\sigma_{eq} = \frac{F}{S_{eq}} = \frac{F}{w\,t_{eq}} = \rho_m \frac{F}{G\,w} \qquad\qquad \text{EQUATION 8.3}$$

where σ_{eq} (in MPa) is the stress "equivalent" to a specimen with the same dimensions (length, L and width, w, both in m) and mass (m, in g), but condensed in a bulk film characterized by equivalents thickness t_{eq} (in μm), volume V_{eq} (in cm^3), and cross-section area S_{eq} (in mm^2); ρ_m is the density (in mg/mm^3) of the electrospun material (1.14 mg/mm^3 for Nylon 66). Applying EQUATION 8.3 to the previously discussed Ny250_dt and Ny250_2dt mats, the resulting stress-strain curves are now closer to each other (FIGURE 8.2).
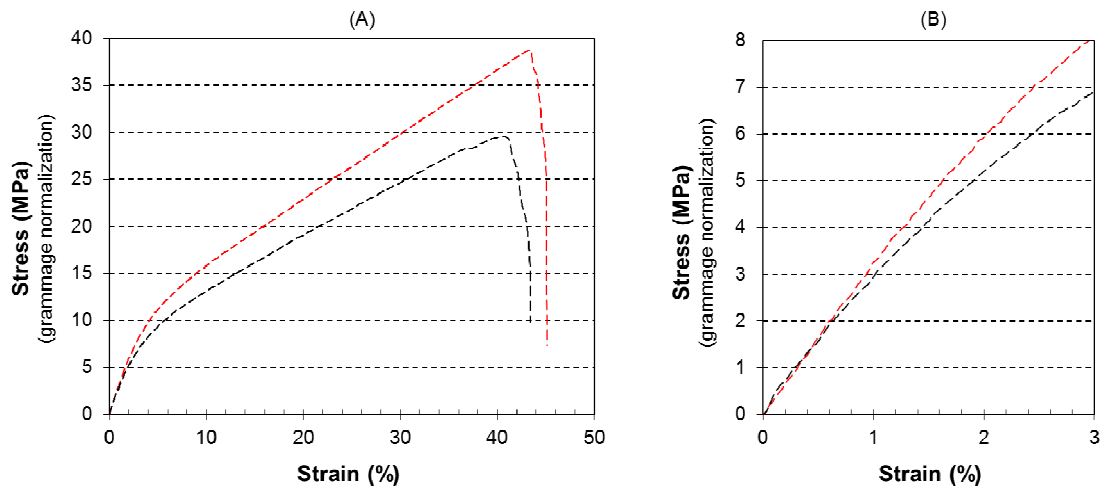
FIGURE 8.2 • (A) Stress-strain curves of the two specimens sampled from Ny250_dt (in red) and Ny250_2dt (in black) mats, obtained following load data normalization based on membrane grammage (EQUATION 8.3); (B) Enlargement of the stress-strain curve in the low deformation range (0÷3 %).

This stress normalization method, however, suffers from some drawbacks too. Indeed, the application of EQUATION 8.3 presumes that the mat grammage is constant across the entire membrane area from which the tensile specimens are sampled out. This assumption, though, may not be true because of the nanofibers additive deposition typical of the electrospinning process, which could lead to local inhomogeneities in fibers distribution. Besides, the grammage evaluation needs a certain amount of material and several measure repetitions to obtain reliable values.

8.2.3 • Tensile test data normalized by means of specimen mass

Using the specimen mass for the load-displacement data normalization, instead of the overall mat grammage, allows for a better match of the recorded load values with the tested specimen, resulting in reliable and absolutely comparable stress-strain curves, as shown in FIGURE 8.3. Hereafter equations are reported to explain the relationship between stress and specimen mass (EQUATION 8.4):

$$\sigma_{eq} = \rho_m \frac{F}{G\,w}$$

$$G = \frac{m}{A} = \frac{m}{L\,w}$$

$$\sigma_{eq} = \rho_m \frac{F}{G\,w} = \rho_m \frac{F}{w} \frac{L\,w}{m} = \rho_m \frac{F}{m} L \qquad\qquad \text{EQUATION 8.4}$$

In this case, the behaviour of the two tested specimens looks utterly comparable: the stress-strain curves are almost superimposed, with a little deviation only at high strain values, in the final nonlinear segment of the curve, where nanomat failure occurs. The differences in the maximum stress are due to the specimens failure mode, usually unpredictable due to peculiar imperfections.
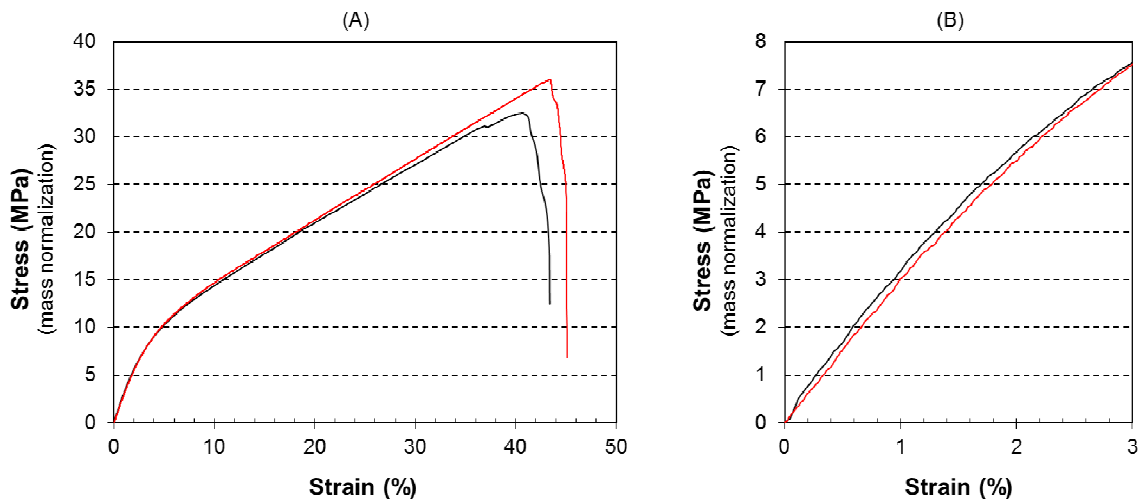

FIGURE 8.3 • (A) Stress-strain curves of the two specimens sampled from Ny250_dt (in red) and Ny250_2dt (in black) mats, obtained according to load normalization based on specimen mass (EQUATION 8.4). (B) Enlargement of the stress-strain curve in the low deformation range (0÷3 %).

By applying this normalization method, it is therefore possible to obtain perfectly reliable and repeatable results, similarly to what happens for bulk materials. A direct comparison between the load normalization based on mat grammage and on specimen mass (according to EQUATION 8.3 and EQUATION 8.4, respectively) is reported in FIGURE 8.4. The graph shows that the use of nanomat grammage for load normalization is less reliable and less convenient than the specimen mass normalization, though it allows to re-normalize tested specimens whose mass is unknown. Whether the specimen

mat grammage nor the nanomat from which the specimens were obtained are unavailable, it is possible to assess the grammage via the linear grammage-thickness relationship, as later demonstrated. Although the grammage normalization of the load is less reliable respect to the mass one, it nevertheless appears better than the "classic" normalization approach based on the specimen cross-section area.
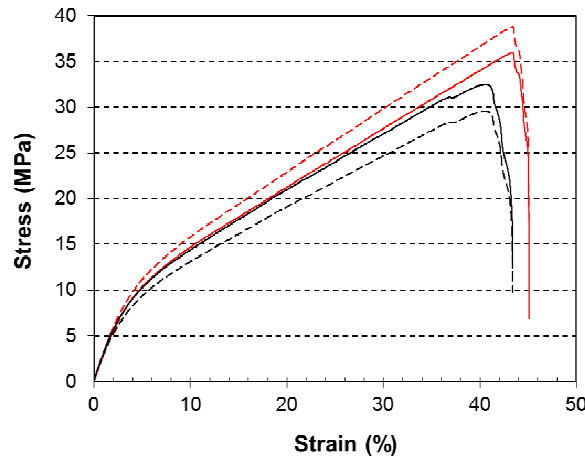

FIGURE 8.4 • Comparison of stress-strain curves of the two specimens sampled from Ny250_dt (in red) and Ny250_2dt (in black) mats, obtained according to load normalization based both on mat grammage (EQUATION 8.3, dashed lines) and on specimen mass (EQUATION 8.4, solid lines).

FIGURE 8.5 shows the comparison between the different approaches to load-displacement curve normalization, reporting for each one its pros and cons.
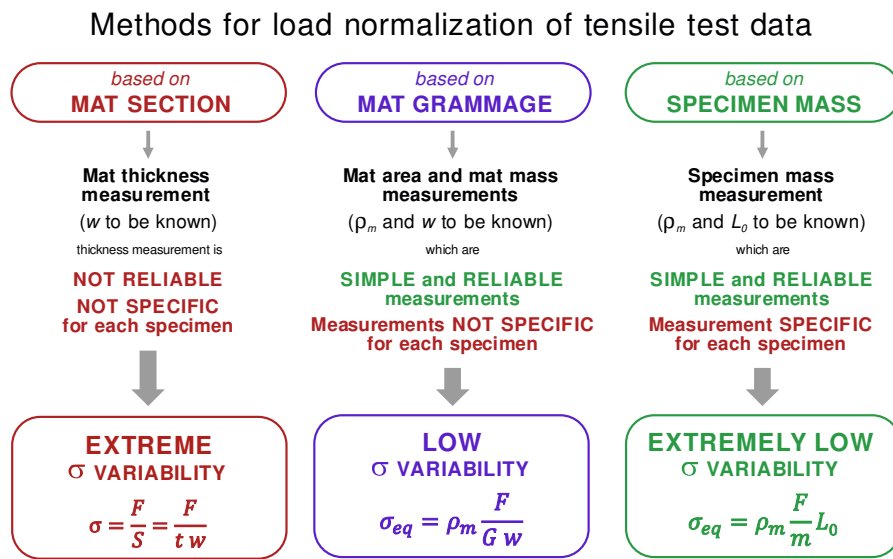

Methods for load normalization of tensile test data

FIGURE 8.5 • Comparison of the different approaches to load normalization.

8.2.4 • Nanomats tensile tests analysis

In this Section the mass normalization approach has been applied to the analysis of tensile tests carried out on different tensile specimen configurations (TABLE 8.3).
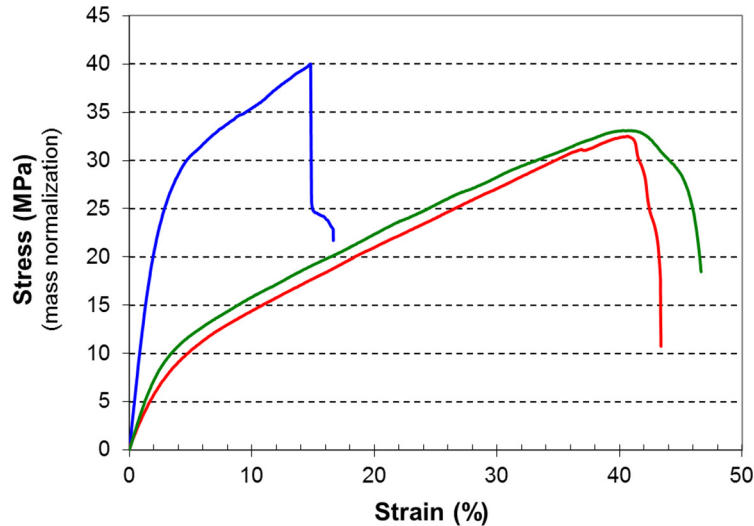

FIGURE 8.6 • Representative stress-strain curves of the three different membrane type (Ny150 blue, Ny250 red, and Ny400 green). The displayed specimens were selected from the 20/45_2dt configuration.

FIGURE 8.6 shows the representative stress-strain curves of the three different membrane types (Ny150, Ny250 and Ny400), while the curves for all the specimen configurations are shown in APPENDIX, SECTION 8.5.3. At first glance, the mechanical behaviour of Ny150 mat is completely different from the other two, which are, instead, very similar. The analysis of these curves will be discussed in detail in the next Sections.

Effect of specimen geometry

Load-displacement curves are characteristic of each specimen, as they are size-dependent. To remove the dependence on geometry, it is necessary to consider the stress-strain curves, which allow characterizing the intrinsic mechanical properties of the material. To evaluate a possible dimensional effect on the mechanical characteristics, for each membrane type several specimens with different dimensions (width, length and grammage, TABLE 8.3) were tested. FIGURE 8.7 shows the elastic modulus and the maximum stress for the specimens obtained from the membrane

Ny250_dt and Ny250_2dt, normalized both on mass (A and C, respectively) and on section (B and D, respectively).

Data from FIGURE 8.7 show that the size of the specimens does not significantly affect both the elastic modulus and the maximum stress. The dramatic differences in numerical values between the two normalization methods are due to the inaccuracies of the section normalization method. Indeed, the thickness measurement, besides not being reliable, also considers the voids inside the nanomat as actively contributing to its response to the tensile stimulus, accounting for a fictious far larger cross-section area than the actual one bearing the load. On the contrary, the mass-based load normalization discards the voids contribution, considering the mat specimen a bulk material characterized by the same length, width and mass, with the exception of the thickness (t_{eq}), and still maintaining the nanofibrous morphology. Similar results were also observed for the Ny150 and Ny400 mat types (histograms are reported in the APPENDIX, SECTION 8.5.4). The results derived from grammage-based load normalization are not presented here because the aim is to compare the effectiveness of the proposed mass-based normalization method with the commonly adopted approach based on section normalization.
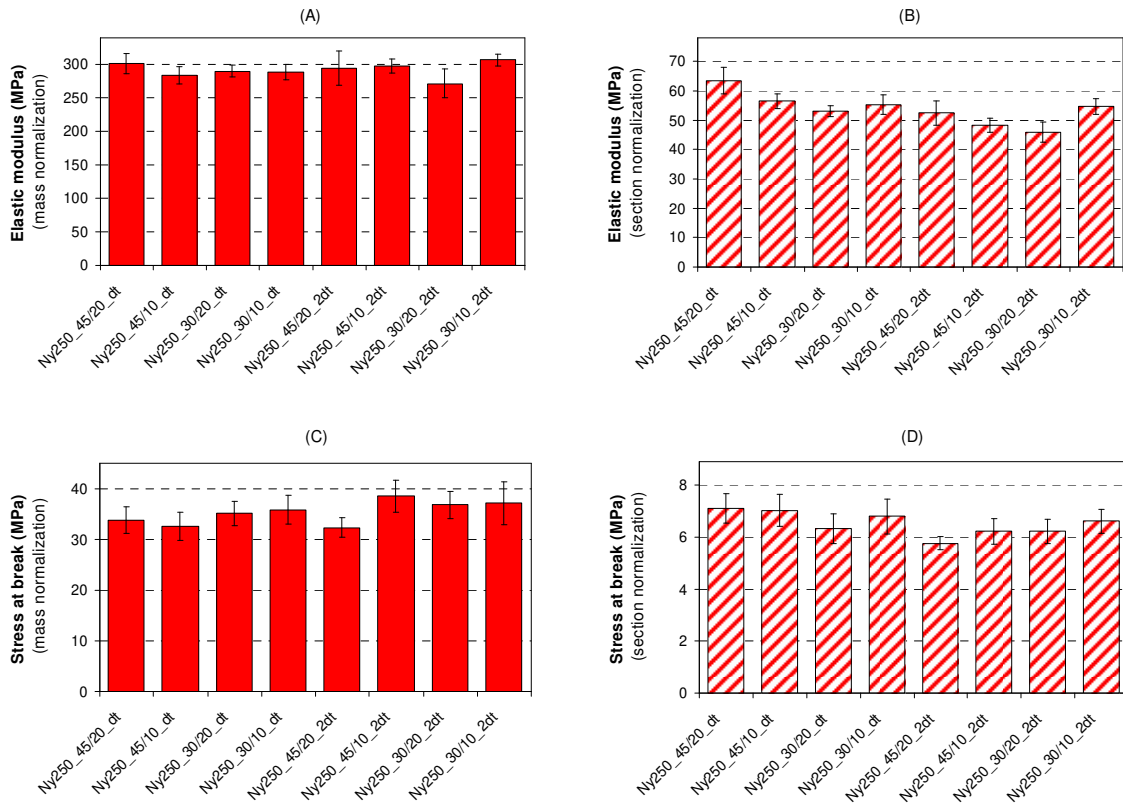
FIGURE 8.7 • Elastic modulus and maximum stress for the specimens obtained from the membrane Ny250_dt and Ny250_2dt, normalized both on mass (A and C respectively, solid filling) and on section (B and D respectively, dotted filling).

Effect of nanofiber diameter

To evaluate the effect of the nanofiber diameter on the mechanical properties of the nanomat, three different types of membranes were electrospun, each characterized by different nanofibers diameter: 150 nm, 250 nm and 400 nm (Ny150, Ny250 and Ny400, respectively).

The histograms show for each specimen configuration the elastic modulus (FIGURE 8.8A), maximum stress (FIGURE 8.8B) and strain at maximum stress (FIGURE 8.8C). Elastic modulus and maximum stress derive from the mass-based load normalization.
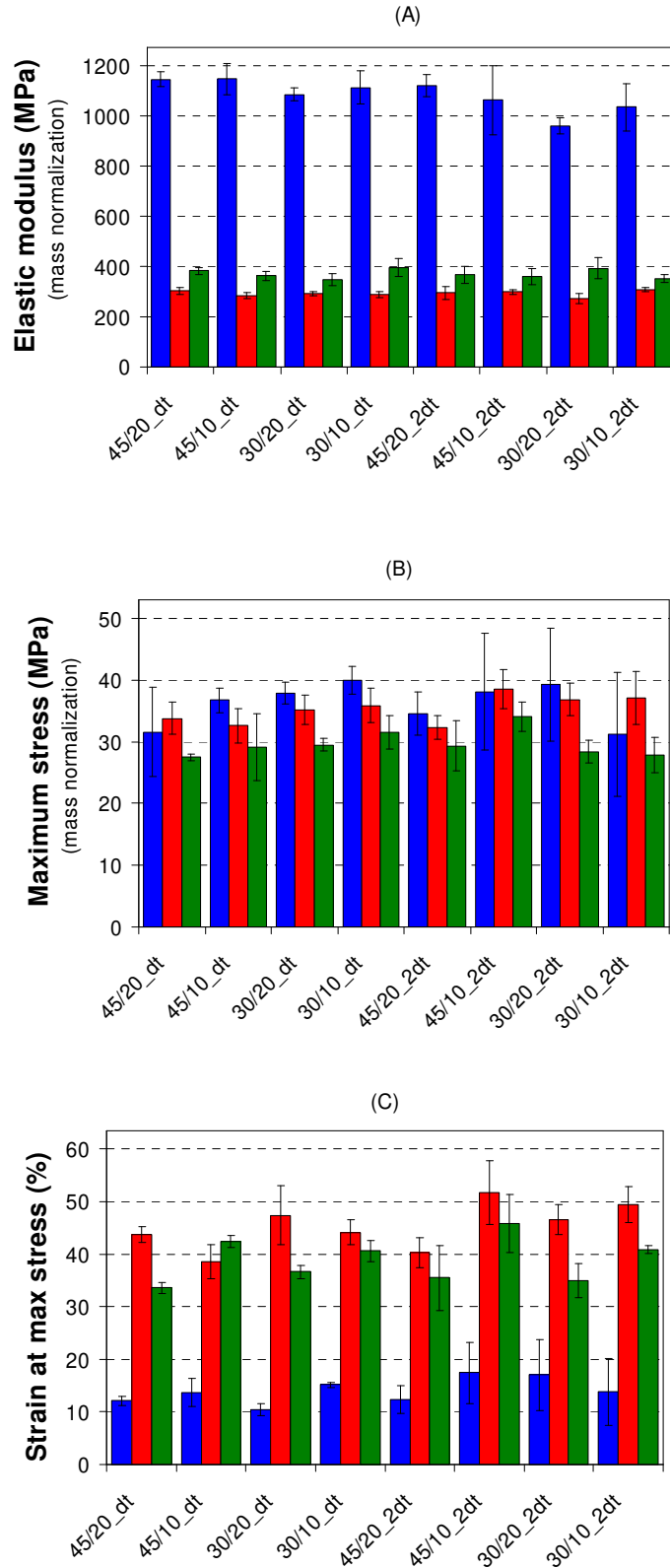
FIGURE 8.8 • (A) Elastic modulus, (B) maximum stress and (C) strain at maximum stress for each specimen configuration reported in TABLE 8.3. In blue Ny150 specimens, in red Ny250 specimens and in green Ny400 specimens.

The tensile properties of each mat type, averaged regardless of the specimen geometry, are collected in TABLE 8.1.

TABLE 8.1 • Average tensile properties for each membrane type.

Membrane type	E (MPa)		σ_{max} (MPa)		$\varepsilon_{\sigma max}$ (%)		U (J/cm^3)	
	Mean ± SD	CV (%)	Mean ± SD	CV (%)	Mean ± SD	CV (%)	Mean ± SD	CV (%)
Ny150	1071 ± 90	8	36 ± 7	19	13 ± 5	38	4.0 ± 1.5	38
Ny250	296 ± 28	9	35 ± 3	9	46 ± 6	13	9.4 ± 1.3	14
Ny400	355 ± 37	10	30 ± 4	13	39 ± 6	15	7.8 ± 1.8	23

The Ny150 membrane type, characterized by a significantly higher elastic modulus than the other two mat types (about three times), is more rigid and consequently displays a more brittle behaviour, with a strain at maximum stress ($\varepsilon_{\sigma max}$) about 1/3 and a halved toughness (U) respect to Ny250 and Ny400. E, σ_{max}, and $\varepsilon_{\sigma max}$ values of the Ny250 and Ny400 membranes are almost comparable, as well as the toughness. It is worth to mention that Ny250 and Ny400 mats show a ductile behaviour, while Ny150 exhibits a more brittle one, as can also be observed from stress-strain curves of FIGURE 8.6.

Two main reasons may be given for explaining the different mechanical behaviour among the mat types: (i) a difference in the polymeric material, such as a variation of the Nylon 66 degree of crystallinity, and (ii) an effect related to the nanofibrous mat morphology, like the number of nanofibers intersections.

The Nylon ability to crystallize may be affected by the processing conditions, which could lead to a different average size of the crystallites and/or affect the degree of crystallinity (see CHAPTER 7). Electrospun Nylon 66 nanofibers may change their degree of crystallinity, as well as the "quality" of the crystallites, depending on the electrospinning solution solvent system [5,33], the presence of nano-reinforcements like graphene which may act as nucleant (see CHAPTER 7), and the nanofiber size [5]. According to Baji *et al.* [5], the fiber diameter strongly affects mechanical properties, resulting in significantly enhanced below a threshold diameter, which in their case was near ≈500 nm for Nylon 66 nanofibers electrospun from a formic acid / dichloromethane solvent system. The nanofibers under study in the present work, especially Ny150 and Ny250, are clearly below this value. Tensile tests, however, show a significant increment

of elastic modulus and strength only for nanofibers with the smallest diameter (150 nm), while thicker fibers mats behave alike. In this context, it is worth mentioning that in the cited work [5] Nylon 66 nanofibers were aligned, while in the present case the tested nanofibers are randomly oriented, so the two cases cannot be straightforwardly compared.

The nanofibrous mats were thus investigated via DSC analysis to evaluate the effect of the nanofiber morphology on the Nylon 66 thermal properties, which may contribute to the observed different mechanical behaviour of the nanomats (FIGURE 8.9).
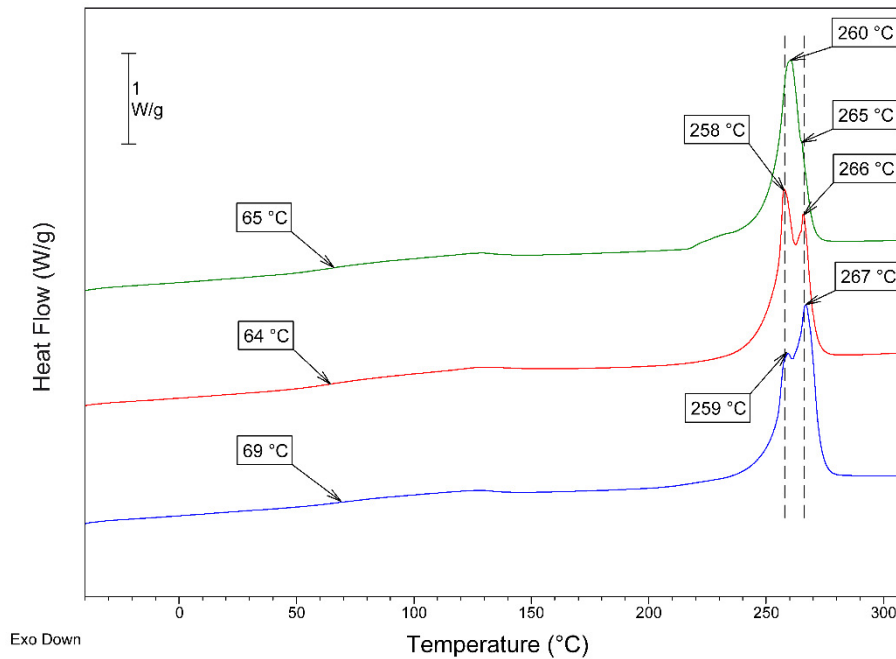

FIGURE 8.9 • DSC analysis of the three membrane types (Ny150 blue, Ny250 red, Ny400 green).

As expected for a semicrystalline polymer, the thermograms show a stepwise variation of the thermal capacity ascribable to the polymer glass transition and an endothermic signal accounting for the melting of the polymer crystalline fraction. The degree of crystallinity (χ_c) was calculated according to the well-known equation:

$$\chi_c = \frac{\Delta H_m}{\Delta H_{m,100\%}} 100$$

where ΔH_m is the melting enthalpy of the sample and $\Delta H_{m,100\%}$ is the melting enthalpy of a hypothetical 100% crystalline Nylon 66, assumed equal to 196 J/g [34]. No differences were found in the χ_c of Ny150, Ny250 and Ny400, which have values of

47%, 45% and 45%, respectively. Analysing their melting peaks, it is worth noting differences in their shape. In particular, the presence of multiple peaks is observed in the mats characterized by fibers with smaller diameters (Ny150 and Ny250), while the Ny400 does not display the peak splitting. The peak positioning (peak temperature) is related to the quality of the crystallites, which present a higher melting temperature for large and more perfect crystals, promoted by the drawing process during electrospinning [33]. The Ny150 and Ny250 present a low-temperature melting peak at 258 °C and a high-temperature one at 266 °C, suggesting a bimodal distribution size of crystals. By contrast, the Ny400 presents an almost symmetrical peak centered at 260 °C, and positioned in the middle of the cited double peaks, with only a very little shoulder at 266 °C. It is worth noting a well pronounced endotherm event at low temperature (onset at 218 °C), which represents the melting of small and less perfect crystallites formed during the nucleation stage of crystallization process. This fraction of crystals, which are anyway counted in the χ_c evaluation, have a less important contribution to the mechanical properties of Nylon. However, since the observed mechanical properties of Ny250 and Ny400 are comparable, the different mechanical behaviour of Ny150 cannot be associated to the differences on their thermal properties. The analysis of the glass transition temperatures (T_gs) shows slight differences, which are not able to justify the high different mechanical behaviours. Indeed, the observed T_gs are almost comparable, with only a slightly higher value for the Ny150 (69 °C vs. 64 °C and 65 °C of Ny250 and Ny400, respectively), accounting for a possible slightly higher orientation of the Nylon 66 amorphous phase of Ny150 mat.

Since the mats thermal behaviour is well comparable, it was investigated whether there is an influence of the nanofibrous morphology on the mechanical properties, particularly the number of intersections between nanofibers (crossings). These can be, for example, localized weldings between nanofibers, electrostatic connections, slipping-resistance points. The knowledge of number and type of intersections, in fact, would be extremely important to interpret the mechanical behaviour of a random nanomat at the macro-scale. While it is very difficult to establish the type of intersections, their numeric estimation is certainly more viable. Different software for image analysis can be adopted for their quantification. However, from SEM micrograph it is impossible to correctly assess the number of intersections through the entire thickness. To this end, an alternative and

easy-to-apply method has been adopted. Several approaches have been proposed to estimate the number of crossings per unit area of stochastic fibrous networks [35–37]. Assuming the nanofibers as infinite length lines, it is possible to model the random mat as a network of lines crossing in points distributed according to a point Poisson process in the plane [36]. As reported in [37], the expected number of crossings per unit area (n_c^{fibers}) depends only on the total fibers length per unit area (τ, in m^{-1}):

$$n_c^{fibers} = \frac{\tau^2}{\pi} \qquad \text{EQUATION 8.5}$$

Assuming a nanofibrous sample consisting of a single continuous cylindrical filament, with an average diameter d, it is possible to estimate its equivalent length (l_{eq}) starting from its volume ($V_{filament}$) by the following steps:

$$V_{filament} = \frac{\pi d^2}{4} l_{eq}$$

$$\frac{m}{\rho_m} = \frac{\pi d^2}{4} l_{eq}$$

$$l_{eq} = \frac{4m}{\rho_m \pi} \frac{1}{d^2} \qquad \text{EQUATION 8.6}$$

where τ is defined as the l_{eq} per unit area (m/m^2). It should be noted that EQUATION 8.5 is true only in the case of two-dimensional networks, as it is assumed that each crossing generates contact between nanofibers. The nanofibers of real networks, instead, may or may not contact each other, depending on the influence of nearby nanofibers. However, considering only 1 g of nanofibers randomly distributed on a 1 m^2, it is reasonably possible to assume that EQUATION 8.5 holds true. By replacing EQUATION 8.6 in EQUATION 8.5, it is possible to estimate n_c^{fibers}, knowing only the mass of the mat (m), the density of the electrospun material (ρ_m), and the average diameter of the nanofibers (d), obtaining:

$$n_c^{fibers} = \frac{16m^2}{\rho_m^2 \pi^3} \frac{1}{d^4} \qquad \text{EQUATION 8.7}$$

FIGURE 8.10 shows, for each nanomat type, the equivalent filament length (l_{eq}) and the number of crossings per unit area (n_c^{fibers}) considering a unitary grammage.

Nanofibrous mat	d	l_{eq}		n_c^{fibers} [a]	
	nm	m	% var.	m^{-2}	% var.
Ny 150	154	4.7E+07	–	7.1E+14	–
Ny 250	256	1.7E+07	-64%	9.3E+13	-87%
Ny 400	405	6.8E+06	-86%	1.5E+13	-98%

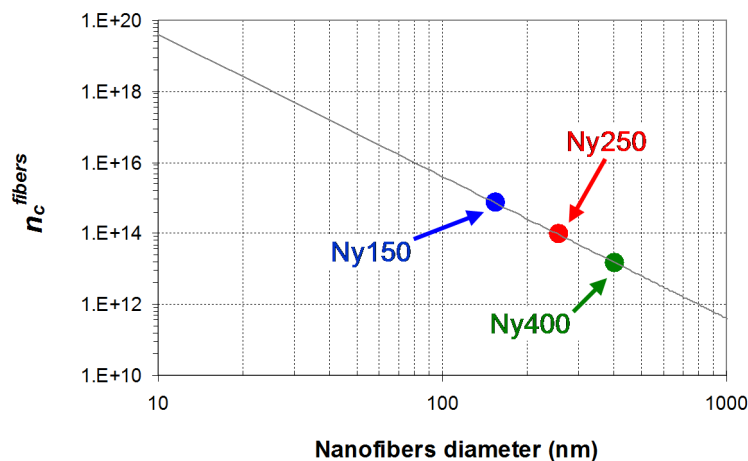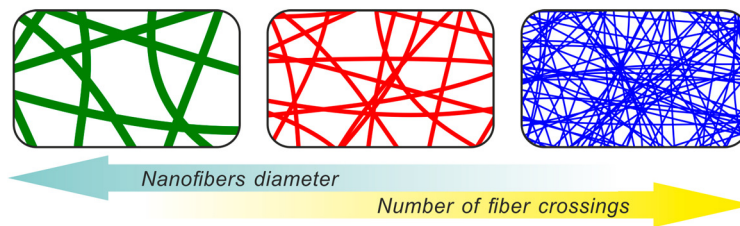[a] evaluated on an area of 1 m^2 for a 1 g of nanofibers (unitary grammage)

FIGURE 8.10 • Equivalent filament length (l_{eq}), number of nanofibers crossings per unit area (n_c^{fibers}) and its plot versus nanofibers diameter (d).

It is interesting to note that l_{eq} is inversely proportional to the square of its diameter (EQUATION 8.6), so nanofibers with smaller diameters determine a higher potential number of intersections. By plotting the number of crossings as a function of the nanofiber diameter in a log-log scale, a linear trend can be observed. Knowing the average value of the nanofiber diameter, it is possible to estimate the n_c^{fibers} for different nanomats, provided the same material is used. It can be observed that the calculated crossing number for the Ny250 and the Ny400 mats are 87% and 98% lower than the Ny150 one, respectively. Given the high difference in the number of n_c^{fibers} that

characterize each nanomat, it can therefore be assumed that the changes in mechanical behaviour are mainly ascribable to this aspect. A similar result was also observed in a numerical study on the mechanical characterization of 2D fibrous networks [38]. As shown in TABLE 8.1, elastic modulus, strain at maximum stress and toughness values of Ny150 mat are substantially different from those of Ny250 and Ny400 membranes, which instead do not diverge significantly in between each other. Therefore, it can be supposed that there is a threshold value of the nanofibers diameter, in the range 150÷250 nm, that leads to a substantial change in the macro-scale mechanical behaviour, and it can be hypothesized that the number of nanofibers crossings is also connected to this aspect. For a high number of crossings (in the case under investigation more than 10^{14} for unitary grammage), indeed, the mechanical properties are higher and the behaviour more brittle. The crossings estimation and the application of the data fitting model explained in the next subsection are applicable only for random fibrous network and not for aligned fibrous mats.

8.2.5 • *Application of the phenomenological data fitting model*

Tensile stress-strain curves of mats with randomly oriented fibers have a peculiar shape, which displays a nonlinear trend followed by a linear one, as largely found in the literature [21,24,29–32,39–42] and presented in CHAPTERS 2 and 7). The tested mats show this behaviour too: the stiffness decreases from an initial value down to an asymptotic constant trend for high strains. In particular, the mechanical behaviour is characterized by three main stages: an initial nonlinear trend (Stage I), followed by a linear one (Stage II), and finally an additional nonlinear behaviour where the stress reaches a maximum value before mat failure (Stage III). To better understand the phenomena the application of a data fitting model can help. The calculated stress (σ) can be expressed as the superimposition of two stress contributions: a linear one (σ_1) and a nonlinear one (σ_2), formulated as in the following equation:

$$\sigma(\varepsilon) = \sigma_1(\varepsilon) - \sigma_2(\varepsilon) = (a\varepsilon + b) - (be^{-c\varepsilon}) = a\varepsilon + b(1 - e^{-c\varepsilon}) \qquad \text{EQUATION 8.8}$$

where *a*, *b* and *c* are parameters experimentally determined to obtain the data fitting. In the present work, the solver tool implemented in Microsoft Excel was used for minimizing the sum of square error (method of least squares).

In FIGURE 8.11A the comparison between the experimental stress-strain curve and the data fitting curve is shown for Ny250 mat (Ny250_20/45_2dt), as well as the average data fitting parameters resulting from the application of EQUATION 8.8 to all the tested specimens.
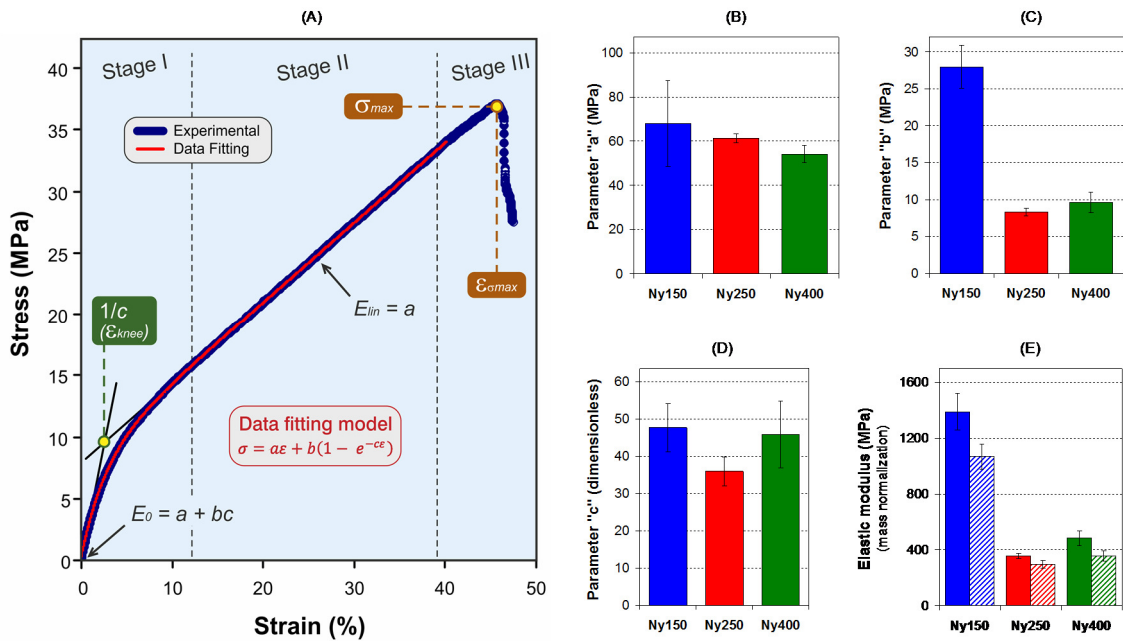

FIGURE 8.11 • (A) Application of the data fitting model to Ny250_20/45_2dt stress-strain curve. (B-D) average data fitting parameter for Ny150 (blue), Ny250 (red) and Ny400 (green) mats. (E) Comparison between E_0 calculated as per EQUATION 8.9 (solid colours) and the elastic modulus calculated as the slope of the tangent to the stress-strain curve (dashed).

In FIGURE 8.12 an example of the data fitting is presented for each representative sample.
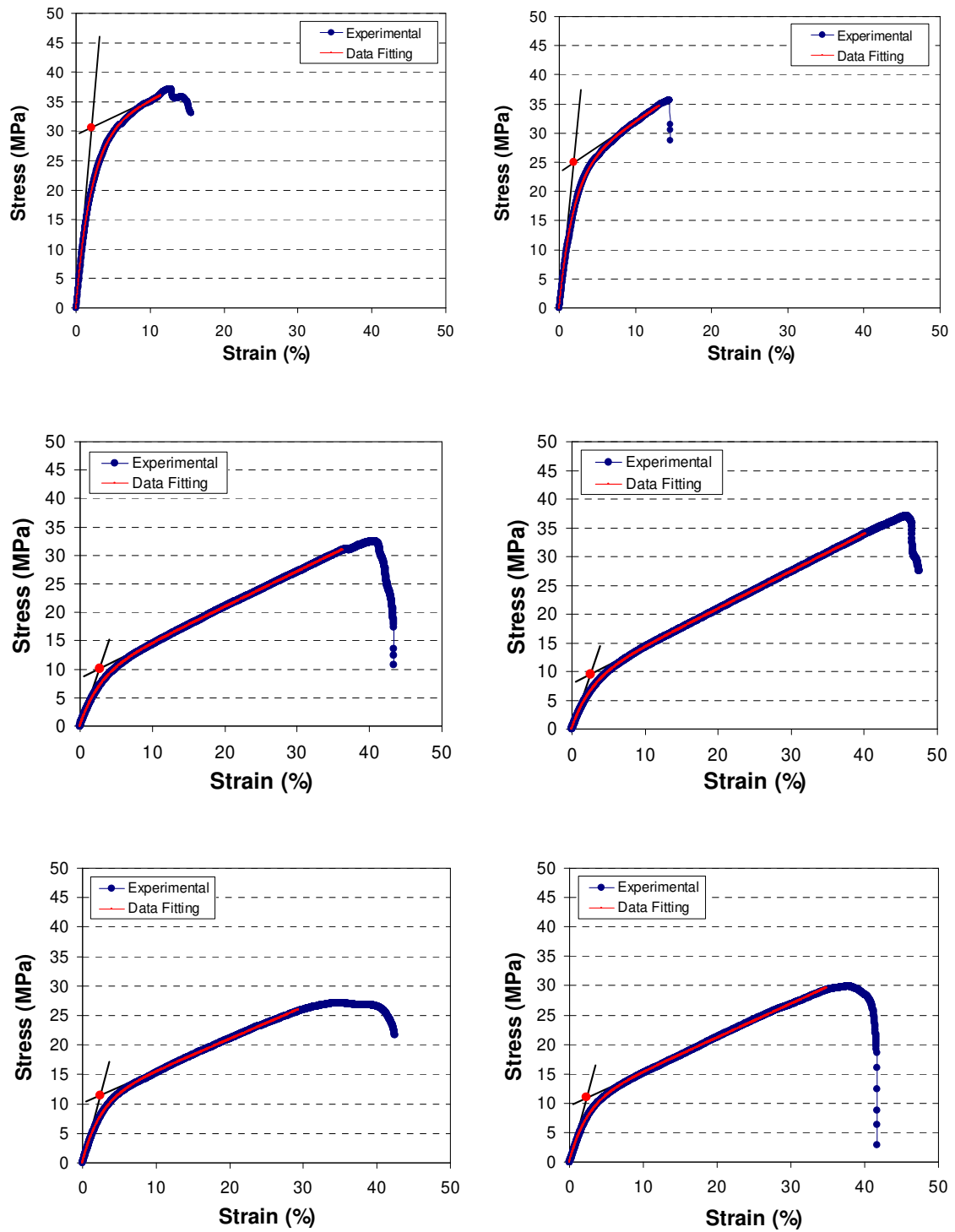
FIGURE 8.12 • Comparison between experimental stress-strain curve and data fitting model for some nanomats of Ny150 (1st row), Ny250 (2nd row) and Ny400 (3rd row) for the configurations 20/45_dt (left column) and 20/45_2dt (right column).

While the common analysis of stress-strain curves involves, mainly, the determination of Young's modulus and the properties at break, the use of the present data fitting model allows to thoroughly analyse the mechanical behaviour of the nonwoven mat.

The elastic modulus is commonly expressed as the slope of the tangent to the stress-strain curve at a low strain. This approach was applied for the elastic modulus calculation in SECTIONS 3.4.1 and 3.4.2, and in APPENDIX, SECTION 8.54, by means of the linear regression of the stress-strain data at the early strain stage (0÷1 %). However, the mat is characterized by a nonlinear trend and a subsequent linear one, as clearly displayed in FIGURE 8.11A. The linear trend, which appears at "higher" strains, should also be considered for a thorough evaluation of the mat tensile properties.

By deriving the stress, as expressed in EQUATION 8.8, respect to the strain, the following relation represents the slope of the tangent to the stress-strain curve:

$$\frac{d\sigma}{d\varepsilon} = E(\varepsilon) = a + bce^{-c\varepsilon}$$

where $E(\varepsilon)$ describes the local material stiffness as a function of the strain. This relation is useful for evaluating the mat stiffness at very low (for $\varepsilon \to 0$) and at very high (for $\varepsilon \to \infty$) strains, allowing to define an initial mat stiffness (or initial Young's modulus, E_0, EQUATION 8.9), and an asymptotic constant stiffness (or the Young's modulus of the linear trend of stress-strain curve, E_{lin}, EQUATION 8.10):

$$E_0 = \underset{\varepsilon \to 0}{Lim} E(\varepsilon) = a + bc \qquad \text{EQUATION 8.9}$$

$$E_{lin} = \underset{\varepsilon \to \infty}{Lim} E(\varepsilon) = a \qquad \text{EQUATION 8.10}$$

Therefore, the mat is characterized by two elastic moduli, E_0 and E_{lin}, accounting for two distinct material behaviours. E_0 is shown in FIGURE 8.11E, as well as the elastic modulus calculated as the slope of the tangent to the stress-strain curve (same data in TABLE 8.1) for the sake of comparison. E_{lin} values, corresponding to a parameter, are shown in histograms of FIGURE 8.11B.

The elastic moduli calculated with the two approaches show a similar trend, but are different in absolute values: on average, E_0 is from one fourth (Ny250) to one third (Ny150 and Ny400) higher than the "classically" determined elastic modulus. This

discrepancy can be explained considering the nonlinear trend displayed by the stress-strain curve in Stage I. At a first look, the curve seems to have an initial "linear" trend and, consequently, a proportional limit within the Hooke's law ($\sigma = E \cdot \varepsilon$) is valid. Deep focus on the curve shows that no Hookean region is detectable, not even for as low a strain as the range considered for the slope determination (0÷1 %). Indeed, the mat local stiffness lowers progressively, as clearly evidenced by the trend of $E(\varepsilon)$. E_0, being the extrapolation of the mat elastic modulus at null strain (for $\varepsilon \rightarrow 0$), has a higher value respect to any other elastic modulus value calculated by the slope tangent method. Consequently, E_0 should be considered a "theoretical" elastic modulus. Nonetheless, it may be useful to obtain a value which is operator-independent, contrarily to the slope tangent method which suffers from the specific strain range considered.

According to EQUATION 8.9 and EQUATION 8.10, E_0 and E_{lin} are only functions of the parameters a, b, c, therefore their deeper analysis may help to interpret the mat mechanical behaviour. The comparison of the experimental parameters (FIGURE 8.11B-D), averaged from the data obtained from all the tested specimen geometries, highlights a significant difference in the b parameter of Ny150 (28±3 MPa) respect to Ny250 and Ny400, that are statistically comparable (8.3±0.5 and 9.6±1.4 MPa, respectively). The other two parameters, a and c, seem to be unrelated to the geometrical/morphological factors of the nanofibrous mat.

The a parameter, as declared by EQUATION 8.10, represents the mat elastic modulus in the linear trend at high strain (Stage II). The obtained values are comparable for all the mat types (54÷68 MPa). In that region the membrane already underwent large deformations: as a result, the fibers, still random at a nanoscale level, are growing oriented in the direction of the applied load. In these conditions, the resulting stiffness should be mostly related to the intrinsic mechanical properties of the material, regardless of its morphology. The a mean value, irrespective of the standard deviation, becomes slightly lower as the diameter increases: this may be attributed to the different mechanical properties derived by the differences of the polymer crystallites "quality", as highlighted by DSC analysis (Section 3.4.2). The high standard deviation of the a parameter in Ny150 (coefficient of variation of 29%, respect to 3% and 8% for Ny250 and Ny400, respectively) stems from the troubles in applying the data fitting model to mats with brittle behaviour, which do not display a sufficient linear trend extension (Stage II).

The b parameter is involved in both σ_1 and σ_2 (EQUATION 8.8), but its contribution is different depending on the strain region considered. At very low strains (for $\varepsilon \to 0$), both σ_1 and σ_2 converge to b value. While, at high strains, σ_1 and σ_2 are partially affected by this parameter. Consequently, the b impact on the resulting $\sigma(\varepsilon)$ is significant in Stage I (nonlinear region), where b acts as a multiplier of the exponential $e^{-c\varepsilon}$. σ_2 describes how rapidly the stress-strain curve deviates from the linear trend at low strains.

The c parameter refers to the region where the stress-strain curve change slope from the E_0 value to the E_{lin} one. More specifically, $1/c$ represents the onset extrapolation of the slope change (ε_{knee}), as can be derived from EQUATIONS 2.7 and 2.8 reported in CHAPTER 2. Ny150 and Ny400 have a similar average c (48 and 46, respectively) which corresponds to $\varepsilon_{knee} = 0.0021$, while Ny250 has $c = 36$ and consequently a higher ε_{knee} (0.0028). All the c values are statistically comparable, nonetheless. This parameter affects only σ_2 and, similarly to b, contributes to $\sigma(\varepsilon)$ via the exponential term.

Since a significant difference is found only for b parameter (for Ny150 mat is three times higher), it is possible to assume that this parameter is related to the morphology of the nanofibrous mat, and in particular to the number of intersections. It is interesting to note that the same trend has been found for the experimental elastic modulus (FIGURE 8.8A and TABLE 8.1).

8.2.6 • Grammage-thickness relationship for grammage re-normalization of load-displacement curves

Finally, with the aim to characterize nanofibrous mats not only mechanically but also morphologically, a study was carried out to assess whether there is a relationship between the thickness and the grammage of a nanomat. This relationship is easily predictable for bulk materials, but it is not for nonwoven fabrics, and particularly for electrospun nanomats, which contain a high fraction of voids. Moreover, this analysis is useful for the grammage re-normalization of load-displacement curves previously normalized on the cross-section area, for which only the thickness of the mat is known. To this end, for each membrane type, thickness, weight, and area (and therefore grammage) of the nanofibrous patches were assessed (detailed description in Sections 2.2 and 2.3 in APPENDIX, SECTIONS 8.5.1 and 8.5.2). At this stage, only one instrument

was used for thickness assessment to obtain comparable measurements. The instrument used is the analog indicator 2 in the low-pressure configuration (iv, TABLE 3), as it allows to compare the measured values with an acceptable resolution. In the following equations the steps to obtain the relationship between the grammage G and the thickness t of the nanomat are reported. By knowing the density ρ_m of the electrospun material, it is possible to express the mass m of the mat as a function of the fiber volume V_f ($m = \rho_m V_f$). Furthermore, the percentage fiber volume $V_{f\%}$ can be expressed as the ratio between the fiber volume V_f and the total volume V of the mat:

$$V_{f\%} = \frac{V_f}{V} = \frac{V_f}{L\,w\,t}$$

where L, w and t are the length, width, and thickness of the nanomat. According to EQUATION 8.2, concerning the grammage G of the nanofibrous mat, and replacing the previous equations, it can be proven that:

$$G = \frac{m}{L\,w} = \frac{\rho_m V_f}{L\,w} = \frac{\rho_m V_{f\%}\,L\,w\,t}{L\,w} = \rho_m V_{f\%}\,t \qquad \text{EQUATION 8.11}$$

EQUATION 8.11 clearly displays the linear relationship between grammage and thickness. This dependence can also be experimentally proved by plotting the values of grammage assessed for each patch as a function of the nanomat thickness (FIGURE 1.13). In the graph are shown the experimental data in terms of the percentage fiber volume $V_{f\%}$ (evaluated via EQUATION 8.11) and are also reported the angular coefficient α of the linear regression lines for each type of membrane. Interestingly, as the nanofibers diameter increases (from Ny150 to Ny400) the slope of the linear regression line, and thus the angular coefficient α, increases ($G = \alpha\,t$). Consequently, it is worth pointing out that to obtain the same grammage with smaller nanofibers diameter (smaller α), it is necessary to electrospin thicker membranes.
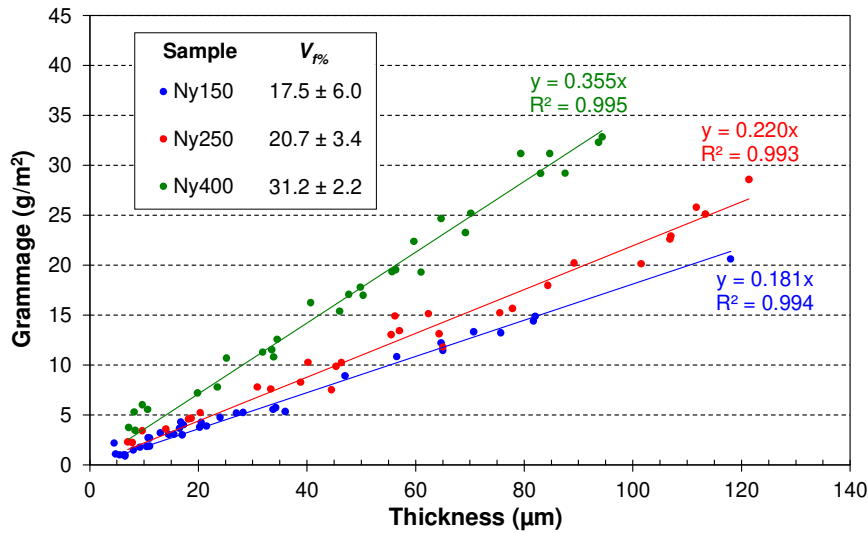
FIGURE 1.13 • Grammage-thickness plot. The coloured dots represent the experimental measurements, while the regression lines represent the calibration lines for each type of membrane (Ny150, Ny200, and Ny400).

This also means that smaller diameter nanofibers generate a higher percentage of porosity during the electrospinning deposition process. Indeed, rearranging EQUATION 8.11, higher diameters (higher α) correspond to higher $V_{f\%}$:

$$V_{f\%} = \frac{G}{\rho_m\, t} = \frac{\alpha\, t}{\rho_m\, t} = \frac{\alpha}{\rho_m} \qquad\qquad \text{EQUATION 8.12}$$

Observing the experimental data (reported in the inset of FIGURE 1.13), a linear relationship between the diameter of the nanofibers and the percentage of fiber volume $V_{f\%}$ was found. The grammage-thickness plot allows to re-normalize previous tensile tests in which the load had been normalized as a function of the cross-section area. In fact, having the calibration lines (in the present study reported for different Nylon 66 mats), it is possible to determine the grammage of any type of nanofibrous mat knowing its thickness.

The grammage-thickness plot allows to re-normalize previous tensile tests in which the load had been normalized respect to the cross-section area. In fact, having the calibration lines (FIGURE 13), it is possible to determine the grammage of any type of nanofibrous mat knowing its thickness. Therefore, given the grammage, it is possible to apply EQUATION 8.3 to obtain more reliable stress-strain curves based on grammage

normalization. The diagram (FIGURE 8.14) shows the possible scenarios, and the relative ways to re-normalize the load data with respect to the mat grammage.
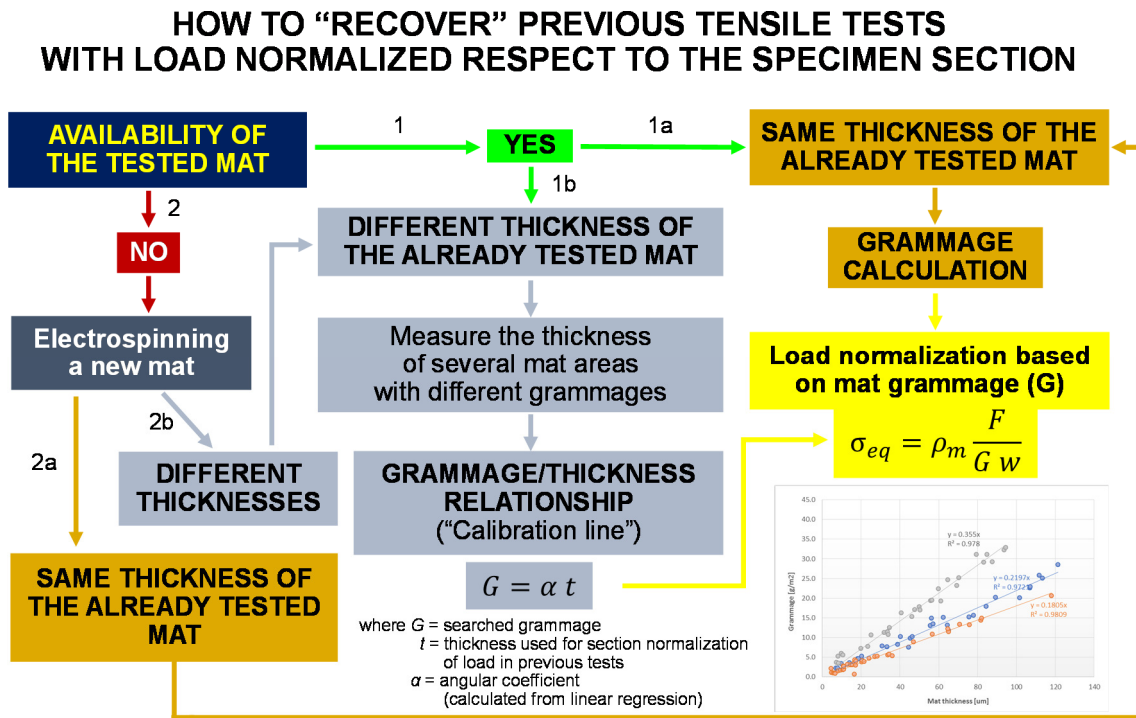

FIGURE 8.14 • Logical diagram to "recover" previous tensile tests with load normalized respect to the specimen cross-section area

If a piece of already tested mat is available (*path 1*), the re-normalization is readily applicable in case the mat has the same thickness (*case 1a*), or possible after the construction of the "calibration line" (*case 1b*). On the contrary, if the tested mat is no longer available, it is necessary to electrospin a new mat (*path 2*) using the previously adopted solution and process parameters, and proceed following *case 2a* or *case 2b* depending on the situation. To apply this method, it is mandatory to adopt the same thickness measuring tool used for the previous cross-section area normalizations.

8.3 • MATERIALS AND METHODS

8.3.1 • Materials

Nylon 66 (Zytel E53 NC010 kindly provided by DuPont) was dried in a stove at 110 °C for minimum 6 hours before use. Trifluoroacetic acid (TFA), formic acid, and chloroform, all reagent grade, were purchased from Sigma-Aldrich and used without further purifications.

8.3.2 • Nylon 66 solutions and nanofibrous mats production

Nylon 66 solutions having a concentration of 9, 13 and 18%wt were prepared in a TFA/formic acid/chloroform 10:60:30 %vol. (11:55:34 wt%) solvent system. Solutions were made dissolving Nylon 66 pellets under magnetic stirring and mild heating (maximum 50 °C) until complete polymer dissolution.

Nanofibrous mats were produced via electrospinning process, with a Spinbow® electrospinning machine unit equipped with four 5 mL syringes (needles 55 mm length and 0.84 mm internal diameter). Fibers were collected on a rotating drum of 150 mm diameter (tangential speed: 0.39 m/s) covered with poly(ethylene)-coated paper. Mats have final dimensions of approximately 350 × 450 mm and they were labelled Ny*XXX* according to the rough average diameter of the obtained fibers. In TABLE 8.2 electrospinning process and environmental parameters for mats production are reported.

TABLE 8.2 • Electrospinning process parameters and nanofibers diameters of produced nanofibrous mats.

Nanofibrous mat	Nylon concentration	Flow rate	Electric potential	Distance	Electric field[a]	Temperature	Relative humidity	Nanofibers diameter[b]
	%wt	mL/h	kV	cm	kV/cm	°C	%	nm
Ny150	9	0.30	21.0	7.0	3.0	20-22	25-28	154 ± 38
Ny250	13	0.80	25.0	6.0	4.2	24-26	28-31	256 ± 42
Ny400	18	0.80	25.0	7.0	3.6	20-22	26-28	405 ± 84

[a] calculated as electric potential to distance ratio

[b] average values derived from at least 100 diameter measurements on SEM micrographs, manually done on single nanofibers by means of the Photoshop measurement tool

For tensile testing, two nanofibrous mats for each membrane type (Ny150, Ny250 and Ny400) were electrospun for a deposition time one twice the other (dt and 2dt), for a

total of 6 nanomats. Nanofibrous mats for the grammage-thickness relationship assessment were electrospun, picking a membrane strip from the drum (approximately 350 × 60 mm) every 45 minutes up to 270', obtaining 6 strips with incremental deposition time (detailed procedure in APPENDIX, SECTION 8.5.1).

8.3.3 • Characterization of nanofibrous mats and grammage/thickness evaluation

Nanofibrous mats were analysed by Scanning Electron Microscopy (SEM, Phenom ProX) to determine nanofibers morphology, after gold sputtering. SEM images of the three nanofibrous mat types under analysis are shown in FIGURE 8.15. Nanofibers diameter, determined measuring at least 50 fibers by an image analysis software, is given as average diameter ± standard deviation in TABLE 8.2.
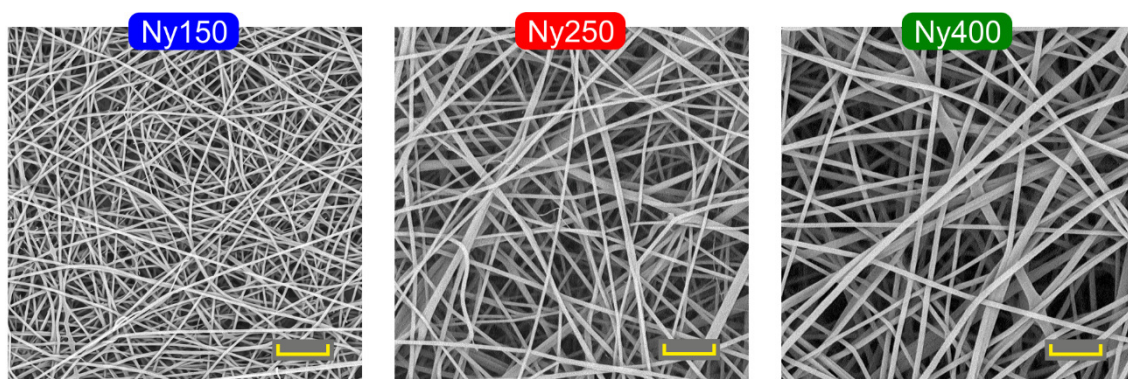

FIGURE 8.15 • SEM images of the three nanomat types. Scale bar: 4μm.

Differential Scanning Calorimetry (DSC) analyses were carried out on a TA Instruments Q2000 DSC Modulated apparatus equipped with RCS cooling system, calibrated with Indium standard. A sample of 7 mg was heated from 20 °C to 120 °C, cooled to –60 °C, then heated again to 320 °C in nitrogen atmosphere (heating/cooling rate 20 °C/min).

Tensile tests were carried out using a Remet TC10 universal testing machine equipped with a 10 N load cell, with a crosshead separation speed of 10 mm/min. Tensile specimens were prepared anchoring the membrane to a paper frame for better handling and to avoid any nanofibers slippage in the machine fixtures, cutting the frame before the test started, as reported in CHAPTER 7, SECTION 7.2.4. Specimens dimensions are reported in TABLE 8.3. For each membrane type (Ny150, Ny250 and Ny400) two mats

were electrospun, one with a deposition time twice as long as the other (called dt and 2dt). Each tensile specimen is identified by the name of the membrane type (Ny*XXX*) followed by the specimen configuration. Elastic modulus was determined via linear regression of stress-strain data in the strain range 0÷1 % for all tested specimens (the selection of this specific range was based on the minimization of the linear fitting error).

TABLE 8.3 • Details of tensile tests specimens.

Tensile specimen configuration	Specimen width (w)	Specimen gage length (L)
	mm	mm
Ny*XXX*_10/30_dt	10	30
Ny*XXX*_10/30_2dt	10	30
Ny*XXX*_10/45_dt	10	45
Ny*XXX*_10/45_2dt	10	45
Ny*XXX*_20/30_dt	20	30
Ny*XXX*_20/30_2dt	20	30
Ny*XXX*_20/45_dt	20	45
Ny*XXX*_20/45_2dt	20	45

Ny*XXX* : membrane type (Ny150, Ny250, Ny400)

Membranes thickness was evaluated using 6 different instruments: (i) a scanning electron microscope, (ii) an analog centesimal indicator, (iii) a digital millesimal indicator, (iv) an analog millesimal indicator with two different pressure configurations, (v) a micrometer and (vi) a digital caliper. SEM measurements were carried out on liquid nitrogen fractured mat sections. Details of the resolution and applied pressure by each measurement tool are reported in TABLE 8.4.

TABLE 8.4 • Technical specifications of measurement tools used for evaluating membranes thickness.

	i	ii	iii	iv	v	vi
Instrument	SEM	Analog indicator 1	Digital indicator	Analog indicator 2	Analog micrometer	Digital caliper
Type of measurment	Electron Microscopy	Mechanical	Mechanical	Mechanical	Mechanical	Mechanical
Producer	Phenom ProX PhenomWorld Netherlands	Borletti Italy	Alpa MegaRod Italy	Borletti Italy	Holex Germany	Alpa Italy
Resolution	≤ 8 nm	10 µm	1 µm	1 µm	10 µm	10 µm
Pressure	n.d.	83 g/cm^2	94 g/cm^2	Low config. 360 g/cm^2 High config. 1062 g/cm^2	Depending on operator	Depending on operator
Color identification				Low configuration / High configuration		

Regarding grammage-thickness relationship, from each membrane strip 5 patches were extracted (nominally 60×25 mm) from different positions along the strip (FIGURE 8.17 in APPENDIX, SECTION 8.5.1). The mat thickness was measured using the analog indicator 2 in the low-pressure configuration (iv, TABLE 8.4), as it allows to compare the measured values with an acceptable resolution. The mat mass was determined using a AS 60/220.R2 Radwag scale with a resolution of 0.01 mg. Detailed description and representation of the adopted procedure are reported in APPENDIX, SECTION 8.5.1. The patch area was evaluated via Matlab software by image processing of scanned images (see APPENDIX, SECTION 8.5.2).

8.4 • CONCLUSIONS

The high porosity, flexibility, and deformability of nanofibrous nonwovens make troublesome their tensile testing, severely affecting results reliability. In this work an accurate, systematic, and critical study concerning tensile testing of nonwoven mats, using electrospun Nylon 66 nanofibrous membranes as a case study has been presented, with three randomly-oriented nanofibrous mats with a different diameter (Ny150, Ny250, and Ny400) were produced, then morphologically, mechanically and thermally characterized. In this frame, the "classical" approach to load normalization by means of specimen cross-section area was compared to a mass-based normalization proposed by the Authors, as well as a normalization based on the mat grammage, overcoming the trouble of the nanomat thickness measurement. The mass-based normalization method allows to obtain reliable and repeatable results, similarly to what happens for bulk materials. Although the grammage-based normalization is less reliable respect to the mass-based one, the use of mat grammage proved to provide better results than the "classic" normalization approach based on the specimen cross-section area. Moreover, the grammage-based method allows to re-normalize already tested specimens whose load-displacement curves were previously normalized on the cross-section area, thus benefitting of improved reliability and comparability of old data. Indeed, a linear dependence between these two parameters was found, whose angular coefficient depends on the nanofiber morphology.

Nanofibrous mat characteristics, such as nanofibers diameter, grammage, and specimen geometry (width and gauge length) were deeply investigated and the mats mechanical performances were interpreted also considering the polymer properties (degree of crystallinity and glass transition temperature), as well as the number of potential nanofibers crossings as a function of the nanofiber diameter. The tensile properties are found mainly dependent on the nanofibers diameter, which in turn strongly impacts the number of nanofibers crossings. Below a threshold value, which lies between 150÷250 nm, the overall mat mechanical behaviour changes from ductile to brittle. At the same time, the elastic modulus has a significant boost, while the mat strength is not affected. In particular, for the Ny150 membrane a Young's modulus of 1071 MPa was found, about three times respect to the other mats under investigation (296 MPa for Ny250 and

355 MPa for Ny400, respectively). Moreover, the experimental stress-strain data were analysed using a phenomenological data fitting model to better interpret the tensile mechanical properties.

The experimental results demonstrate the higher reliability of the proposed mass-based load normalization, providing a simple, effective and universally applicable method for obtaining tensile stress-strain curves characterized by high reproducibility.

8.5 • APPENDIX

8.5.1 • *Specimens for grammage-thickness relationship*

For the grammage-thickness relationship assessment, a nanomat for each membrane type (Ny150, Ny250 and Ny400) was electrospun for a total time of 270 min. For each membrane type, 6 poly(ethylene)-coated paper strips (with a dimension of 350×60 mm approximately) were fixed with the tape onto the collecting drum, as reported in FIGURE 8.16. During the electrospinning process, a membrane strip was picked from the drum every 45 minutes, so obtaining 6 strips with incremental deposition time for each membrane type.
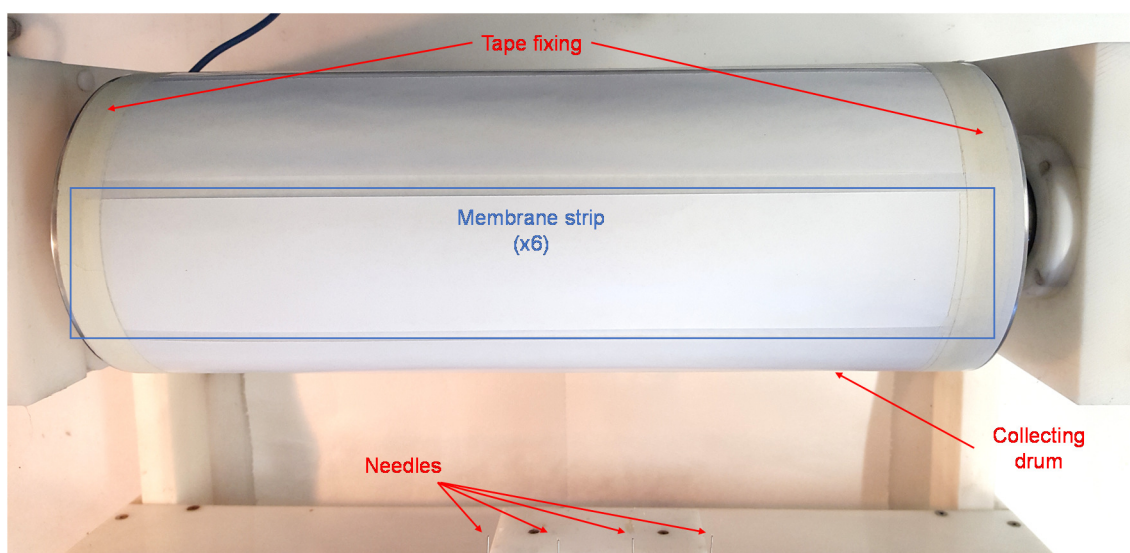

FIGURE 8.16 • Electrospinning set-up for the grammage-thickness relationship

At the end of the electrospinning process, from each membrane strip 5 patches with a nominal size of 60×25 mm were extracted. As reported in FIGURE 8.17, the sampling positions of the patches were: left (L), center-left (CL), center (C), center-right (CR), right (R). In this way, 30 patches were obtained for each type of membrane, resulting in an overall amount of 90 patches.
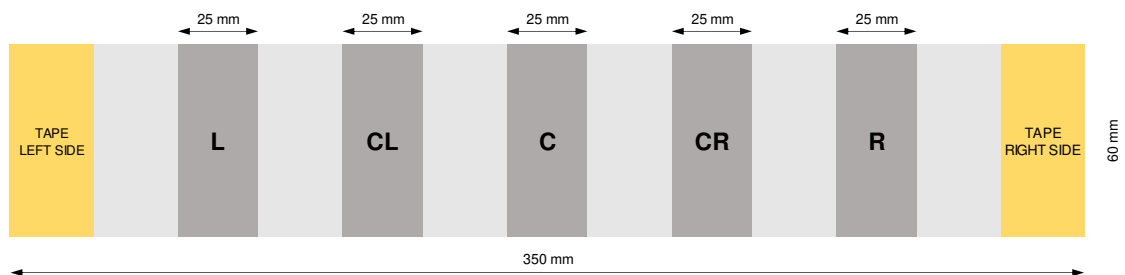
FIGURE 8.17 • Patches sampling positions for each membrane strip

For each patch, thickness, weight, and area of the nanofibrous mat were assessed. To evaluate the mat thickness, the overall thickness of the nanofibrous mat together with the supporting paper was measured in 6 different equidistant zones (red dots FIGURE 8.18). Then the thickness of the sole support paper was measured in the same zones to determine the membrane thickness by difference.
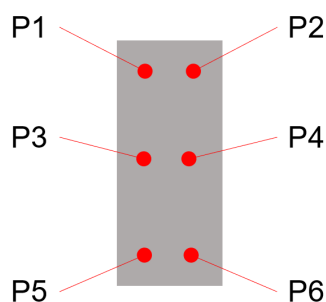

FIGURE 8.18 • Sampling positions for mat thickness evaluation

The 6 thickness values for each patch were averaged and used, together with the mass and area values, to build the grammage-thickness graph (FIGURE 1.13). That required a total of 1080 thickness measurements. At this stage, only one instrument was used for thickness measurement to obtain comparable measurements. The analog indicator 2 in the low-pressure configuration (iv, TABLE 8.4) was used, as it allows to compare the measured values with an acceptable resolution.

The mat mass from each patch was determined by weight (nanofibrous mat with paper support minus supporting paper) using a AS 60/220.R2 Radwag scale with a resolution of 0.01 mg. Authors suggest adopting a scale with an appropriate resolution, at least equal to 5% of the specimen mass.

Finally, each patch area was evaluated via Matlab software by image processing of scanned images (detailed procedure in APPENDIX, SECTION 8.5.2).

8.5.2 • *Evaluation of the patch area*

To obtain the grammage-thickness relationship for the different types of membranes (Ny150, Ny250 and Ny400), it was necessary to evaluate for each patch not only the mass and thickness but also the grammage. The calculation of the grammage requires the knowledge of both the mass and the surface area of each patch.

To carefully assess the area, after measuring both the mass and the thickness of each nanofibrous patch by subtracting the thickness of the supporting paper from the overall thickness (nanomat + supporting paper), the supporting papers were retained and analyzed. The area evaluation was carried out on the supporting paper as it is easy to handle, unlike the nanofibrous mat. Every single patch of supporting paper was properly classified by an alphanumerical code so that it can be uniquely referred to as its nanofibrous sample. The number identifies the membrane stripe (from 1 to 6, increasing with electrospinning deposition time), whilst the letters identify the relative position of each patch inside the considered stripe: left (L), center-left (CL), center (C), center-right (CR), right (R).

The patches were scanned through a Kyocera TASKalfa 3551ci KX photocopier at a resolution of 600 dpi, to have a high precision on the edges and therefore an accurate evaluation of the area. A ruler was placed on the scanning plane together with the patches to verify that there was no scaling during the copy (FIGURE 8.19A). Subsequently, the scans were imported into Adobe Photoshop and, for each of them, the correlation between pixels and millimeters was assessed. The images were then segmented in B/W at a 50% threshold and the ruler area removed, leaving only the patches (FIGURE 8.19B).

The images thus obtained were imported into Matlab software and analyzed with the Image Segmenter tool. This allows, by creating a binary mask, to segment and convert the images into logical class. The images were then analyzed with the Image Region Analyzer tool, which allows obtaining the area in pixels of each patch (FIGURE 8.20). Finally, knowing the pixel-millimeters conversion coefficient previously established, it

is possible to transform in mm² the area values expressed in pixel, and so calculate the patch grammage as the mass on area ratio.

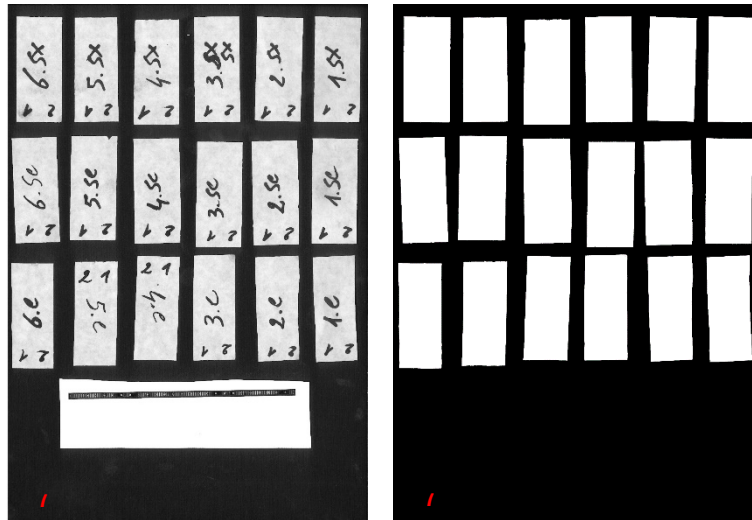
FIGURE 8.19 • (A) Representative scan of Ny250 membrane and (B) the same image segmented in B/W at a 50% threshold
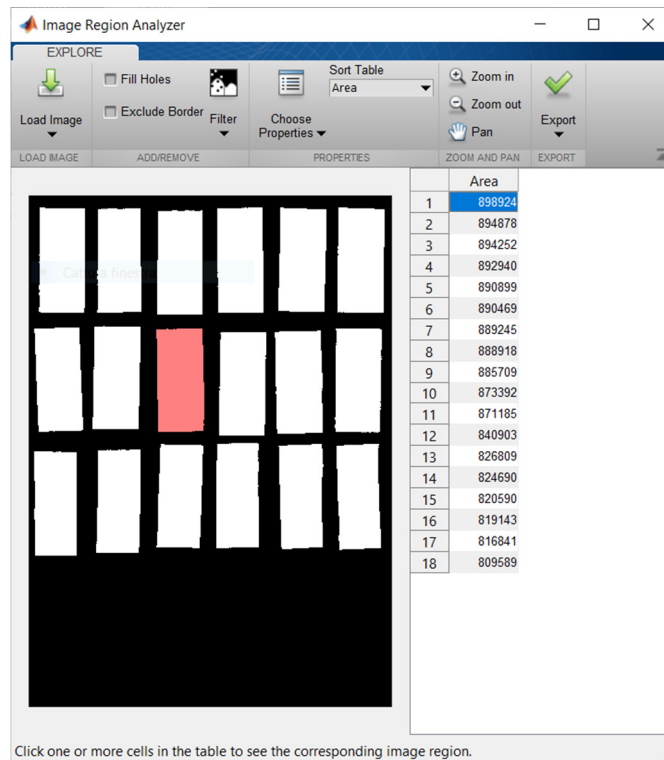
FIGURE 8.20 • Representative Image Region Analyzer tool (Matlab) screenshot reporting the area of each patch in pixels

8.5.3 • *Tensile stress-strain curves*
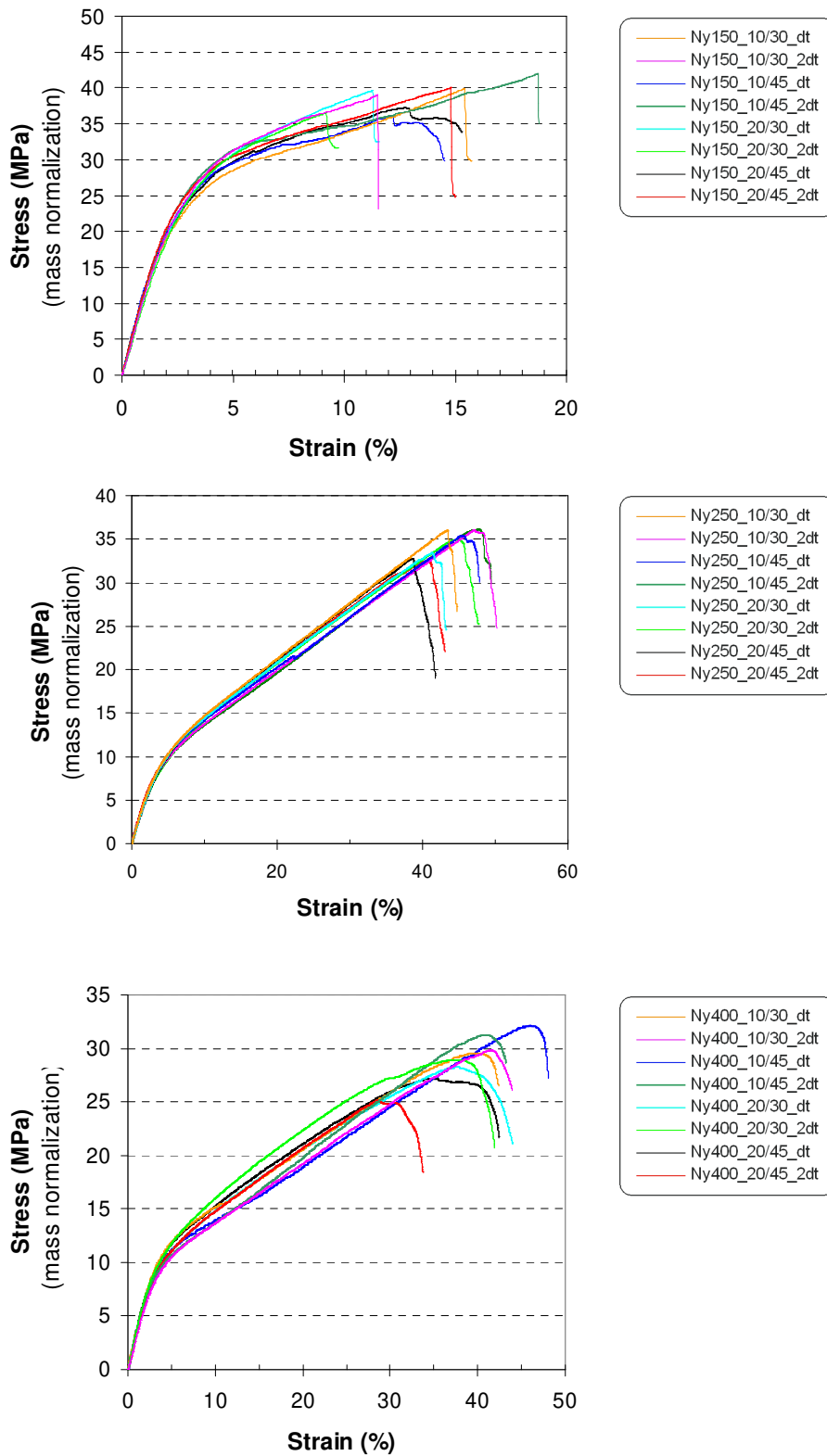
FIGURE 8.21 • Representative stress-strain curves of the different specimen configurations for each membrane type

8.5.4 • *Effect of the specimen geometry on the tensile properties*
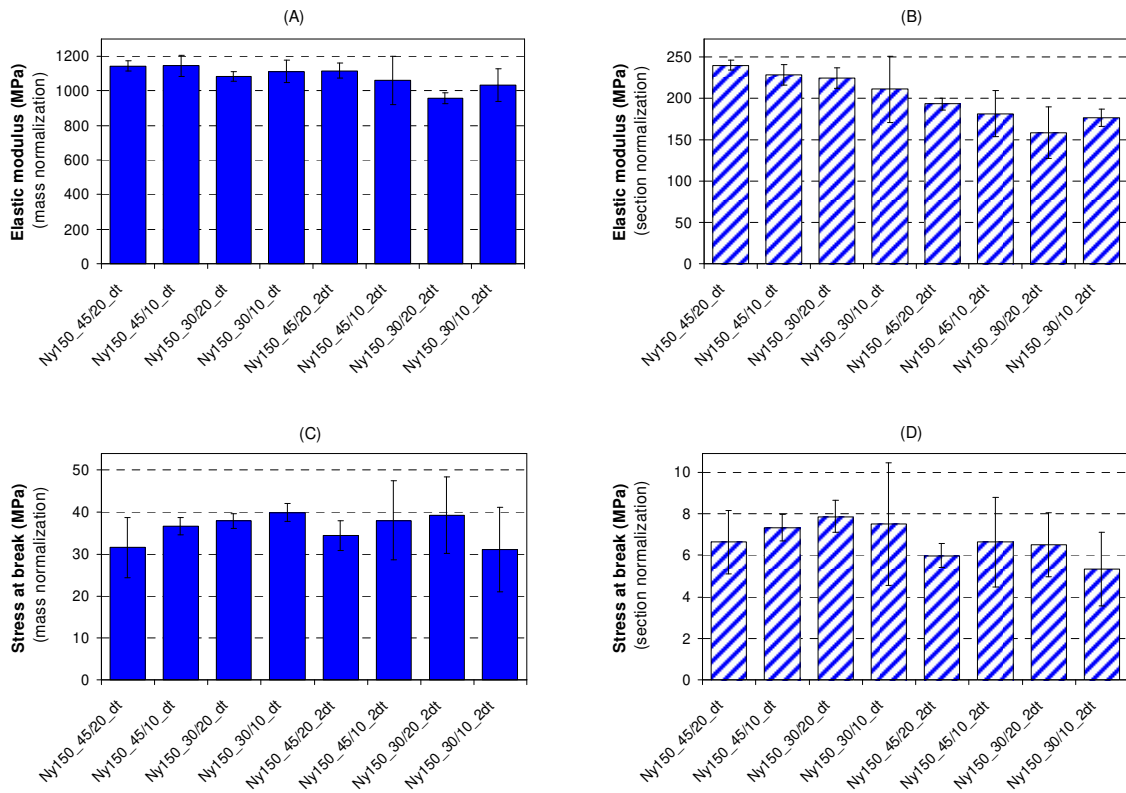
FIGURE 8.22 • Elastic modulus and maximum stress for the specimens obtained from the membrane Ny150_dt and Ny150_2dt, normalized both on mass (A and C respectively) and on cross-section area (B and D respectively)

FIGURE 8.23 • Elastic modulus and maximum stress for the specimens obtained from the membrane Ny250_dt and Ny250_2dt, normalized both on mass (A and C respectively) and on cross-section area (B and D respectively)

FIGURE 8.24 • Elastic modulus and maximum stress for the specimens obtained from the membrane Ny400_dt and Ny400_2dt, normalized both on mass (A and C respectively) and on cross-section area (B and D respectively)
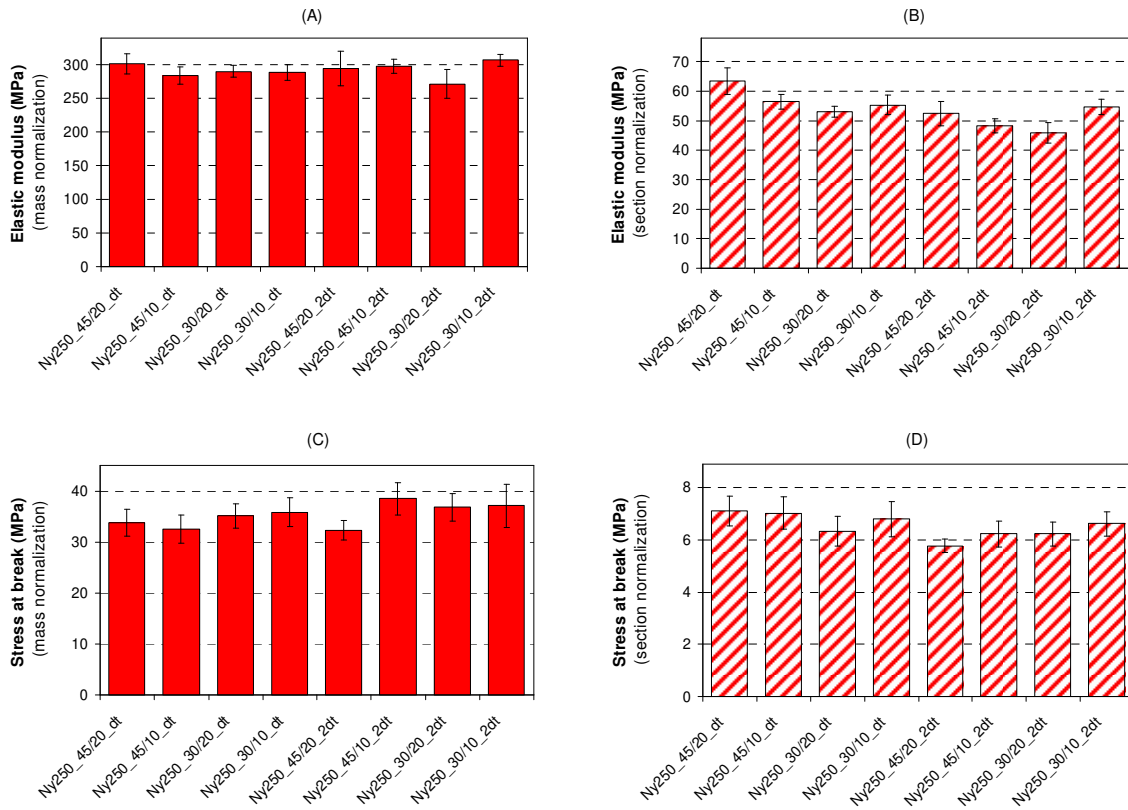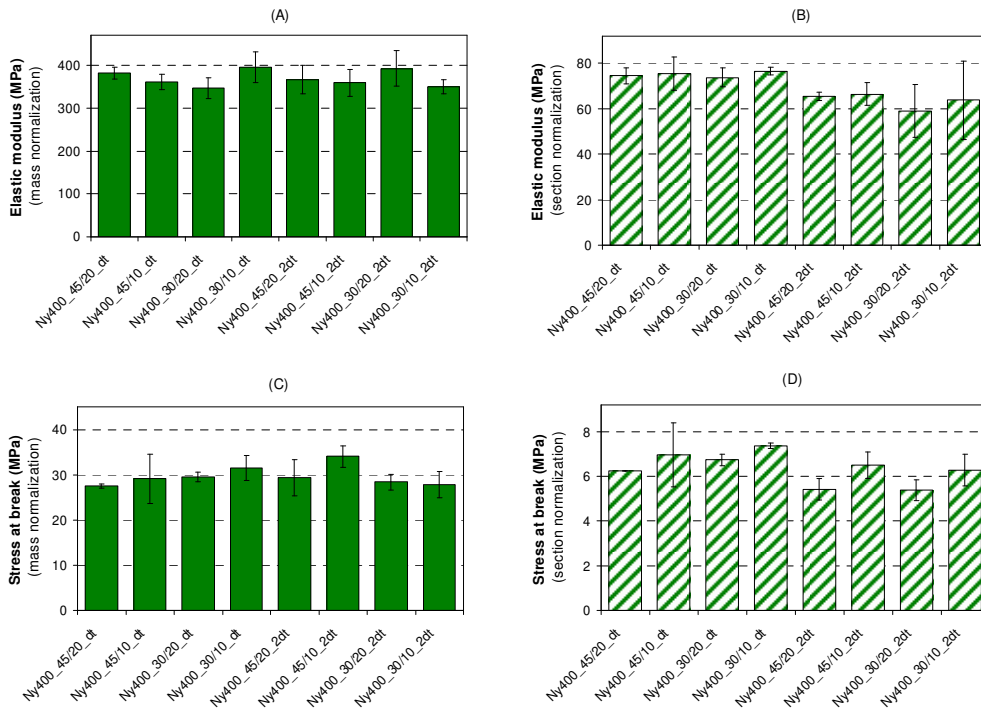
References

[1]   BS EN ISO 9092:2019 - Nonwovens – Vocabulary, (2019).

[2]   J. Nawab, Textile Engineering, De Gruyter, Berlin, Boston, 2016.
        https://doi.org/10.1515/9783110413267.

[3]   S.J. Russell, Handbook of Nonwovens, Elsevier, 2007.

[4]   D. Semnani, Geometrical characterization of electrospun nanofibers, in: Electrospun Nanofibers,
        Elsevier, 2017: pp. 151–180. https://doi.org/10.1016/B978-0-08-100907-9.00007-6.

[5]   A. Baji, Y.-W. Mai, S.-C. Wong, Effect of fiber diameter on the deformation behavior of self-
        assembled carbon nanotube reinforced electrospun Polyamide 6,6 fibers, Mater. Sci. Eng. A. 528
        (2011) 6565–6572. https://doi.org/10.1016/j.msea.2011.05.012.

[6]   X. Qin, S. Subianto, Electrospun nanofibers for filtration applications, Electrospun Nanofibers.
        (2017) 449–466. https://doi.org/10.1016/B978-0-08-100907-9.00017-9.

[7]   A. Sensini, C. Gualandi, A. Zucchelli, L.A. Boyle, A.P. Kao, G.C. Reilly, G. Tozzi, L.
        Cristofolini, M.L. Focarete, Tendon Fascicle-Inspired Nanofibrous Scaffold of Polylactic
        acid/Collagen with Enhanced 3D-Structure and Biomechanical Properties, Sci. Rep. 8 (2018)
        17167. https://doi.org/10.1038/s41598-018-35536-8.

[8]   Q.P. Pham, U. Sharma, A.G. Mikos, Electrospinning of Polymeric Nanofibers for Tissue
        Engineering Applications: A Review, Tissue Eng. 12 (2006) 1197–1211.
        https://doi.org/10.1089/ten.2006.12.1197.

[9]   D. Fabiani, F. Grolli, M. Speranza, S.V. Suraci, T.M. Brugo, A. Zucchelli, E. Maccaferri,
        Piezoelectric Nanofibers for Integration in Multifunctional Materials, in: 2018 IEEE Conf. Electr.
        Insul. Dielectr. Phenom., IEEE, 2018: pp. 14–17. https://doi.org/10.1109/CEIDP.2018.8544896.

[10]   D. Fabiani, F. Grolli, G. Selleri, M. Speranza, T.M. Brugo, E. Maccaferri, D. Cocchi, A.
        Zucchelli, Nanofibrous piezoelectric structures for composite materials to be used in electrical
        and electronic components, Proc. Nord. Insul. Symp. (2019) 1–5.
        https://doi.org/10.5324/nordis.v0i26.3263.

[11]   D. Bonincontro, F. Fraschetti, C. Squarzoni, L. Mazzocchetti, E. Maccaferri, L. Giorgini, A.
        Zucchelli, C. Gualandi, M.L. Focarete, S. Albonetti, Pd/Au Based Catalyst Immobilization in
        Polymeric Nanofibrous Membranes via Electrospinning for the Selective Oxidation of 5-
        Hydroxymethylfurfural, Processes. 8 (2020) 45. https://doi.org/10.3390/pr8010045.

[12]   D. Cocchi, F. Musiari, T.M. Brugo, A. Pirondi, A. Zucchelli, F. Campanini, E. Leoni, L.
        Mazzocchetti, Characterization of aluminum alloy-epoxy bonded joints with nanofibers obtained
        by electrospinning, J. Adhes. 96 (2020) 384–401.
        https://doi.org/10.1080/00218464.2019.1666716.

[13]   R. Palazzetti, A. Zucchelli, Electrospun nanofibers as reinforcement for composite laminates
        materials – A review, Compos. Struct. 182 (2017) 711–727.
        https://doi.org/10.1016/j.compstruct.2017.09.021.

[14]   L. Mazzocchetti, T. Benelli, E. Maccaferri, S. Merighi, J. Belcari, A. Zucchelli, L. Giorgini, Poly-
        m -aramid electrospun nanofibrous mats as high-performance flame retardants for carbon fiber
        reinforced composites, Compos. Part B Eng. 145 (2018) 252–260.
        https://doi.org/10.1016/j.compositesb.2018.03.036.

[15]   BS EN ISO 10319:1996 - Geotextiles — Wide-width tensile test, (1996).

[16]   BS EN ISO 1924-2:2008 - Paper and board — Determination of tensile properties, Draft Int.
        Stand. ISO/DIS 1924-2. (2008).

[17]   BS ISO 1924-3:2005 - Paper and board — Determination of tensile properties, 3 (2005).

[18]   BS EN ISO 9073-2:1997 - Textiles — Test methods for nonwovens — Part 2: Determination of
        thickness, Management. 3 (1997).

[19]   BS EN ISO 534:2011 - Paper and board — Determination of thickness, density and specific volume, (2011).

[20]   X. Yu, C. Li, H. Tian, L. Yuan, A. Xiang, J. Li, C. Wang, A.V. Rajulu, Hydrophobic cross-linked zein-based nanofibers with efficient air filtration and improved moisture stability, Chem. Eng. J. 396 (2020) 125373. https://doi.org/10.1016/j.cej.2020.125373.

[21]   X. Yang, Y. Pu, Y. Zhang, X. Liu, J. Li, D. Yuan, X. Ning, Multifunctional composite membrane based on BaTiO3@PU/PSA nanofibers for high-efficiency PM2.5 removal, J. Hazard. Mater. 391 (2020) 122254. https://doi.org/10.1016/j.jhazmat.2020.122254.

[22]   U.Y. Karatepe, T. Ozdemir, Improving mechanical and antibacterial properties of PMMA via polyblend electrospinning with silk fibroin and polyethyleneimine towards dental applications, Bioact. Mater. 5 (2020) 510–515. https://doi.org/10.1016/j.bioactmat.2020.04.005.

[23]   S.J. Kim, B.M. Hong, W.H. Park, The effects of chitin/chitosan nanowhiskers on the thermal, mechanical and dye adsorption properties of electrospun PVA nanofibrous membranes, Cellulose. 27 (2020) 5771–5783. https://doi.org/10.1007/s10570-020-03191-w.

[24]   B. Li, F. Xiong, B. Yao, Q. Du, J. Cao, J. Qu, W. Feng, H. Yuan, Preparation and characterization of antibacterial dopamine-functionalized reduced graphene oxide/PLLA composite nanofibers, RSC Adv. 10 (2020) 18614–18623. https://doi.org/10.1039/D0RA03224G.

[25]   F. Tuğcu-Demiröz, S. Saar, S. Tort, F. Acartürk, Electrospun metronidazole-loaded nanofibers for vaginal drug delivery, Drug Dev. Ind. Pharm. 46 (2020) 1015–1025. https://doi.org/10.1080/03639045.2020.1767125.

[26]   S. Tiwari, A. Gaur, C. Kumar, P. Maiti, Electrospun hybrid nanofibers of poly(vinylidene fluoride) and functionalized graphene oxide as a piezoelectric energy harvester, Sustain. Energy Fuels. 4 (2020) 2469–2479. https://doi.org/10.1039/D0SE00033G.

[27]   M. Mushtaq, M. Wasim, M. Naeem, M. Khan, S. Yue, H. Saba, T. Hussain, M. Siddiqui, A. Farooq, Q. Wei, Composite of PLA Nanofiber and Hexadecyl Trimethyl-Ammonium Chloride-Modified Montmorillonite Clay: Fabrication and Morphology, Coatings. 10 (2020) 484. https://doi.org/10.3390/coatings10050484.

[28]   A. Góra, L. Tian, S. Ramakrishna, S. Mukherjee, Design of Novel Perovskite-Based Polymeric Poly(l-Lactide-Co-Glycolide) Nanofibers with Anti-Microbial Properties for Tissue Engineering, Nanomaterials. 10 (2020) 1127. https://doi.org/10.3390/nano10061127.

[29]   H. Gallah, F. Mighri, A. Ajji, J. Bandyopadhyay, Flexible electrospun PET/TiO2 nanofibrous structures: Morphology, thermal and mechanical properties, Polym. Adv. Technol. 31 (2020) 1612–1623. https://doi.org/10.1002/pat.4890.

[30]   D. Chuan, R. Fan, Y. Wang, Y. Ren, C. Wang, Y. Du, L. Zhou, J. Yu, Y. Gu, H. Chen, G. Guo, Stereocomplex poly(lactic acid)-based composite nanofiber membranes with highly dispersed hydroxyapatite for potential bone tissue engineering, Compos. Sci. Technol. 192 (2020) 108107. https://doi.org/10.1016/j.compscitech.2020.108107.

[31]   S. An, H.S. Jo, G. Li, E. Samuel, S.S. Yoon, A.L. Yarin, Sustainable Nanotextured Wave Energy Harvester Based on Ferroelectric Fatigue☐Free and Flexoelectricity☐Enhanced Piezoelectric P(VDF☐TrFE) Nanofibers with BaSrTiO 3 Nanoparticles, Adv. Funct. Mater. 30 (2020) 2001150. https://doi.org/10.1002/adfm.202001150.

[32]   S. Hu, J. Wu, Z. Cui, J. Si, Q. Wang, X. Peng, Study on the mechanical and thermal properties of polylactic acid/hydroxyapatite@polydopamine composite nanofibers for tissue engineering, J. Appl. Polym. Sci. 137 (2020) 49077. https://doi.org/10.1002/app.49077.

[33]   M. Gazzano, C. Gualandi, A. Zucchelli, T. Sui, A.M. Korsunsky, C. Reinhard, M.L. Focarete, Structure-morphology correlation in electrospun fibers of semicrystalline polymers by simultaneous synchrotron SAXS-WAXD, Polymer (Guildf). 63 (2015) 154–163. https://doi.org/10.1016/j.polymer.2015.03.002.

[34]   L. Zhao, W. Kai, Y. He, B. Zhu, Y. Inoue, Effect of aging on fractional crystallization of poly(ethylene oxide) component in poly(ethylene oxide)/poly(3-hydroxybutyrate) blends, J. Polym. Sci. Part B Polym. Phys. 43 (2005) 2665–2676. https://doi.org/10.1002/polb.20552.

[35]   O. Kallmes, H. Corte, The Structure of Paper - The statistical geometry of an ideal two dimensional fiber network, Tappi J. (1960).

[36]   R.E. Miles, Random polygons determined by random lines in a plane, II, Proc. Natl. Acad. Sci. (1964). https://doi.org/10.1073/pnas.52.5.1157.

[37]   S.J. Eichhorn, W.W. Sampson, Relationships between specific surface area and pore size in electrospun polymer fibre networks, J. R. Soc. Interface. (2010). https://doi.org/10.1098/rsif.2009.0374.

[38]   P. Chavoshnejad, M.J. Razavi, Effect of the Interfiber Bonding on the Mechanical Behavior of Electrospun Fibrous Mats, Sci. Rep. 10 (2020) 1–10. https://doi.org/10.1038/s41598-020-64735-5.

[39]   K. Molnar, L.M. Vas, T. Czigany, Determination of tensile strength of electrospun single nanofibers through modeling tensile behavior of the nanofibrous mat, Compos. Part B Eng. 43 (2012) 15–21. http://dx.doi.org/10.1016/j.compositesb.2011.04.024.

[40]   W. Li, Y. Zong, Q. Liu, Y. Sun, Z. Li, H. Wang, Z. Li, A highly stretchable and biodegradable superamphiphobic fluorinated polycaprolactone nanofibrous membrane for antifouling, Prog. Org. Coatings. 147 (2020) 105776. https://doi.org/10.1016/j.porgcoat.2020.105776.

[41]   X. Zhang, X. Yang, G.G. Chase, Filtration performance of electrospun acrylonitrile-butadiene elastic fiber mats in solid aerosol filtration, Sep. Purif. Technol. 186 (2017) 96–105. https://doi.org/10.1016/j.seppur.2017.06.002.

[42]   T. Tanimoto, A new vibration damping CFRP material with interlayers of dispersed piezoelectric ceramic particles, Compos. Sci. Technol. 67 (2007) 213–221. https://doi.org/10.1016/j.compscitech.2006.08.022.

Chapter 9

CONCLUSIONS

Searching for systems able to limit the catastrophic consequences of composite laminates failure is fundamental for increasing people's safety and reliability of components, leading to economic savings too. Delamination is the most serious drawback which afflicts laminates, still limiting their widespread use as metals replacement. Moreover, stiff composites display low damping capacity, which may contribute to delamination triggering, as presented in the introduction (CHAPTER 1).

In this experimental thesis, the production and use of advanced electrospun nanofibrous mats for hindering delamination, improving damping capacity, and for sensing of composite laminates was discussed.

Rubbery nanofibrous mats to be interleaved between prepreg laminae during object manufacturing, i.e. in the lamination step, were proposed as a smart approach for hampering delamination and enhancing damping capacity. Two different "elastomeric polymeric systems" able to be electrospun via single-needle electrospinning were presented and discussed. The choice of polymers with specific characteristics allowed the creation of dimensionally stable rubbery nanofibers without the need of a crosslinking step. As illustrated in SECTION 1.4 of CHAPTER 1, most of the rubbery fibers already proposed in the literature are just proof-of-concepts, and rubber crosslinking is mandatory to try to maintain the fibrous/nanofibrous structure.

Polymeric blends, made of Nitrile Butadiene Rubber (NBR) and a thermoplastic semi-crystalline counterpart, were electrospun to produce rubbery nanofibers. NBR was chosen as the elastomer component, also for its high compatibility with epoxy resins, while the semi-crystalline polymers with different thermal properties enable the retention of the nanofiber structure. It was demonstrated that the electrospinning fast solvent evaporation rate (higher than solvent casting and spin coating) is able to induce in blends with "liquid" NBR a thermoplastic elastomeric (TPE) structure that holds stable over time without any further processing, like crosslinking.

In the case of NBR/poly(ε-caprolactone) (NBR/PCL) pair it was found the formation of a homogeneous blend with a low-T_g region due to blended NBR and PCL amorphous phases, and a crystalline phase which allows the morphology retention at least for two years (CHAPTER 2). Even though NBR/PCL pair has a slight relative solubility, the phase separation is avoided thanks to the abovementioned fast solvent evaporation occurring during electrospinning, thus freezing the natural tendency to phase separate, as stated by the thermodynamics. When a low melting temperature polymer was used as the semi-crystalline counterpart, like PCL ($T_m \approx 60$ °C), the rubbery mat may diffuse during curing cycle and mix with the epoxy resin, making it more toughened. In this case, the energy required for cracks to form and propagate rises. It was found a dramatic increase of the energy release rate (G) at initiation and propagation stages (up to 5.8× and 4.4× the reference values, respectively) in Mode I loading, while in Mode II the improvement is limited (up to +34% of G_{II}), as presented in CHAPTER 3. By increasing the NBR content from 20 to 60%wt, the composite damping increases, but at the expenses of a decreased maximum operating temperature (lowering of E' onset, T_g). The system also proved to be easily tailorable: simply acting on the percentage of rubber in the nanofiber and/or the number of interleaved mats, the best compromise between damping and maximum operating temperature can be achieved. Despite this drawback, the application of rubbery nanofibers for localized modification of laminates in critical spots, such as free edges, holes, ply-drops and adhesive bonding, surely provides a flexible, easy and a valid solution for hampering microcracks formation and propagation where interlaminar stresses are concentrated the most.

NBR/PCL nanofibrous mats effect on CFRP damping was deeply investigated in CHAPTER 4 via single cantilever beam vibration tests. Results show a maximum damping enhancement of 77%, maintaining original stiffness and strength under T_g, as assessed via three-point bending tests at different temperatures.

To bypass the abovementioned possible T_g lowering of nano-modified CFRPs, a different blend was proposed (CHAPTER 5): PCL was replaced by Nomex, a semi-crystalline polyaramide with a high-T T_g (≈ 280 °C). In this case, Nomex is unaffected by the applied curing cycle. While the NBR liquid rubber is still free to mix with the epoxy resin, the Nomex is not. Therefore, NBR/Nomex mats can act at the same time by the so-called "bridging" mechanism and the already mentioned matrix toughening like

happens with NBR/PCL mats. Mode I and Mode II loading tests show a significant improvement of interlaminar fracture toughness, especially G_I (up to +180%), still maintaining both the original laminate stiffness and T_g. Such results pave the way to the extensive and reliable use of NBR/Nomex mats in composite laminates to improve delamination resistance. It was also established that pure Nomex nanofibers dramatically worsen the delamination resistance, with a G_I drop of 50-70%, probably due to low adhesion between polymer and epoxy resin. NBR/Nomex nanofibers do not affect the damping capacity of nano-modified CFRPs, showing almost the same damping behaviour of pristine composite.

The concerns related to composites reliability can be faceted not only by increasing their "intrinsic" delamination resistance, but also by implementing systems able to warn in time possible threats, avoiding component failure. The possibility of exploiting piezoelectric nanofibrous mats for producing self-sensing laminates capable of detecting impacts was demonstrated in CHAPTER 6. In particular, Glass Laminate Aluminium Reinforced Epoxy (GLARE) was nano-modified with poly(vinylidenefluoride-trifluoroethylene) (PVDF-TrFE) nanofibers to add sensing capability. The piezoelectric signal was extracted exploiting the aluminium foils already present in GLARE, thus avoiding the addition of dedicated electrodes that may lower its overall mechanical performance. To discard triboelectric and ambient noise, it was fundamental to ground the external GLARE aluminium foils, leading to an excellent piezoelectric response, which follows well the signal generated by a commercial load cell. Non-destructive impact tests were performed using an instrumented drop-weight tower to investigate the real-time electrical response of the self-sensing laminate. It was found excellent sensor linearity, defined as sensor signal versus impact force, of 0.99. Future studies will focus on the evaluation of the impact strength of the self-sensing hybrid laminate.

Even if nanofibers are nano-objects, it is possible to reinforce them with nano-reinforcements for tailoring peculiar properties. CHAPTER 7 showed the possibility of adding graphene nanoplatelets for obtaining Nylon 66 nanofibrous mats with improved tensile mechanical properties (up to +61% Young's modulus, +85% maximum strength), potentially useful to boost the delamination resistance of CFRP laminates.

As also resumed here, nanofibrous nonwovens show high versatility and outstanding properties, with reduced weight. However, the assessment of their real mechanical

properties is complex due to the high material flexibility and deformability exhibited, which severely affect results reliability. In CHAPTER 8 it was presented an accurate, systematic, and critical study concerning tensile testing of nonwovens, using electrospun Nylon 66 random nanofibrous mats as case study. To bypass the non-reliable measurement of mat thickness, it was proposed a mass-based normalization of load, allowing to obtain reliable and repeatable results, similarly to what happens for bulk materials. It was also adopted a method which takes into account the mat grammage for calculating tensile stress. Although the grammage-based normalization is less reliable than the mass-based one, the use of mat grammage proved to provide better results than the "classic" normalization approach based on the specimen cross-section area. Moreover, the grammage-based method allows to re-normalize already tested specimens whose load-displacement curves were previously normalized on the cross-section area, thus benefitting of improved reliability and comparability of old data. Indeed, a linear dependence between mat grammage and thickness was found, whose angular coefficient depends on the specific nanofiber morphology. Nanofibers diameter and specimen geometry were investigated too for thoroughly describing the nanomat tensile behaviour, also considering the polymer thermal properties and the nanofibers crossings number as a function of the nanofibers diameter. Results show no influence of specimen geometry (gauge length, width and grammage) on recorded tensile properties, while nanofibers diameters can affect elastic modulus, maximum stress, strain at max stress and toughness. It was calculated that the number of nanofibers crossings is related to fiber diameter. Below a certain threshold, the cited properties suddenly change: by decreasing the diameter, the crossings rise and the mat behaviour becomes more stiff and fragile. Stress-strain data were also analysed using a phenomenological data fitting model to better interpret the tensile mat behaviour. Mass-based normalization of load and data fitting model were successfully applied also to NBR/PCL, NBR/Nomex and graphene-reinforced Nylon 66 nanofibrous mats presented in CHAPTERS 2, 5 and 7, respectively.